Physical Object Identification and Authentication Applications by

Rudolf Schraml

Cumulative dissertation submitted to the
Faculty of Natural Sciences, University of Salzburg
in partial fulfillment of the requirements
for the Doctoral Degree.

Thesis Supervisor
Univ.-Prof. Mag. Dr. Andreas Uhl

Department of Computer Sciences
University of Salzburg
Jakob Haringer Str. 2
5020 Salzburg, AUSTRIA

Salzburg, Nov 2020

Abstract

In the scope of Industry 4.0 cyber-physical systems (CPSs) are the core building-blocks enabling to connect the real world with the virtual, more specifically both worlds conflate to each other. This requires to collect data of real world objects and processes.

This cumulative thesis deals with biometric identification of objects in two different domains: (i) Round wood identification in the wood industry: Efficient tracking of roundwood as well as quality analysis and measurement are key technologies to improve the wood supply chain management and roundwood processing to fulfil economical, ecological and social requirements. In this thesis, we show the basic feasibility of roundwood tracking based on digital log end images. (ii) Fish identification in intensive aquaculture: The movement from mass to smart fish production requires to consider each fish as individual instead of viewing at the total stock of fish in a sea cage or tank. The goal of smart fish farming is based on the principle of eco-intensification, which means to improve fish welfare in order to increase the overall profit. We show the feasibility of Atlantic salmon identification based on iris imagery as an approach to move towards precision fish farming.

For both applications, we investigated the distinctiveness and stability of the utilized biometric characteristics (annual ring pattern of roundwood, fish iris pattern). Both are required properties and moreover quality criteria of a biometric characteristic.

Furthermore, this cumulative thesis treats physical authentication of medical drugs. Contrary to object identification, the goal is to determine if an object belongs to certain class of objects which show the same physical properties. Physical object authentication, as considered in this thesis, is referred to as classification-based authentication. This cumulative thesis proves the feasibility of classification-based drug authentication based on packaging material properties.

For each of the three different applications covered in this cumulative thesis: (i) data has been acquired and pre-processed, (ii) feature extraction and comparison or classification methods have been adopted and developed and (iii) experimental evaluations have been performed.

Abstract (German)

Im Rahmen von Industrie 4.0 sind sogenannte Cyber-Physische Systeme (CPS) Kernbausteine, die die reale Welt mit der virtuellen Welt verbinden, genauer gesagt, beide Welten verschmelzen miteinander. Dies erfordert das Sammeln von Daten von Objekten und von Prozessen der realen Welt.

Diese kumulative Arbeit befasst sich mit der biometrischen Identifizierung von Objekten in zwei verschiedenen Anwendungsbereichen: (i) Identifizierung von Rundholz in der Holzindustrie: Effiziente Rückverfolgbarkeit von Rundholz sowie Qualitätsanalyse sind Schlüsseltechnologien zur Verbesserung des Rohstoffeinsatzes und der Rundholzverarbeitung, um wirtschaftliche, ökologische und soziale Kriterien zu erfüllen. In dieser Arbeit zeigen wir die grundlegende Machbarkeit der Rundholzverfolgung anhand digitaler Stammendbilder. (ii) Identifizierung von Fischen in intensiver Aquakultur: Der Übergang von Massenproduktion zu einer smarten Fischproduktion erfordert, dass jeder Fisch als Individuum betrachtet wird, anstatt des Gesamtbestandes an Fischen in einem Behälter zu betrachten. Das Ziel einer intelligenten Fischzucht basiert auf dem Prinzip der Öko-Intensivierung, d.h. der Verbesserung des Fischwohls, um damit schlussendlich den Gesamtgewinn zu steigern. In dieser Arbeit zeigen wir die Machbarkeit der Identifizierung von Lachs anhand von Irisbildern.

Für beide Anwendungen wurde die Unterscheidungskraft und Stabilität der verwendeten biometrischen Merkmale (Jahresringmuster aus Rundholz, Fischirismuster) untersucht und ausgwertet. Beides sind Qualitätskriterien eines biometrischen Merkmals.

Darüber hinaus befasst sich diese kumulative Arbeit mit der physischen Authentifizierung von Arzneimitteln. Im Gegensatz zur Objektidentifikation besteht das Ziel darin zu überprüfen, ob ein Objekt zu einer bestimmten Klasse von Objekten gehört, die dieselben physikalischen Eigenschaften aufweisen. Die in dieser Arbeit berücksichtigte physische Objektauthentifizierung wird als klassifikationsbasierte Authentifizierung bezeichnet. Wir belegen die Machbarkeit einer klassifizierungsbasierten Arzneimittelauthentifizierung auf der Grundlage der Eigenschaften des Verpackungsmaterials.

Für jede der drei verschiedenen Anwendungen, die in dieser kumulativen Arbeit behandelt werden, wurden: (i) Daten erfasst und vorverarbeitet, (ii) Methoden zur Merkmalsextraktion und Merkmalsvergleich oder zur Merkmalsklassifizierung entwickelt und (iii) experimentelle Versuche und Auswertungen durchgeführt.

Acknowledgments

Every journey comes to an end at some point. When I decided spontaneously in 2005 to try it again in a course of study, I had no idea, what possibilities this could offer in future. Admittedly, the first semesters were not easy for me, but the solid basic training made it possible for me, to acquire competences in different areas of computer science that I had never imagined before. At the end of my bachelor studies, I stumbled on Prof. Andreas Uhl's website about possible master thesis topics. As a graduate of a higher technical college for forest industry, I was attracted by topics dealing with wood imaging. I asked Prof. Uhl at an early stage of my master studies, which definitely marks the beginning for my work in the direction of this thesis. Since then, I've been working in this research area and was able to experience a lot during this time and developed myself scientifically and personally.

Apart from the scientific contributions that are summarized in this thesis, there were also special events during this time, I would like to mention in a chronological order, as a reminder and thanks. I started my PhD shortly after finishing master studies in 2013.

2014 was a good year, the first publication was accepted and I remember the journey by night train to my first international conference (ICIP'2014) in Paris. Further contributions were under review and at the beginning of 2015 two more conference contributions were accepted. A first journal article was in preparation, which got accepted later in this year. A special highlight in 2015 was a trip to Guatemala with an environmental activist and start-up founder for a log tracing system to the Maya Biosphere reserve. Not only the trip itself was very exciting, there were also interesting discussions with authorities and institutions about log tracing and possible approaches to fight against illegal logging. My personal highlights were a meeting in the U.S. Agency for International Development in Guatemala City and a meeting at the regional office of the government's National Council of Protected Areas (CONAP) in Peten. Together, with the owner of Bedell Guitar's and members from the World Ressources Institute (WRI), we were introduced to the different concessions in the reserve and we started our trip to the Custosel concession hold by 85 families. For a short video, I refer to the blog post at the Bedell guitar webpage [1]. At the end of 2015 I traveled to Nancy in France for data acquisition and to discuss a future cooperation. Furthermore in September 2015 we attendend the ICIP'2015 in Quebec (Canada), where I and my colleague Heinz Hofbauer extended our stay to climb and travel around.

2016 was very challenging, because the "TreeBio" project ended. In the end, however, this was entirely positive, because it enabled me to work on other research topics, such as drug packaging authentication. Apart from that, we started to write new research proposals for the wood biometrics topic. I learned a lot, especially, that you shouldn't give up. At the end of 2017 we got the French-Austrian research project "TreeTrace" accepted, which was initiated in 2015. Further, in 2016, I finished my teacher education and I started my year of training at the economic high school WRG Salzburg.

2017 I was involved in the EU project "PROTECT" and continued our work on drug packaging authentication, where we got a paper accepted at WIFS'2017 in France. At this time, some approaches and research directions led to nothing, which can also be part of a dissertation. Since September 2017 to the present I am teaching computer science at the Higher Technical College for Forest Products and Industry in Kuchl. Another highlight of my PhD was an invitation to the

[1] https://bedellguitars.com/blog/tom-bedell-sourcing-mahogany-in-guatemala

Global Timber Tracking Network Meeting and the Forest Legality Week in Washington. There I met people I was in Guatemala with and learned a lot about wood identification methods. At the end of December, Andreas Uhl sent me to Norway to discuss a project proposal about fish monitoring. This proposal was not successful, so far, but we got granted a data acquisition project which is described in my thesis for our work on fish identification.

2018 was an intense year, because of lots of travelling for the fish data acquisition to Norway and the start of the TreeTrace project with a project kick-off in May in Nancy. Before this meeting I was invited by the company Otmetka to come to Uppsala in Sweden to discuss a cooperation and to promote our vision for biometric log tracking in the forest-based industry to members of the Swedish Timber Measurement Council. 2018 will always be remembered since my first child Ludwig was born in June and we bought an apartment in the mountains close to my hometown.

In 2019, my scientific work was characterized by the data acquisition for the TreeTrace project and the work on the fish iris identification article. At the time of writing this abstract its August 2020 and we work with the TreeTrace datasets. I am happy as well as satisfied to finish the writing of my PhD thesis just before the birth of my second child Mathilda.

Now its time to come to an end on this journey. I would like to thank my doctoral supervisor Andreas Uhl for all his support and advises and my colleagues from our research group. We had a lot of fun and discussions. Finally, thanks to my lovely parents and my beloved partner Tanja, for their patience and support, even, if they have not always had it easy with me.

Salzburg, August 2020 Rudolf Schraml

Am Ende ist das, was uns letzendlich bleibt, die Erinnerung.

Contents

1. Introduction

In the past decade the interaction of the Internet of Things (IoT) and the Internet of Services (IoS) triggered the beginning of the 4th industrial revolution. The move from Industry 3.0 to Industry 4.0 is characterized by an increasing digitization. Nowadays, Cyber Physical Systems (CPS) are the building block of numerous developments in industry and economy that are identified or supplemented with the attribute "Smart". The main paradigm is the connection between computational and real world physical entities as well as processes, thereby collecting and using data to move towards intelligent and autonomous systems in order to support or replace humans. CPSs constitute disruptive technologies requiring to rethink, change or replace well established processes and technologies in many domains. In a CPS the communication between physical entities is established by the IoT. A basic requirement for the IoT is that physical objects can be identified and addressed. In the scope of this thesis, we define a physical object as a living or non-living real world object, which is non-electric and it is not able to communicate. The most common technology to enable identification of such objects in the industry is labeling using Radio Frequency Identification (RFID) technology. Each object is attached with a RFID transponder providing an unique object identifier. RFID is a low cost and versatile technology to set up IoT systems. Another approach comes down to identify objects based on their physical properties. Apparently, this enables physical marking free identification of objects which shows advantages in terms of counterfeit protection and zero marking efforts.

One obvious and promising approach to establish physical object identification is to transfer concepts of human biometrics to other fields of applications. This is of interest as identification is a basic requirement to move towards Agriculture 4 .0. Research showed that biometric identification is feasible for a variety of livestock animals (e.g. cattle [1] or sheep [3] identification). Identification of livestock individuals enables to move from mass to smart production without the need of physical marking. Depending on the application and animal this may has advantages in terms of animal welfare and reduced costs. Moreover, biometric identification is counterfeit proof compared to some of the physical marking-based approaches. This cumulative thesis deals with physical object identification and authentication. More specifically with three different applications in this field, which were topics of different research projects during my time as PhD student in the research group headed by Andreas Uhl. The peculiarity or commonality in all three applications is that instead of physically marking the objects in the respective application, physical characteristics of the objects are used for identification or authentication. First, in the wood industry roundwood traceability is a basic requirement to fulfil economical, social and environmental issues. State-of-the-art approaches for roundwood log tracking rely on physical marking which suffers from costs and anti-counterfeiting. For the second application, fish identification in intensive aquaculture is investigated. The movement from mass to smart production requires continuous monitoring of individual fish. This enables to move towards eco-intensification, i.e. to improve the overall profit by improving fish welfare criteria while reducing costs (e.g. feeding, medication). The third application deals with drug counterfeiting which causes economic loss and poses risks to the patients health. As an alternative solution to drug package serialization in this thesis a classification-based drug packaging authentication approach is presented and investigated.

Section 1.1 and Section 1.2 introduce to physical object identification and authentication. In Chapter 2 for each application an introduction and discussion on open challenges is presented

followed by our contributions.

1.1. Physical Object Identification

As already noted in the introduction, our work in this field is inspired by human biometrics and the basic idea to transfer biometric concepts to other fields of applications.

In the past, biometric systems based on various characteristics, like finger ridge structure, iris or retina pattern, palm, finger- or hand vein pattern, ear shape and many more have been proposed. Even if biometrics are human related, biometric recognition has been transferred to various fields of applications. In the past decades, a variety of research has shown biometrically-inspired approaches for recognition of vegetables, plants, animals and products. Photo and in general visual identification has a long history in animal individuals identification and has already been shown to be feasible for a variety of vertebrates (e.g. for primates [8]). In [17] the authors refer to Physimetrics in case that non-living physical objects are recognized based on object specific characteristics. Introductory, a short overview on biometric systems and performance evaluation is presented followed by a discussion on stability and distinctiveness which are both main quality criteria of a biometric characteristic.

1.1.1. Biometric systems

According to the ISO standard ISO/IEC 2382-37:2017 [12] a biometric system has the purpose to recognize individuals based on behavioural or physiological biometric characteristics. In the context of biometrics, an individual is restricted to humans. For a specific characteristic biometric features can be extracted in order to establish biometric recognition. The elements of a biometric system are: Capture, Feature Extraction, Template Generation, Template Comparison and Decision [18]. In Fig. 1.1 a schematic overview of the biometric toolchain is illustrated.

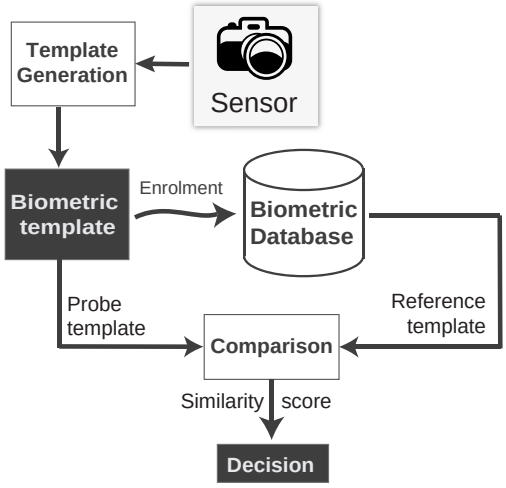

Figure 1.1.: Biometric recognition toolchain

The first step in the toolchain is to capture a digital representation of the utilized biometric characteristic, which is referred to as biometric sample. Commonly, biometric characteristics are captured by an image, which then is the biometric sample. Subsequently, biometric feature

extraction is applied to the biometric sample. The overall target means to extract a compact and distinctive representation of the biometric information. Based on the extracted features, a biometric template is created. In the schematic overview, the Template Generation block includes feature extraction and template formation. In order to enable biometric recognition, the individual needs to be enrolled first, i. e. the biometric template is stored as biometric reference data record in a biometric database. This is referred to as biometric enrolment. Depending on the biometric system metadata of the individual is stored in the same database or in a separate way.

A biometric recognition system either performs biometric verification or identification. For biometric verification the system makes the decision whether an individual is the individual it claims to be or not. For this purpose, a biometric template (=probe template) is generated for the individual, which is then compared to the biometric template of the claimed identity (=reference template) stored in the biometric database. The result of the comparison is a comparison score. Based on this score and a system threshold a decision is made, if the individual is the individual it claims to be. Consequently, biometric verification requires to perform a 1:1 comparison. In case of biometric identification, the biometric system has to determine the identity of an individual without prior knowledge. Thus, it is required to search the corresponding reference template in the biometric database which relates to a 1:n comparison. A common strategy, is that the probe template is compared to all reference templates in the database and the comparison with the best comparison score specifies the identity of the individual. However, if the best comparison shows a score below a certain threshold, the system can make the decision that the individual is not enrolled in the system.

1.1.2. Performance evaluation

As stated, in [7], biometric systems are inherently probabilistic, which is crucial, when considering the performance of a biometric system. According to the ISO/IEC 19757-2:2019[13] standard three types of performance evaluation can be assessed: Technology, Scenario and Operational evaluation.

In case of technology evaluation different algorithms for template generation and comparison are evaluated offline for a specific dataset. The dataset contains a number of biometric samples for each individual contained in the dataset. The main advantage, is that the evaluation is repeatable and enables to perform detailed investigations. A best practice would be to utilize technology evaluation to select appropriate algorithms for scenario evaluation. Scenario evaluation is done online and evaluates live biometric recognition for a set of different individuals, which request to be recognized by the system in a constrained environment. This includes the sensor and acquisition of biometric samples for the individuals. Thus, the evaluation is not repeatable due to the variations which result from the acquisition process. Again, scenario evaluation is done prior to operational evaluation where a biometric system is tested in regular operation on a set or subset of individuals. Operational evaluation enables to test the system for issues when using it in a real world scenario.

As outlined, the best practice to develop and evaluate a biometric system is to run technology, scenario and operational evaluation in a sequence. Because this thesis deals with the feasibility of object identification for two different applications, we deal with technology evaluation only. For technology evaluation, for all biometric samples in the dataset biometric templates are computed and compared to each other which results in a comparison/ similarity score for each pair of biometric templates. Comparisons scores computed between templates from the same individual are referred to as genuine scores and scores computed between templates from different individuals as impostor scores. The corresponding probability distributions are de-

noted as genuine and impostor score distributions or as intra- and interscore distributions.

The performance of a biometric system is assessed based on the errors it produces. The relevant errors as well as performance metrics differ for biometric verification and identification systems. For verification performance evaluation the False Match Rate (FMR) and False Non Match Rate (FNMR) are computed. FMR and FNMR depend on a system threshold which can be adjusted depending on the security level which is targeted. A general verification performance metric is the Equal Error Rate (EER), which specifies the threshold for which FMR and FNMR are equal. In case of scenario and operational evaluation the FMR is referred to as False Acceptance Rate (FAR) and the FNMR as False Rejection Rate (FRR). However, the FAR and FRR include system related failures like the failure to acquire or failure to enrol which are not relevant in the scope of this thesis. Besides the EER there are other verification performance measures like the Zero False Match Rate (ZFMR) and Zero False Non Match Rate (ZFNMR). By computing the FMR and FNMR for varying thresholds an extensive overview on the different performance metrics can be provided. Visually this is established by plotting the results in a Receiver Operating Characteristic (ROC) graph or in a Detection Error Trade-off (DET) curve. A ROC graph plots the true positive rate (1-FNMR) against the FMR. A DET curve plots the FNMR against the FMR.

For biometric identification the Rank-k recognition rate is a common performance metric. Commonly, only the Rank-1 recognition rate is of interest. In case of technology evaluation, closed-set identification is assessed where it is assumed that all individuals are enrolled. In order to compute the Rank-k recognition rate the cumulative match characteristic (CMC) is computed. For this purpose, for each individual in the dataset one template is selected as enrolled template and another one is selected as probe. The templates from all individuals, which were selected as enrolled templates, are referred to as gallery set and the probe templates as probe set. Subsequently, for each probe template the comparison scores to all templates in the gallery are sorted so that the scores are ordered with descent similarity. For the sorted scores it is assessed at which index the probe to enrolled template comparison score is ranked. Only if the corresponding score is ranked before index k the identification was correct. The selection of gallery and probe templates for each individual is repeated and for Rank-k recognition rate computation the probability of how often the correct gallery template is ranked better or equal to Rank-k is computed.

1.1.3. Distinctiveness and Stability

In [7] the authors conclude, that biometric system errors can be reduced, but not eliminated. It is essential, that errors are computed in a transparent and standardized way. In case of technology evaluation, performance evaluation can be repeated for different template generation and comparison algorithms. A remaining issue is that the same algorithm may show different performances for different datasets. Consequently, the utilized dataset must enable to assess the performance with respect to different quality criteria of the utilized biometric characteristic. Subsequently, two main criteria are introduced and discussed with respect to technology evaluation. The authors of [7] note that no (human) biometric characteristic is known to be entirely distinctive and stable.

Distinctiveness is the main prerequisite for a biometric characteristic in order to enable biometric recognition. It expresses that the biometric characteristic enables to distinguish between different individuals. Stability is the second prerequisite and expresses that the biometric characteristic is stable over time. Apart from the biometric characteristic itself there are various other factors which impact distinctiveness and stability. This leads to variability which can be either classified as externally or internally caused. Externally caused variations are diverse but a typi-

cal source is the biometric system itself. Basically, it is impossible to capture a biometric sample from a biometric characteristic twice without variation. In case of imaging based sampling typical variations are geometric distortions (scale, rotation and tilt) as well as illumination distortions (shadows, varying contrast). Second, template generation as well as comparison may introduce variation for different samples from the same individual. Further externally caused variations affect the biometric characteristic itself. Such variations are caused by mechanical or environmental influences and degrade or change the biometric characteristic to a certain extent.

In order to investigate the feasibility of physical object identification, based on a specific characteristic distinctiveness and stability, need to be assessed. As introduced, the first step is technology evaluation which requires appropriate datasets suited to assess both, distinctiveness and stability. This is critical because for assessing the basic feasibility variation is a problem which can make it difficult to answer this basic question. On the other hand, technology evaluation requires to consider real world feasibility and therefore variation which reflects real world conditions needs to be included.

The purpose of these considerations is to highlight the importance of the dataset(s) used for technology evaluation. The composition of the dataset depends on the object, the biometric characteristic, which is utilized for biometric recognition and the respective application. For this thesis and the two investigated object identification applications different datasets were acquired. These datasets enabled to present detailed investigations on distinctiveness and stability for each application.

1.2. Physical Object Authentication

In the scope of this thesis an object belongs to a specific class and all objects belonging to this class share common extrinsic characteristics. Thus, we refer to classification-based physical object authentication. This enables to predict, if a given object belongs to this class or not. The class of the object, which is authenticated, can be referred to as authentication class.

Basically, authentication works similar to biometric verification, where a probe template is compared to just one reference template belonging to the claimed identity. However, there are two main differences: (i) In case of biometric verification the claimed identity is the authentication class composed of just one object. For authentication there is not just a single object which belongs to a class, there are multiple and different objects which all belong to the same class. Different objects belonging to the same class are referred to as instances. (ii) Physical object authentication, as considered in this thesis, refers to supervised classification in the field of machine learning. Same as for biometric recognition the authentication system requires to get to know the authentication class first. Thus, the utilized characteristic needs to be sampled from different object instances of this class. The samples from different instances of the authentication class are utilized to extract features and to train an authentication model using a specific classifier. The authentication model is used for classification, i. e. to predict, if a given object instance is authentic or not. Typically, biometric verification and moreover identification are not learning-based, i.e. the comparison scores are computed directly between the probe and reference templates by utilizing distance metrics to compute the comparison score of the corresponding feature sets. Supervised classification tasks are one-class, binary or multi-class classification. For one-class classification only data of the specific class are utilized for training and the trained classifier predicts if a given sample belongs to this class or not. For multi-class classification, samples from n-classes are used for training and the trained classifier predicts to which of the n-classes a given sample belongs. For binary-classification n=2 and the classifier predicts to which of the two classes the sample belongs. Multi-class and binary classification are almost always done in a closed-set scenario. All classes are already known at training time.

In case of a controlled classification environment this is feasible if it is ensured that only samples from known classes are requested to be classified. Applications closely related to the topics covered in this thesis are wood species and fish species identification. For example, in [4] tree species identification for 20 Canadian species has been investigated and in [35] the authors showed a deep learning approach to distinguish between 20 fish species. Nevertheless, as noted in [23] for various applications it is more realistic to consider an open-set scenario, i. e. testing samples from unknown classes are requested to be classified. As such, in an open-set scenario the classifier should be able to handle unknown data.

Classification-based object authentication can be considered as binary open-set classification problem. The goal is to predict if an object belongs to the authentication class or not. For training of the authentication model, the positive class and a limited subspace of other (=known) classes is available. What remains are many unknown classes. The overall goal is to discriminate between the authentication class and all other classes including known as well as unknown classes not available at the training stage. In [23] such a binary open-set classifier is referred to as 1-vs-set machine.

The training stage is crucial in order to select and tune a classifier. For this purpose, an appropriate dataset is required. Contrary to biometric systems, this dataset is not only used to assess the experimental authentication performance; it may serves as basis to train the authentication model for a real world application. For our research on classification drug packaging authentication a new dataset was acquired and used to asses the basic feasibility in a binary openset classification scenario.

2. Contributions and Discussion

The contributions of this cumulative thesis are arranged according to the investigated applications. Section 2.1 and Section 2.2 outline our contributions in the field of roundwood and fish identification, respectively. Section 2.3 describes our work on drug packaging authentication.

2.1. Roundwood recognition

Nowadays supply chain management has become a fixed place in all fields of the industry. Industrialization attached to globalization made it necessary, to improve raw material as well as the distribution of the products on an international scale. Efficient tracking of timber as well as quality analysis and measurement are key technologies to establish intelligent information or production systems towards wood industry 4.0. State-of-the-art roundwood tracking methods rely on physical marking (plastic badges or RFID tags). Besides the advantage of bulk reading, RFID technology is cost intensive and requires specialized sensing technology. Recent trends like DNA fingerprinting of trees are time consuming and utilized to verify the origin or species of wood to prevent trade of protected timber species. The first works [5, 6, 11] on biometric log recognition investigated log tracking within the sawmill, concentrating on the outer shapes of logs as biometric features by using 2D and 3D scanners to extract geometric wood properties [5, 6, 10]. The utilized capturing devices are however not applicable at forest site. Furthermore, [9, 11] showed that knot positions as biometric features are suited to enable traceability between logs and the cut boards.

By superficially comparing the patterns of human fingerprints to annual ring patterns of wood log ends, one finds a close resemblance (see Fig. 2). Timber offers characteristics on log end faces in terms of annual rings, pith position, shape and dimension. This observation raised

(a) Log end **(b)** Human finger

Figure 2.1.: Similarity between the annual ring pattern and the human finger ridge pattern.

the question, if wood logs can be identified using digital images of log ends referred to as cross-section (CS) images. A first work on log end biometrics was presented in [2] as an effort to curb poaching of trees. In the experimental evaluation digital images of tree stumps and the corresponding log ends are utilized, both showing up strong saw kerf patterns. Results show that the combination of log end shape and saw cut pattern information, represented by Zernike polynomials, achieves a high accuracy for log to stump recognition. Recently and closely related, biometric tracking of wood boards using surface images was investigated in [20, 21, 15].

Tracking logs based on log end images could get a cutting edge technology. CS-Images can be taken at any point of the log supply and processing chain using everyday devices, like smartphones, low-cost industrial cameras or hightech devices like computed tomography (CT) scanners. This enables to pass information of each single log/tree from the forest-based industries to the sawmill industry as well as in the sawmill. Expectable impacts are various and affect different levels. Economically, processes in the forest-based industries could change significantly and from the viewpoint of industry 4.0 the level of automatization will increase drastically. After cutting a tree, the log ends are captured and each log is enrolled in a system. At this point, we could move towards industry 4.0 by analysing the log end images and computing quality related as well as measurement information, which is attached to a log record in a central system.

In this thesis, different aspects of roundwood tracking using CS-Images were investigated. The majority of contributions were elaborated in the scope of the Austrian Science Fund (FWF) project TRP254 entitled with "Traceability of logs by means of digital images (TreeBio)". The conducted research can be assigned to two research aspects which relate to stability and distinctiveness of the biometric characteristic.

2.1.1. Stability investigations

In [26, 25] we focused on the stability of the annual ring pattern as a biometric characteristic. In general, the recognition performance of a biometric system is affected by external and internal variations of the biometric characteristic. Regarding the annual ring pattern three different variation types emerged from our research: Temporal, Longitudinal and Surface variations.

- Temporal variations of the annual ring pattern correspond to ageing effects in human biometrics. However, as the annual ring pattern does not age temporal variations relate to discolourations and deformations caused by environmental influences like light and humidity.
- Longitudinal variations are caused by the changing CS pattern along the longitudinal axis of a log. This occurs in reality when logs are cross-cut in the sawmill. Often clean log end faces are required in order to assess the quality.
- Surface variations emerge when a log is cross-cut and different cutting tools are utilized. For example, the first cut in the forest is performed with a chain saw and the second cut, i. e. the clearance cut in the sawmill by a circular saw which changes the appearance of the pattern. Surface variations are accompanied by longitudinal variations of the annual ring pattern.

Both works rely on the idea to transfer concepts of human biometrics to roundwood biometrics. Specifically, the texture feature-based fingerprint recognition approach as proposed by [14] has been adopted and modified to be applicable for annual ring patterns. The experiments in [26] focus on temporal and longitudinal CS variations assessed on 35 time-delay captured slices from one log. As expected, our results show, that with an increasing time span between two images of the same slice the similarity expressed by the comparison score gets worse. The same is shown in case of an increasing longitudinal distance between two slices. However, results indicate, that adjacent slices have a high similarity, i.e. a good comparison score. For our investigations in [25], further two logs were cut in slices and captured twice, one with rough surfaces and one with sanded surfaces. Additional, to annual ring pattern features the impact of including shape features was tested. Results show, that the respective fusion of both increases the performance in terms of stability. Furthermore, it can be concluded that CS surface

variations show no impact and that cutting log ends up to 7.5 centimetres in thickness is no issue, even if the surface changes. A very interesting result is that knots are disturbing factors but do not introduce any propagative effects to the annual ring pattern and the CS shape.

2.1.2. Distinctiveness investigations

So far, it was not clear, if log end biometrics will be suited to discriminate between a large set of tree logs. A first glance at the distinctiveness of wood logs based on CS-Images was presented in [31]. In addition to fingerprint-recognition based methods the applicability of iris-recognition based approaches was assessed. For this purpose, two datasets at two different sawmills were acquired. Together the datasets comprise CS-Images from 150 different wood logs. Furthermore, the impact of enhancement is assessed. Results show that fingerprint and iris recognition based approaches can be transferred to the field of wood log tracking and that both are suited for log identification. In the experiments, the fingerprint based approach and all iris configurations which used Log-Gabor features achieved 100% recognition rate. Furthermore, all results indicate that shape information of the CS area is required to achieve an acceptable recognition rate and that enhancement significantly improves the performance. Same as in [25], for the fingerprint-based approaches the fusion of annual ring pattern and shape information improved the identification performance.

Based on this observation, in [33] we assessed the discriminative power of geometric log end features for the same dataset as in [31]. Geometric features were extracted based on groundtruth data for the CS boundaries and pith positions. Results show that radial distances from the pith and centroid center to the CS boundary and Zernike moments show a high discriminative power. The validation of these features for automated CS boundary detection [34] and pith estimation [34] showed that Zernike moments achieve the highest reliability. For groundtruth data the verification performances are comparable to those achieved in [31].

For the experiments in [32] an additional dataset (129 logs) including rotational as well as scale variations were acquired. Three different strategies for rotational pre-alignment were introduced and assessed. In the experimental evaluation we investigated the basic performance of the strategies and their impact on the verification and identification performances for different fingerprint- and iris-based configurations, respectively.

Finally, in [29] we show first results for the hyperspectral images from 200 log end discs, which is described in the next section. We utilized the fingerprint-based approach to compute comparison scores between the different spectral CS-Images captured for each disc. Results indicate that there are up to five spectral bands (one of each spectral range), which contain independent information from each other. This assumption is supported by the mean interscores which were computed for each spectral band and showed that higher spectral bands (>760nm) seem to be better to discriminate between the 200 log end discs. These results are only a first investigation on this topic and more research based on more sophisticated approaches is required to draw fundamental conclusions.

2.1.3. Open challenges & future research

Our contributions, achieved within the FWF project "TreeBio", indicate the principal feasibility of roundwood tracking based on log end images. However, there remain various challenges which need to be investigated in the future. So far, our research focused on RGB CS-Images which were captured in a restricted setting. In the forest-based and the sawmill industry the utilized cameras will be divers and the performance of log end biometrics is assumed to be influenced strongly by acquisition conditions (including sensor type, dirt on the log, type of

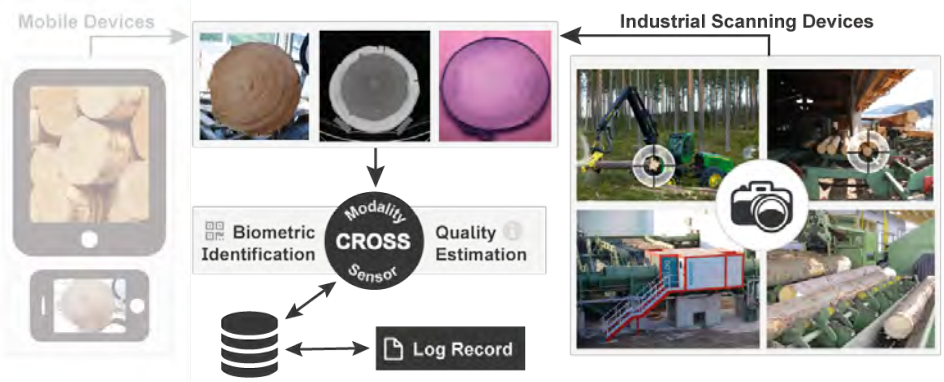

Figure 2.2.: FWF-ANR TreeTrace: Cross-Sensor/ Cross-Modality Tracking & Quality Estimation

sawing, illumination conditions, etc.). In [24] our future vision for biometric log recognition has been presented. Fig. 2.2 illustrates the basic idea for a system, which works in a sensor independent manner and utilizes sensor data for early quality estimation of log quality properties.

The follow-up project "TreeTrace" (2018-2021), which is a joint Austrian - French FWF-ANR project (I 3653), is based on this vision. On the Austrian side, University of Applied Sciences in Salzburg has the lead and our research group of the University of Salzburg is national research partner.

In this project, we deal with cross-modality and cross-sensor log end tracking and quality estimation based on CS-imagery captured using industrial scanning devices as illustrated in Fig. 2.2. Our role in this project is to investigate if log end biometrics are suited to identify logs based on digital log-end images captured in the forest and a second CS-Image captured by a camera or computed tomography (CT) scanner at the sawmill. Furthermore, the question is which imaging modality should be used to for CS-Image acquisition in the forest. Finally, as it is not clear if log end biometrics are suited to discriminate between a large amount of trees, this is a further important research questions which will be tackled in the project.

Within this project we already finished the acquisition of a dataset which is referred to as "100LogsDataset" and was already utilized for our experiments in [29]. 100 wood logs were collected in autumn 2018 near Corcieux, France and all log ends were fresh cut. We had no information, if some of the 4 to 5m logs belong to the same tree or not. At forest site from each log end several images with different rotation were captured. After the transport to Freiburg a thin slice was cut from each log end and the ends were captured again, same as in the forest. Exemplary RGB log end images for both log ends from #E001 are shown in the first two and last two columns of Fig. 2.3, respectively. Subsequently, each log was scanned with a CT scanner. Two exemplary CT CS-Images from the bottom and top end of log #E001 are shown in the first two and last two columns of Fig. 2.4, respectively. The slices were transported to Munich and scanned with two hyperspectral cameras. A detailed description on the hyperspectral imaging is provided in [29]. Additionally, RGB images with a DSLR camera were taken. Subsequently, all slices were transported to the Holztechnikum Kuchl in Austria, where they were sanded and captured again with the DSLR camera. Exemplary RGB CS-Images from the rough and sanded slices from both log ends of log #E001 are shown in Fig. 2.5. Finally, the slices corresponding to the bottom end of each log were transported to Munich again where the hyperspectral scanning was repeated. Expemplary hyperspectral images for the rough discs of log #E001 are shown in Fig. 2.6. For future research, it is essential, that log end biometrics are extended to work with mobile devices being applicable in almost every environment. The high variability of the images to process constitutes one of the technical barriers to be lifted in the future.

Figure 2.3.: 100LogsDataset: CT CS-Images from log #E001. The first two images are from the bottom and the last two from the top end of the log.

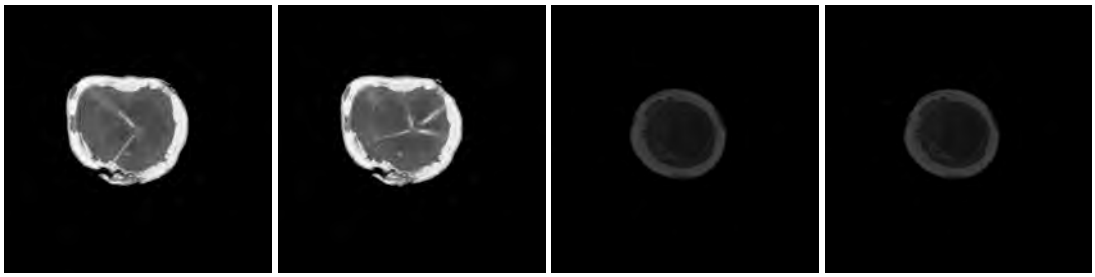

Figure 2.4.: 100LogsDataset: RGB CS-Images from both log ends of log #E001 captured in the forest and at the FVA Freiburg logyard.

Figure 2.5.: 100LogsDataset: RGB CS-Images from discs from both log ends of log #E001 captured with rough and sanded surfaces.

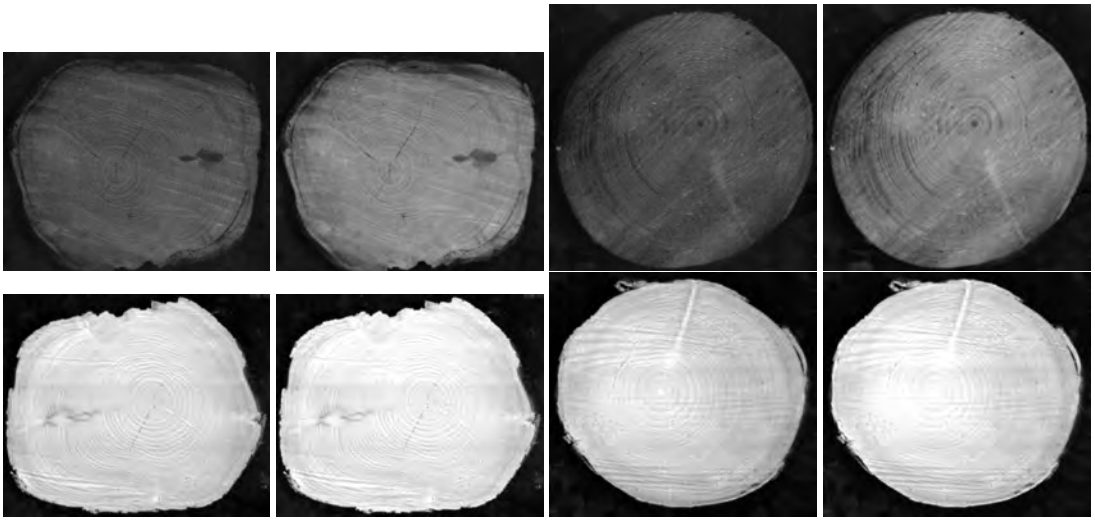

Figure 2.6.: 100LogsDataset: Hyperspectral CS-Images for the discs from both log ends of log #E001 captured with Specim FX10 and FX17.

Publications (sorted chronologically)

[26] R. Schraml, J. Charwat-Pessler, and A. Uhl. Temporal and longitudinal variances in wood log cross-section image analysis. In *IEEE International Conference on Image Processing (ICIP'14)*, pages 5706–5710, Paris, FR, Oct. 2014

[33] R. Schraml, A. Petutschnigg, and A. Uhl. Validation and reliability of the discriminative power of geometric wood log end features. In *Proceedings of the IEEE International Conference on Image Processing (ICIP'15)*, pages 3665–3669, Quebec, CAN, 2015

[31] R. Schraml, H. Hofbauer, A. Petutschnigg, and A. Uhl. Tree log identification based on digital cross-section images of log ends using fingerprint and iris recognition methods. In *Proceedings of the 16th International Conference on Computer Analysis of Images and Patterns (CAIP'15)*, LNCS, pages 752–765, Valetta, MLT, 2015. Springer Verlag

[25] R. Schraml, J. Charwat-Pessler, A. Petutschnigg, and A. Uhl. Towards the applicability of biometric wood log traceability using digital log end images. *Computers and Electronics in Agriculture*, 119:112–122, 2015

[24] R. Schraml, J. Charwat-Pessler, K. Entacher, A. Petutschnigg, and A. Uhl. Roundwood tracking using log end biometrics. In *Proceedings of the Annual GIL Meeting (GIL'2016)*, LNI, pages 189–192. Gesellschaft für Informatik, 2016

[32] R. Schraml, H. Hofbauer, A. Petutschnigg, and A. Uhl. On rotational pre-alignment for tree log end identification using methods inspired by fingerprint and iris recognition. *Machine Vision and Applications*, 27(8):1289–1298, 2016

[29] R. Schraml, K. Entacher, A. Petutschnigg, T. Young, and A. Uhl. Matching score models for hyperspectral range analysis to improve wood log traceability by fingerprint methods. *Mathematics*, 8(7):10, 2020

2.2. Fish identification

So far, identification of individual fish was mainly required for aquaculture studies. We envision, that fish identification is a basic requirement to move towards precision fish farming in intensive aquaculture as illustrated in Fig. 2.7.

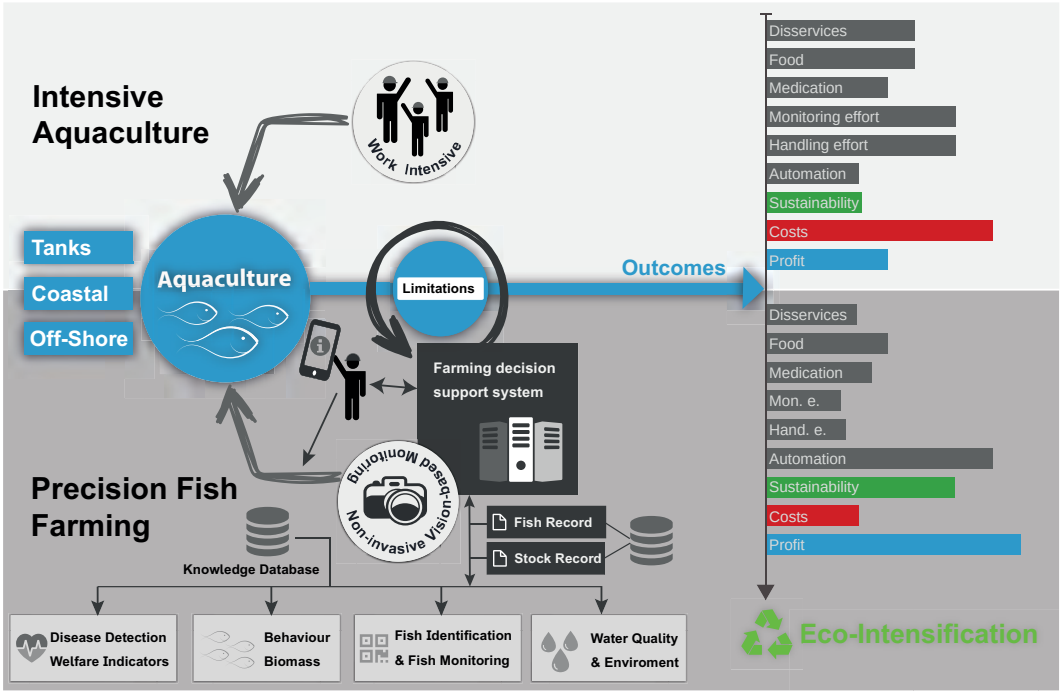

Figure 2.7.: Vision to move towards precision fish farming in intensive aquaculture

The basic idea is to move from mass to smart fish production requiring to consider each fish as individual instead of considering the total stock. As illustrated, this should be established by the Identification & Monitoring component of the system. Based on assigning information to each fish the possible components could perform biomass estimation, disease detection as well as feeding optimization. This system is based on the concept of eco-intensification. The idea is, to improve the health and well-being of the fish to ultimately reduce the alleged adverse effects, thereby reducing costs and increasing the overall profit. In regard to intensive aquaculture the vision is a farming decision support system which, performs autonomous tasks on the one hand and additionally supports the farmer by providing key measures of the stock gathered by considering each fish individually on the other hand.

State-of-the art approaches for fish identification are invasive and require to tag or mark each fish [22]. This is costly in terms of time, expensive and very critical as physical markers may pose health and behavioral problems. For these reasons, we focus on biometric fish identification. Research published in the aquaculture community refers to the term photo identification in case that biometric identification of aquatic individuals using images is performed. So far, various approaches dealing with fish photo identification were presented. Only a few apply machine vision and if so, only to assist naked eye identification.

Data acquisition for our ongoing research in this field was collected in the scope of the AquaExcel transnational access project (TNA) funded by the European Unions Horizon 2020

research and innovation program under grant agreement No. 652831 (AquaExcel2020). In this TNA project with the name "FISHID" we got access to the "Research Station for Sustainable Aquaculture" of Nofima in Norway. At the station Nofima provided a tank with #330 juvenile Atlantic salmon. For the first acquisition session all 330 fish were captured. For image acquisition each fish was anaesthetized first. Subsequently, the fish was moved into an aquarium, where he/she was captured with a digital camera several times. Then the fish was moved into a tent on top of which a digital camera was placed. Again the fish was captured several times with introducing some movement including rotation in-between. Finally, the Dino-Lite USB microscope was used to acquire iris image of the fish. Only the last 30 fish were tagged and kept in the tank. These 30 fish were captured again in three further acquisition sessions with approximately two months time delay in-between. Exemplary images for one fish are illustrated in Fig. 2.8.

(a) Lateral skin pattern in an aquarium

(b) Lateral skin pattern in a tent

(c) Iris image

Figure 2.8.: FISHID - dataset: Exemplary images captured from one fish during the first data acquisition event in Norway.

For the publication, which is part of this cumulative thesis, the iris dataset was utilized. The fundamental research question was, if the Atlantic salmon fish iris is suited as biometric characteristic to discriminate between different fish. In [30] we showed the principal feasibility of Atlantic salmon fish iris identification. In the experimental evaluation the distinctiveness and stability of the salmon iris were investigated based on the short term and long term data captured in the TNA project. Besides image acquisition a fully automated identification system was proposed. This included iris localization using a CNN-based semantic segmentation approach and rotational pre-alignment prior to feature extraction. Rotational pre-alignment is required in order to compensate for large rotational differences between two iris images from the same fish in the long term dataset. Results show, that the fish iris is highly distinctive and enables to discriminate between the 330 fish in the short term dataset showing identification rates over 95%. However, regarding stability the results for the long term dataset showed that the Atlantic salmon iris has a low stability and changes over time. This lead to the conclusion that Salmon iris identification is feasible but it is required to update the biometric template of each fish regularly.

2.2.1. Open challenges & future work

As outlined in the future work section in [30] research should consider data acquired in realistic environment. Fish could be forced to pass a narrow tube, where the lateral/ dorsal skin pattern or the fish iris is captured. If technology evaluation based on such data is successful, the next step would be to move to scenario evaluation, i. e. to tag a certain amount of fish and to test under real conditions. Furthermore, due to the low stability of the fish iris a template updating

approach needs to be implemented and tested. For our research on fish identification, we proceed with the lateral images captured in the tent and aquarium as shown in Fig. 2.8. Same as for the iris the body part showing the most promising pattern needs to be localized automatically and distinctiveness and stability of the pattern need to be assessed. Contrary to the iris localization, it is not clear, which part in terms of size and position is the best part. Furthermore, in addition to texture-feature based feature extraction CNN-based feature extraction using transfer learning will be tested for technology evaluation. Same as for the fish iris, the next step for lateral image-based identification would be to move to scenario evaluation. Even if technology evaluation is successful it is not clear if the quality of lateral images captured in a realistic environment is suited for identification. Moreover, capturing images in a realistic environment introduces external variations like affine transformations. It is therefore likely, that solutions for these variations must be found first on the basis of a new dataset and technology evaluation, and only then it will move towards a realistic scenario which, can be assessed based on scenario evaluation.

Publications (sorted chronologically)

[30] R. Schraml, H. Hofbauer, E. Jalilian, D. Bekkozhayeva, M. Saberioon, P. Cisar, and A. Uhl. Towards fish individuality-based aquaculture. *IEEE Transactions on Industrial Informatics*, page 10, 2020. in press

2.3. Drug packaging authentication

The third investigated application in this thesis deals with drug anti-counterfeiting. In the past decade product counterfeiting became a serious worldwide issue. In case of pharmaceutical products, counterfeits cause economic losses and threaten the consumer/ patient health. Within the member states of the European Union the Falsified Medicines Directive (FMD) defines the requirements for a traceability system in the scope of pharmaceutical products. The current solution relies on printing 2D barcodes on each drug package, which among other data contains a unique serial number. This number is utilized to track each single drug instance from the producer to the consumer. The required authentication database is managed by the European Medicines Verification Organisation (EMVO). It is likely that this database will attract criminals in order to get compromised, i. e. to enter serial codes of forged packages. On the other hand, valid serial-codes could be printed on faked drugs.

The Munich and Salzburg based company eMundo had the idea to assess the authenticity of a drug based on its packaging. The basic assumption or observation was, that the packaging of a fake drug differs from its original. For this purpose, the general feasibility of fake drug package detection was investigated in a short term project called "CounterFighter". The main issue at the beginning was that it was not possible for us to get a sufficient amount of fake drugs in order to develop and test if the package print is suited to discriminate between fake and original. Thus, we focused on a different research direction which did not require fake drugs. The basic idea is inspired by the concept of physically-uncloneable-functions (PUFs). A PUF is a challenge-response function which depends on the physical nature of an object and cannot be expressed mathematically [19]. We relate to non-electric PUFs and more specifically to paper-based PUFs. Thereby, the fibre structure of a paper-based product is used as a intrinsic characteristic to enable physical object identification. This means that the fibre structure in a specific region of a paper or packaging product is highly unique and enables to discriminate it from other, i.e. to recognize it again. Regarding drug authentication this means that every instance of a drug can be identified based on the fibre structure of the cardboard packaging in a specific region. This is referred to as serialization-based authentication. On the contrary to serialization-based authentication we investigated if the cardboard fibre structure of a specific drug shows common features for all instances. As shown in Fig. 2.9 this requires to move from serialization to classification. In order to investigate the feasibility of classification-based drug authentication we deal with drug pills packaged in a cardboard housing and blister. Guided

Figure 2.9.: The basic idea for drug authentication is to move from serialization-based to classification-based authentication.

by an app the user disassembles the packaging and takes images of the cardboard (CB), blister top (BT) and blister bottom (BB) textures as illustrated in Fig. 2.10. These textures are denoted

Figure 2.10.: Schematic illustration of the different modalities which are captured for the classification-based drug packaging approach.

as modalities and the corresponding texture images are labelled as I_{CB}, I_{BT} and I_{BB}. Furthermore, an image of the product code (I_{PC}) or manually entering the code or selecting the corresponding drug from a list is required. Together, these images compose an authentication vector $\hat{AV} = (I_{CB}, I_{BT}, I_{BB}, I_{PC})$ which is further processed. For preprocessing I_{CB}, I_{BT} and I_{BB} are segmented to show only texture and the texture pattern is enhanced. For the subsequent authentication step either a CNN-based or a support vector machine (SVM) based classifier can be utilized. In case of a SVM-based classifier, as done in our research, for each modality image texture features are computed which produce a feature vector for each modality $(FV_{CB}, FV_{BT}, FV_{BB})$. Typically, for CNN-based classifiers the preprocessed images are directly utilized as input.

Based on the product code image, the product ID is determined and the corresponding pretrained models for each modality (M_{CB}, M_{BT}, M_{BB}) are utilized to compute similarity or probability scores (P_{CB}, P_{BT}, P_{BB}) in the range $[0, 1]$. The closer to 1 the more likely the texture is authentic. The closer to 1 the more likely the given feature vector is authentic, the closer to 0 the higher is the probability that the feature vector was computed from fake material. Finally, a decision function $f(P_{CB}, P_{BT}, P_{BB}) = (v, p)$ needs to be defined, where $v \in \{1, -1\}$ gives the final authenticity vote of the authentication system and $p \in [0, 1]$ specifies a probability score for the final vote which is then presented to the user.

So far, three publications emerged from our research. In our first work [16] we showed that 9 different drugs from 3 manufacturers and some forged ones can be classified based on their cardboard fiber texture. Results show, that it is not possible to discriminate between drugs from the same manufacturer because they likely use the same cardboard packaging material. For drugs from different manufacturers the results show, that they can be classified with 100% accuracy. However, the utilzed testset was fairly small and as outlined in the introduction authentication, especially in the considered application, is not a closed-set multi-class classification problem.

Thus for our experiments in [27] a new dataset was acquired and experiments for binary openset classification were presented. For data acquisition 45 drug from 28 different manufacturers were collected from different pharmacies in Salzburg. For each drug between 1 and

15 package instances were collected. From each instance non-overlapping sections of the cardboard, blister top and blister bottom textures were captured with a digital camera. In the experimental evaluation two fundamental research questions were tackled:

- ***Positional invariance*** For the cardboard fiber structure it was not clear, if the fiber structure shows constant features in different sections and if the features enable to discriminate between cardboard's from different drugs.

- ***Instance generalisation*** Furthermore, it was not clear, if and how the fiber structure varies between different instances. Typically, a classifier will be trained with features from one instances and the questions was if it is able to authenticate the other instances. Instance generalisation is a specialization of positional invariance and reflects a real world scenario.

Regarding positional invariance, the achieved results indicate, that for all three modalities the textural features are constant and enable to recognize the same drug class with a high accuracy. The same can be stated for instance generalisation. Results show that textural features for all three modalities are constant across different instances of the same drug. However, all images were captured with a DSLR camera and for a real world application the use of a mobile device is envisioned.

Thus, for the experiments in [28] the dataset was extended by images captured with two mobile devices. This enabled to investigate a single sensor as well as a cross-sensor scenario, which relates to a mobile device based drug packaging authentication system. In our previous work only low level features were utilized, no feature encoding was applied and no modality fusion was tested. Thus, in addition to the low level features, high level features and feature encoding were utilized and tested. Furthermore, a simple majority voting for all three modalities was tested. The experimental evaluation for the single sensor scenario shows, that mobile devices are principally suited for drug packaging authentication. However, in case of the cross-sensor scenario results show, that the performance decreases significantly.

2.3.1. Open Challenges

Our research in this field demonstrates the basic feasibility of classification-based drug packaging authentication. Texture images from different parts of the packaging material are suited to authenticate the corresponding drug, i.e. to distinguish it from other packagings from other drugs. In case of a real world application, mobile device cameras should be utilized to capture the packaging textures. In [28] the focus was on mobile device-based as well as cross-sensor authentication. Results show that the utilized SVM-based approach is not suited for cross-sensor authentication if the packaging texture scales vary. In case of a mobile device solution robustness to scale variations is crucial. Without additional equipment, e.g. a distance part, the textures will be captured at different scales and viewing angles. Even if a distance part is used, different cameras with different lenses cause varying texture scales, when capturing the same packaging texture. Future work needs to deal with all issues caused by the unconstrained imaging conditions in a mobile device scenario. One research direction could be to improve the scale invariance of the classifier. We have tested two different approaches for a SVM and CNN-based classifier but the results were not satisfactory: First, we tried to train the classifier with textures and varying scales in the expected scale variation range. For the second approach we tried to compensate scale variations in the preprocessing pipeline. This should be achieved by estimating scale space of the texture and resecaling the textures before training the classifier, i.e. the target is to train the classifier on a single scale of the considered texture. The training scale is then utilized as evaluation scale to adapt the scale of the texture prior to classification.

Even if these two approaches have not led to success, CNN-based classifiers are promising for further studies, because they work better and more robustly than SVM-based approaches in many other areas of applications. It is planned to make public our dataset to the community in the near future.

Publications (sorted chronologically)

[16] C. Kauba, L. Debiasi, R. Schraml, and A. Uhl. Towards drug counterfeit detection using package paperboard classification. In *Advances in Multimedia Information Processing – Proceedings of the 17th Pacific-Rim Conference on Multimedia (PCM'16)*, volume 9917 of *Springer LNCS*, pages 136–146, Xi'an, CN, 2016

[27] R. Schraml, L. Debiasi, C. Kauba, and A. Uhl. On the feasibility of classification-based product package authentication. In *IEEE Workshop on Information Forensics and Security (WIFS'17)*, page 6, Rennes, FR, December 2017

[28] R. Schraml, L. Debiasi, and A. Uhl. Real or fake: Mobile device drug packaging authentication. In *Proceedings of the 6th ACM Workshop on Information Hiding and Multimedia Security (IH&MMSec 2018)*, pages 121–126, Innsbruck, AUT, 2018

3. Publications

This chapter presents publications as originally published, reprinted with permission from the corresponding publishers. The copyright of the original publications is held by the respective copyright holders, see the following copyright notices. In order to fit the paper dimension, reprinted publications may be scaled in size and/or cropped.

TEMPORAL AND LONGITUDINAL VARIANCES IN WOOD LOG CROSS-SECTION IMAGE ANALYSIS

Rudolf Schraml [a] *Johann Charwat-Pessler* [b] *Andreas Uhl* [a]

[a] University of Salzburg, Jakob Haringer Str. 2, 5020 Salzburg, Austria
[b] University of Applied Sciences Salzburg, Markt 136a, 5431 Kuchl, Austria

ABSTRACT

In this work two practical issues of biometric log recognition using log end images are investigated: Temporal and longitudinal variances of log cross-sections (CSs). These variances are related to the requirement of robustness for biometric characteristics. A texture feature-based fingerprint matching technique is used to compute matching scores between CS images. Our experimental evaluation is based on the temporal and longitudinal variances of 35 slices of a single tree log which where captured at four time delayed sessions. Results indicate, that biometric log recognition using log end images is robust and is able to overcome both issues. This work contributes to the development of a biometric log recognition system by showing that a texture feature-based matching technique is applicable to log CSs.

Index Terms— Biometric log traceability, Cross-section analysis, Texture feature-based matching technique

1. INTRODUCTION

Traceability of wood logs is a basic requirement to manage economical and social issues. In economic terms, traceability of wood logs is required to map the ownership structure of each log. Due to the ecological rethinking social aspects like sustainability have become more important. So-called wood certificates like the Pan European Forest Certification (PEFC) are based on traceability and are a must have for all end-sellers.

Currently, log traceability is established by physically marking each log (see [1]). State-of-the-art systems propose the usage of Radio Frequency Identification (RFID) to reach traceability from forest site to further processing companies (see [2],[3]). Another idea relies on biometric recognition of wood logs. In the works of [4],[5],[6],[7],[8] approaches to establish biometric log traceability within the sawmill were presented. The approaches presented in [4],[5],[7] utilized 2D and 3D scanners to extract geometric wood properties. In [6],[8] a computer tomography scanner was used to extract knot positions to enable traceability between logs and the cut boards. Due to low recognition rates, these approaches are not applicable for industrial usage within the sawmill and are even less suitable to deal with the increasing variety of trees at forest site. Furthermore, the utilized capturing devices are expensive and not applicable in the forest based industries.

Similar as for human fingerprint recognition, we assume that annual ring patterns of log ends can be used to recognize wood logs. Log end images can be captured by digital cameras at forest site and processing companies. This work contributes to the development of a biometric log recognition approach using log end images by investigating two practical issues: Temporal and longitudinal variances of cross-sections (CSs) in wood logs. For human biometrics, robustness of the utilized biometric characteristic is a basic requirement. In case of CSs robustness is related to the temporal changes caused by environmental conditions and the longitudinal variations of the CS pattern within a tree log. Temporal changes are caused by light and humidity and result in deformations like cracks and discolourations. Longitudinal variations result from log end cutting or from capturing different log ends.

For our investigations the FingerCode approach by [9], [10] is adopted to CS images. Additionally, a Log-Gabor extension of the fingerprint enhancement approach by [11] is utilized to enhance the annual ring pattern. Thus, our work additionally sheds light on the general applicability of texture features for CS matching. For the experimental evaluation 35 slices of a single log are utilized. Each slice was captured four times at time-delayed sessions. This testset enables the computation of the temporal variances between time-delayed sessions from each cross-section slice. Longitudinal variances are computed among the CS images of the 35 slices of the testset.

At, first Section 2 introduces the computation and matching of Gabor-based features from CS images. The experimental setup and results are presented in Section 3 followed by the conclusion in Section 4.

2. CROSS-SECTION CODES (CS-CODES)

The CS-Code computation is based on the FingerCode approach proposed in [9] and [10]. This technique utilizes

THIS WORK IS PARTIALLY FUNDED BY THE AUSTRIAN SCIENCE FUND (FWF) UNDER PROJECT NO. TRP-254.

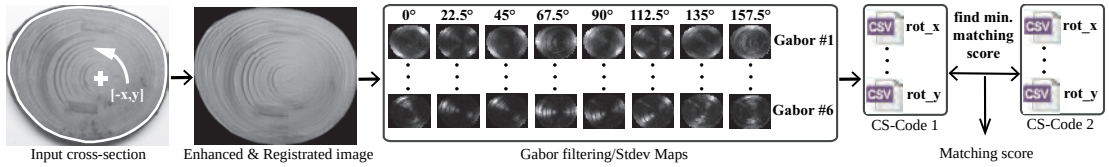

Fig. 1: CS-Code computation and matching scheme

a Gabor-based descriptor which extracts local ridge orientations of a fingerprint. In the next section the CS image registration & enhancement procedure is considered in detail. Subsequently, in Section 2.2 the CS-Code computation and the matching procedure between CS-Codes extracted from different CS images is outlined.

2.1. Cross-section registration & enhancement

Due to cutting disturbances annual ring enhancement is a crucial task for any subsequent feature extraction procedure. As opposed to human fingerprints, the frequency of the annual ring pattern is strongly varying. Our enhancement procedure is based on the fingerprint enhancement approach presented in [11]. CS registration is performed in three steps. The left image in Fig. 1 shows an example for an input CS image. The CS border and the pith position have to be determined in advance (see [12],[13]). For image registration the image is rotated around the pith position, cropped to the CS bounding box and finally scaled to 512 pixels in width. Rotation can be performed to generate rotated versions of each CS image or to align the CS to a unique position (eg. according to the center of mass). For CS image enhancement the CS is subdivided in half/ non-overlapping blocks (eg. 16x16 pixels). Enhancement is performed in three consecutive stages: Local orientation estimation, local frequency estimation and adaptive filtering.

At first, for each block principal component analysis of the local Fourier Spectrum is performed to determine its local orientation (see [12]). Commonly, CSs are disturbed due to cutting. Thus, wrong orientations are slightly corrected by low-pass filtering the local orientation field with a Gaussian filter. Next, for each block and its local orientation the dominant frequency is determined. For this purpose, the local Fourier Spectrum of each block is subdivided into subbands and sectors. The dominating frequency of a block is determined by summing up all frequency magnitudes in each sector subband. It is assumed that the maximum sector-subband represents the dominating frequency. If the maximum sector does not correspond to the block orientation the result is neglected. In a further step for each neglected value the local frequency is interpolated using a Gaussian filter.

In the filtering stage the Fourier Spectrum of each block is filtered with a Log-Gabor (introduced by [14]) which is tuned to its local orientation and frequency. Furthermore, experiments showed that a bandwidth of three times the variance of the Fourier Spectrum and as spread value the blocksize/4 are well suited for filtering. By using the fast inverse Fourier transform the filtered Fourier Spectra are utilized as new block values. Boundary effects are reduced by using half-overlapping blocks. An exemplary result of the registration & enhancement procedure is depicted in Fig. 1.

2.2. Cross-section code computation & matching

As suggested in [9] a Gabor filterbank is used to extract annual ring pattern features. Because of the constant ridge frequencies in human fingerprints a single Gabor filter and its rotated versions are sufficient. The frequencies of annual ring patterns are strongly varying and thus different Gabor filters are required to capture additional information from the annual ring frequencies in different orientations. For a CS image width of 512 pixels six different Gabor filters are suggested. For each Gabor filter eight rotated versions are created. Consequently, the Gabor filterbank consists of 48 filters.

The CS-Code computation is performed in three stages. In the first stage the enhanced input image is filtered with each filter in the filterbank. Each filtered image is subdivided into blocks (e.g. 32x32 pixels). For all blocks the absolute deviations of the gray values are computed. The absolute deviations of each image are stored into a matrix, which can be denoted as Standard Deviation Map (Stdev Map). In the middle of Fig. 1, the filtering and Stdev map computation procedure is illustrated. Altogether 48 Stdev Maps are computed and stored as one-dimensional vectors in a CSV file.

Rotational variances are compensated by repeatedly computing features for rotated versions of the input image. Compared to fingerprints, the rotational misalignment range of a CS image is not restricted to a certain range. One strategy to solve this issue, is to perform rotational pre-alignment in the registration & enhancement stage to restrict the misalignment range. For the utilized testset in our experiments the misalignment range lies between $-15°$ to $15°$. As shown in Fig. 1 for each input image a set of CS-Codes $(rot_{-15}, ..., rot_0, ..., rot_{15})$ is computed.

Matching is performed by computing the minimum matching score between all CS-Codes from two CS images. The matching score between to CS-Codes can be computed with a set of distance metrics. Two bin-by-bin distances (L1-Norm - L_1, L2-Norm - L_2), one cross-bin distance (EMD -

see [15]) and a simple 2D-matching distance are examined. The 2D-matching distance computes for each block the average L_1 distance between its Stdev value and the Stdev values of all adjacent blocks.

3. EXPERIMENTS AND RESULTS

In the experimental evaluation temporal and longitudinal variances are analysed using a testset of 35 CS slices from a single tree log. The first experiment assesses the temporal variances between time-delayed captured images from equal CSs. In the second experiment longitudinal variances between different CSs along the longitudinal axis of tree logs are assessed.

Testset: The 35 CS slices are from two sections which were cut from one spruce tree log with a spacing of approximately three centimetres. 18 slices were cut from the first and 17 slices from the second section. The slices were cut with a bandsaw and the thickness of the slices is approximately two centimetres. Each slice was captured four times (Canon EOS 5D Mark II) with different time spans between each capturing session. For the last session, the slices were stored in a balanced climate of 21° and 60% humidity. All images were captured under equal light conditions in a photo studio. For a constant rotational alignment between different sessions pins were utilized as position markers. The distance between the CS slice and the camera was fixated using a tripod. In Fig. 2 the four images of Slice #10 are illustrated. Additionally, for all images the CS borders and pith positions were manually marked and are available as xy-coordinates.

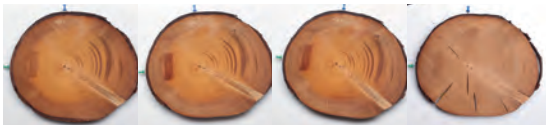

Fig. 2: Testset example: Slice #10 - Section 2 / Sessions 1-4

Computational details: For each of the four images from each CS slice 31 CS-Codes $(rot_{-15}, ..., rot_0, ..., rot_{15})$ are computed. In the registration & enhancement stage the rotated CSs are scaled to 512 pixels in width and for enhancement 32x32 half-overlapping pixels blocks are utilized. The CS-Codes are computed using 16x16 non-overlapping blocks for the Stdev maps. The utilized Gabor filterbank is build up on six different Gabor filters tuned to 8 directions:

$$G(\lambda, \theta, \sigma, \gamma) = G(\lambda, \sigma) =$$
$$((2.5, 2), (2.5, 2), (3.5, 3), (4.5, 3), (5.5, 3), (6.5, 3)),$$
$$\theta = \{0, 22.5, ..., 135, 157.5\}, \gamma = 0.7$$

In addition to the 31 CS-Codes of each CS slice, further seven CS-Codes $(rot_{45}, rot_{90}, ..., rot_{270}, rot_{315})$ were computed. These rotations are not in the expected misalignment range considered in the matching procedure. Thus, these CS-Codes are utilized to simulate a set of CS-Codes descending from different tree logs, i.e. used to simulate interclass variances.

Subsequently, three different variances are computed. Temporal variances are the matching scores among the CS-Codes of the four different session images from one CS slice. Longitudinal variances are computed among the CS-Codes of the images from each session. Finally, interclass variances are computed among the CS-Codes as described above. The CS-Code framework and the experiments are implemented in JAVA.

3.1. Results

The results are assessed in two stages. For each distance metric and the different variances, the corresponding matching score distributions (SDs) are computed. Note that these correspond to genuine and impostor distributions in biometrics [16]. First, the intersections between the SDs of the temporal, longitudinal and interclass variances for the different distances metric are evaluated. Subsequently, we analyse the temporal and longitudinal variances of the best distance metric.

SD intersection analysis: According to the percent of intersection between the temporal, longitudinal and interclass SDs the best distance metric is determined. Thereby, the intersections between the temporal/ longitudinal SDs and the interclass-SD are used as main evaluation criteria. The lower the overlap between those SDs, the more suitable is the distance metric to distinguish between CS-Codes from different tree logs. In case of a real world application a high percentage of intersection between the temporal and longitudinal SDs is very important. Only then a biometric system is robust to temporal and longitudinal variances. In Table 1 the percentages

Distance Metric	Temp-Long	Temp-Inter	Long-Inter
EMD	82.25%	24.66%	33.00%
L_1	68.51%	1.31%	6.00%
L_2	72.10%	3.77%	14.00%
2D-matching	67.53%	2.86%	13.00%

Table 1: Intersections of the score distributions (SDs)

of intersections between the SDs for all evaluated distance metrics are listed. The lowest overlaps between the temporal/ longitudinal SDs and the interclass SD are reached using the L_1 norm (see Fig. 3a). Using the L_1 norm, there is an overlap of 1.31% between the temporal and the interclass SD. Furthermore, the overlap between the longitudinal and interclass SD is very low and accounts 6%. Although, the interclass variances are generated using the the same testset the low overlaps between the temporal/longitudinal SDs and the interclass SD indicate that it is possible to separate CS-Codes computed from different tree logs. Considering the temporal and longitudinal SDs, it is a bit surprising that the overlaps are very high. In this regard, a detailed analysis of the temporal and longitudinal SDs brings some interesting insights as follows.

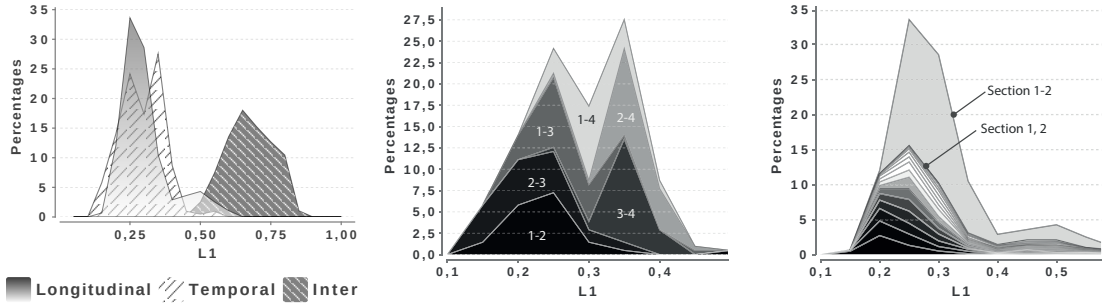

(a) Matching score distributions (b) Temporal SD - stacked session subset chart (c) Longitudinal SD - stacked distance subset chart

Fig. 3: Temporal/longitudinal and interclass score distribution (SD) analysis

Temporal variances: In Fig. 3b the subset structure of the temporal SD (L_1 norm) is illustrated. The labelled subset areas in the chart illustrate the proportions of the matching scores between different sessions and are stacked one above the other. The labels specify the indexes of the sessions used to compute the matching scores. Overall, the highest CS-Code distances arise in subsets where one session is compared to Session #4. This results from storing the CSs in a balanced climate between Sessions #3 and #4. This caused remarkable visual changes. Due to the decreasing moisture content, the contrast and intensity of the annual ring pattern changes and cracks as well as discolourations arise. As expected, the lowest CS-Code distances are computed between Sessions 1-2 and 2-3. All in all, the results indicate that an increasing time span between two images of the same CS deteriorates the CS-Code distance.

Longitudinal variances: Finally, the longitudinal variances (L_1 norm) are assessed. It can be assumed that with an increasing longitudinal distance between two CS slices the CS-Code distance increases too. The chart in Fig. 4 illustrates the mean matching scores for different slice distances grouped session-wise. For each session the mean CS-Code distances increase with an increasing slice distance. Lastly, the chart in Fig. 3c illustrates different subsets of the longitudinal SD. The largest subset labelled "Section 1-2" contains all matching scores between all slices from the first tree section to all slices from the second section. In this particular case, the slice distances range between 1 to 35 slices. The second subset "Section 1,2" contains all matching scores between the slices of the two sections. As in Fig. 4, this subset is further subdivided into subsets according to the slice distance of the compared slices. The bottom subset area contains all matching scores with slice distance 1. From bottom up the slice distance increases. Considering the subset peaks, the chart illustrates that with an increasing slice distance the CS-Code distances shift remarkable to higher values.

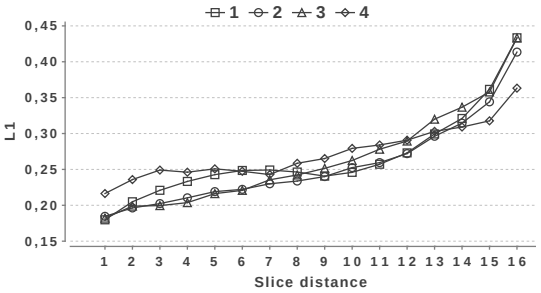

Fig. 4: Longitudinal variances - matching score analysis

4. CONCLUSION

In conclusion it can be stated that preliminary expectations about longitudinal and temporal variances of CSs of tree logs are confirmed by the results of our experiments. In this work Gabor-features of CS slice images of a tree log are computed and compared with respect to the temporal and longitudinal variances. These variances are related to the robustness of biometric log traceability using log end images. Results show that with an increasing time span between two images of the same CS the CS-Code distance increase too. Furthermore, it is shown that adjacent CS slices show low CS-Code distances and with an increasing slice distance the CS-Code distances increase. Finally, our results indicate that biometric systems using log end images are able to overcome issues caused by environmental influences and log length cutting or capturing different log ends.

In future work more matured features should be extracted and the performance of a biometric log recognition framework using a real world testset should be assessed.

5. REFERENCES

[1] Dennis P. Dykstra, George Kuru, Rodney Taylor, Ruth Nussbaum, William B. Magrath, and Jane Story, "Technologies for wood tracking," Tech. Rep., World Bank - WWF Alliance report, 2003.

[2] S. Korten and C. Kaul, "Application of RFID (Radio frequency identification) in the timber supply chain," *Croatian Journal of Forest Engineering*, vol. 29, no. 1, 2008.

[3] I. Ehrhardt, H. Seidel, and N. Doden, "Potentials for savings by implementing rfid and telematic technologies in the timber and biomass supply chain," in *In Procs. of the International Conference on Biosystems Engineering*, Tartu, EST, 2010, vol. 8, pp. 47–59.

[4] S. Chiorescu and A. Grönlund, "The fingerprint approach: using data generated by a 2-axis log scanner to accomplish traceability in the sawmill's log yard," *Forest Products Journal*, vol. 53, pp. 78–86, 2003.

[5] S. Chiorescu and A. Grönlund, "The fingerprint method: Using over-bark and under-bark log measurement data generated by three-dimensional log scanners in combination with radiofrequency identification tags to achieve traceability in the log yard at the sawmill," *Scandinavian Journal of Forest Research*, vol. 19, no. 4, pp. 374–383, 2004.

[6] Jens Flodin, Johan Oja, and Anders Grönlund, "Fingerprint traceability of sawn products using x-ray log scanning and sawn timber surface scanning," in *Proccedings of Quality control for wood and wood products: COST Action E 53 the first conference*, 2007.

[7] Jens Flodin, Johan Oja, and Anders Grönlund, "Fingerprint traceability of logs using the outer shape and the tracheid effect," *Forest Products Journal*, vol. 58, no. 4, pp. 21–27, 2008.

[8] J. Flodin, J. Oja, and J. Grönlund, "Fingerprint traceability of sawn products using industrial measurement systems for x-ray log scanning and sawn timber surface scanning," *Forest Products Journal*, vol. 58, pp. 11, 2008.

[9] A. K. Jain, S. Prabhakar, L. Hong, and S. Pankanti, "Filterbank-based fingerprint matching," *IEEE Transactions on Image Processing*, vol. 9, no. 5, pp. 846–859, May 2000.

[10] A. Jain, A. Ross, and S. Prabhakar, "Fingerprint matching using minutiae and texture features," in *Procs. of the International Conference on Image Processing (ICIP'01)*, Thessaloniki, GR, 2001, vol. 3, pp. 282–285.

[11] Lin Hong, Yifei Wan, and Anil Jain, "Fingerprint image enhancement: Algorithm and performance evaluation," *IEEE Trans. Pattern Anal. Mach. Intell.*, vol. 20, no. 8, pp. 777–789, Aug. 1998.

[12] R. Schraml and A. Uhl, "Pith estimation on rough log end images using local fourier spectrum analysis," in *Proceedings of the 14th Conference on Computer Graphics and Imaging (CGIM'13)*, Innsbruck, AUT, Feb. 2013.

[13] Kristin Norell and Gunilla Borgefors, "Estimation of pith position in untreated log ends in sawmill environments," *Computers and Electronics in Agriculture*, vol. 63, no. 2, pp. 155–167, 2008.

[14] H. Knutsson and G. H. Granlund, "Texture analysis using two-dimensional quadrature filters," in *IEEE Computer Society Workshop on Computer Architecture for Pattern Analysis and Image Database Management*, Pasadena, USA, 1983.

[15] Y. Rubner, C. Tomasi, and L.J. Guibas, "A metric for distributions with applications to image databases," in *Computer Vision, 1998. Sixth International Conference on*, 1998, pp. 59–66.

[16] D. Maltoni, D. Maio, A. K Jain, and S. Prabhakar, *Handbook of fingerprint recognition*, Springer New York, 2009.

VALIDATION AND RELIABILITY OF THE DISCRIMINATIVE POWER OF GEOMETRIC WOOD LOG END FEATURES

Rudolf Schraml [a] *Alexander Petutschnigg* [b] *Andreas Uhl* [a]

[a] University of Salzburg, Jakob Haringer Str. 2, 5020 Salzburg, Austria
[b] University of Applied Sciences Salzburg, Markt 136a, 5431 Kuchl, Austria

ABSTRACT

Recent investigations on biometric log recognition using end face images indicated that shape information is beneficial for the biometric system performance. This study assesses the discriminative power and reliability of geometric features which are computed by means of segmented cross-sections and their pith positions.

The experimental evaluation is based on cross-section images from 150 different logs, for which the ground truth of the boundary and pith position is known. By assessing the verification performance for ground truth data and automated segmentation/ pith estimation procedures this work highlights the basic discriminative power of geometric log end features and further validates their reliability in case of using automated procedures.

Index Terms— Geometric Log End Features, Biometric Log Traceability, Wood Log Cross-section Analysis

1. INTRODUCTION

Biometric tracking of wood logs is a potential approach to establish traceability without the necessity for physical markers like plastic badges or Radio Frequency Identification (RFID) transponders. A biometric log recognition system based on log end images could be used to track the ownership from the forest based industries to further processing companies. Another application is to discover illegally harvested tree logs based on cross-section (CS) images of their stumps [1].

In recent publications [2, 3] we have investigated the general applicability and robustness of a texture-feature based approach [4, 5] for a biometric log recognition system. The experiments were based on CS slices from three different logs and the results indicated a high degree of robustness to temporal, longitudinal and surface variations which arise in a real world application. Based on these findings we explored the applicability of fingerprint and iris-recognition based methods to identify 150 different tree logs in [6]. The best fingerprint-based approach utilized shape information in the matching procedure. Furthermore, the iris-based approaches rely on polar-transformation which is based on the CS boundary and pith position. Basically, the results showed that shape information is required to achieve an acceptable verification and identification performance. So far, all experiments were conducted using ground truth (GT) data of the CS boundaries and pith positions.

The present study has the objective to assess the discriminative power of geometric log end features based on GT data and to validate their reliability in case of performing automated CS segmentation (SEG) and pith estimation (PE).

For the experiments the test set used in [6] is used and different geometric features are extracted based on the CS boundaries and pith positions. In assessing the verification performance for GT data this work investigates the basic discriminative power of these features. In validating the reliability of geometric features, for different configurations of SEG and PE approaches, this work contributes to the further development of a biometric log recognition system.

Section 2 introduces the utilized SEG and PE approaches. Subsequently, a set of geometric features based on the CS boundary and pith position is presented. The experimental setup and results are presented in Section 3 followed by the conclusion in Section 4.

2. GEOMETRIC LOG END FEATURES

The computation of geometric log end features relies on the boundary and the pith position of a CS. Furthermore, the pith position and CS boundary are required for any CS registration procedures. Scale and rotational variances can be compensated by rotating the CS around the pith position and scaling the CS to a certain size. Before describing a set of geometric log end features, we briefly introduce the utilized SEG and PE approaches.

2.1. Pith Estimation and CS Segmentation

PE is based on the assumption that local orientations of annual ring patches point into the direction of the pith. For this purpose, local orientation estimates are computed using two Fourier spectrum analysis approaches: Peak and Principal Component Analysis (PCA) as suggested in [7]. The image is subdivided into blocks and the intersections of their

THIS WORK IS PARTIALLY FUNDED BY THE AUSTRIAN SCIENCE FUND (FWF) UNDER PROJECT NO. TRP-254.

local orientation estimates are summed up in an accumulator array. This array is smoothed with a Gaussian and the maximum intersection cell is used as pith estimate.

For SEG the pith position (either the GT or the PE result) is utilized as initial starting point for the similarity based region growing procedure suggested in [8]. Similar as for PE, the input image is subdivided into blocks. Four clusters, each consisting of four blocks, are initialized close around the pith position. The subsequent region growing procedure is based on intensity histogram distances between the blocks of a cluster which are computed using the Earth Movers Distance (EMD). Blocks along the cluster boundaries that fulfil the similarity criteria are added to each cluster until no more blocks can be added. Finally, the clusters are merged and the respective concave hull is utilized as SEG result.

2.2. Geometric Feature Extraction

Once the CS boundary and the pith position are determined several geometric features can be computed [9, p.323ff]. Fig. 1a illustrates an exemplary CS image and in Fig. 1b an overview of important geometric measurements is provided. Subsequently, the set of utilized features is presented. A_{CS} and P_{CS} give the area and perimeter of the CS and BB specifies the minimum bounding box.

HU Moments (H_{1-7}) = seven invariant image moments proposed by [10].
Zernike Moments (Z) = 10 orders of complex Zernike moments are computed for the CS shape [11, 12].
Circularity (C) = $4\Pi \cdot (A_{CS}/P_{CS}^2)$, describes how similar to a circle the CS is.
Rectangularity (R) = A_{CS}/A_{BB}, ratio between A_{CS} and the area of the minimum bounding rectangle (A_{BB}).
Eccentricity (E) = BB_W/BB_H, ratio between width and height of the minimum bounding box.
Pith Eccentricity (PEC) = distance between the centroid (CM) of the CS and the pith position (PP) normalized using the width of the BB_W.
Centroid distances (CD) = centroid (CM) to border distances per degree ($CD_\phi, \phi \in \{1°, \ldots, 360°\}$) normalized by $\max CD_\phi$.
Pith distances (PD) = the pith to border distances per degree ($PD_\phi, \phi \in \{1°, \ldots, 360°\}$) normalized by $\max PD_\phi$.

3. EXPERIMENTS AND RESULTS

The experimental setup is chosen to assess two questions. First, the general biometric performance of geometric features is assessed by using GT data. Second, we validate their reliability in case of different configurations for SEG and PE.

Testset: For the experiments the same test sets (TS_1, TS_2) as in [6] are utilized. TS_1 consists of 50 tree logs. Each log was captured four times with and without flash. To investigate

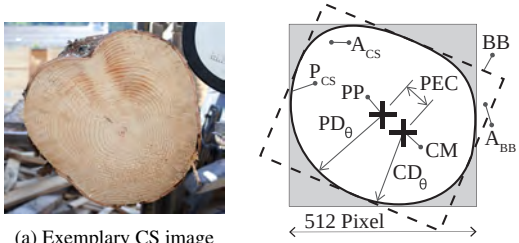

(a) Exemplary CS image (b) Geometric features

Fig. 1: Geometric feature extraction illustration.

the impact of a clearance cut in the sawmill the ends of eight logs from TS_1 were cross-cut and captured once again, with and without flash. For TS_2 105 strongly bended logs were captured three times without flash. Commonly, bended logs show a high amount of reaction wood. This leads to elliptical shaped CSs. For each CS image the pith position and the CS border were determined manually.

Computational details For each CS image the CS boundary and pith position is determined using four different configurations. Two approaches for SEG and two for PE are utilized. For SEG these approaches distinguish in using grey value (SEG-G) or RGB histograms (SEG-C) for computing the EMD between two blocks. In case of PE the Peak (PE-PEAK) or PCA (PE-PCA) approach for local orientation estimation are utilized. For each configuration and the respective PE approach different variations for estimating the pith are assessed. The first variation (P_1) estimates the pith using local orientations computed from the entire image (see Fig. 3a). In the experiments P_1 is used as seed point for SEG. The second variation (P_2) is computed by just using local orientations within the CS boundary (see Fig. 3b). As shown in [7], local orientation estimates close to the pith are more circular and thus the third variation (P_3) is computed within the half-sized CS boundary. P_1,P_2,P_3 are computed using half-overlapping 16x16 pixels blocks. The fourth variation (P_4) is computed like P_3 with the difference that a block-overlapping factor of four is utilized.

Additionally, three variations are computed using a saw cut suppression mode. This mode computes the orientation

Fig. 2: 1st Row (TS_1): Respectively, two CS-Images from two different logs - one captured with flash and one without flash. 2nd Row (TS_2): Four CS-Images from different logs.

(a) PE within the total image (b) PE within the CS boundary (c) PE within the scaled CS boundary

Fig. 3: Illustration of the pith estimation (PE) variations.

distribution for all local orientations in the considered region. If the most frequent orientation has a frequency remarkably higher than the mean plus two times the variance the corresponding magnitudes in all Fourier spectra are zeroed and the local orientation estimates are recomputed. The saw-cut suppressed PE variations are denoted as P_{2SS},P_{3SS},P_{4SS}.

For all configurations and the GT data the geometric features described in Section 2 are computed. For each feature the matching scores between all CS-Images of both testsets are computed and finally the matching scores are normalized.

3.1. Results

Initially, the verification performance of geometric features based on GT data (i.e. manually determined pith position and CS boundary) is assessed. The performance is assessed for each feature separately and for score level fusion [13, p.225] for different numbers (k) of features. These are determined using Selective Floating Forward Selection (SFFS) [14] which is configured to minimize the overlap between the inter- and intraclass distribution.

Second, the accuracies for the SEG/PE configurations and the PE variations are considered in detail. The most accurate PE variation is then utilized as pith estimate to evaluate the verification performance in case of automated SEG and PE. Basically, the verification performance is assessed considering the EER and margin of error (MOE) which is estimated for a 90% level of confidence using subset partitioning [15].

Groundtruth-based Verification Performance The results in Table 2 show that several features achieve respectable EERs. In case of E,PEC,RD,CD and Z the EERs are below 10%. The overall best EER is achieved using PD which shows an EER of 1.4%. In case of SFFS, the results in Table 1 show that the best result is achieved with (PD,CD,Z) EER=0.54%. Based on these results it can be stated that these features principally have a high discriminative power.

CS segmentation and pith estimation accuracy The SEG accuracy is specified by the F-Measure between the GT mask and the SEG result. The PE accuracy is given as the pixel distance between the GT and the estimated pith position. In Table 3 the mean and standard deviations for the accuracies of all configurations are summarized. SEG-C and SEG-G show a similar segmentation performance although there are big

SEG/PE	k=2	k=3	k=4
GT	PD,CD 0.74±0.8	PD,CD,Z 0.54±0.5	PD,CD,Z,R 0.68±0.6
SEG-G/PE-PCA	PD,H_4 20.12±2.4	PD,H_4,R 20.07±2.6	PD,H_4,R,H_7 20.10±2.3
SEG-G/PE-PEAK	PD,C 21.84±2.8	PD,E,C 22.52±3.2	PD,CD,E,C 23.28±3.2
SEG-C/PE-PCA	PD,CD 15.75±2.6	PD,CD,E 15.81±3.1	PD,CD,E,H_6 15.88±3.3
SEG-C/PE-PEAK	PD,CD 15.36±3.4	PD,CD,R 15.34±3.4	PD,CD,R,E 15.61±3.1

Table 1: EER±MOE[%]: SFFS-based score level fusion. Z is not considered in case of SEG/PE.

differences when considering the particular results for each CS in detail. This can be observed for the P_2 results showing remarkable PE accuracy differences between the SEG-C and SEG-G configurations.

Overall PE results for SEG/PE the best accuracy is reached with SEG-G/PE-PEAK and P_{4SS}. The particular results are illustrated in Fig. 4. For each log end the mean, min. and max. accuracy for SEG and PE is depicted. The chart illustrates that the segmentation accuracies for TS_1 are better than for TS_2. This is caused by the deformed CSs in TS_2 (see Fig. 2) which likely show reaction wood on their end faces. This observation is also visible for the PE accuracies which are better in case of TS_1. Furthermore, it can be recognized that there is no direct relationship between SEG and PE accuracy.

However, the results show that for the GT-based configurations the P_2 and P_{2SS} variations achieve the best PE accuracies. In difference to the GT-based PE results, the accuracies for SEG-C and SEG-G using P_3 and P_4 are remarkably better. We assume that this is caused by the segmentation errors which influence the performance of P_2 and P_{2SS}. Due to down-scaling the CS border for P_3 and P_4 the probability of using wrong orientation estimates is reduced. In comparing the results for P_3 and P_4 to P_{3SS} and P_{4SS} the improved PE accuracy in case of sawcut suppression is recognizable.

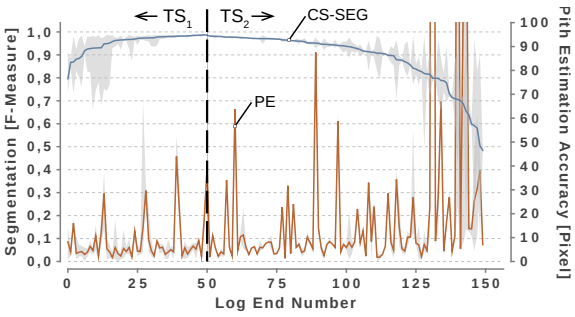

Fig. 4: Mean, min. and max. accuracies for SEG-G/PE-PEAK and P_{4SS} grouped by the images of each log end.

SEG/PE	HU_1	HU_2	HU_3	HU_4	HU_5	HU_6	HU_7	C	R	E	PEC	CD	PD	Z
GT	11.6±3.1	13.8±3.4	19.7±3.9	25.1±4.5	30.7±5.5	28.2±5.9	29.5±5.3	17.4±5.0	22.1±4.2	8.1±1.8	7.2±1.2	2.8±2.4	1.4±0.7	6.3±1.2
SEG-G/PE-PCA	33.6±2.6	34.1±2.0	39.2±3.5	42.1±1.8	42.4±1.7	37.2±2.6	41.3±2.3	34.8±2.9	40.0±0.4	29.8±2.4	29.1±3.4	28.1±3.2	20.0±2.5	5.6±1.0
SEG-G/PE-PEAK	32.8±2.8	33.7±2.9	38.5±3.5	41.2±2.1	40.6±2.1	37.0±2.5	41.6±2.0	36.0±2.7	38.3±0.7	28.9±2.4	28.6±3.0	27.1±3.5	20.3±3.0	5.6±1.0
SEG-C/PE-PCA	29.7±2.1	31.8±1.9	36.5±3.8	41.7±1.5	44.2±1.2	35.6±2.3	40.6±2.0	29.1±3.2	36.3±2.1	24.0±2.5	27.6±2.9	20.3±3.4	16.6±2.8	5.5±1.1
SEG-C/PE-PEAK	31.0±2.6	32.0±2.6	36.6±3.5	40.6±1.5	41.2±1.3	36.3±2.0	40.3±1.8	30.5±3.1	36.7±0.8	24.1±2.5	26.2±2.9	19.4±3.4	15.2±2.8	5.4±1.0

Table 2: EER±MOE[%] for each geometric feature and all configurations.

SEG/PE	F-Measure	P_1	P_2	P_{2SS}	P_3	P_{3SS}	P_4	P_{4SS}
GT/PE-PCA	–	–	18.9 ±20.1	19.5 ±19.6	16.8 ±25.8	15.4 ±18.9	16.8 ±32.9	14.4 ±19.5
GT/PE-PEAK	–	–	13.2 ±24.9	11.5 ±14.5	20.2 ±33.3	21.3 ±32.0	19.7 ±35.9	22.1 ±38.4
SEG-G/PE-PCA	0.91 ±0.11	24.9±37.1	20.9 ±40.1	21.7 ±42.6	18.5 ±44.2	17.8 ±40.8	17.7 ±44.8	16.5 ±40.6
SEG-G/PE-PEAK		24.0 ±39.3	16.1 ±43.1	15.9 ±42.6	14.8 ±45.1	13.7 ±41.6	14.2 ±45.4	13.0 ±41.6
SEG-C/PE-PCA	0.93 ±0.10	24.9 ±37.1	22.0 ±45.3	23.0 ±47.6	19.0 ±44.2	17.8 ±40.4	17.6 ±44.2	17.1 ±42.5
SEG-C/PE-PEAK		24.0 ±39.3	18.1 ±54.5	18.1 ±53.9	17.2 ±56.9	15.7 ±53.3	17.1 ±57.7	14.7 ±51.5

Table 3: CS segmentation and pith estimation accuracy evaluation.

Real world verification performance Based on the PE accuracy evaluation P_{4SS} is selected for computing the geometric features in case of automated SEG/PE.

The verification performance results for all configurations are summarized in Table 1 and 2. Equal as for the GT-based configuration, the best EERs for each particular feature are achieved with the features E,PEC,RD and Z. It is astonishing that the Zernike moments show EERs that totally outperform the other features. In addition, the EERs computed with the automated configurations outperform the GT-based EER achieved with Z.

The intra- and interclass distribution for the best EER = 5.4% (SEG-C/PE-PEAK) and Zernike moments (Z) is depicted in Fig. 5a. The chart shows that the intraclass distribution is splitted into two parts. The left part belongs to intraclass distances between CS images with a high segmentation accuracy and the right part to distances between worse segmented CS images.

Regarding all EERs, except the HU features, the results in Table 2 show that using SEG-C improves all EERs compared to the SEG-G results. Furthermore, the SEG-G and SEG-C results show that the PE-PEAK approach achieves better EERs compared to the PE-PCA approach.

Beneath the Zernike moments, the radial pith and centroid distances (PD and CD) achieve the next best EERs. For all configurations PD performs better than CD. The best EER for PD and the automated configurations is achieved with SEG-C/PE-PEAK and accounts 15.2 %. Considering all configurations, it can be stated that HU moments are less suited as geometric CS features. The EERs for each particular feature indicate that the SEG-C/PE-PEAK configuration is the best for the computation of geometric features.

Finally, the fusion based EERs presented in Table 1 are assessed. For the GT-based configuration all fusion results lead to an improvement of the verification performance. The fusion of PD,CD,Z achieves an EER of 0.54% (see Fig. 5b). In case of the automated configurations Z is neglected because the fusion results were less interesting. However, just

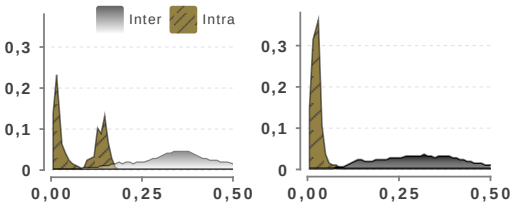

(a) SEG-C/PE-PEAK: Zernike moments (Z) - EER=5.4%

(b) GT: Fusion of PD,CD,Z - EER=0.54%.

Fig. 5: Selected intra-, interclass score distributions [X-Axis: Matching Score, Y-Axis: Probability]

for one configuration (SEG-C/PE-PCA) the fusion of PD,CD improves the best EER (16.6%) achieved with PD to 15.75%. For all other results feature fusion does not improve the EERs of the automated configurations.

4. CONCLUSION

This work assesses the discriminative power of geometric log end features and validates their reliability in case of performing automated CS segmentation and pith estimation. The experimental evaluation forms a solid basis for the further development of a biometric log recognition system.

In case of GT-data the verification performance evaluation showed that radial distances (CD,PD) and Zernike moments (Z) show a high discriminative power. Score level fusion of these features leads to an EER of 0.54%. The validation of these features for automated segmentation and pith estimation showed that Zernike moments achieve the highest reliability. Compared to Zernike moments the EERs for CD and PD are strongly influenced by automated segmentation and pith estimation.

Future work should investigate the fusion of the best geometric features with annual ring pattern features.

5. REFERENCES

[1] W.A. Barrett, "Biometrics of cut tree faces," in *Advances in Computer and Information Sciences and Engineering*, Tarek Sobh, Ed., pp. 562–565. Springer Netherlands, 2008.

[2] R. Schraml, J. Charwat-Pessler, and A. Uhl, "Temporal and longitudinal variances in wood log cross-section image analysis," in *IEEE International Conference on Image Processing 2014 (ICIP 2014)*, Paris, FR, Oct. 2014.

[3] R. Schraml, J. Charwat-Pessler, A. Petutschnigg, and A. Uhl, "Robustness of biometric wood log traceability using digital log end images," Tech. Rep. 2014-08, Department of Computer Sciences, University of Salzburg, Austria, `http://www.cosy.sbg.ac.at/tr`, 2014.

[4] A. K. Jain, S. Prabhakar, L. Hong, and S. Pankanti, "Filterbank-based fingerprint matching," *IEEE Transactions on Image Processing*, vol. 9, no. 5, pp. 846–859, May 2000.

[5] A. Jain, A. Ross, and S. Prabhakar, "Fingerprint matching using minutiae and texture features," in *Procs. of the International Conference on Image Processing (ICIP'01)*, Thessaloniki, GR, 2001, vol. 3, pp. 282–285.

[6] R.Schraml and A.Uhl, "Tree log identification based on digital cross-section images of log ends using fingerprint and iris recognition methods," Tech. Rep. 2015, Department of Computer Sciences, University of Salzburg, Austria, `http://www.cosy.sbg.ac.at/tr`, 2015.

[7] R. Schraml and A. Uhl, "Pith estimation on rough log end images using local Fourier spectrum analysis," in *Proceedings of the 14th Conference on Computer Graphics and Imaging (CGIM'13)*, Innsbruck, AUT, Feb. 2013.

[8] R. Schraml and A. Uhl, "Similarity based cross-section segmentation in rough log end images," in *Proceedings of the 10th Artificial Intelligence Applications and Innovations Conference (AIAI'14)*, L. Iliadis et al., Eds., Rhodes, GR, 2014, vol. 436 of *Springer IFIP AICT*, pp. 614–621.

[9] I. Pitas, *Digital Image Processing Algorithms and Applications*, John Wiley & Sons, Inc., New York, NY, USA, 1st edition, 2000.

[10] Ming-Kuei Hu, "Visual pattern recognition by moment invariants, computer methods in image analysis," *IRE Transactions on Information Theory*, vol. 8, 1962.

[11] R. Mukundan and K. R. Ramakrishan, *Moment Functions in Image Analysis: Theory and Applications*, chapter Zernike Moments, pp. 57–70, World Scientific Publishing Company, 1988.

[12] Chee-Way Chong, P. Raveendran, and R. Mukundan, "An efficient algorithm for fast computation of pseudo-zernike moments," *International Journal of Pattern Recognition and Artificial Intelligence*, vol. 17, no. 6, pp. 1011–1023, 2003.

[13] Anil K. Jain, Arun A. Ross, and Karthik Nandakumar, *Introduction to Biometrics*, Springer US, 2011.

[14] P. Pudil, J. Novovičová, and J. Kittler, "Floating search methods in feature selection," *Pattern Recognition Letters*, vol. 15, no. 11, pp. 1119–1125, 1994.

[15] Ruud M. Bolle, Nalini K. Ratha, and Sharath Pankanti, "Error analysis of pattern recognition systems: The subsets bootstrap," *Comput. Vis. Image Underst.*, vol. 93, no. 1, pp. 1–33, Jan. 2004.

Tree log identification based on digital cross-section images of log ends using fingerprint and iris recognition methods*

Rudolf Schraml[1], Heinz Hofbauer[1], Alexander Petutschnigg[2], and Andreas Uhl[1]

[1] Department of Computer Sciences, University of Salzburg, Austria
[2] Department of Forest Products Technology and Timber Construction, University of Applied Sciences Salzburg, Austria

Abstract. Tree log biometrics is an approach to establish log traceability from forest to further processing companies. This work assesses if algorithms developed in the context of fingerprint and iris recognition can be transferred to log identification by means of cross-section images of log ends. Based on a test set built up on 155 tree logs the identification performances for a set of configurations and in addition the impacts of two enhancement procedures are assessed.
Results show, that fingerprint and iris recognition based approaches are suited for log identification by achieving 100% detection rate for the best configurations. In assessing the performance for a large set of tree logs this work provides substantial conclusions for the further development of log biometrics.

1 Introduction

Commonly the term biometrics stands for the study of behavioural or physiological characteristics to identify living people. But the theoretical background and the concepts of human biometrics have been carried over to the recognition of plants, vegetables, animals, industrial products and most relevant for this study to the recognition of tree logs or boards [20]. This study deals with concepts of fingerprint and iris recognition and explores their applicability to the identification of tree logs using cross-section images (CS-Images) of log ends.

In order to close the traceability gap between the forest site and the further processing companies tree log identification is an economic requirement to map the ownership of each log. Additionally, social aspects have become more important and sustainability certificates like Pan European Forest Certification (PEFC) and Forest Stewardship Council (FSC) are a must have for all end-sellers. Finally, traceability is legally bound by the European Timber Regulation (EUTR) to prohibit illegal logging in the EU [4].

State-of-the art traceability approaches rely on physically marking each log and in the past decade huge efforts were taken to push the development of new traceability approaches. For example, the final report of the Indisputable Key Project [19] promotes the usage of Radio Frequency Identification transponders to establish log traceability.

First investigations on the hypothesis that logs are separate entities on the basis of biometric log characteristics were carried out in the works of [2, 3, 5]. For the purpose of tracking logs within the sawmill 2D and 3D scanners were utilized to extract geometric

* This work is partially funded by the Austrian Science Fund (FWF) under Project No. TRP-254.

wood properties as biometric features. Such devices are not applicable for industrial usage at forest site.

On account of the fact, that log end faces show features in terms of annual rings, pith position, shape and dimension it is assumed that CS-Images of log ends can be used as biometric characteristic to set-up a biometric system. A first work on log biometrics using CS-Images was presented by [1] as an effort to curb poaching of trees. For this purpose, pseudo Zernike moments are computed for CS-Images captured from poached tree stumps and first results were presented for a small testset. The achieved results were quite good but the extracted features more or less rely on the cutting pattern and the shape of the CS.

By superficially comparing annual ring patterns of log ends to human fingerprints one perceives their similarity. Based on this observation, [16] investigated temporal and longitudinal variances of CS-Images of a single tree log. The authors adopted the FingerCode approach [7] to compute and compare templates from CS-Images. Furthermore, in [15] the impact of different real world CS variation types on the robustness of biometric log recognition is assessed. Although the authors draw first conclusions on the identification performance, the utilized testset is too small and the results are not convincing.

In considering the identification performance for 150 different tree logs this work demonstrates that a biometric system using log end images is suited for log tracking. Additionally to the fingerprint-based approach utilized in [16, 15], this work evaluates the applicability of well-known iris recognition approaches. Furthermore, it is not clear to which extent the enhancement procedure utilized in [16, 15] influences the verification and identification performance. For this purpose, all approaches are evaluated with and without enhancement. Results show, that enhancement basically is beneficial to overcome issues caused by CS variations.

Section 2 introduces the computation and matching of log templates using approaches from fingerprint and iris recognition. Subsequently, the experimental evaluation is presented in Section 3 followed by the conclusions in Section 4.

2 CS-Code Computation and Matching

An exemplary enrolment and identification scheme for log biometrics is depicted in Fig. 1. Enrolment of a tree log is performed in the forest. After a tree log is cut and processed by a harvester the log end is captured by a digital camera mounted on the harvester head. Templates of logs which are computed by means of CS-Images are denoted as CS-Codes. For enrolment the computed CS-Code is stored in

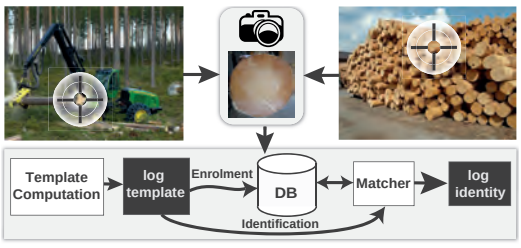

Fig. 1: Exemplary enrolment and identification schemes

the database. Identification can be performed at each stage of the log processing chain where an appropriate capturing device is available. Typically, identification is required when a log is delivered to a sawmill. Independent of the template computation approach procedure the CS-Image is registered and enhanced preliminary. The fingerprint- and iris-based CS-Code computation schemes are depicted in Fig. 2.

2.1 CS Registration and Enhancement

For registration the pith position and CS boundary have to be determined in advance. Automated approaches for pith estimation and CS segmentation were presented in [18, 12] and [17], respectively. The CS-Image is rotated around the pith position, cropped to the CS boundary box and scaled to 512 pixels in width. Rotation is performed to generate rotated versions of the input image or to align the CS to a unique rotational position.

The registered CS-Image is then utilized for the enhancement procedure. Commonly, the annual ring pattern is disturbed due to cutting and there arise different types of intraclass CS variations in real world identification scenarios [15]. The purpose of enhancement is to strengthen the annual ring pattern contrast and to compensate CS variations. Similarly to fingerprint enhancement [6], three consecutive stages are performed: Local orientation estimation, local frequency estimation and local adaptive filtering. Initially, the CS-Image is subdivided into half-overlapping blocks to reduce boundary effects caused by local filtering. On the basis of registered CS-Images which are scaled to 512 pixels in width, 32×32 pixels blocks are a good choice in terms of timing performance and capturing local annual ring pattern information.

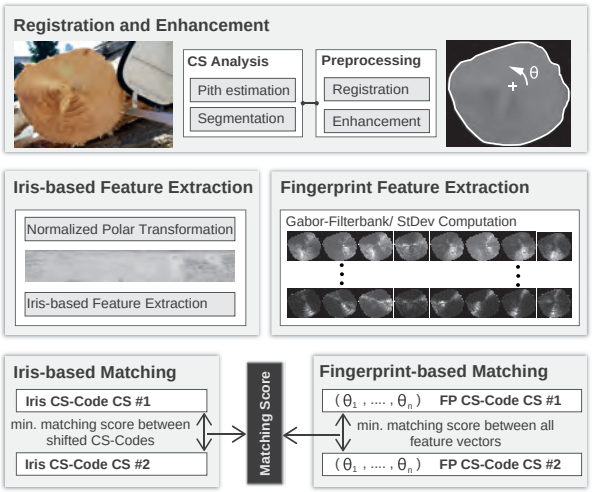

Fig. 2: Fingerprint- and iris-based template computation and matching schemes

In the first stage, the local orientation of each block is determined based on peak estimation in the Fourier Spectrum (see [18]). Next, the local orientation field is low-pass filtered with a Gaussian to correct wrong orientation estimates. Based on the orientation estimates of each block the corresponding dominant frequency in the Fourier Spectrum is determined. Therefore, the Fourier Spectrum of each block is subdivided into sub-bands and sectors and the dominating frequency is defined as the sector sub-band which shows the maximum integral of its magnitudes. If this sector sub-band does not correspond to the block orientation it is neglected and the local frequency is interpolated using a Gaussian. Finally, the Fourier Spectrum of each block is filtered with a Log-Gabor which is tuned to the block orientation and frequency. As in [16] a bandwidth of three times the variance of the Fourier Spectrum and as spread value the blocksize/4 is utilized. After filtering, the filtered spectra are inverse transformed and utilized as new block values.

In this work additionally a variant of this procedure is evaluated which differs in the local orientation estimation procedure. Initially, local orientations are computed for each block as described above. Subsequently, the pith position is used to detect wrong orientation estimates in case the angular distance between the block origin/pith position and the local orientation estimate exceeds a threshold. Thereby, the threshold for a each block is specified by $t = \lambda * log(\text{pith distance})$, where λ is an arbitrary value and the pith distance is the distance between the block origin and the pith. Thus, the threshold increases with an increasing pith distance which takes into account that annual rings close to pith are more circular. For each local orientation estimate which exceeds this threshold the estimate is replaced by the direction to the pith position. All further steps are performed like as for the first approach (exemplary enhancement results see Fig. 6).

2.2 Fingerprint-based CS-Codes

Same as in [16, 15] the FingerCode approach is adopted to compute and compare CS-Codes from CS-Images. With intent to capture different annual ring pattern frequencies the utilized Gabor filterbank is built up on six different filters and for each filter eight rotated versions are created.

CS-Code computation is performed in three stages: First, the registered and enhanced CS-Image is filtered with each filter in the filterbank. The filtered images are further subdivided into blocks (e.g. 16×16 pixels). For all blocks of each filtered image, the grey value standard deviations are computed and stored into a matrix. Values of blocks which are not within the CS border are assigned with a marker value. These markers are used to discriminate between background and CS in the matching procedure. All matrices are stored as a one-dimensional vector.

Compared to fingerprints, the rotational misalignment range of a CS-Image is not restricted to a certain range. Rotational variances are compensated by repeatedly computing features for rotated versions of the input CS-Image. All feature vectors computed for different rotations $(\Theta_1, \ldots, \Theta_n)$ compose the CS-Code of a CS-Image.

Matching procedures Matching between two CS-Images is performed by computing the minimum matching score (MS) between all feature vectors $(\Theta_1, ..., \Theta_n)$ of the CS-Codes from both CS-Images.

Three different matching procedures are evaluated to investigate the impact of including shape information. The MS is computed by:

$$MS(CS_1, CS_2) = \frac{1}{M} \sum_{i=0}^{n} D(CS_1(i), CS_2(i)) \tag{1}$$

where CS_1, CS_2 are two feature vectors of the CS-Codes which are compared, i specifies the index of the feature value in both vectors and MCS_1, MCS_2 are masks which allow to differentiate between background and CS.

The first matching procedure MS_{AP} uses a distance function which just uses feature value pairs which are in the intersection of both CSs . For normalization, M is defined by the amount of considered feature value pairs: $M = |MCS_1 \cap MCS_2|$. Thus, this procedure relies on the discriminative power of the annual ring pattern.

$$D_{AP} = \begin{cases} |CS_1(i) - CS_2(i)| & \text{if } i \in MCS_1 \cap MCS_2 \\ 0 & \text{otherwise} \end{cases} \tag{2}$$

For the second procedure $MS_{AP\&S}$ the distance function $D_{AP\&S}$ includes a penalty value $P_{AP\&S}$. The penalty is added to all feature value pairs which are in the symmetric difference of the CS masks and for normalization $M = |MCS_1 \cup MCS_2|$ is used. Hence, the MS increases for differently shaped CSs. $P_{AP\&S}$ is defined by the mean value of the feature value distributions of both feature vectors.

$$D_{AP\&S} = \begin{cases} |CS_1(i) - CS_2(i)| + P_{AP\&S} & \text{if } i \in MCS_1 \triangle MCS_2 \\ |CS_1(i) - CS_2(i)| & \text{if } i \in MCS_1 \cap MCS_2 \\ 0 & \text{otherwise} \end{cases} \tag{3}$$

Finally, the third procedure uses score level fusion of the MS_{AP} score and the False Negative Rate (F) which is computed for (MCS_1, MCS_2). F is defined as the ratio between the symmetric difference of the two masks and total amount of pixels in the smaller mask. For score level fusion MS_{AP} and F are normalized using the factors σ_{AP}, σ_F. They are precomputed based on the feature value ranges of MS_{AP} and F so that they become equally weighted in the score level fusion.

$$\mathrm{F} = \frac{MCS_1 \triangle MCS_2}{\min(|MCS_1|, |MCS_2|)},\ MS_{AP,F} = MS_{AP} \cdot \sigma_{AP} + F \cdot \sigma_F \tag{4}$$

2.3 Iris-based CS-Codes

The pith of a cross-section is a unique feature which can be used as reference point. In combination with the CS border it is used to polar transform CS-Images. In this work polar transformed CS-Images are treated like polar iris images and it is evaluated if iris feature extractors and comparators are applicable for log biometrics.

For this purpose, the registered and enhanced CS-Image is transformed by using bicubic interpolation. For normalization each pixel in the polar image is stretched according to the max. pith to border radius. Two different formats for the polar-transformation are evaluated. The first is equal to the usual format demanded by many iris feature extractors: 512×64 pixels. Compared to the size of the iris, CSs are larger and the

transformation is not restricted to an annular shaped ring. In case of more than 64 annual rings the common polar transformation format of 512×64 pixels causes a loss of information. Because of that and the quadratic format of the registered CS-Images, in addition a format of 512×512 pixels is evaluated. The polar transformation scheme is depicted in Fig. 3 and exemplary polar transformed CS-Images for both formats are shown in Fig. 6. For iris recognition based CS-Code computation and template matching the USIT package [14] is utilized.

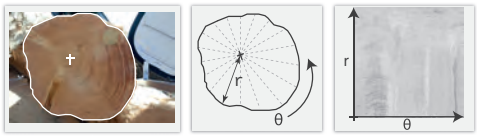

Fig. 3: CS-Image polar transformation scheme

3 Experiments

In the experiments the verification and identification performances for different configurations are assessed. Introductory, the testset is outlined and the experimental setup for the utilized configurations is described (see Section 3.1). Finally, the results are presented and discussed in Section 3.2.

Testset Two testsets (TS_1 and TS_2) are utilized. For TS_1 50 different tree logs were captured four times with and without flash. Additionally, the ends of eight logs were cross-cut and captured once again, with and without flash. In TS_2 105 logs were captured three times without flash. For each CS-Image the pith position and the CS border were determined manually and are utilized for the experiments.

3.1 Experimental Setup

For all CS-Images of the testsets CS-Codes and MSs were computed for different configurations and enhancement procedures. Subsequently, the setup for the enhancement procedures and the different CS-Code computation approaches are outlined.

Fig. 4: Testset One (TS_1): Each row shows four CS-Images of a single log. The first two CS-Images illustrate the difference of capturing the log end with and without flash. The latter two images are taken after the log end was cross-cut, with and without flash.

Fig. 5: Testset Two (TS_2): CS-Images from 4 logs

Enhancement The first procedure, entitled as ENH_1, is equal to the procedure suggested in [16]. As described in Section 2.1 the second just differs in the local orientation estimation procedure and is entitled as ENH_2. For comparison, all configurations are additionally evaluated without enhancement ENH_{NO}. Exemplary results for ENH_{NO} and ENH_2 are shown in Fig. 6.

Fingerprint (FP) configurations Rotational variances are compensated by computing feature vectors for rotations in the range from $-15°$ to $15°$. The CS-Codes are computed using 16×16 non-overlapping blocks and the Gabor filterbank is build up on six different filters tuned to 8 directions: $G(\lambda, \theta, \sigma, \gamma) = G(\lambda, \sigma) = ((1.5, 2), (2.5, 2), (3.5, 3), (4.5, 3), (5.5, 3), (6.5, 3)), \theta = \{0, 22.5, ..., 135, 157.5\}, \gamma = 0.7$

Iris configurations Different configurations based on the feature extractors and comparators provided by the USIT package [14] are utilized. Compared to iris images, the resolution of CS-Images is higher and the polar transformation is not restricted to an annular ring.

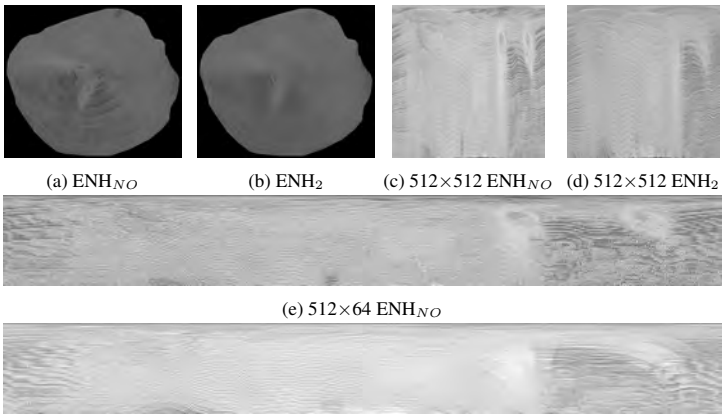

(a) ENH_{NO} (b) ENH_2 (c) 512×512 ENH_{NO} (d) 512×512 ENH_2

(e) 512×64 ENH_{NO}

(f) 512×64 ENH_2

Fig. 6: Illustration of the impact of enhancement for CS-Image #2 - TS_2. The original CS-Image is depicted in the top left image of Fig. 5.

In case of 512×64 pixels we utilize the following feature extractors: lg [11], ko [8], cr [13] and qsw [9]. Except for ko which uses koc as comparator all MSs are computed using the Hamming distance (hd).

For 512×512 pixels polar CS-Images the lg algorithm was extended to formats bigger than the 512×64 in accord with the original algorithm by defining the region of interest (ROI) through a number of rows r with a height h_r. Like the original, a row is condensed into a 1-D signal which is run through the Gabor filtering process. Since it is not clear which configuration of r and h_r is best we choose to use a variance of combinations, including combinations where the ROI does not span the whole polar-transformed CS-Image. However, unlike the iris biometry case which excludes the outer iris boundary, which frequently exhibits occlusions by cilia, we choose to exclude the inner residual part of the polar CS-Image. This part consists of a low number of pixels which are stretched to the polar CS-Image width, thus providing nearly no usable information. Note that the size of the feature vector is dependent on h_r.

Furthermore the algorithm by Ko et al. was simply adopted by allowing bigger textures without adapting the cell-size which is averaged. Note that as a result the length of the feature vector increases with the size of the texture. Rotational variances are compensated by shifting the CS-Codes in a range between -7 to 7 feature vector positions.

3.2 Results and Discussion

The experimental evaluation is performed in two stages. First, we evaluate the verification and identification performance for all configurations. Based on the Equal Error Rates (EERs) and Rank 1 recognition rates conclusions on the general applicability of the FP and iris approaches and the impact of enhancement are presented. Second, a closer examination on the intra- and interclass matching score distribution (SD) subsets points out how the enhancement and CS variations affect the intra- & interclass separability and thus the biometric system performance. Note that the intra- and interclass SDs correspond to the genuine and impostor distributions in biometrics [10].

Verification Performance Evaluation The EERs for all configurations computed for TS_1 and TS_2 are depicted in Table 1. Most important for this work, most of the EERs are quite low and show a high degree of separability between the intra- and interclass SD for a large set of tree logs. Same as in [15] the EERs of the FP configurations show that shape information improves the verification performance.

Except MS_{AP}, all other configurations include shape information in some way, e.g. the polar transformation relies on the CS boundary. Basically, the results for MS_{AP} show the discriminative power of the annual ring pattern solely and it is very amazing that MS_{AP} and ENH_2 achieves an EER of 0.9%.

	Configuration	ENH_{NO}	ENH_1	ENH_2
FP	MS_{AP}	15.7	1.7	0.9
	$MS_{AP\&S}$	1.85	0.74	0.68
	$MS_{AP,F}$	1.53	0.37	0.17
IRIS 512x512	lg, hd(16/32)	0.21	0.68	0.82
	lg, hd(50/10)	0.16	0.72	0.32
	lg, hd(64/08)	0.16	0.76	0.51
	ko, koc	2.73	4.88	4.24
IRIS 512x64	cr, hd	5.27	3.41	4.97
	lg, hd	1.34	3.64	5.42
	qsw, hd	3.44	5.73	8.33
	ko, koc	4.95	8.09	7.35

Table 1: EERs [%] for the FP and iris configurations

As expected, the utilized enhancement procedures improve the EERs of all FP configurations. Furthermore, the results of the FP configurations show that ENH_2 leads to better EERs than ENH_1.

For the iris configurations enhancement does not improve the EERs. This is very likely caused by the block artefacts of the enhancement procedures which are carried to the polar CS-Images. The best EERs for the iris configurations are reached using lg as feature extractor. Furthermore, the different variations for lg in terms of number of rows and row height $lg, hd(r \ / \ h_r)$ show that an increasing number of rows improves the verification performance. Overall configurations the best EERs are achieved using lg, hd(50,10) and lg, hd(64,08). Although lg, hd(50,10) ignores 12 pixel of each image the results are equal to the second configuration. Regarding the two different polar transformation formats, the results show that the larger format improves the EERs for the feature extractors which are assessed for both formats (lg and ko).

In Fig. 7 the intra- and interclass SDs for selected FP and iris configurations are depicted in the first and second row, respectively. These charts point out a significant difference which is not recognizable when considering just the EERs. Basically, they illustrate that the intra- and interclass SDs of the depicted FP and iris configurations are statistically significantly different.

For the FP configurations the charts for the three different matching procedures (ENH_{NO}) illustrate that by including shape information the separability is improved. Compared to the FP configurations, the interclass SDs of the iris configurations show a low variance and are thus narrow shaped. On the other hand, the intraclass SDs show a high variance and are broad shaped. Thereby, an increasing number of rows enforces this observation and the separability increases.

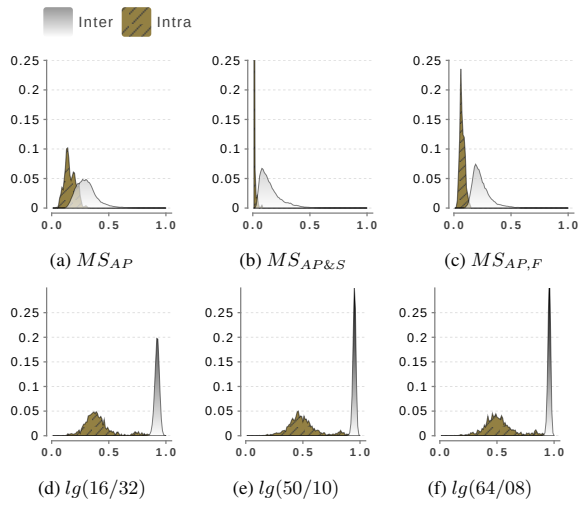

(a) MS_{AP} (b) $MS_{AP\&S}$ (c) $MS_{AP,F}$

(d) $lg(16/32)$ (e) $lg(50/10)$ (f) $lg(64/08)$

Fig. 7: Intra-, Interclass SDs for selected FP and Iris configurations (ENH_{NO}). [X-Axis: Matching Score, Y-Axis: Probability]

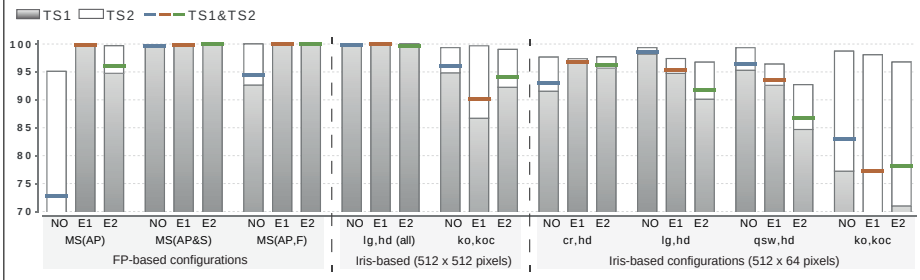

Fig. 8: Identification performance evaluation - Rank 1 detection rates.

3.3 Identification Performance Evaluation

An overview on the identification performance is depicted in Fig. 8. For each configuration, the Rank 1 recognition rates are given for TS_1, TS_2 and for the combination of both (TS_1 & TS_2). Results show, that the recognition rates for TS_1 are lower than for TS_2. The total recognition rate for TS_1 & TS_2 is somewhere in-between. The lower rates for TS_1 are caused by the higher degree of CS-variations in TS_1.

For the FP configurations each matching procedure achieves 100% recognition rate for at least one enhancement procedure. Surprisingly, nearly all iris configurations which use lg and 512×512 pixels achieve a recognition rate of 100% independent of the enhancement.

3.4 Intra-, Interclass Subset Analysis

In order to illustrate the impact of the testset structure and the enhancement procedures on the performance an analysis of the intra- and interclass SD subsets is presented. For this purpose, the cumulative distribution functions (CDFs) of the intra- and interclass SDs of each testset are considered individually for MS_{AP} (without and with enhancement). The intraclass CDFs in Fig. 9a illustrate that the intraclass MSs of TS_1 are infe-

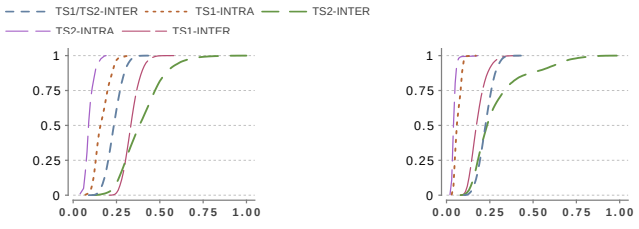

(a) MS_{AP}/ ENH_{NO} (b) MS_{AP}/ ENH_2

Fig. 9: CDFs for the intra-/ interclass SD subsets of two selected configurations.
[X-Axis: Matching Score, Y-Axis: Probability]

rior than those from TS_2. Thereby, Fig. 9b shows that ENH_2 reduces this difference and the intraclass CDFs get closer and shift to the left. Although the interclass CDFs also shift slightly to the left the overlap between the intra- and interclass CDFs decreases and thus the performance is improved. The inferior intraclass MSs of TS_1 are caused by CS variations included in TS_1.

The CDFs for all intraclass SD subsets of TS_1 computed with MS_{AP}/ ENH_{NO} are shown in Fig. 10. As expected, the CS-Images captured with and without flash (F, NF) are quite similar to each other. Furthermore, CS-Images of CSs captured with flash (F) are more similar to each other than those captured without flash (NF). MSs computed between CS-Images captured without and those with flash (NF-F) show up inferior MSs. Finally, and as investigated in [16, 15] the chart illustrates the impact of cross-cutting the log end on the performance. Matching scores computed between the initial log end CS-Images and the cross-cut log end CS-Images are shown in the subsets: F-CF, F-CNF, NF-CF and NF-CNF. Fig. 10 illustrates that these subsets show inferior MSs compared to the other subsets.

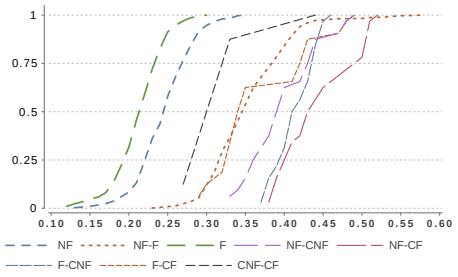

Fig. 10: Intraclass SD Subset Analysis for TS_1. NF = No Flash, F = Flash, CNF = Cut No Flash, CF = Cut Flash. [X-Axis: Matching Score, Y-Axis: Probability]

4 Conclusions

This work demonstrates that FP and iris recognition based approaches can be successfully transferred to the field of wood log tracking. Based on the variety of 155 logs the results are a first indication for the applicability of log biometrics to log identification.

In case of the FP recognition based approach the best results were achieved by including shape information in the matching procedure $MS_{AP,F}$. Furthermore, the results show that the performance of the FP configurations is significantly improved by the enhancement procedures. For the iris recognition based approaches the best results were achieved using lg features and hd as comparator. Thereby, a larger format and an increasing number of rows for the feature extraction is beneficial for the performance.

In the identification performance experiments the FP based approach and all iris configurations which use lg and 512×512 pixels achieve 100% detection rate at Rank 1. It can be concluded that Gabor features are well suited to extract discriminative annual ring pattern features.

Future research should deal with the impact of automated pith estimation and CS segmentation on the biometric system performance.

References

1. Barrett, W.: Biometrics of cut tree faces. In: Sobh, T. (ed.) Advances in Computer and Information Sciences and Engineering, pp. 562–565. Springer Netherlands (2008)
2. Chiorescu, S., Grönlund, A.: The fingerprint approach: using data generated by a 2-axis log scanner to accomplish traceability in the sawmill's log yard. Forest Products Journal 53, 78–86 (2003)
3. Chiorescu, S., Grönlund, A.: The fingerprint method: Using over-bark and under-bark log measurement data generated by three-dimensional log scanners in combination with radiofrequency identification tags to achieve traceability in the log yard at the sawmill. Scandinavian Journal of Forest Research 19(4), 374–383 (2004)
4. EuropeanParliament: Regulation (EU) No 995/2010 of the European Parliament and of the council of 20th October 2010 laying down the obligations of operators who place timber and timber products on the market (2010)
5. Flodin, J., Oja, J., Grönlund, A.: Fingerprint traceability of logs using the outer shape and the tracheid effect. Forest Products Journal 58(4), 21–27 (2008)
6. Hong, L., Wan, Y., Jain, A.: Fingerprint image enhancement: Algorithm and performance evaluation. IEEE Trans. Pattern Anal. Mach. Intell. 20(8), 777–789 (Aug 1998)
7. Jain, A.K., Prabhakar, S., Hong, L., Pankanti, S.: Filterbank-based fingerprint matching. IEEE Transactions on Image Processing 9(5), 846–859 (May 2000)
8. Ko, J.G., Gil, Y.H., Yoo, J.H., Chung, K.I.: A novel and efficient feature extraction method for iris recognition. ETRI Journal 29(3), 399 – 401 (2007)
9. Ma, L., Tan, T., Wang, Y., Zhang, D.: Efficient iris recognition by characterizing key local variations. IEEE Transactions on Image Processing 13, 739–750 (2004)
10. Maltoni, D., Maio, D., Jain, A.K., Prabhakar, S.: Handbook of fingerprint recognition. Springer New York (2009)
11. Masek, L.: Recognition of Human Iris Patterns for Biometric Identification, Master's thesis, University of Western Australia, 2003
12. Norell, K., Borgefors, G.: Estimation of pith position in untreated log ends in sawmill environments. Computers and Electronics in Agriculture 63(2), 155–167 (2008)
13. Rathgeb, C., Uhl, A.: Secure iris recognition based on local intensity variations. In: Proceedings of the International Conference on Image Analysis and Recognition (ICIAR'10). Springer LNCS, vol. 6112, pp. 266–275. Povoa de Varzim, Portugal (Jun 2010)
14. Rathgeb, C., Uhl, A., Wild, P.: Iris Recognition: From Segmentation to Template Security, Advances in Information Security, vol. 59. Springer Verlag (2013)
15. Schraml, R., Charwat-Pessler, J., Petutschnigg, A., Uhl, A.: Robustness of biometric wood log traceability using digital log end images. Tech. rep., University of Salzburg (2014)
16. Schraml, R., Charwat-Pessler, J., Uhl, A.: Temporal and longitudinal variances in wood log cross-section image analysis. In: IEEE International Conference on Image Processing 2014 (ICIP 2014). Paris, FR (Oct 2014)
17. Schraml, R., Uhl, A.: Similarity based cross-section segmentation in rough log end images. In: Proceedings of the 10th Artificial Intelligence Applications and Innovations Conference(AIAI 2014). IFIP Advances in Information and Communication Technology, vol. 436, pp. 614–621. Springer Heidelberg Berline, Rhodes, GR (2014)
18. Schraml, R., Uhl, A.: Pith estimation on rough log end images using local Fourier spectrum analysis. In: Proceedings of the 14th Conference on Computer Graphics and Imaging (CGIM'13). Innsbruck, AUT (Feb 2013)
19. Uusijärvi, R.: Indisputable key project. `http://interop-vlab.eu/ei_public_deliverables/indisputable-key` (2010), [last accessed: 28.07.2011]
20. Wayman, J., Jain, A., Maltoni, D.: Biometric Systems. Springer Berlin / Heidelberg (2005)

Computers and Electronics in Agriculture 119 (2015) 112–122

Contents lists available at ScienceDirect

Computers and Electronics in Agriculture

journal homepage: www.elsevier.com/locate/compag

Original papers

Towards the applicability of biometric wood log traceability using digital log end images ☆

R. Schraml [a,*], J. Charwat-Pessler [b,*], A. Petutschnigg [b], A. Uhl [a]

[a] University of Salzburg, Jakob Haringer Str. 2, 5020 Salzburg, Austria
[b] University of Applied Sciences Salzburg, Markt 136a, 5431 Kuchl, Austria

ARTICLE INFO

Article history:
Received 28 October 2014
Received in revised form 5 October 2015
Accepted 10 October 2015
Available online 2 November 2015

Keywords:
Biometric log traceability
Roundwood tracking
Log end biometrics
Cross-section analysis
Log end face analysis

ABSTRACT

Log traceability in the timber based industries is a basic requirement to fulfil economical, social and legal requirements. This work introduces biometric log recognition using digital log end images and explores the robustness to a set of log end cross-section (CS) variations. In order to investigate longitudinal and surface CS variations three tree logs were sliced and captured in different sessions. A texture feature-based technique well known from fingerprint recognition is adopted to compute and match biometric templates of CS images captured from log ends. In the experimental evaluation insights and constraints on the general applicability and robustness of log end biometrics to identify logs in an industrial application are presented. Results for different identification performance scenarios indicate that the matching procedure which is based on annual ring pattern and shape information is very robust to log length cutting using different cutting tools. The findings of this study are a further step towards the development of a biometric log recognition system.

1. Introduction

Many efforts had been made in the past in order to investigate illegal logging, its associated causes and how to prevent from illegal logging in future. Besides corruption on different governmental authority levels and land reclamation for mining, plantations or agriculture, illegal logging is known to be one of the main driving forces promoting deforestation (Richards et al., 2003; Smith et al., 2003; Kuemmerle et al., 2009). Deforestation is a phenomenon comprising timber harvesting, timber trade and disposal occurring around the world and affects biodiversity, hydrological cycles and contributes considerably soil erosion.

These problems were officially addressed at the UN Conference on Environment and Development (UNICED) held in Rio de Janeiro in 1992 and concluded in a document called Agenda 21. This document provides voluntary commitments on sustainable forest management and development and offers a basis for non-governmental, independent forest certification (United Nations, 1992). According to a report supported by the World Bank in 2003, illegal logging is still considered a major threat to the environment (Dykstra et al., 2003). Efforts in fighting illegal logging on the EU level led to the Forest Law Enforcement Governance and Trade Action Plan (FLEGT) defined in 2003 and the EU Timber Regulation (EUTR) prohibiting the trade of illegally harvested timber and wood products derived therefrom. This regulation, initially proposed by the Commission in 2008, is legally binding on all EU member states, each being responsible for national implementation, and has come into force since March 2013. This regulation claims traceability of timber and timber products throughout the supply chain providing information on operators, traders and, if possible, of retailers (EuropeanParliament, 2010).

Traceability of timber and wood products is generally expected to restrict illegal logging and is supposed to benefit companies and consumers (Tzoulis and Andreopoulou, 2013). In fact empirical information on quantities, and links to internationally traded wood are indispensable in order to assess causal relationships for illegal logging and to take effective steps preventing deforestation in future (Kastner et al., 2011). A contemporary managed database in conjunction with log labelling would certainly provide this information and serves as basis to impede illegal logging, fraud and misuse in future.

Abbreviations: CS, cross section; MS, matching score; SD, score distribution; NK, no knots; SDG, slice distance group; EER, equal error rate; CMC, Cumulative Match Characteristic; F(N)MR, False (Non) Match Rate.

☆ This work is partially funded by the Austrian Science Fund (FWF) under Project No. TRP-254.

* Corresponding authors.
E-mail addresses: rschraml@cosy.sbg.ac.at (R. Schraml), johann.charwat-pessler@fh-salzburg.ac.at (J. Charwat-Pessler).

http://dx.doi.org/10.1016/j.compag.2015.10.003
0168-1699/

A wide variety of log traceability systems have been applied in order to identify and track logs in the past. Each method so far has shown limitations due to costs, practical implementation or weather conditions. The applications range from punching, coloring or barcoding log ends to more recently developed techniques as DNA fingerprinting and usage of RFID transponders (Tzoulis and Andreopoulou, 2013).

Another approach is to track logs using biometric log characteristics. Investigations on the hypothesis that logs are separate entities on the basis of biometric log characteristics were presented in the works of Chiorescu and Grönlund (2003, 2004), Flodin et al. (2007, 2008a,b), which highlight the potential of biometric log recognition. The approaches presented in Chiorescu and Grönlund (2003, 2004) and Flodin et al. (2008a) utilized 2D and 3D scanners to extract geometric wood properties for tracking logs within the sawmill environment. The utilized capturing devices are however, not applicable at forest site. Furthermore, Flodin et al. (2007, 2008b) showed that knot positions as biometric features are suited to enable traceability between logs and the cut boards, reaching a recognition rate of 95%. On account of the fact that timber offers characteristics on log end faces in terms of annual rings, pith position, shape and dimension it is assumed that cross-section images of log ends can be used as biometric characteristic for log identification. Approaches for pith estimation and annual ring measurements in images of rough log ends were presented in Norell and Borgefors (2008), Schraml and Uhl (2013), Marjanen et al. (2008) and Norell (2009), respectively. Images containing a cross-section (CS) of a wood log are denoted as cross-section images (CS-Images) throughout this work.

A first work on log biometrics using CS-Images (log end biometrics) was presented in Barrett (2008) as an effort to curb poaching of trees. In the experimental evaluation digital images of tree stumps and the corresponding log ends are utilized, both showing up strong saw kerf patterns. Results show that the combination of log end shape and saw cut pattern information, represented by Zernike polynomials, achieves a high accuracy for log to stump recognition. In Schraml et al. (2014) temporal and longitudinal annual ring pattern variations were investigated based on time-delay captured CS-Images of 35 slices from a single log.

By using CS-Images from 150 different logs (Schraml et al., 2015a) showed that fingerprint based and iris-recognition based approaches are suited to achieve 100% identification accuracy. It turned out that, in addition to annual ring pattern information shape information is required to achieve this accuracy. Based on this observation in Schraml et al. (2015b) the discriminative power for a set of geometric log end features was validated.

In this study we elaborate the robustness of log end biometrics to practical issues of an industrial application. Different CS-Images of the same log end show up strong variations. For example, CS-Image capturing and weather conditions may lead to strong variations: e.g. varying image quality caused by motion blur or different lighting conditions and snow or dirt which covers parts of the CS. These variations are not considered in this work. Furthermore, industrial log processing causes specific types of CS variations. For this work we focus on longitudinal and surface variations of cross-sections (CSs). Longitudinal variations result from log end cutting and surface variations arise when different cutting tools are utilized for the first cut, in the forest, and the clearance cut, by further processing company (e.g. chain-saw and circular-saw).

The experimental evaluation is based on a testset which consists of 99 CS-Slices from three different tree logs. In addition to the 35 CS-Slices from the single log used in Schraml et al. (2014), 64 CS-Slices from further two logs are utilized. By assessing two objectives this work contributes to the ongoing research on log end biometrics.

The first objective is to investigate the verification performance with respect to the impact of surface and longitudinal variations on the intraclass variability and the separability between the intra- and interclass score distributions. In this context we also assess whether the CS surface has an impact on the longitudinal variations of each log.

The second objective is to investigate the identification performance. Initially, the basic impact of surface and longitudinal variations on the identification performance is assessed. Second, different real world-like identification scenarios are evaluated.

First, Section 2 introduces the computation and matching of biometric templates from CS-Images. The experimental setup is presented in Section 2.4 followed by the results in Section 3. Section 4 concludes this work and in Section 5 directions for future work are outlined.

2. Materials and methods

By superficially comparing the patterns of human fingerprints to annual ring patterns of wood log ends, one finds a close resemblance. Human fingerprint recognition is well-investigated and there exist mainly three groups of approaches: Minutiae-based, Correlation-based and Feature-based approaches (Maltoni et al., 2009). Apart from the presence of the pith as detectable feature, CS patterns do not exhibit further constant features like minutia's in fingerprints. Hence, minutiae-based approaches are not qualified for log CSs.

Basically, the scheme of a biometric recognition system is set up on five components: Data acquisition, Preprocessing, Feature Extraction, Template Generation and Template Matching. In case of log end biometrics, data acquisition is the capturing of digital CS-Images of log ends. For preprocessing the CS in the CS-Image is separated from the background, aligned and subsequently the CS is enhanced. Due to the ability of feature-based methods to capture information of the fingerprint ridge pattern they can be extended to work with CS patterns. We have adopted the texture feature-based FingerCode approach by Jain et al. (2000, 2001) to extract features from CS-Images. The extracted features of a CS-Image are stored as feature vector into the biometric template which we denote as cross-section code (CS-Code). The CS-Code of a CS-Image is composed by a set of feature vectors which are computed for differently rotated versions of the CS-Image.

Finally, template matching is the task of verification or identification of an individual or subject. In case of wood logs, identification is required. For this purpose, the individual/subject must be enrolled in the biometric system. In Fig. 1 exemplary enrolment and identification schemes are depicted. Enrolment could be done during the harvesting procedure in the forest. A digital camera mounted on a

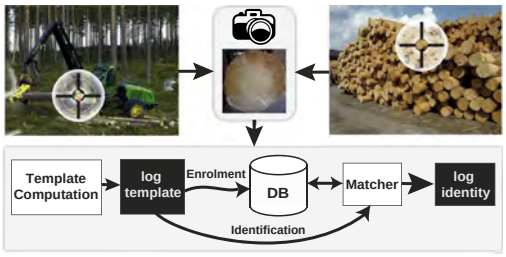

Fig. 1. Exemplary enrolment and identification schemes for a biometric log recognition system. The enrolment can be done in the forest using a digital camera mounted on a harvester.

harvester (e.g. Mattila and Viittanen, 1999) could be utilized to capture one end of each fresh cut log. Subsequently, the first four steps of the biometric system chain are completed and the computed log template (CS-Code) is stored in a database. Additionally, informational meta data can be assigned to each log template: On the one hand the harvester operator can assign visually observed information and the ownership of each log. Furthermore, geometric measurements of the harvester head and the geospatial position of the log origin can be appended. On the other hand automated CS analysis can be performed to estimate properties related to the quality of each log, e.g. annual ring counting to estimate the strength or detection of quality related wood properties like reaction wood.

Now identification of each log can be performed at each stage of the log processing chain. CS-Images for identification in the sawmill could be captured at the sorting station, at the sawmill yard or at any conveyor belt equipped with a capturing device. Subsequently, the CS-Image is processed by the biometric system and a log template is computed which is matched to all log templates in the database. If the matching score (MS) exceeds a certain system threshold the best match specifies the identity of the log. Furthermore, additional meta data can be retrieved or appended from/to the log record in the database. Templates of logs which were further processed and are no longer required should be removed from the database. May the log template is passed to another biometric system which enables board tracking (biometric approach: Pahlberg et al., 2015) and connects each board to the log template from which it descends. However, for chain of custody certification specific log template information has to be linked or passed through to the final product.

In the next three sections a detailed introduction on preprocessing (Section 2.1), CS-Code computation (Section 2.2) and three matching procedures (Section 2.3) between two CS-Codes is given. Finally, in the last Section 2.4 basics for the experimental evaluation are introduced.

2.1. Cross-section registration & enhancement

Due to the cutting pattern annual ring enhancement is a crucial task for any subsequent feature extraction procedure. As opposed to human fingerprints, the frequency of the annual ring pattern is strongly varying. Similar as in our previous works (Schraml et al., 2014, 2015a) enhancement is based on the fingerprint enhancement approach presented by Hong et al. (1998). In Schraml et al. (2015a) we showed that a slight variation of the procedure utilized in Schraml et al. (2014) further improves the biometric system performance and is thus also used in this work.

Preliminary to enhancement the CS in a CS-Image has to be registered. For registration, the CS border and pith position have to be determined (e.g. Schraml and Uhl, 2014, 2013; Norell and Borgefors, 2008). Subsequently, the CS-Image is rotated around the pith position, cropped to the CS bounding box and finally scaled to 512 pixels in width (see Fig. 2). Rotation can be performed to generate rotated versions of each CS-Image or to align the CS to a unique position (e.g. according to the center of mass).

For enhancement three consecutive stages are performed: Local orientation estimation, local frequency estimation and local adaptive filtering. First, the CS is subdivided in half-overlapping blocks (e.g. 32×32 pixels). Half-overlapping blocks are used to reduce boundary effects caused by local filtering. For each block principal component analysis of the local Fourier spectrum is performed to determine its local orientation (see Schraml and Uhl, 2013). Commonly, CSs are disturbed, due to cutting, which leads to faulty orientation estimates. For this purpose the local orientation is compared to the direction given by the block-centre to pith position vector (block-pith vector). If the angular distance between the local orientation estimate and the block-pith vector orientation exceeds a certain threshold (t) the local orientation estimate is considered being wrong. For each block t is defined by $t = \lambda * \log(\text{pith distance})$, where λ is an arbitrary value and the pith distance is the length of the block-pith vector. Thus, the threshold increases with an increasing pith distance which takes into account that annual rings close to pith are more circular. Local orientation estimates which exceed this threshold are replaced by the block-pith vector orientation.

Next, for each block and its local orientation the dominant frequency is determined. For this purpose, the local Fourier spectrum of each block is subdivided into sub-bands and sectors. For each sector and each particular sub-band the integral of the contained magnitudes is computed. The sector sub-band which shows the maximum sum of magnitudes represents the dominating frequency. If the local orientation which corresponds to this sector

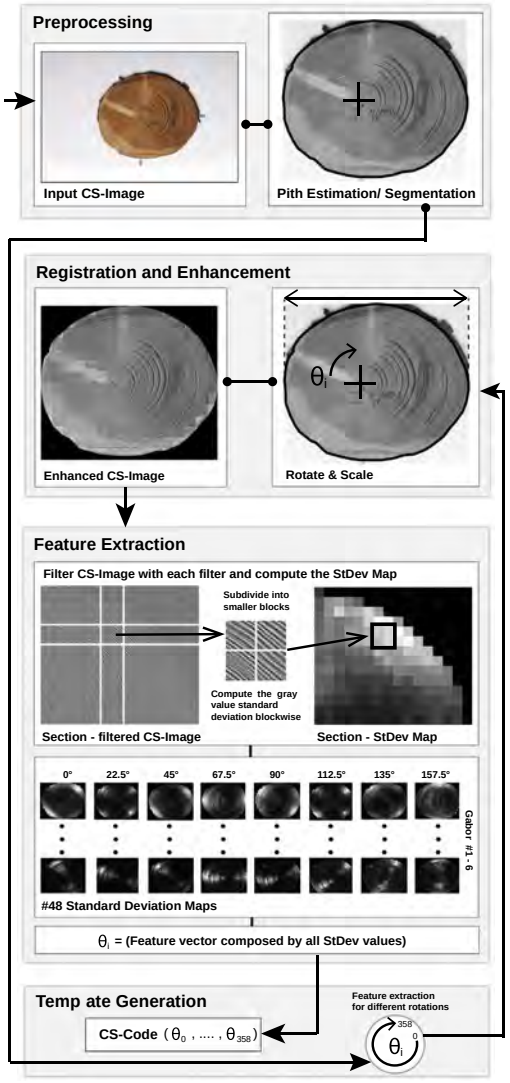

Fig. 2. Log template/CS-Code computation illustration.

sub-band is not the same as the previously determined block orientation it is neglected. In this case the local frequency is interpolated using a Gaussian.

Finally, in the filtering stage the Fourier spectrum of each block is filtered with a Log-Gabor (introduced by Knutsson and Granlund, 1983) which is tuned to the local orientation and frequency of the corresponding block. Similar as in Schraml et al. (2014, 2015a) a bandwidth of three times the variance of the Fourier spectrum and a spread value of blocksize/4 are utilized. The filtered Fourier spectra are inverse Fourier transformed and the results are subsequently used as new block values. An exemplary result of the registration & enhancement procedure is depicted in Fig. 2.

2.2. Cross-section code computation

The CS-Code computation is based on the FingerCode approach proposed in Jain et al. (2000, 2001). This technique utilizes a Gabor-based descriptor which extracts local ridge orientations of a fingerprint. Because of the constant ridge frequencies in human fingerprints a single Gabor filter and its rotated versions are sufficient. The frequencies of annual ring patterns are strongly varying and thus different Gabor filters are required to capture additional information from the annual ring frequencies in different orientations. For a CS-Image width of 512 pixels six different Gabor filters are suggested. For each Gabor filter eight rotated versions are created. Consequently, the Gabor filterbank consists of 48 filters:

$$\begin{aligned} G(\lambda,\theta,\sigma,\gamma) &= G(\lambda,\sigma) \\ &= ((1.5,1),(2.5,2),(3.5,3),(4.5,3),(5.5,3),(6.5,3)), \\ \theta &= \{0,22.5,\ldots,135,157.5\},\gamma = 0.7 \end{aligned}$$

Feature extraction (Fig. 2) is performed in three stages. In the first stage the enhanced CS-Image is filtered with each filter in the filterbank. Each filtered image is subdivided into blocks (8×8 pixels). For all blocks of each filtered image the gray value standard deviations are computed and stored into a matrix, which is denoted as Standard Deviation (StDev) map. Altogether 48 StDev maps are computed and are stored as one-dimensional feature vector (θ) in the CS-Code. Blocks which are not within the CS border are assigned a marker value which is relevant for CS-Code matching. Furthermore, two CS-Images of the same log end or CS-Slice can be rotated differently. Rotational differences are compensated by computing feature vectors for rotated versions of the input CS-Image in the expected misalignment range. Although the misalignment range in this work is much smaller, feature vectors for 180 rotations in two degree steps are computed and used for matching. Hence, it can be evaluated if there exist rotated versions of two CS-Slice images from different tree logs which are incidentally similar to each other. All feature vectors computed for different rotations ($\theta_0,\theta_2,\ldots,\theta_{356},\theta_{358}$) compose the CS-Code of a CS-Image (see Template Generation in Fig. 2).

2.3. Cross-section code matching

In contrast to fingerprints where the shapes are commonly not utilized, the CS shape is obviously a biometric feature itself. By investigating three different matching procedures the discriminative power of the annual ring pattern, the shape and a fusion of both is evaluated.

The first procedure which just considers annual ring pattern information is denoted as annual ring pattern MS (MS_{AP}) and is defined as the minimum MS between the feature vectors of both CS-Codes:

$$\begin{aligned} &MS_{AP}(\text{CS-Code}_1,\text{CS-Code}_2) = \min MS(\theta_i,\theta_j) \\ &\text{where} \quad \theta_i \in \text{CS-Code}_1(\theta_0,\ldots,\theta_{358}), \\ &\theta_j \in \text{CS-Code}_2(\theta_0,\ldots,\theta_{358}) \end{aligned} \tag{1}$$

Due to interpolation in the registration procedure (rotation and scaling) the best MS is achieved when comparing all feature vectors of both CS-Codes. The MS between two feature vectors of two CS-Codes is computed by:

$$MS(\theta_i,\theta_j) = \frac{1}{M}\sum_{k=0}^{n} D(\theta_i(k),\theta_j(k)) \tag{2}$$

where $\theta_i,\ \theta_j$ are two feature vectors of the CS-Codes which are compared, k specifies the index of the feature value in both vectors, n is the max. number of feature values and M is a normalization factor. The utilized distance function is given by:

$$D = \begin{cases} |\theta_i(k) - \theta_j(k)| & \text{if } k \in MCS_i \cap MCS_j \\ 0 & \text{otherwise} \end{cases} \tag{3}$$

As noted in Section 2.2, background feature values are specified by a certain marker. Hence, we define MCS_i and MCS_j as the corresponding masks of the feature vectors which allow to differentiate between background and CS. Just feature vector value pairs which are in the intersection of both CSs are utilized for computing MS_{AP} and the score is normalized by the amount of the considered feature value pairs: $M = |MCS_1 \cap MCS_2|$.

The second procedure (MS_F) is a measure describing the similarity of the shapes of two CSs. MS_F is defined as the minimum False Negative Rate (F) between the masks of the feature vectors of both CS-Codes:

$$MS_F(\text{CS-Code}_1,\text{CS-Code}_2) = \min F(MCS_i,MCS_j) \tag{4}$$

The False Negative Rate (F) between two different masks (MCS_i, MCS_j) is computed by:

$$F = \frac{MCS_i \Delta MCS_j}{\min(|MCS_i|,|MCS_j|)} \tag{5}$$

Finally, the last procedure ($MS_{AP,F}$) is based on score level fusion (Jain et al., 2011, p. 225) of MS_{AP} and MS_F. For score level fusion both scores are combined using different scaling factors (see Eq. (6)). The scaling factors ($\sigma_{AP}, \sigma_{MS_F}$) are determined from their score distributions to ensure that both contribute equally to the combined MS.

$$MS_{AP,F} = MS_{AP} \cdot \sigma_{AP} + MS_F \cdot \sigma_F \tag{6}$$

2.4. Experimental setup

2.4.1. Testset

The experimental evaluation is based on cross-section slices (CS-Slices) from three different European spruce logs (Log 1 – L1, Log 2 – L2, Log 3 – L3). For L1 and L2, a section of 40 centimetres was cut into 16 CS-Slices. The CS-Slices were cut with a bandsaw and the thickness of each CS-Slice is approximately 2.5 centimetres. The sections of L1 and L2 were showing a diameter of around 230 mm and 290 mm respectively.

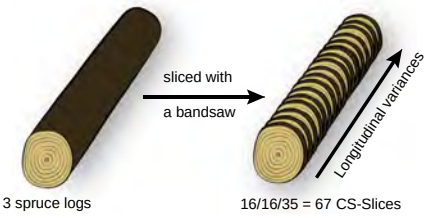

Fig. 3. In total 67 CS-Slices from three different logs are cut-off.

Table 1
Testset overview.

3 Logs	# CS-Slices	# CS-Images	Illustration
Log 1 – L1	16	2 (Rough & Sanded)	Fig. 4a
Log 2 – L2	16	2 (Rough & Sanded)	Fig. 4b
Log 3 – L3	35	4 (Time delay)	Fig. 5

Subsequently, just one surface of each CS-Slice was captured two times (Nikon D90). The first CS-Image was taken from the fresh cut CS-Slices. For the second CS-Image, the surfaces of the CS-Slices were polished using a sandpaper (P 150). In the first row of Fig. 4 the two captured CS-Images of one CS-Slice from L1 and L2 are depicted.

To increase the number of interclass scores, a third log (L3) with a total of 35 CS-Slices with 2 cm spacing is utilized. Each CS-Slice was captured with four different time delays (Fig. 5). For a detailed dataset description we refer to Schraml et al. (2014) (see Table 1). For all CS-Images in the testset the pith position and the border of the were determined manually and are utilized for CS registration and defining the CS-Masks in the experiments. The CS-Images in Fig. 4 illustrate the preprocessing steps for the CS-Images of the CS-Slices L1 #2 and L2 #10. In the first row the original images are depicted. The second and third row show the registered and enhanced versions of the CS-Images, respectively. The four time-delay captured CS-Images of CS-Slice L3 #10 are depicted in Fig. 5.

2.4.2. Evaluation background

Before presenting the results, relevant basics for the experimental evaluation are introduced. First, a short introduction on biometric performance evaluation is presented. Subsequently, three types of wood log CS variations are defined and the construction of the intra- and interclass score distributions (SDs) used in the evaluation is described.

Biometric performance evaluation. Commonly, a biometric system operates either in verification or identification mode and the term recognition is used universally.

For verification the system compares a query template to just one template of the database (1:1 comparison). This template is specified by the claimed identity of the query template. The system accepts or rejects the claimed identity of the individual/object. For identification a query template is compared to all templates in the database (1:N comparison) and if the best match exceeds a certain system threshold it specifies the identity of the query template.

Generally, a biometric system is assessed based on the errors it produces (Maltoni et al., 2009). Two major verification system errors (False Match Rate (FMR) and False Non Match Rate (FNMR)) result from the calculation of the intra- and interclass SDs which are commonly denoted as genuine and impostor SD, respectively. The intraclass SD contains all MSs computed between a set of templates of the same individual. The interclass SD contains the MSs between templates of different individuals. Consequently, the FMR includes all MSs between different individuals which are incorrectly accepted by the system. On the other hand the FNMR gives the proportion of MSs which were rejected although the score is computed between templates of the same individual. For verification performance evaluation the equal error rate (EER) is a general benchmark. The EER is defined as the error where FMR and FNMR are equal.

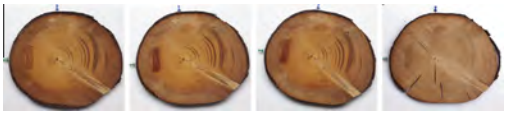

Fig. 5. Temporal variations: L3 CS-Slice #34, sessions 1–4 (Schraml et al., 2014).

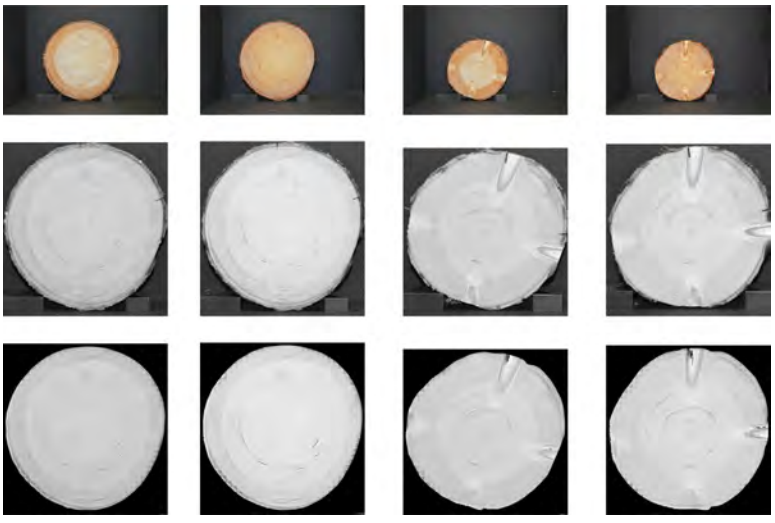

(a) L1 #2 rough (b) L1 #2 sanded (c) L2 #10 rough (d) L2 #10 sanded

Fig. 4. Testset examples: Slices #2 and #10 from L1 and L2, respectively. The CS-Images in the first row depict the original CS-Images and in row two and three the registered and enhanced CS-Images used for CS-Code computation are illustrated.

The identification performance is evaluated by matching a set of probe templates to all templates enrolled in the database (Jain et al., 2007). We refer to closed-set identification where it is assumed that all individuals/objects of the probe templates are enrolled in the system. The MSs between each probe template and all database templates are ordered according to the MS. The ordered MSs of each probe template are used to compute the probability that the correct template is ranked within the top k-ranked MSs. The probabilities for each rank are illustrated in a curve which is denoted as Cumulative Match Characteristic (CMC).

Wood log cross-section variability. Two basic requirements for biometric recognition are uniqueness and permanence of the utilized biometric characteristic. Uniqueness expresses that the biometric characteristic and the computed templates of different individuals are strongly varying and permanence is the requirement that they do not change over time. Related to those requirements there are two basic issues which a biometric system must handle: Intraclass variability and Interclass similarity which contribute to the F NMR and FMR, respectively. Interclass similarity is the problem that different individuals may show up similar biometric characteristics. Intraclass variability is an issue due to internal and external caused variations between a set of templates of the same individual. External variations occur due to irregularities in the template generation procedure, e.g. different sensors or capturing environments. Furthermore, the visual appearance of the biometric characteristic is affected or modificated by external influences, e.g. the saw cut pattern. Internal variations are eventually caused by an intrinsic modification or change of the biometric characteristic itself, e.g. temporal variations caused by the ageing process. In case of human biometrics, it is attempted to overcome external and internal changes/modifications by updating the stored templates in the database.

In case of wood logs, several external and internal caused variations/modifications of CSs of a single log have an impact on the intraclass variability. So far, three different variation types emerged from our research:

- **Temporal variations** correspond to the issue of ageing in human biometrics. In case of wood log ends, the visual appearance of a CS changes rapidly. Due to the rapidly changing moisture content at the log end faces and the sun exposure the CS shows up discolourations or deformations (e.g. cracks). In Fig. 5 four time-delay captured CS-Images of a CS-Slice from L3 illustrate temporal variations.
- **Longitudinal variations** are caused by the changing CS pattern along the longitudinal axis of a single tree log. Consequently, they address the issue of length-cutting a log in the sawmill. Cut-off lines are utilized in many sawmills for different reasons. For example, clean log end faces (no stones and sand) are beneficial to protect the cutting blades and to aid the log quality assessment. On the other hand, log end cutting leads to a loss of material and is not tolerable in certain fields of the sawmill industry. An illustration for longitudinal variations of the CSs from a single log is presented in Fig. 6.

Fig. 6. Longitudinal variations: L2 CS-Slices #1, 4, 8, 16.

Table 2
Intraclass SD groups.

CS variation	SD group details
Longitudinal SD	L1 & L2: MSs between the rough or sanded CS-Images of their CS-Slices
Surface SD	L1 & L2: MSs between the rough and sanded CS-Image of each CS-Slice

- **Surface variations** result from differently finished or cut surfaces of a particular CS. In this work surface variations between saw cut CS surfaces and the sanded CS surface counterparts are assessed (see Fig. 4). Another scenario which is closely related to industrial biometric log recognition involves CS surface variations caused by different cutting tools (e.g. chain-, band- or circular saw). Probably the first cut in the forest and the cleansing cut in the sawmill are performed with different devices. This results in a mixture of longitudinal and surface variations.

For the testset CS-Images of the CS-Slices from L1, L2 and L3 we tried to avoid external variations which are caused by the capturing procedure.

Intra-/interclass score distributions (SDs). For the evaluation, the MSs between all CS-Images of L1, L2 and L3 are computed using the proposed matching procedures. The intra-/interclass SDs for a single matching procedure are constructed by grouping the MSs into the respective SD. Hence, the interclass SD contains all MSs computed between the CS-Images of L1, L2 and L3. The intraclass SD is built up on the MSs between CS-Images of the same log and is further subdivided into two SD groups corresponding to the variation type (see Table 2). Temporal variations which are represented by the MSs between the four time-delay captured CS-Images of each CS-Slice from L3 were investigated in Schraml et al. (2014) and are not treated in this work. The longitudinal SD shows the similarity between CS-Images which were captured at different longitudinal positions of the same log. In this work we consider the longitudinal variations of L1 and L2. For this purpose, the longitudinal SD is built up on the MSs between the CS-Images of rough or sanded CS-Slices from L1 and L2. The surface SD includes all MSs between the saw cut CS surfaces and the sanded CS surface counterparts of each CS-Slice from L1 and L2.

3. Results and discussion

The results of the experiments are subdivided into two sections. Section 3.1 presents investigations on the separability between the intra- and interclass SD. For this purpose, the verification performance of the biometric system for different matching procedures is assessed and the EERs are considered.

Because of the manifold structure of the intraclass SD an exhaustive analysis of the longitudinal and surface SD group is presented in Section 3.2. Based on the results, fundamental conclusions on the intraclass variability and the impact on the separability between the intra- and interclass SD are drawn. Finally, Section 3.3 treats the identification performance for different real world scenarios.

3.1. Intra-/interclass SD separability

In Fig. 7 the intra-/interclass SDs for all three matching procedures are illustrated. Most important, the charts show that the best EER is achieved by $MS_{AP,F}$ which uses both annual ring pattern and shape information. Furthermore, the EERs for MS_{AP} and MS_F illustrate that for the considered three logs shape information is less discriminative compared to annual ring pattern information. In addition, Table 3 depicts EERs for different intra-/interclass SD

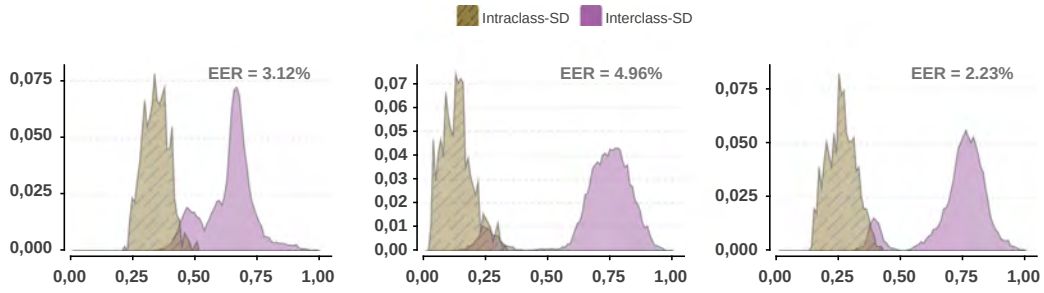

(a) MS_{AP} (b) MS_F (c) $MS_{AP,F}$

Fig. 7. Intra-/interclass score distributions (SD) for different matching procedures. [*X*-Axis: Matching Score, *Y*-Axis: Probability].

Table 3
EERs [%] for all matching procedures and different subsets of L1, L2, L3.

Logs	MS_{AP}	MS_F	$MS_{AP,F}$	
L1–L2	5.6	12.79	12.85	6.21
L1–L3	0.11	0.48	0.0	0.0
L2–L3	3.57	5.07	0.0	0.0
L1–L2–L3	3.12	5.38	4.96	2.23

subsets of the three logs. The results for MS_F and L1–L2 illustrate that L1 and L2 have a similar shape which causes a bad EER of 12.85%. In case of L1–L3 and L2–L3 the shapes are very distinctive which leads to a zero EER. Considering MS_{AP} and the annual ring pattern distinctiveness the results show that the pattern of L1 is more similar to L3 than the pattern of L2 to L3. It can be concluded that for different tree logs the discriminative power of the annual ring pattern and the shape varies significantly. Consequently, the robustness of log end biometrics benefits from using shape and annual ring pattern information together.

Generally, an EER of ~2% for $MS_{AP,F}$ is astonishing because the intraclass SD includes all longitudinal MSs for all slice distances. Our experiments in Schraml et al. (2014) showed that the similarity between different CS-Slices of a log deteriorates with an increasing distance between the considered CS-Slices. A detailed analysis of the intraclass SD groups (Longitudinal and Surface SD) allows to gather further insights.

3.2. Intraclass SD analysis

In this section the longitudinal and surface SD groups of which the intraclass SD is build up are assessed in detail.

3.2.1. Longitudinal SD

The longitudinal SD contains the MSs between the rough or sanded CS-Images of the CS-Slices from L1 and L2. Four subsets of the longitudinal SD are assessed in detail: Rough & Sanded longitudinal MSs of L1 and L2. The MSs of each subset are grouped according to the neighbourhood distance of the compared CS-Slices. In case of 16 CS-Slices for each log the distance between two CS-Slices ranges from 1 to 15 which leads to 15 slice distance groups (SDGs). For example, SDG 1 contains all MSs of each CS-Slice to the adjacent neighboured CS-Slices.

In Fig. 8 the mean values of each subset and SDG for all matching procedures are depicted. For MS_{AP} it is expected that the longitudinal MSs increase the higher the slice distance between two CS-Slices is. An increase or change of the MSs for higher slice distances can also be expected for MS_F and $MS_{AP,F}$. In Schraml et al. (2014) our experiments based on CS-Slices from L3 confirmed this expectation.

Let's consider MS_{AP}: At a glance, the results for MS_{AP} (Fig. 8a) raise doubt on the correctness of the previous results and the basic assumption. Considering the longitudinal MSs of the first log (SANDED L1, ROUGH L1) the expected increase is interrupted for both subsets. This interrupt is also shown for the second log (SANDED L2, ROUGH L2) for the SDGs 14, 15. Interestingly, these interrupts can be recognized for MS_F and the fusion procedure $MS_{AP,F}$ too.

A closer examination of the CS-Slices of L1, L2 and L3 provides an answer for the differing results. For L3 just the CS-Slices at the log ends show up knots. Hence, for larger distances the longitudinal MSs (MS_{AP}) increase additionally and the expected trend becomes strengthened. In contrast to L3, L1 and L2 show up knotty

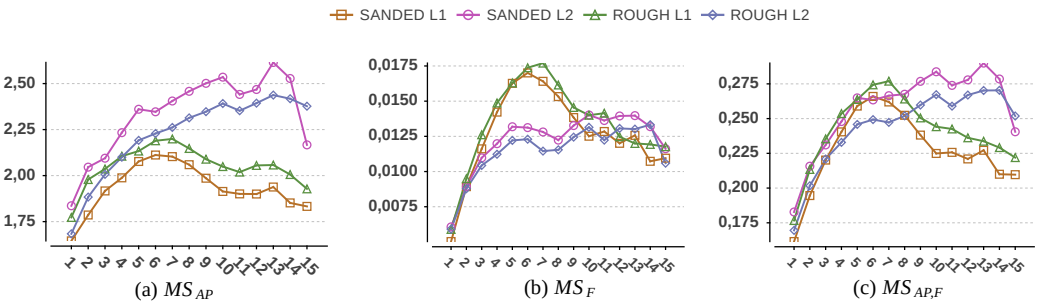

(a) MS_{AP} (b) MS_F (c) $MS_{AP,F}$

Fig. 8. Intraclass SD: Rough and Sanded longitudinal MSs of L1 and L2 grouped by the slice distance. [*X*-Axis: Slice Distance Group, *Y*-Axis: Matching Score].

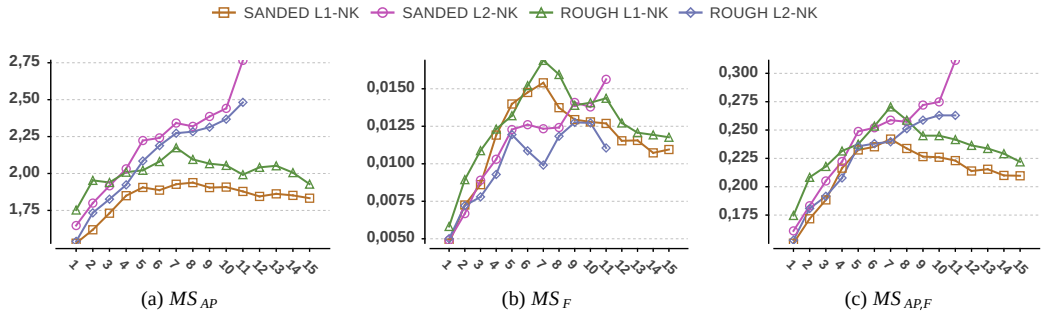

(a) MS_{AP} (b) MS_{F} (c) $MS_{AP,F}$

Fig. 9. Longitudinal variance analysis excluding knotty CS-Slices – L1(#9, 10, 14), L2(#1, 2, 10, 11, 15, 16). [*X*-Axis: Slice Distance Group, *Y*-Axis: Matching Score].

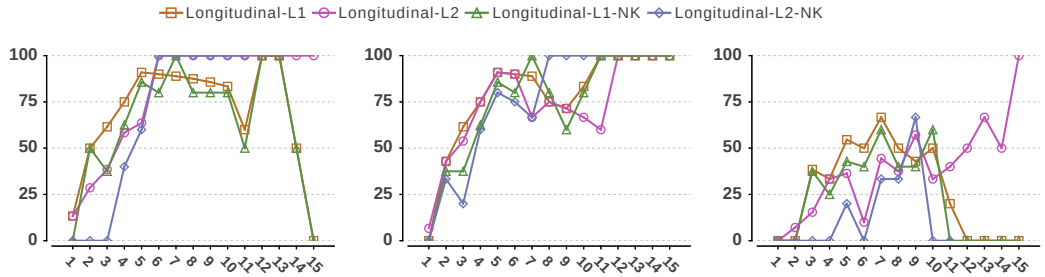

(a) MS_{AP} (b) MS_{F} (c) $MS_{AP,F}$

Fig. 10. Interclass fractions for the slice distance groups (SDGs) of each longitudinal SD subset. [*X*-Axis: Slice Distance Group, *Y*-Axis: Interclass Fraction (%)].

CS-Slices situated in the middle of each log. For L1 three (#9, 10, 14 – see Fig. 4d) and for L2 six CS-Slices (#1, 2, 10, 11, 15, 16) show up between one and four knots. By omitting MSs from those knotty CS-Slices the results in Fig. 9 approximately show the expected trend. Quite interesting is the good MS at SDG 15 for SANDED L2 (MS_{AP}) which results from one equally located knot in the CS-Slices #1 and #16.

This leads to two major conclusions: Less surprising, the results demonstrate that MSs between non-knotty (NK) and knotty CS-Slices are remarkably worse. Second, the results indicate that knots do not introduce any propagative effects to the annual ring pattern and the CS shape.

In comparing the results from L1 to L2 it is visible that the ranges of the longitudinal MSs for different logs vary. Figs. 8 and 9 illustrate that the MSs of L2 are worse compared to L1, especially when considering larger slice distances. However, it can be stated that the longitudinal MSs of each log are getting worse with an increasing slice distance.

Longitudinal SD/interclass fractions. The longitudinal increase of the MSs leads to the conjecture that for higher slice distances it is not possible to separate between longitudinal MSs and interclass MSs. This conjecture is validated by considering the interclass fraction of the MSs of all SDGs for each longitudinal SD subset. The interclass fraction of a SDG is specified as the percentage of MSs (within a longitudinal SD subset and SDG) which intersect with the interclass SD. The interclass fractions of each longitudinal SD subset and SDG are illustrated in Fig. 10. For MS_{AP} and MS_{F} the results confirm the expectation that for larger slice distances the fraction of MSs which intersects with the interclass SD increases. The differences between the knot-including and knot-free SDs are not significant. Just for the Longitudinal-L2-NK SD and MS_{AP} the fractions of the first three SDGs (1–3) are pushed down to zero.

Most important, the results for $MS_{AP,F}$ illustrate that by the fusion of pattern and shape information the interclass fractions decrease for all subsets. The robustness to longitudinal variations is improved significantly by feature fusion.

3.2.2. Surface SD

The surface SD is examined in context of the previously analysed longitudinal SD subsets and the interclass SD. Again, the main objective is to assess the separability between the surface SD subsets and the interclass SD. In case of the CS-Images of L1 and L2 the surface MSs are the only MSs between CS-Images from equal CS-Slices in our experiments. The surface MSs between the rough and sanded CS-Images are considered for L1 and L2, separately. For all SDs the cumulative distribution functions (CDF) are computed and illustrated for each matching procedure (see Fig. 11). The CDF of a SD gives the probability that a certain MS exists that is ranged less or equal to that MS. Furthermore, the CDF illustrates the median value at a probability of 0.5 – half of the MSs are lower and half of the MSs are higher than the median. The CDFs of a certain intraclass SD group/subset and the interclass SD are used to observe their overlap and to draw conclusions about their separability.

Generally, it is expected that the surface SD subsets consist of very good MSs and their CDFs are thus aligned in front (=left hand side) of the longitudinal SD CDFs. For all surface SD subsets and matching procedures no overlaps with the interclass CDF are shown. For MS_{F} the surface SD subsets show very good MSs because the shape difference between the rough and sanded

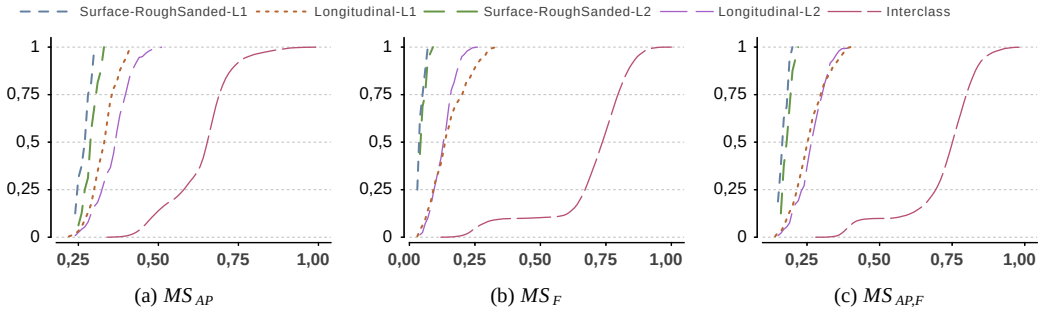

Fig. 11. Cumulative distribution functions (CDFs) for different longitudinal and surface SD subsets and the interclass SD. [*X*-Axis: Matching Score, *Y*-Axis: Probability].

CS-Image of a CS-Slice is very low. The overlaps between the longitudinal SDs and the interclass SD have been discussed in the previous section. Again, the results for $MS_{AP,F}$ show that fusion improves the separability between the longitudinal SD subsets and the interclass SD.

3.3. Identification performance

So far, all evaluations were related to the verification performance of log end biometrics. Based on the gathered insights, two investigations on the identification performance are presented: First, the MSs for each CS-Slice of L1 and L2 are ordered and the ranks for different intraclass MS groups/subsets and the interclass MSs are analysed. Hence, general statements on the rank orders can be presented.

Second, the identification rates for four specific identification scenarios are presented. All scenarios illustrate the impact of cutting the log end on the identification performance. As such, it is elaborated how the width of the piece which is cut-off influences the performance. Additionally, the impact of using different cutting tools is assessed.

3.3.1. Cumulative CS-Slice matching score ranks

Commonly, the CMC depicts how the biometric system ranks the MSs between a set of probe templates and all database templates. The CMC curve illustrates the probability that the correct (intraclass) MS is ranked within the first *k*-ranks. In case of 100% identification rate the CMC curve shows a detection rate of 100% at the first rank. For this investigation, the SD-MS rankings of five different intraclass groups/subsets and the first observation of an interclass SD-MS are assessed.

For each CS-Slice the MSs between each of its templates and all other templates in the database are ordered in an ascending order. In Fig. 12 the detection rates for four SD groups/subsets and the interclass SD are depicted:

- SURFACE: Detection rate for the MSs between the rough and sanded CS-Images of each CS-Slice.
- ROUGH-LONG, SANDED-LONG for L1 & L2: Detection rates for longitudinal MSs from slice distance group 1 or 2. These are of interest in an industrial application (e.g. cutting the log end once or twice).
- INTER: Detection rate for observing the first interclass MS.

For example, in Fig. 12a the SURFACE curve shows that there is ~30% chance of finding the corresponding rough or sanded surface as the best match and ~95% chance to find it among the top 10 ranked matches. The INTER curve shows that there is 0% risk of finding a CS-Slice from another log as the best match but ~5% risk of finding a CS-Slice from another log among the top 20 ranked matches.

Based on the CMC curves we can draw interesting conclusions on the identification performance of the biometric system. Most important, for all matching procedures and CS-Slices each considered intraclass SD group/subset shows up high detection rates at the best (=lowest) ranks. On the other hand, the probability of observing a well ranked (<15) interclass SD-MS is nearly zero. In case of $MS_{AP,F}$ nearly all intraclass SD-MSs are ranked in front of the first interclass SD-MS occurrence. Notice that a larger amount of different logs in the testset could have a big impact on the results.

In comparing the surface SD ranks to the longitudinal SD subset ranks the results lead to an interesting observation. The MSs (MS_{AP}) of the rough and sanded longitudinal SDs of L1 and L2 are ranked in the range of the surface SD-MSs. Thus the results distinguish from

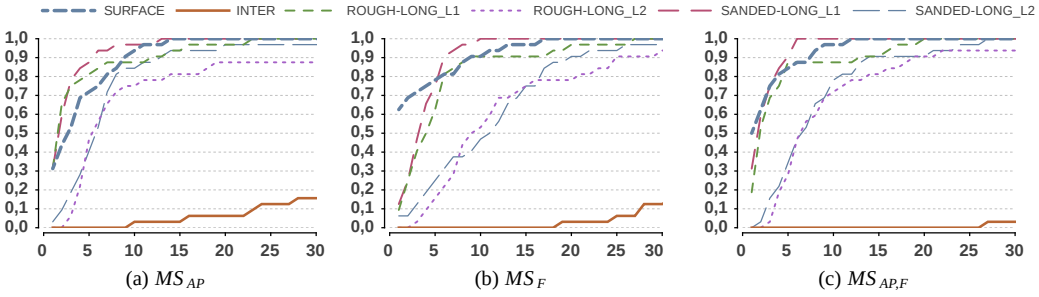

Fig. 12. Cumulative matching score ranks. [*X*-Axis: Rank, *Y*-Axis: Detection Rate].

the verification performance results in Fig. 11 where the surface CDFs show better MSs than the longitudinal CDFs. This illustrates that CS-Images of adjacent neighboured CS-Slices with the same kind of surface show up a high annual ring pattern similarity to each other. Because of longitudinal shape variations the results for MS_F show that the longitudinal MSs are ranked worse compared to the SURFACE MSs.

Again, the results depict a higher longitudinal CS variability of L2 which is demonstrated by the higher ranked (=worse) MSs for the longitudinal SD subsets of L2.

Concluding, the results show that the first occurrence of an interclass MS is worse ranked (=higher ranked) compared to the intraclass MSs. The interclass CMC curves for $MS_{AP,F}$ show that for feature fusion the interclass detection rates shift remarkably to higher ranks.

3.3.2. Identification performance – test scenarios

Finally, the identification performance for different scenarios is assessed. A test scenario requires to specify a probe set and a gallery set. The gallery specifies the enrolled templates of the individuals/objects contained in the database. The probe set is a set of templates of individuals/objects which are used to query the biometric system. For each probe template the matches/MSs to all database templates are computed. The computed matches/MSs for each probe template are ordered and the rank of the correct match/MS is determined. Subsequently, for each rank the probability that the correct match/MS is equal or better ranked is computed. For illustration these probabilities are depicted in a CMC chart. The probability that the correct match is ranked at the first position is denoted as identification rate or detection rate. Basically, all scenarios evaluate the impact of cutting the log end in the sawmill.

Scenario #1, #2 – same cutting tool. For these scenarios it is assumed that the first cut in the forest and the second cut in the sawmill is performed with the same cutting tool. Hence, no surface variations due to different cutting tools are introduced. For this purpose Scenario #1 (Rough-Rough) is based on rough CS-Images and Scenario#2 (Sanded-Sanded) is based on sanded CS-Images of L1 and L2. As probe templates for Scenario#1, #2 the rough or sanded CS-Images of each CS-Slice are utilized, respectively.

For each scenario and probe template it is assumed that just one equally surfaced CS-Image of the same log which belongs to a certain slice distance group (SDG) is enrolled in the gallery set. For evaluation the SDGs 1–5 are considered. Furthermore, templates of all CS-Images from L3 and equally surfaced CS-Images of the other log (L1 or L2) are included in the gallery. For each probe template the rank of the correct match is computed and in Table 4 the results for both scenarios are summarized. For each scenario the identification rates for different SDGs and matching procedures are illustrated.

The results for Scenario#1 and #2 in Table 4 show high detection rates for the first four SDGs. The results illustrate that for SDG 4 and 5 the detection rates of MS_F decrease to a higher degree than for MS_{AP}. Basically, it is recognizable that the identification rates for both scenarios and matching procedures are somewhat equal. Consequently, the CS shape has less impact on the identification performance of Scenario#1 and #2. For $MS_{AP,F}$ and the SDGs 1, 2 the identification rates account 100% for both scenarios. These results are a first indication that log end biometrics are probably robust to cutting the log end in a range of five centimetres (2 CS-Slices = 5 cm). In case of $MS_{AP,F}$ the rates for higher SDGs are still in a range between 84% and 97%. In Fig. 13 the CMC curves for $MS_{AP,F}$ and both scenarios are illustrated.

Scenario #3, #4 – different cutting tools. In difference to the first two scenarios, Scenario #3 and #4 investigate the impact of different surfaced CSs. Thus, it is assumed that the first cut in the forest and the second cut in the sawmill are performed with different cutting tools. Based on the CS-Images of L1 and L2 two scenarios are constructed. Scenario #3 (Rough-Sanded) assumes that the first cut is represented by a rough CS-Image of a CS-Slice and the second cut is represented by a sanded CS-Image of a neighboured CS-Slice. Scenario #4 (Sanded-Rough) assumes that the cuts are performed in the reverse order. Consequently, these scenarios simulate a mixture of longitudinal and surface CS variations. For both scenarios the rank-orders for the correct matches are computed in the same way as for the first two scenarios (see Table 5). The results for Scenario #3 in Table 5 illustrate that for all matching procedures the identification performance decreases for higher SDGs. Compared to Scenario#1 and #2, the identification rates for MS_{AP} are worse. This is caused by the CS surface variations which cause a decrease of the identification performance for MS_{AP}. Nevertheless, the results for $MS_{AP,F}$ are convincing and for SDG 1, 2 an error free identification performance is achieved (Fig. 13).

Finally, the results for all scenarios indicate that log end biometrics are robust to longitudinal variations and mixtures of surface and longitudinal variations to a certain degree. Furthermore, and equal as in Schraml et al. (2015a) all evaluations showed that the fusion of annual ring pattern and shape information is valuable to increase the performance of the biometric system.

Table 4
Scenario#1, #2 – Identification rates for different slice distance groups (SDGs) and matching procedures (MPs).

MP/SDG	1	2	3	4	5
#1 Rough-Rough					
MS_{AP}	1.0	1.0	0.97	0.97	0.91
MS_F	1.0	0.94	0.91	0.84	0.78
$MS_{AP,F}$	1.0	0.97	0.91	0.81	0.75
#2 Sanded-Sanded					
MS_{AP}	1.0	0.97	0.94	0.91	0.69
MS_F	1.0	0.94	0.91	0.88	0.66
$MS_{AP,F}$	1.0	1.0	0.94	0.81	0.66

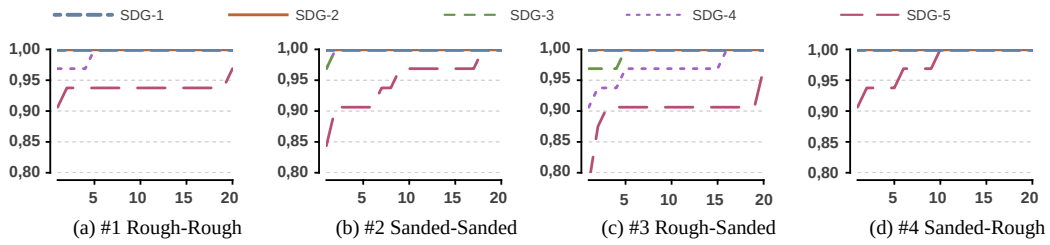

Fig. 13. $MS_{AP,F}$: CMC curves for the different scenarios and slice distance groups. [*X*-Axis: Rank, *Y*-Axis: Detection Rate].

Table 5
Scenario#3, #4 – Identification rates for different slice distance groups (SDGs) and matching procedures (MPs).

MP/SDG	1	2	3	4	5
#3 Rough-Sanded					
MS_{AP}	0.97	0.91	0.91	0.72	0.69
MS_{F}	0.94	0.88	0.91	0.63	0.56
$MS_{AP,F}$	1.0	0.94	0.91	0.81	0.66
#4 Sanded-Rough					
MS_{AP}	0.94	0.88	0.84	0.78	0.69
MS_{F}	0.91	0.81	0.84	0.66	0.56
$MS_{AP,F}$	1.0	1.0	0.97	0.81	0.78

4. Conclusions

The findings of this study show that log end biometrics are promising to discriminate between different tree logs in an industrial application. It can be concluded that the robustness of the biometric system to CS variations depends to a high degree on the template computation approach and the matching procedure.

In comparing the results for three different matching procedures it is obvious that biometric feature fusion increases the robustness significantly. In regard to the verification performance, a combination of annual ring pattern and shape features increases the robustness to longitudinal CS variations. Furthermore, the analysis of the intraclass SD groups illustrates that CS surface variations are not crucial for the verification performance.

Based on the identification performance experiments we conclude that biometric log recognition is qualified to overcome the issue of cutting log ends in the sawmill. Results show a successful identification within cutting off slices up to ∼5 centimetres in thickness, even if the second cut in the sawmill is performed with another cutting tool.

The analysis of the longitudinal CS variations for different SDGs shows that knots are disturbing factors. This is caused by the fact that the current approach is not dealing with knots on CSs. Surprisingly, the results indicate that knots do not introduce any propagative effects to the annual ring pattern and the CS shape. Thus, future work should investigate the similarity between non-knotty parts of knotty CSs and their neighboured knot free CSs.

5. Future work

Although the results of this study together with the results in Schraml et al. (2015a,b) are very promising, further experiments on a large set of tree logs are indispensable to assess the identification performance in a real world environment. Furthermore, future work has to deal with the impact of typical external CS surface variations which are caused by dirt, snow or ice during transportation or storage. Regarding log template computation and matching, the applicability of other feature extraction methods should be assessed and new approaches should be developed. Finally, further research should deal with the impact of automatic pith estimation and CS segmentation approaches to the biometric system performance.

References

Barrett, W., 2008. Biometrics of cut tree faces. In: Sobh, T. (Ed.), Advances in Computer and Information Sciences and Engineering. Springer, Netherlands, pp. 562–565.

Chiorescu, S., Grönlund, A., 2003. The fingerprint approach: using data generated by a 2-axis log scanner to accomplish traceability in the sawmill's log yard. For Prod J 53, 78–86.

Chiorescu, S., Grönlund, A., 2004. The fingerprint method: using over-bark and under-bark log measurement data generated by three-dimensional log scanners in combination with radiofrequency identification tags to achieve traceability in the log yard at the sawmill. Scand. J. For. Res. 19, 374–383.

Dykstra, D.P., Kuru, G., Taylor, R., Nussbaum, R., Magrath, W.B., Story, J., 2003. Technologies for Wood Tracking. Technical Report. World Bank – WWF Alliance Report.

EuropeanParliament, 2010. Regulation (EU) No 995/2010 of the European Parliament and of the Council of 20th October 2010 Laying Down the Obligations of Operators who Place Timber and Timber Products on the Market.

Flodin, J., Oja, J., Grönlund, A., 2007. Fingerprint traceability of sawn products using X-ray log scanning and sawn timber surface scanning. In: Proceedings of Quality Control for Wood and Wood Products: COST Action E 53 the First Conference.

Flodin, J., Oja, J., Grönlund, A., 2008a. Fingerprint traceability of logs using the outer shape and the tracheid effect. For. Prod. J. 58, 21–27.

Flodin, J., Oja, J., Grönlund, J., 2008b. Fingerprint traceability of sawn products using industrial measurement systems for X-ray log scanning and sawn timber surface scanning. For. Prod. J. 58, 11.

Hong, L., Wan, Y., Jain, A., 1998. Fingerprint image enhancement: algorithm and performance evaluation. IEEE Trans. Pattern Anal. Mach. Intell. 20, 777–789.

Jain, A., Ross, A., Prabhakar, S., 2001. Fingerprint matching using minutiae and texture features. In: Proc. of the International Conference on Image Processing (ICIP'01), Thessaloniki, GR. pp. 282–285.

Jain, A.K., Flynn, P., Ross, A.A., 2007. Handbook of Biometrics. Springer, New York, USA.

Jain, A.K., Prabhakar, S., Hong, L., Pankanti, S., 2000. Filterbank-based fingerprint matching. IEEE Trans. Image Process. 9, 846–859.

Jain, A.K., Ross, A.A., Nandakumar, K., 2011. Introduction to Biometrics. Springer, US.

Kastner, T., Erb, K.H., Nonhebel, S., 2011. International wood trade and forest change: a global analysis. Glob. Environ. Change 21, 947–956.

Knutsson, H., Granlund, G.H., 1983. Texture analysis using two-dimensional quadrature filters. In: IEEE Computer Society Workshop on Computer Architecture for Pattern Analysis and Image Database Management, Pasadena, USA.

Kuemmerle, T., Chaskovskyy, O., Knorn, J., Radeloff, V.C., Kruhlov, I., Keeton, W.S., Hostert, P., 2009. Forest cover change and illegal logging in the ukrainian carpathians in the transition period from 1988 to 2007. Remote Sens. Environ. 113, 1194–1207.

Maltoni, D., Maio, D., Jain, A.K., Prabhakar, S., 2009. Handbook of Fingerprint Recognition. Springer, New York, USA.

Marjanen, K., Ojala, P., Ihalainen, H., 2008. Measurement of annual ring width of log ends in forest machinery. In: Proceedings of the SPIE Conference on Image Processing: Algorithms and Systems.

Mattila, P., Viittanen, J., 1999. Method and Measuring Apparatus used in Conjunction with a Tree-working Device.

Norell, K., 2009. An automatic method for counting annual rings in noisy sawmill images. In: Proceedings of the Conference on Image Analysis and Processing (ICIAP). Springer, Berlin/Heidelberg, pp. 307–316.

Norell, K., Borgefors, G., 2008. Estimation of pith position in untreated log ends in sawmill environments. Comput. Electron. Agric. 63, 155–167.

Pahlberg, T., Hagman, O., Thurley, M., 2015. Recognition of boards using wood fingerprints based on a fusion of feature detection methods. Comput. Electron. Agric. 111, 164–173.

Richards, M., Wells, A., Del Gatto, F., Contreras-Hermosilla, A., Pommier, D., 2003. Impacts of illegality and barriers to legality: a diagnostic analysis of illegal logging in Honduras and Nicaragua. Int. For. Rev. 5, 282–292.

Schraml, R., Charwat-Pessler, J., Uhl, A., 2014. Temporal and longitudinal variances in wood log cross-section image analysis. In: IEEE International Conference on Image Processing 2014 (ICIP'14), Paris, FR. pp. 5706–5710.

Schraml, R., Hofbauer, H., Petutschnigg, A., Uhl, A., 2015a. Tree log identification based on digital cross-section images of log ends using fingerprint and iris recognition methods. In: Proceedings of the 16th International Conference on Computer Analysis of Images and Patterns (CAIP'15). Springer, Valetta, MT, pp. 752–764.

Schraml, R., Petutschnigg, A., Uhl, A., 2015b. Validation and reliability of the discriminative power of geometric wood log end features. In: Proceedings of the IEEE International Conference on Image Processing (ICIP'15), Quebec, CAN.

Schraml, R., Uhl, A., 2013. Pith estimation on rough log end images using local fourier spectrum analysis. In: Proceedings of the 14th Conference on Computer Graphics and Imaging (CGIM'13), Innsbruck, AUT.

Schraml, R., Uhl, A., 2014. Similarity based cross-section segmentation in rough log end images. In: Iliadis, L., et al. (Eds.), Proceedings of the 10th Artificial Intelligence Applications and Innovations Conference (AIAI'14), Rhodes, GR. pp. 614–621.

Smith, J., Obidzinski, K., Subarudi, S., Suramenggala, I., 2003. Illegal logging, collusive corruption and fragmented governments in Kalimantan, Indonesia. Int. For. Rev. 5, 293–302.

Tzoulis, I., Andreopoulou, Z., 2013. Emerging traceability technologies as a tool for quality wood trade. Procedia Technol. 8, 606–611.

United Nations, 1992. United Nations Conference on Environment & Development. Agenda 21, Rio de Janeiro, BR.

A. Ruckelshausen et al. (Hrsg.): Intelligente Systeme - Stand der Technik und neue Möglichkeiten,
Lecture Notes in Informatics (LNI), Gesellschaft für Informatik, Bonn 2016 189

Roundwood Tracking using Log End Biometrics

Rudolf Schraml[1], Johann Charwat-Pessler[2], Karl Entacher[2], Alexander Petutschnigg[2] und Andreas Uhl[1]

Abstract: Log end biometrics is a physically marking free approach to establish log traceability from forest-site to further-processing companies. Within an Austrian research project questions regarding the applicability of log end biometrics were investigated. This work introduces to biometric log end recognition, summarizes our research and provides an outlook on future work.

1 Introduction

Biometric tracking of wood logs is a potential approach to establish log traceability without the necessity for physical markers like plastic badges or RFID transponders. A biometric log recognition system based on log end images could be used to track the ownership from the forest based industries to further processing companies. Furthermore, the ongoing process optimization in the forest-based and the sawmill industry demands for technologies which efficiently identify wood logs and pass log specific information along the log processing chain.

By analogy to human biometrics, it is assumed that wood logs are unique entities which can be recognized using log characteristics. The approaches presented in [CG03, CG04, FOG08] utilized 2D and 3D scanners to extract geometric wood properties for tracking logs within the sawmill environment. The utilized capturing devices are however, not applicable at forest site.

On account of the fact that timber offers characteristics on log end faces in terms of annual rings, pith position, shape and dimension it is assumed that cross-section (CS) images of log ends can be used as biometric characteristic for log identification. In this work the concept of log end biometrics is introduced and the results of our research are summarized (Sect. 2). We conclude with an outlook on future research needs (Sect. 3).

2 Log End Biometrics

In the FWF joint project TRP254 entitled with "*Traceability of logs by means of digital images (TreeBio)*" we mainly contributed to the research on this field. For biometric log tracking, each log needs to be enrolled by the biometric system (Figure 1). A digital

[1] University of Salzburg, Jakob Haringer Str. 2, 5020 Salzburg, Austria
[2] University of Applied Sciences Salzburg, Markt 136a, 5431 Kuchl, Austria

camera mounted on a harvester could be utilized to capture one log end of each fresh cut log. Subsequently, the log end image is processed by the system and a log template is computed which is stored, with additional meta data, to the database. Identification of each log can be performed at each stage of the log processing chain. Images for identification in the sawmill could be captured at the sorting station, at the sawmill yard or at any conveyor belt equipped with a capturing device. Subsequently, the image is processed by the biometric system and a log template is computed which is matched to all log templates in the database. The best match specifies the identity of the log.

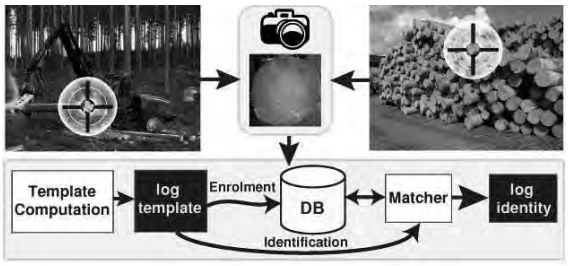

Figure.1: Exemplary enrolment and identification schemes

In our first work [SCPU14] longitudinal and temporal variances of CSs (annual ring patterns) are investigated based on 35 time-delay captured slices from a single log. For human biometrics, robustness of the utilized biometric characteristic is a basic requirement. In case of CSs robustness is related to the temporal changes caused by environmental conditions and the longitudinal variations of the CS pattern within a tree log. Temporal changes are caused by light and humidity and result in deformations like cracks and discolorations. Longitudinal variations result from log end cutting. Results show that, with an increasing time span between two images of the same CS the matching score gets worse. Longitudinal adjacent CS slices (~2.5cm) show good matching scores. An increasing longitudinal slice distance between two CS slices deteriorates the matching score.

In our second work [Sc15b] we shed light on the question if log end biometrics are suited to discriminate between a large set of tree logs. For that purpose we explored the applicability of fingerprint and iris-recognition based methods to identify 150 different tree logs. Additionally, for both methods the impact pact of enhancement is assessed. Results show that fingerprint and iris recognition based approaches can be transferred to the field of wood log tracking and that both are suited for log identification. In the experiments the fingerprint based approach and all iris configurations which use Log-Gabor features achieve 100% recognition rate. Furthermore, all results indicate that shape information of the CS area is required to achieve an acceptable recognition rate and that enhancement significantly improves the performance.

Based on these observations, in [SPU15] we assessed the discriminative power of geometric log end features for the same testset. Geometric features were extracted based on

groundtruth data for the CS boundaries and pith positions. Results showed that radial distances from the pith and centroid center to the CS boundary and Zernike moments (Z) show a high discriminative power. The validation of these features for automated CS boundary detection [SU14] and pith estimation [SU13] showed that Zernike moments achieve the highest reliability.

Finally, in [Sc15a] additionally to the single log used in [SCPU14] further two logs are used in the experiments. This enabled to consider CS surface variations which arise if different cutting tools are utilized for the first cut in the forest and the clearance cut in the further processing company (e.g. chain-saw and circular saw). Three different matching procedures enable to present results for annual ring pattern features, shape features and the fusion of both. Results show that feature fusion increases the robustness and that CS surface variations are not crucial for the performance. We conclude that biometric log recognition is qualified to overcome the issue of cutting log ends in the sawmill up to 7.5 centimeters in thickness, even if the second cut in the sawmill is performed with another cutting tool. Furthermore, it is shown that knots are disturbing factors but knots do not introduce any propagative effects to the annual ring pattern and the CS shape.

3 Outlook and Discussion

Our results are very promising and indicate that digital CS images are well suited for log identification in the described setting. However, sawmills usually do not have such cameras installed and the accuracy of the approach is strongly influenced by acquisition conditions (sensor type, dirt, illumination etc.). The future vision is that a biometric log recognition system works in a more sensor independent manner and further processes the available sensor data to determine log quality properties (see Figure 2).

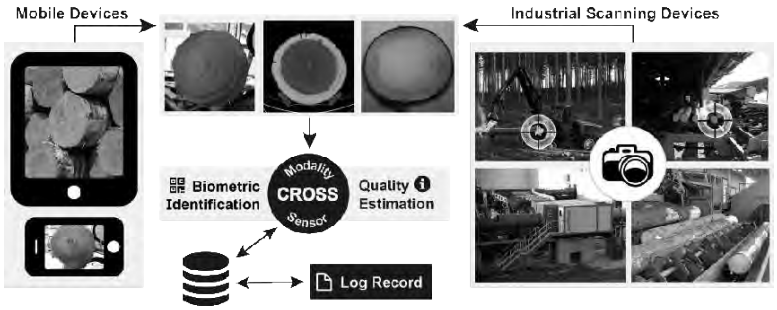

Figure.2: Cross-Sensor and Cross-Modality Log Tracking and Quality Estimation

Collecting and storing data for each single log at different stages of the log processing chain improves the correct allocation of logs, changes and leads to new processes and is thus beneficial to increase the yield.

Furthermore, it can be assumed that CT scanning will become state-of-the-art in the sawmill industry, resulting in corresponding data available at sawmills that can be potentially used for log tracking and wood quality assessment. The question if it is possible to identify tree logs based on a digital RGB log-end image captured in the forest and a second image captured by a CT scanner in the sawmill. Furthermore, the question arises how to link measurement and grading information between the forest and the further-processing companies. Consequently, future research has to deal with cross-modality and cross-sensor log tracking and quality estimation (Figure 2).

Literaturverzeichnis

[Ba08] Barrett, W.A.: Biometrics of Cut Tree Faces. In (Sobh, Tarek, ed.): Advances in Computer and Information Sciences and Engineering, pp. 562–565. Springer, 2008.

[CG03] Chiorescu, S.; Grönlund, A.: The Fingerprint approach: using data generated by a 2-axis log scanner to accomplish traceability in the sawmill's log yard. Forest Products Journal, 53:78–86, 2003.

[CG04] Chiorescu, S.; Gröonlund, A.: The Fingerprint Method: Using Overbark and Underbark Log Measurement Data Generated by Three-dimensional Log Scanners in Combination with Radiofrequency Identification Tags to Achieve Traceability in the Log Yard at the Sawmill. Scand. Journal of Forest Research, 19(4):374–383, 2004.

[FOG08] Flodin, J.; Oja, J.; Gröonlund, A.: Fingerprint traceability of logs using the outer shape and the tracheid effect. Forest Products Journal, 58(4):21–27, 2008.

[Sc15a] Schraml, Rudolf; Charwat-Pessler, Johann; Petutschnigg, Alexander; Uhl, Andreas: Towards the applicability of biometric wood log traceability using digital log end images. Computers and Electronics in Agriculture, 119:112–122, 2015.

[Sc15b] Schraml, R.; Hofbauer, H.; Petutschnigg, A.; Uhl, A.: Tree Log Identification Based on Digital Cross-Section Images of Log Ends Using Fingerprint and Iris Recognition Methods. In: Proceedings of the 16th International Conference on Computer Analysis of Images and Patterns. LNCS. Springer, pp. 752–765, 2015.

[SCPU14] Schraml, R.; Charwat-Pessler, J.; Uhl, A.: Temporal and longitudinal variances in wood log cross-section image analysis. In: IEEE International Conference on Image Processing (ICIP'14). Paris, FR, October 2014.

[SPU15] Schraml, R.; Petutschnigg, A.; Uhl, A.: Validation and Reliability of the Discriminative Power of Geometric Wood Log End Features. In: Proceedings of the IEEE International Conference on Image Processing (ICIP'15). 2015.

[SU13] Schraml, R.; Uhl, A.: Pith Estimation on Rough Log End Images using Local Fourier Spectrum Analysis. In: Proceedings of the 14th Conference on Computer Graphics and Imaging (CGIM'13). Innsbruck, AUT, February 2013.

[SU14] Schraml, R.; Uhl, A.: Similarity based cross-section segmentation in rough log end images. Proceedings of the 10th Artificial Intelligence Applications and Innovations Conference. Springer, pp. 614–621, 2014.

Machine Vision and Applications
DOI 10.1007/s00138-016-0814-2

SPECIAL ISSUE PAPER

On rotational pre-alignment for tree log identification using methods inspired by fingerprint and iris recognition

Rudolf Schraml[1] · **Heinz Hofbauer**[1] · **Alexander Petutschnigg**[2] · **Andreas Uhl**[1]

Received: 30 November 2015 / Revised: 28 September 2016 / Accepted: 30 September 2016

Abstract Tree log end biometrics is an approach to track logs from forest to further processing companies by means of log end images. The aim of this work is to investigate how to deal with the unrestricted rotational range of cross sections in log end images. Thus, the applicability of three different rotational pre-alignment strategies in the registration procedure is assessed. Template computation and matching is based on fingerprint and iris recognition techniques which were adopted and extended to work with log end images. To address these questions, a testset built up on 279 tree logs is utilized in the experiments. The evaluation assesses the basic performance of the rotational pre-alignment strategies and their impact on the verification and identification performances for different fingerprint- and iris-based configurations. Results indicate that rotational pre-alignment in the registration procedure is the main component to deal with rotation in log end biometrics. The best configurations achieve identification rates >93 %. By showing that cross sections in log end images can be rotated to a distinctive position, this work is a first step towards real word log end biometrics.

Keywords Rotation invariant log end biometrics · Tree log tracking · Wood traceability · European timber regulation · Chain of custody

This work is partially funded by the Austrian Science Fund (FWF) under Project No. TRP-254.

✉ Rudolf Schraml
rudi.schraml@gmail.com

[1] Department of Computer Sciences, University of Salzburg, Salzburg, Austria

[2] Department of Forest Products Technology and Timber Construction, University of Applied Sciences Salzburg, Salzburg, Austria

Published online: 04 November 2016

Abbreviations

CS	Cross section
TS	Testset
NORC	No rotation compensation
CM	Center of mass
EER	Equal error rate
MS	Matching score

1 Introduction

Tracking of tree logs is an economic requirement to map the ownership of each log. Additionally, social aspects have become more important and sustainability certificates, e.g. Forest Stewardship Council (FSC), are a must have for all end-sellers. Finally, traceability is legally mandated by the European Timber Regulation or the U.S. Lacey Act to prohibit illegal logging.

In the industry, commonly approaches which rely on physically marking each log are utilized and radio-frequency identification (RFID) is promoted as future technology. Without doubt RFID technology shows a lot of advantages. However, physical marking requires time and suffers costs. Wood log biometrics is a physically marking-free approach to establish log traceability.

By superficially comparing annual ring patterns of log ends to the patterns of human fingerprints, one finds a close resemblance. Wood logs offer characteristics on log end faces in terms of annual rings, pith position, shape and dimension. The pith as growth centre is an unique reference point which is similar to the core point of a fingerprint. Furthermore, log ends are circularly shaped and in combination with the pith the annual ring pattern can be polar-transformed like the texture of an iris.

Our research on log end biometrics [13–16] treated fundamental questions related to biometric tracking of wood logs using fingerprint and iris recognition based approaches. In Ref. [14,16] we investigated the robustness of log end biometrics to temporal, longitudinal and surface variations based on cross-sectional images (CS-Images) captured in a controlled environment. In Ref. [15,16] we investigated whether log end biometrics is basically suited to discriminate between 150 different logs. In Ref. [16] we assessed the discriminative power of geometric log end features and we proved their reliability in case of automated cross-sectional (CS) segmentation [17] and pith estimation [18]. Similar as in [1] the experimental evaluation showed that Zernike polynomials are the most reliable geometric features. However, the achieved verification performances showed that just geometric features are not discriminative enough for log end identification. Finally, in [15] we explored the general applicability of methods inspired by fingerprint and iris recognition to identify tree logs. Our experiments for 150 tree logs from two testsets showed that for both approaches an identification performance of 100 % can be achieved.

However, so far all CS-Images of each log were captured with nearly no variation with respect to scale and rotation. Rotational variations are a key issue in log end biometrics and it is not clear if log ends can be rotated to a distinctive position just using features which can be detected in CS-Images. Furthermore, the issue of finding a distinctive rotational log position is becoming important for the sawmill industry. Research showed that log positioning at the saw intake and individual cutting increases the value of each log up to 21 % [2].

In this study we assess the suitability of three different rotational pre-alignment strategies which basically rely on the pith position and the CS boundary. Suitability is therefore assessed in two steps. In the first step the basic performance of each strategy to align each CS to a distinctive position is assessed. Therefore, the results of an image registration algorithm are evaluated. In the second step, the impact of rotational pre-alignment on the verification and identification performances for a set of fingerprint- and iris-based approaches is assessed. In addition to the two testsets from [15], a third testset with 109 different tree logs, showing strong rotational variations, is utilized for the experiments.

Section 2 introduces the computation and matching of log templates for the fingerprint- and iris-based approaches. Subsequently, the experimental evaluation is presented in Sect. 3 followed by the conclusions in Sect. 4.

2 CS-Code computation and matching

An exemplary enrolment and identification scheme for log end biometrics is depicted in Fig. 1. Enrolment of a tree log is performed in the forest. After a tree log is cut and processed by a harvester, the log end is captured by a digital camera mounted on the harvester head. Templates of logs which are computed by means of CS-Images are denoted as CS-Codes. For enrolment the computed CS-Code is stored in the database. Identification can be performed at each stage of the log processing chain where an appropriate capturing device is available. Typically, identification is required when a log is delivered to a sawmill. The CS-Image of a log, for which identification is required, is processed by the biometric system and the computed CS-Code is matched to all enrolled CS-Codes in the database. The best ranked match, if it exceeds a certain threshold, determines the identity of the log.

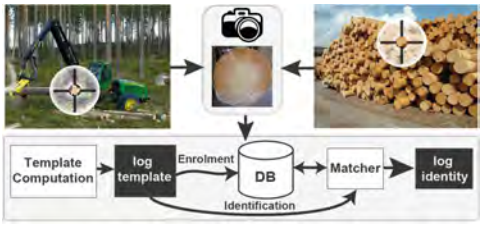

Fig. 1 Enrolment and identification schemes

2.1 Rotational pre-alignment strategies

Biometric systems compute a compact representation (=template) of a biometric characteristic captured of an individual/object. Because of privacy, timing and memory considerations captured raw data is not stored in the system. Templates are designed in order to enable fast matching with respect to the spatial interrelationship of the extracted features. This is a key to achieve a high discriminative power, and thus registration is an important task in biometrics. Pre-alignment in the registration procedure refers to absolute alignment: The characteristic is pre-aligned independent of a reference just by using intrinsic features [8]. Image registration algorithms (see Sect. 3.2.1) require relative alignment and are not applicable in this case since a template cannot be used in a registration procedure (where two images are required). The goal of registration is to align the captured characteristic to a distinctive position independent of affine transformations like rotation or scale.

In fingerprint recognition different approaches for rotational pre-alignment were proposed. Several algorithms use the core point and a further feature (e.g. computed from the shape or the orientation field) for pre-alignment. No final solution has been found so far [8]. However, fingerprints show key points denoted as minutia and minutiae point clouds are well suited for relative alignment (e.g. [11]) in the match-

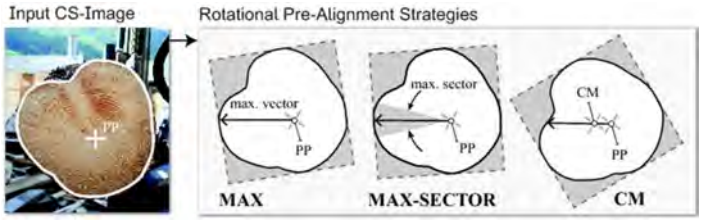

Fig. 2 Different rotational pre-alignment strategies for CS registration are assessed

ing procedure. In case of iris recognition just small rotational variances are expected which are commonly compensated in the template matching procedure.

In log end biometrics rotation is one of the main issues. Compared to an iris, the rotational range of a log end is not restricted and compared to a fingerprint just the pith as keypoint is available for alignment. Rotation in log end biometrics needs to be considered in both, the template computation and the template matching procedure which refers to rotational pre-alignment and rotation compensation, respectively:

Rotational pre-alignment In the registration step of the template computation procedure the goal is to rotationally pre-align the CS in a log end image to a distinctive position. Optimally, CSs in different CS-Images of the same log end can be rotated to almost the same position.

Rotation compensation To compensate the remaining rotational variances different strategies in the feature extraction and template matching procedure can be applied. However, rotation compensation during feature extraction and template matching increases the computational expense and probably decreases the discriminative power.

In principle, the better CSs can be pre-aligned to distinctive positions in the registration procedure, the less other components of the biometric system have to deal with issues caused by rotational variances.

As there is no evidence whether log ends can be rotated to a unique position, we evaluate three different rotational pre-alignment strategies in the registration procedure to address this question. All approaches require the pith position and the CS boundary as input. Automated approaches for pith estimation and CS segmentation were presented in [10,17] and [18], respectively. For each approach the rotational pre-alignment vector between the pith position and the CS border is determined differently (Fig. 2):

- **MAX** = the max. pith to border distance vector.
- **MAX-SECTOR** = the centre vector of the sector (angular width = 30°) containing the max. sum of the pith to border distances.
- **CM** = the pith to CS boundary vector which passes through the center of mass (CM) of the CS boundary polygon.

Subsequently, the CS is rotated around the pith in order to situate the rotational pre-alignment vector at a certain position. For this work the vector is placed on the left horizontal axis. Remaining rotational variances are considered differently for the fingerprint-based and the iris-based approaches as described in Sects.2.2 and 2.3, respectively.

2.2 Fingerprint-based CS-Codes

Human fingerprint recognition is well-investigated, and there exist mainly three groups of approaches: minutiae-based, correlation-based and feature-based approaches [8]. Apart from the presence of the pith as detectable feature, CS patterns do not exhibit further constant features like minutia's in fingerprints. Hence, minutiae-based approaches are not qualified for log CSs.

For this reason and same as in [13–15] the texture-feature-based approach by [4] is adopted and extended to compute and compare CS-Codes from CS-Images. Compared to the almost constant ridge frequency of a fingerprint annual ring frequencies vary significantly. Thus, the Gabor filterbank is extended to six different filters instead of a single one. For preprocessed CS-Images scaled to 512 pixels we suggest the following Gabor filterbank settings to capture the expected variety of occurring annual ring widths: $G(\lambda, \theta, \sigma, \gamma) = G(\lambda, \sigma) = ((2, 1), (3.5, 2), (4.5, 3), (5.5, 3), (6.5, 3), (7.5, 3)), \theta = \{0, 22.5, \ldots, 135, 157.5\}, \gamma = 0.7$. λ is the filter wavelength, θ represents the orientation, σ is the standard deviation and γ specifies the filter aspect ratio.

Remaining rotational variances are compensated by repeatedly computing features for rotated versions of the already rotation compensated CS-Image. All feature vectors computed for different rotations $(\Theta_1, \ldots, \Theta_n)$ compose the CS-Code of a CS-Image. The amount of feature vectors computed for different rotations has to be chosen carefully, because each additional feature vector suffers computational expense.

The computation of a feature vector (Θ_i) for a certain rotation is performed in four steps (see Fig. 3). As input the CS-Image, pith position, CS boundary and the rotational pre-alignment vector Θ_0 are required. First, and according to the rotation of Θ_i the CS-Image is rotated around the pith and

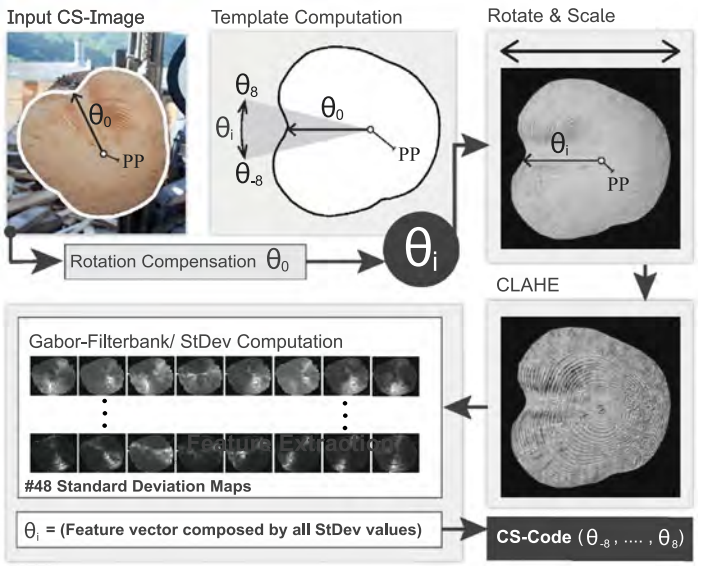

Fig. 3 Fingerprint-based template computation: Feature vectors are computed in a predefined sector specified by the rotational pre-alignment vector Θ_0

the CS is cropped to the CS boundary box and scaled to 512 pixels in width. Subsequently, the rotated, cropped and scaled CS-Image is enhanced. Commonly, the annual ring pattern is disturbed due to cutting and there arise different types of intraclass CS variations in real-world identification scenarios [13]. The purpose of enhancement is to strengthen the annual ring pattern contrast and to compensate CS variations. In this work for enhancement contrast limited adaptive histogram equalization (CLAHE, [6]) is applied to the registered image.

The enhanced CS-Image is filtered with each filter in the filterbank. The filtered images are further subdivided into blocks (16×16 pixels). For all blocks of each filtered image, the grey value standard deviations are computed and stored into a matrix. Values of blocks which are not within the CS border are assigned with a marker value. These markers are used to discriminate between background and CS in the matching procedure. All matrices are stored as one-dimensional vector.

Fingerprint-based matching procedures Matching between two CS-Images is performed by computing the minimum matching score (MS) between all feature vectors $(\Theta_1, \ldots, \Theta_n)$ of the CS-Codes from both CS-Images.

Like in Ref. [13] three different matching procedures are evaluated to investigate the discriminative power of the annual ring pattern, the shape and a fusion of both: The first procedure which just considers annual ring pattern information is denoted as annual ring pattern MS (MS_{AP}) and is defined as the minimum matching score between the feature vectors of both CS-Codes:

$$\begin{aligned} \text{MS}_{AP}\,(\text{CS-Code}_1, \text{CS-Code}_2) &= \min \text{MS}\left(\theta_i, \theta_j\right) \\ \text{where}\quad \theta_i &\in \text{CS-Code}_1\,(\theta_0, \ldots, \theta_{358})\,, \\ \theta_j &\in \text{CS-Code}_2\,(\theta_0, \ldots, \theta_{358}) \end{aligned} \tag{1}$$

Due to interpolation in the registration procedure (rotation and scaling) the best MS is achieved when comparing all feature vectors of both CS-Codes. The MS between two feature vectors of two CS-Codes is computed by:

$$\text{MS}(\theta_i, \theta_j) = \frac{1}{M} \sum_{k=0}^{n} D\left(\theta_i(k), \theta_j(k)\right) \tag{2}$$

where θ_i, θ_j are two feature vectors of the CS-Codes which are compared, k specifies the index of the feature value in both vectors, n is the max. number of feature values and M is a normalization factor. As distance function (D) the L1 norm is utilized (as our experiments showed that the L1 norm performs better than the L2 norm [14]):

$$D = \begin{cases} \left|\theta_i(k) - \theta_j(k)\right| & \text{if } k \in MCS_i \cap MCS_j \\ 0 & \text{otherwise} \end{cases} \tag{3}$$

As noted, background feature values are specified by a certain marker. Hence, we define MCS_i and MCS_j as the corresponding masks of the feature vectors which allow to differentiate between background and CS. Just feature vector value pairs which are in the intersection of both CSs are utilized for computing MS_{AP} and the score is normal-

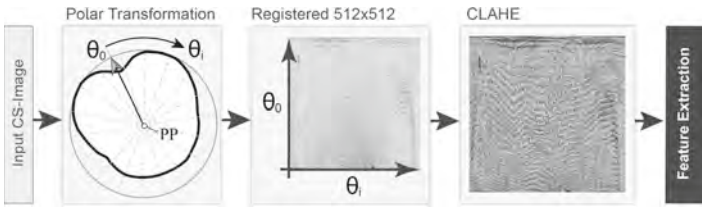

Fig. 4 Iris-based template computation: CS-Images are polar-transformed and enhanced using CLAHE

ized by the amount of the considered feature value pairs: $M = |\mathrm{MCS}_1 \cap \mathrm{MCS}_2|$.

The second procedure (MS_F) is a measure describing the similarity of the shapes of two CSs. MS_F is defined as the minimum False Negative Mask Overlap Score (F) between the masks of the feature vectors of both CS-Codes:

$$\mathrm{MS}_F\ (\text{CS-Code}_1, \text{CS-Code}_2) = \min F\left(\mathrm{MCS}_i, \mathrm{MCS}_j\right) \tag{4}$$

The false negative mask overlap score (F) between two different masks ($\mathrm{MCS}_i, \mathrm{MCS}_j$) is defined as the ratio between the symmetric difference ($\triangle$) from both masks and the area of the smaller mask:

$$F\left(\mathrm{MCS}_i, \mathrm{MCS}_j\right) = \frac{\left|\mathrm{MCS}_i \triangle\ \mathrm{MCS}_j\right|}{\min\left(\left|\mathrm{MCS}_i\right|, \left|\mathrm{MCS}_j\right|\right)} \tag{5}$$

Finally, the last procedure ($\mathrm{MS}_{\mathrm{AP},F}$) is based on score level fusion [5, p.225]. Therefore, the $\mathrm{MS}_{\mathrm{AP}}$ and MS_F scores are mapped to the [0,1] range using min-max normalization. The lower and upper bounds of the score ranges are determined using the scores computed in the experiments. For score level fusion the normalized scores $\mathrm{MS}'_{\mathrm{AP}}$ and MS'_F are utilized:

$$\mathrm{MS}_{\mathrm{AP},F} = \frac{\mathrm{MS}'_{\mathrm{AP}} + MS'_F}{2} \tag{6}$$

2.3 Iris-based CS-Codes

For the iris-based approaches the pith position is used as reference point to polar transform the CS-Image using bi-cubic interpolation. The registration compensation vector (Θ_0) computed by one of the rotational pre-alignment strategies is therefore used as initial vector for the polar transformation. Θ_0 is aligned at the left boundary of the polar-transformed CS-Image (see Fig. 4). For normalization each pixel in the polar image is stretched according to the length of Θ_0 which is specified as the max. pith to CS border radius.

Polar-transformed CS-Images can be treated like polar iris images. Compared to the size of the iris, CSs are larger and the transformation is not restricted to an annular shaped ring. In case of more than 64 annual rings the common polar transformation format of 512×64 pixels causes a loss of information. Our results in [15] showed that the larger format significantly outperforms the smaller one. Consequently, for this work just the larger format with 512×512 pixels is utilized.

Two feature extractors from the USIT package [12] were extended to work with a larger polar CS-Image format of 512×512 pixels. First, the Log Gabor (LG) algorithm by Masek [9] was extended in accordance with the original algorithm by defining the region of interest (ROI) through a number of rows r with a height h_r. Like the original, a row is condensed into a 1-D signal which is run through the Gabor filtering process. Since it is not clear which configuration of r and h_r is best we choose to use a variance of combinations, including combinations where the ROI does not span the whole polar-transformed CS-Image. However, unlike the iris biometry case which excludes the outer iris boundary, which frequently exhibits occlusions by cilia, we choose to exclude the inner residual part of the polar CS-Image. This part consists of a low number of pixels which are stretched to the polar CS-Image width, thus providing nearly no usable information. Note that the size of the feature vector is dependent on h_r.

Furthermore the algorithm by Ko et al. (KO) [7] was simply adopted by allowing bigger textures without adapting the cell-size which is averaged. Note that as a result the length of the feature vector increases with the size of the texture. The extended algorithms are directly applied to the polar-transformed and CLAHE enhanced CS-Images. Both algorithms compute a CS-Code composed of a single feature vector.

Iris-based matching procedures For the matching of iris-based CS-Codes KO uses a specific comparator [7] and LG the Hamming distance. Figure 5 shows a schematic overview of iris-based rotation compensation. If the rotational pre-alignment vector Θ_0 is computed different for the same input CS-Image a given point in both images (E_1) appears at different angular locations, the radial distance stays the same. The rotational variance is reduced to a translation in the normalized texture.

The feature vector values (=bits) of the iris-based CS-Code are extracted along a fixed grid in the normalized texture. Consequently, a bit shift in the iris-based CS-Code corresponds to a translation in the normalized texture. In this way bit-shifts on the iris-based CS-Codes are suited to compensate remaining rotational variations.

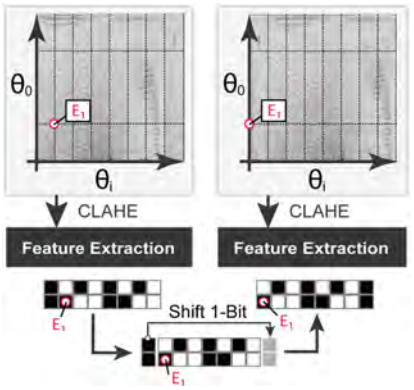

Fig. 5 Iris-based CS-Code Shifting

Similar as for the fingerprint-based matching procedure, the final MS between two iris-based CS-Codes is determined between all combinations of shifted CS-Codes.

3 Experiments

In the experimental evaluation verification and identification performances for different configurations are assessed. Additionally, the rotational pre-alignment performances are assessed using an image registration algorithm. Introductory, the testsets are outlined and the experimental setup for the utilized configurations is described.

Testsets (TS_1, TS_2, TS_3) The first two testsets were already used for the experiments in [15,16]. The CS-Images of TS_1 and TS_2 were captured with a tripod and showed nearly no variances with respect to affine transformations. For TS_1 50 different tree logs were captured four times with and without flash. Additionally, the ends of eight logs were cross-cut and captured once again, with and without flash. In TS_2 120 logs were captured three times without flash (in [15,16] 105 of TS_2 were used). The new testset TS_3 consists of 109 different logs where each log was captured between 10 to 14 times without flash. All images were taken handholding the camera which was rotated for each new CS-Image. For each CS-Image the pith position and the CS border were determined manually and are utilized as groundtruth data for the experiments. Samples of each testset are shown in Fig. 6.

3.1 Experimental set-up

For all CS-Images of the testsets CS-Codes and MSs were computed for different configurations of the fingerprint- and iris-based approaches.

Fingerprint configurations Remaining rotational variances are compensated by computing feature vectors for rotations in the range from $-8°$ to $8°$ in $2°$ steps. The CS-Codes are computed using 16×16 non-overlapping blocks. The Gabor filterbank is build up on six different filters tuned to eight directions.

Iris configurations Remaining rotational variances are compensated by shifting the iris-based CS-Codes in a range between -21 to 21 feature vector positions. This approximately equals the rotation compensation range of $-8°$ to $8°$ for the fingerprint configurations.

Fig. 6 *1st Row* (TS_1): Respectively, two CS-Images from two different logs—one captured with flash and one without flash. *2nd Row* (TS_2): Four CS-Images from different logs. *3rd Row* (TS_3): Four CS-Images illustrating the rotational variations

Furthermore, results for $IRIS_V$ and $IRIS_H$ are presented. $IRIS_H$ means that the annual ring patterns in the polar-transformed CS-Image are aligned horizontally as common. For $IRIS_V$ the polar-transformed CS-Image is rotated by 90°. Commonly, feature extraction in iris recognition aims to extract information from vertically aligned structures and thus may performs better if we rotate the polar-transformed CS-Images. Note, that in case of $IRIS_V$ CS-Code shifting does not correspond to a rotational shift in the input CS-Image. More or less, this corresponds to vertically shifting the unrolling center (=pith position) up/down in the input CS-Image. For LG three different configurations in terms of number of rows and row height LG (r, h_r) are utilized: LG (16,32), LG (64,08) and LG (50,10).

3.2 Results and discussion

The experimental evaluation is performed in three stages. First, the performances of the rotation compensation strategies are assessed utilizing image registration algorithms. Second, the verification performances for all fingerprint/iris configurations and all rotational pre-alignment strategies are assessed. Finally, we assess the identification performances of the best configurations in case of rotational pre-alignment.

For a better examination the results in each stage are provided for TS_1 and TS_2 together (TS_{12}), TS_3 and all three testsets (ALL). Additionally, all configurations are assessed without rotational pre-alignment (NORC).

3.2.1 Rotational pre-alignment performance

The performances of the rotational pre-alignment strategies are assessed using the image registration approach by [19] (provided for MATLAB) which gives an estimate for the rotational error between two images.

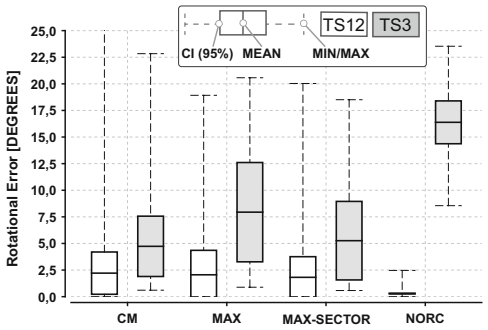

Fig. 7 Rotational variations computed by the image registration approach proposed in [19]

All CS-Image of TS_{12}, TS_3 were rotationally pre-aligned using the three different strategies. Subsequently, for each strategy the remaining rotational errors between the pre-aligned CS-Images of each log were computed employing accurate image registration [19]. The rotational error statistics for each strategy (mean, variance and confidence intervals for a level of 95 %) each strategy and TS_{12}, TS_3 are depicted in Fig. 7. Results for NORC confirm that the rotational variations in TS_{12} are very low and that TS_3 shows large rotational variations. The rotational variations in TS_3 cover a range of approximately 45°. Furthermore, the results indicate that all rotational pre-alignment strategies are suited to reduce rotational variations in TS_3. Results for TS_{12} show that all rotational pre-alignment strategies introduce rotational variations. Taking all statistics into account the lowest rotational variances are shown for the MAX-SECTOR rotational pre-alignment strategy.

3.2.2 Verification performance evaluation

The verification performance is assessed based on the Equal Error Rate (EER) and the margin of error (MOE) achieved for each configuration. The MOE is estimated for a 95 % level of confidence using subset partitioning [3]. The EERs computed for all configurations, rotational pre-alignment strategy and testsets are shown in Table 1. To improve the overview EERs for some configurations are summarized and the MOEs are only shown for the CM pre-alignment strategy. Note, that the results for NORC and TS_{12} are comparable to the results presented in [15].

Rotation compensation strategies Initially, the verification performances achieved for the different rotational pre-alignment strategies are assessed. In case of NORC the EERs for TS_{12} are much better than the EERs for TS_3. This confirms the results of the rotational pre-alignment performance evaluation and shows that the large rotational variances in TS_3 cannot be compensated by the template computation and matching procedures of the fingerprint- and iris-based approaches. The impact of rotational pre-alignment becomes obvious comparing the EERs for TS_3 achieved for NORC to those achieved with rotational pre-alignment (MAX, MAX-SECTOR and CM). The best (=lowest) EERs for TS_3 and ALL are achieved when CM is used for pre-alignment. In case of rotational pre-alignment this also accounts for the TS_{12} EERs. Furthermore, the results show that for all configurations the EERs for MAX-SECTOR are better (=lower) than for MAX. Considering the EERs it can be stated that CM is the best of the three rotational pre-alignment strategies, especially when considering the results for TS_3.

Fingerprint-based configurations In case of the fingerprint-based configurations the results for NORC-MS_{AP} differ from the results presented in [15]. Compared to the EER

Table 1 EERs [%] and ± MOE [%] for the fingerprint- and iris-based configurations

		NORC			MAX			MAX-SECTOR			CM		
	Configuration	TS_{12}	TS_3	ALL	TS_{12}	TS_3	ALL	TS_{12}	TS_3	ALL	TS_{12}	TS_3	ALL
FP	MS_{AP}	1.22									1.11 ±0.5	1.28 ±2.9	1.26 ±0.5
	MS_F	0.35	> 7	> 5	> 6	> 4	> 2	> 3	> 3	> 3	1.54 ±1.3	6.85 ±2.3	5.54 ±0.8
	$MS_{AP,F}$	0.54									**0.64 ±0.4**	1.32 ±2.1	1.41 ±0.5
$IRIS_H$	LG(16,32)	0.4									1.32 ±1.1	2.44 ±0.4	2.06 ±0.8
	LG(64,08)	0.97	> 20	> 17	> 4	> 12	> 11	> 3	> 6	> 5	2.13 ±1.3	2.29 ±0.5	2.12 ±0.7
	LG(50,10)	0.67									1.92 ±0.9	2.39 ±0.5	2.55 ±0.9
	KO	0.99									5.28 ±1.5	7.89 ±1.8	7.33 ±0.9
$IRIS_V$	LG(16,32)	0.92									0.91 ±0.6	1.21 ±1.7	1.26 ±0.5
	LG(64,08)	0.83	> 6	> 5	> 3	> 9	> 7	> 2	> 4	> 4	1.11 ±0.8	**0.81 ±1.8**	**0.9 ±0.6**
	LG(50,10)	0.67									0.97 ±0.9	1.14 ±1.7	**0.9 ±0.6**
	KO	0.96									3.15 ±1.1	3.81 ±1.9	3.48 ±0.7

$EER < 2\%$: Yellow coloured results signalize all EERs <2 %. Best TS **EER & MOE:** Green coloured and bold face marked results show the best EERs and MOEs for each testset achieved with rotational pre-alignment

Table 2 LG (64,08)-EERs[%] for CS-Code shifting/no CS-Code shifting

Configuration	NORC	MAX	MAX-SECTOR	CM
$IRIS_H$	20.51/50.80	12.11/28.21	6.67/17.83	2.12/18.68
$IRIS_V$	5.46/6.74	7.18/7.81	3.79/3.86	0.90/0.96

achieved for MS_{AP}-ENH_{NO} (15.7 %) in [15] the EER for NORC-MS_{AP}-TS_{12} (1.22 %) is much better. This improvement is attributed to the better-contrast normalization due to CLAHE. In our previous works we applied local contrast normalization and the size of the local regions was probably set too large. However, the MS_{AP}-ENH_1 and ENH_2 results in [15] (1.7 and 0.9 %) are in the range of the results for NORC-MS_{AP}-TS_{12} in this work (1.22 %).

The results for MS_F lead to new interesting insights. In case of NORC-MS_F-TS_{12} (0.35 %) the shape has a stronger discriminative power than the annual ring pattern (MS_{AP} = 1.22 %). Fusion of both leads to no further improvement of the EER ($MS_{AP,F}$ = 0.54 %). In case of CM feature fusion fusion improves the EER and MOE for TS_{12} ($MS_{AP,F} = 0.64 \pm 0.4\,\%$). The best fingerprint-based results for TS_3 and ALL are achieved with CM-MS_{AP} and account 1.28 and 1.26 %, respectively. Fusion leads to no improvement.

Iris-based configurations For the iris-based configurations the EERs for all LG configurations and NORC - TS_{12} are slightly worse compared to the ENH_{NO} results shown in [15]. Note that testset TS_{12} was extended by CS-Images of 15 logs and we use a different contrast normalization in this work. On the other hand, it seems that KO profits from CLAHE and the EER for KO-NORC-TS_{12} (0.99 %) is much better than the comparable EER for KO-ENH_{NO} (2.73 %) in [15].

$IRIS_H$ vs. $IRIS_V$ Basically, for most of the iris configurations the $IRIS_V$ results outperform the $IRIS_H$ results. As noted, iris recognition aims to extract vertical aligned structures. All results for $IRIS_V$ clearly confirm that the utilized feature extractors perform better if we rotate the polar-transformed CS-Images. The overall best EER with 0.9 ± 0.6 % for ALL testsets in Table 1 is achieved with $IRIS_V$-CM-LG (50,10) and LG (64,08).

$IRIS_H$/$IRIS_V$ CS-Code shifting The improvements for $IRIS_V$ are astonishing because CS-Code shifting in the matching procedure is not suited to compensate rotational variations. To illustrate this, in Table 2 we present EERs for LG (64,08), $IRIS_H$ and $IRIS_V$ where no CS-Code shifting in the matching procedure is performed.

For a better overview the EERs achieved with shifting are also shown. In case of $IRIS_H$ the results show that with shifting the EERs get better for each rotational pre-alignment strategy. On the other hand the results for $IRIS_V$ demonstrate that the results are not that improved by shifting. We assume that shifting in case of $IRIS_V$ is suited to compensate small radial variations. However, accompanied by the results in Table 2 the results confirm the assumption that KO and LG achieve a significantly better performance in case of textures showing vertically aligned structures.

Basic insights In accordance with our results in [15] the verification performance evaluation shows that the EERs for the best fingerprint- and iris-based configurations are quite

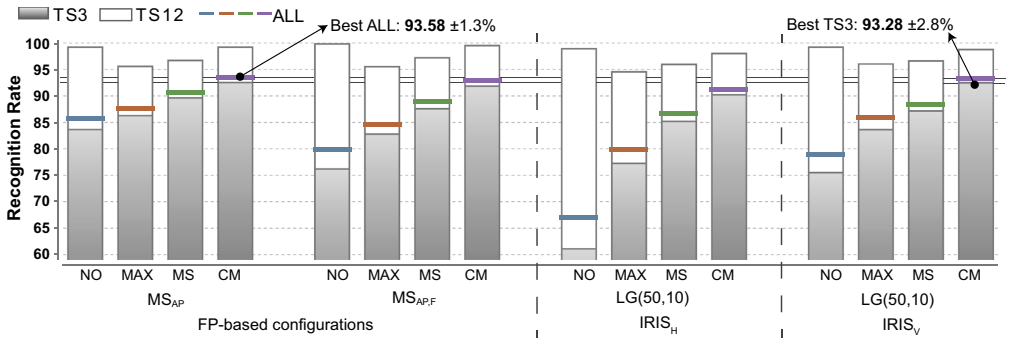

Fig. 8 Identification performance evaluation—Rank 1 detection rates

low and show a high degree of separability between the intra- and interclass score distributions for a large set of tree logs. Considering the rotational variations in the new TS_3 results show that rotational pre-alignment in the registration procedure improves the robustness to rotational variations. Furthermore, the results for TS_{12} in case of NORC and CM indicate that there is nearly no decrease in the verification performance due to rotational pre-alignment. Note, that in case of rotational pre-alignment rotational variations are introduced to TS_{12} which basically contains no rotational variations.

3.3 Identification performance evaluation

For the identification performance evaluation, the best configurations for the fingerprint-based $IRIS_H$ and $IRIS_V$ configurations were preselected, and the respective results are depicted for all rotational pre-alignment strategies in Fig. 8. For each configuration and the different testsets, the Rank 1 identification rates are presented.

In accordance with the verification performance results, the recognition rates for TS_{12} are better than for TS_3. The total recognition rate for ALL is somewhere in-between. For the fingerprint-based configurations the results for TS_{12} and $MS_{AP,F}$ show that the fusion of annual ring pattern and shape information does increase the identification performance significantly. In case of TS_3 and ALL the results for $MS_{AP,F}$ show that fusion decreases the identification performances slightly.

For $IRIS_H$ and $IRIS_V$ the best configurations with respect to the best recognitions rates for ALL are shown. The $IRIS_H$ and $IRIS_V$-LG(50,10) configurations confirm that for $IRIS_V$ the identification performance increases significantly. The best identification rate and MOE ($93.58 \pm 1.3\,\%$) for ALL is achieved with MS_{AP} and CM. In difference to the verification performance results the identification rates for CM are not that excessively better than those achieved with the other rotational pre-alignment strategies. However, same as in the verification performance evaluation results show that for all configurations the CM rotational pre-alignment strategy achieves the highest identification rates, especially when considering the results for TS_3 and ALL.

4 Conclusions

This work demonstrates that rotational pre-alignment in the registration procedure is suited to overcome rotational variations in log end biometrics. Along with our results in [15] it is shown that fingerprint and iris recognition techniques can be successfully transferred to the field of wood log tracking. Based on the variety of 279 different logs the results indicate the applicability of log end biometrics to log identification.

Due to the best verification performance results and the high identification rates, we conclude that CM is the best of the investigated rotational pre-alignment strategies. For the fingerprint-based approach the results show that the annual ring pattern feature MS_{AP} - ALL achieves a very good EER for CM ($1.26\,\%$). No improvement by including shape information in the matching procedure ($MS_{AP,F}$) can be observed. In case of the iris-based approaches LG outperforms the results of KO and IRIS $_V$ performs better than $IRIS_H$. The best EER ($0.9 \pm 0.6\,\%$) is achieved with $IRIS_V$-CM-LG(50,10) or LG(64,08). In the identification performance experiments the best fingerprint and iris-based configurations achieve detection rates $>93\%$ at Rank1.

The next stage of our research will be to investigate the impact of automated pith estimation [17] and CS segmentation [18] on the biometric system performance. Furthermore, the performance for $IRIS_V$ raises the general question for the best filters and filter parameters and to assess further feature descriptors for feature extraction.

Acknowledgements Open access funding provided by [Paris Lodron University of Salzburg].

References

1. Barrett, W.: Biometrics of cut tree faces. In: Sobh, T. (ed.) Advances in Computer and Information Sciences and Engineering, pp. 562–565. Springer, Netherlands (2008)
2. Berglund, A., Broman, O., Grönlund, A., Fredriksson, M.: Improved log rotation using information from a computed tomography scanner. Comput. Electron. Agric. **90**, 152–158 (2013)
3. Bolle, R.M., Ratha, N.K., Pankanti, S.: Error analysis of pattern recognition systemsthe subsets bootstrap. Comput. Vis. Image Underst. **93**(1), 1–33 (2004)
4. Jain, A., Ross, A., Prabhakar, S.: Fingerprint matching using minutiae and texture features. In: Proceedings of the International Conference on Image Processing (ICIP'01), vol. 3, pp. 282–285. Thessaloniki, GR (2001)
5. Jain, A.K., Ross, A.A., Nandakumar, K.: Introduction to Biometrics. Springer, New York (2011)
6. Karel, Z.: Graphics Gems iv. Chap. Contrast Limited Adaptive Histogram Equalization. Academic Press Professional, Inc., San Diego (1994)
7. Ko, J.G., Gil, Y.H., Yoo, J.H., Chung, K.I.: A novel and efficient feature extraction method for iris recognition. ETRI J. **29**(3), 399–401 (2007)
8. Maltoni, D., Maio, D., Jain, A.K., Prabhakar, S.: Handbook of Fingerprint Recognition. Springer, New York (2009)
9. Masek, L.: Recognition of human iris patterns for biometric identification. Master's thesis, University of Western Australia (2003)
10. Norell, K., Borgefors, G.: Estimation of pith position in untreated log ends in sawmill environments. Comput. Electron. Agric. **63**(2), 155–167 (2008)
11. Ramoser, H., Wachmann, B., Bischof, H.: Efficient alignment of fingerprint images. In: Proceedings of the 16th International Conference on Pattern Recognition, vol. 3, pp. 748–751 (2002)
12. Rathgeb, C., Uhl, A., Wild, P.: Iris Recognition: From Segmentation to Template Security, Advances in Information Security, vol. 59. Springer (2013)
13. Schraml, R., Charwat-Pessler, J., Petutschnigg, A., Uhl, A.: Towards the applicability of biometric wood log traceability using digital log end images. Comput. Electron. Agric. **119**, 112–122 (2015)
14. Schraml, R., Charwat-Pessler, J., Uhl, A.: Temporal and longitudinal variances in wood log cross-section image analysis. In: IEEE International Conference on Image Processing (ICIP'14). Paris, FR (2014)
15. Schraml, R., Hofbauer, H., Petutschnigg, A., Uhl, A.: Tree log identification based on digital cross-section images of log ends using fingerprint and iris recognition methods. In: Proceedings of the 16th International Conference on Computer Analysis of Images and Patterns (CAIP'15), LNCS, pp. 752–765. Springer (2015)
16. Schraml, R., Petutschnigg, A., Uhl, A.: Validation and reliability of the discriminative power of geometric wood log end features. In: Proceedings of the IEEE International Conference on Image Processing (ICIP'15) (2015)
17. Schraml, R., Uhl, A.: Pith estimation on rough log end images using local fourier spectrum analysis. In: Proceedings of the 14th Conference on Computer Graphics and Imaging (CGIM'13). Innsbruck, AUT (2013)
18. Schraml, R., Uhl, A.: Similarity based cross-section segmentation in rough log end images. In: Iliadis, L., et al. (eds.) Proceedings of the 10th Artificial Intelligence Applications and Innovations Conference (AIAI'14), IFIP AICT, vol. 436, pp. 614–621. Springer, Rhodes, GR (2014)
19. Vandewalle, P., Ssstrunk, S., Vetterli, M.: A frequency domain approach to registration of aliased images with application to super-resolution. EURASIP J. Appl. Signal Process. (special issue on Super-resolution) **2006** (2006). Source Code: http://lcav.epfl.ch/software/superresolution

Alexander Petutschnigg is a full professor and head of department for Forest Products Technology at the University of Applied Sciences Salzburg. His research interests are in supply chain optimization, product- and process development, wood and biogenic resources.

Rudolf Schraml is a PhD student at the University of Salzburg. His research interests are in wood image processing focusing on biometric tracking of wood logs using digital log end images.

Andreas Uhl is a full professor at the Computer Sciences Department at the University of Salzburg, Austria, where he leads the Multimedia Signal Processing and Security Lab. His research interests are in image and video processing, biometrics, visual data encryption, medical image analysis, and high-performance computing.

Heinz Hofbauer holds a doctoral degree in computer science. He works as a researcher at the University of Salzburg and has published extensively in the fields of content and media security and biometrics.

Towards Drug Counterfeit Detection Using Package Paperboard Classification

Christof Kauba, Luca Debiasi, Rudolf Schraml, Andreas Uhl

Department of Computer Sciences,
University of Salzburg,
Jakob Haringer Str. 2, 5020 Salzburg, Austria
{ckauba,ldebiasi,rschraml,uhl}@cosy.sbg.ac.at

Abstract. Most approaches for product counterfeit detection are based on identification using some unique marks or properties implemented into each single product or its package. In this paper we investigate a classification approach involving existing packaging only in order to avoid higher production costs involved with marking each individual product. To detect counterfeit packages, images of the package's interior showing the plain structure of the paperboard are captured. Using various texture features and SVM classification we are able to distinguish drug packages coming from different manufacturers and also forged packages with high accuracy while a distinction between single packages of the same manufacturer is not possible.

Keywords: Drug Counterfeit Detection, Paper Structure Classification, Texture Classification

1 Introduction

Counterfeit products are a serious world wide issue affecting all industries. A recent OECD study [13] reports that in 2013 about 2.5% of the world wide traded products were faked ones. For the European Union (EU) a remarkably higher value of 5% for faked and imported products is reported.

In case of medical products counterfeit medicines and drugs lead to an economic loss and are all the worse a threat for the health of the consumers and patients. The International Medical Products Taskforce (IMPACT) of the World Health Organization (WHO) estimated a share of 1% of faked products in the developed countries and 10 to 30% in many developing countries [16]. Consequently, medical product authentication is becoming increasingly important. On European level the Falsified Medicines Directive (FMD) 2011/62/EU should be implemented until 2018. The overall aim is to improve patient safety stipulating an efficient anti-counterfighting system. Unique identifiers (2D barcodes) will be used to track and authenticate each medical package along the supply chain. A central repository system is required to enable authentication of each package. Such a system will not be available in developing countries. Furthermore, it suffers costs and is exposed to getting compromised by the forgers.

Another approach to verify the originality of a product is to use intrinsic features visible on the packaging or the product itself. For this work we focus on authentication of a medical product using intrinsic features from the packaging surface. Literature in this field relates to package fingerprinting based on the theory of physically uncloneable functions (PUFs). Paper PUFs use the fiber structure of paper as physical/intrinsic characteristic. The approaches presented in [10,1,3] show that the micro-structure in a certain region of a paper or package material is discriminative enough to identify it. Detailed investigations on paper identification, using a public available microstructure dataset [18], are presented in [5,4]. In [5] the authors explore the applicability of two approaches to overcome geometric distortions. The same approaches and a hybrid one are used to investigate package identification using mobile phones in [4]. Furthermore, in [6] a new feature descriptor for micro-structure identification using mobile phones is introduced. By comparing the performances for different PUFs the results in [20] indicate that the approach by [3] outperforms the approaches by [18,5,4] but it requires a commodity scanner. Thus, in [19] the authors showed that mobile devices and the camera built-in flash lights can also be used to capture images as required for [3].

As shown, research exclusively deals with identification of paper or packages. To the best of our knowledge no works which consider paper or package classification have been presented so far. Like in the work of [17] we assume that the fibre structure pattern of the packaging material is suited for classification, i.e. for a certain medical product the packaging fibre structure shows constant features. If so, one step for checking the authenticity of a medical product could be to assess if the packaging material is the same as used for the original product. To answer this question, we perform a preliminary study for nine different medical products from three different manufacturers and some forged packages for one medical product. The results of this work enable to draw conclusions which are a first step towards medical product authentication using the packaging material.

Section 2 introduces the basic concept of paper classification. The experimental setup and the data set acquisition are described in Section 3. Our experimental results together with a discussion of these results can be found in Section 4. Section 5 concludes this paper.

2 Paper Texture Classification

This section describes our proposed approach using paper texture classification for package counterfeit detection. The general procedure is the following: At first an image of the interior of the package is taken and several patches are extracted from random positions in the image. These patches are then preprocessed. Afterwards different features are extracted from the preprocessed patches. Based on these features a classifier returns a decision predicting the class a questioned image is belonging to (by utilizing a pre-trained SVM). The steps are explained in the following.

2.1 Image Acquisition

Several images of the package's interior are captured at different positions. For the image acquisition a Canon 70D (100mm lens and flash light), mounted on a tripod, was utilized. The flashlight was placed besides the package. The camera is set to the smallest possible distance from the package (about 30 cm) trying to capture as most as possible of the paper's fibre-structure. An image of the acquisition setup can be seen in figure 1 together with an acquired image from the interior of a sample package.

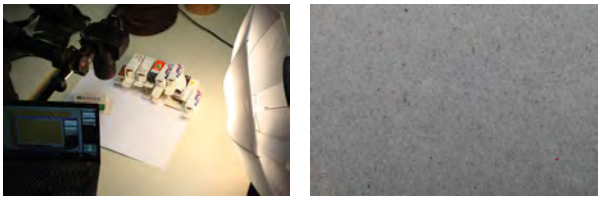

Fig. 1: Set-up for image acquisition of the fiber structure on the inside of a drug package (left) and acquired image sample (right).

2.2 Preprocessing

During preprocessing of the images a contrast limited adaptive histogram equalization (CLAHE) [21] is applied in order to improve contrast and enhance the paper structure. After this contrast enhancement all images are converted to grayscale and several patches are extracted from random positions in the images to reduce the computational effort and increase the amount of data that can be extracted from each package. Figure 2 shows the paper structure of different packages extracted from the random patches after preprocessing.

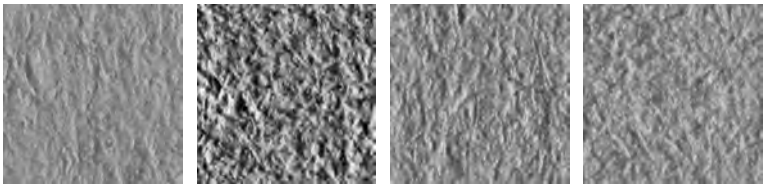

Fig. 2: Example preprocessed image patches

2.3 Feature Extraction Techniques

All techniques tested in this work are usually used for texture classification, image tampering detection and printer/paper identification and are applied on

the preprocessed images taken from the inside of the package. The techniques utilized in this work are briefly described in the following list, further information on the single techniques can be found in the corresponding papers.

- Histogram
  Gray-level histogram of all pixels as the extracted feature.
- LBP: Local Binary Patterns
  The local binary patterns (LBP) by Ojala *et al.* [14] observe the variations of pixels in a local neighbourhood and are represented in a histogram.
- DMD: Dense Micro-block Difference
  Texture classification approach by Metha *et al.* [9] which captures the local structure from the image patches at high scales, but instead of the pixels small blocks which capture the micro-structure of the image are processed.
- RI-LPQ: Rotation-Invariant Local Phase Quantization
  The rotation-invariant local phase quantization (RI-LPQ) by Ojansivu *et al.* [15] consists of two stages: Estimation of the local characteristic orientation for a given image patch and directed descriptor extraction.
- Dense SIFT: Dense Scale Invariant Feature Transform
  Lowe [8] proposed a technique used in object recognition which is commonly known as scale invariant feature transform (SIFT). This technique is invariant to image scale and rotation and robust against various affine distortions, addition of noise, illumination changes and changes of the viewpoint.
- GLCM: Gray-level Co-occurence Matrix
  Mikkilineni *et al.* proposed to use gray-level co-occurence features for printer identification in [11]. The features model the spatial relationships among the pixels of an image to represent its texture information.
- WP: Weber Pattern
  In [12] Muhammad proposed a multi-scale local texture descriptor which was applied as part of an image forgery framework.
- BSIF: Binarized Statistical Image Features
  The Binarized Statistical Image Features (BSIF) proposed by Kannala *et al.* in [7] rely on pre-computed local image descriptors which efficiently encode texture information.
- LSB+JD: Least Significant Bitplane + Jaccard Distance
  Extraction of the images least significant bitplane (LSB-plane) and calculate the Jaccard distance between the LSB-planes of two images.

2.4 Classification Approach

The features extracted with the techniques described in the previous section are used to classify the images of the various kinds of drug packages.

The classifier is designed according to the improved Fisher vector (IFV) SVM classifier in [2]. The features are soft-quantized using a Gaussian mixture model (GMM), decorrelated and dimensionality reduced by PCA to obtain a Fisher vector (FV) encoding. A pre-trained linear SVM is then used to classify the IFV encoded features. The SVM is trained using a subset of the package's images which is subsequently not used for the testing (evaluation) step.

3 Experimental Settings

The following section describes the dataset used in this work, which contains images showing the paper structure of different forged and original drug packages. Furthermore a description of the two different dataset splits and our evaluation methodology to avoid overlapping between training and testing data is given.

3.1 Dataset

Table 1: Number of genuine (G) and forged (F) packages in the data set with drug name, corresponding ID and manufacturer (MF).

ID	Name	# G	# F	MF
1	Levitra	3	4	A
2	Kijimea Reizdarm	2	0	B
3	Kijimea Immun	1	0	B
4	Kijimea Derma	2	0	B
5	Narumed	3	0	B
6	Deseo	4	0	B
7	Signasol	2	0	B
8	Neradin	4	2	B
9	Unistop	2	0	C

Unfortunately, only a limited number of drug packages was available for our work. In particular we have packages of 9 different kinds of drugs from 3 different manufacturers denoted by A, B and C.

For all 9 kinds of drugs we have genuine packages and for 2 of them we also have forged packages. The forged packages for the *Levitra* drug (ID 1) are real counterfeits confiscated by customs, while the forged packages for the *Neradin* drug (ID 8) have been purpose-made by the manufacturer of the drug.

Table 1 lists the number of genuine and forged packages for each kind of drug (ID 1...9). We acquired 10 to 20 slightly shifted and overlapping images from each of the packages' interiors from which 5 patches of 512×512 pixels are extracted at random position within each image. The extracted patches correspond to a section of approximately $4.1 \times 4.1mm$, or $16.81mm^2$, of the package. From this data we generated two distinct data sets to analyze two different issues using the paper structure of the packages:

1. Is it possible to distinguish different packages of the same manufacturer?
2. Is it possible to distinguish packages of different manufacturers?

The first data set, *SMDP* (Same Manufacturer Different Packages), contains images from packages of the same manufacturer, which correspond to the manufacturer B in table 1. We only considered packages of this manufacturer since it is the only one from which we had more than one different type of drug package.

The second data set, *FGDM* (Forged and Genuine Different Manufacturers), contains images from all the packages, genuine and forged, from all manufacturers in table 1.

3.2 Evaluation Methodology

To investigate the two questions of section 3.1, we split the evaluation according to the two data sets SMDP and FGDM.

For the SMDP data set, where we want to find out if it is possible to distinguish between different types of drug packages from the same manufacturer, images having the same drug ID are defined as corresponding to the same class. A class thus can contain images from different packages of the same drug. Forged and genuine packages are furthermore split into different classes. This yields 8 different classes, because we have 7 different types of drug packages for manufacturer B and for one drug we also have 2 packages, which have been forged by the manufacturer.

To find out if it is possible to distinguish packages of different manufacturers (FGDM data set), images having the same manufacturer ID are defined as corresponding to the same class. Forged and genuine packages are again split into different classes for the *Levitra* drug produced by manufacturer A, but not for the *Neradin* drug of manufactuer B because these forgeries have been produced by the manufacturer and use the same material as the genuine packages. The different classes for the SMDP and FGDM data set are summarized in table 2.

Table 2: Evaluation classes and corresponding IDs with number of packages

Name	# Packages	SMDP Class ID	FGDM Class ID
Levitra forged	4	-	1
Levitra genuine	3	-	2
Kijimea Reizdarm genuine	2	1	3
Kijimea Immun genuine	1	2	3
Kijimea Derma genuine	2	3	3
Narumed genuine	3	4	3
Deseo genuine	4	5	3
Signasol genuine	2	6	3
Neradin forged	2	7	3
Neradin genuine	4	8	3
Unistop genuine	2	-	4

The acquired images of the drug packages are slightly overlapping, this might lead to patches of the same image belonging to both, the training and the testing subset. Hence we used leave one package out (LOPO) for the selection of the training and testing images/patches: Training is done with randomly selected patches from all images except the images from one specific package. The patches for the testing subset are then randomly selected only out of images from this package. If there is only a single package in a class, like for the class with ID 2 in the case of the SMDP data set, the patches for this class are only used to train the classifier. Thus, no intra-class comparisons for this class exist and the average precision is not calculated and shown as 0 in the plots. By using the LOPO approach for the evaluation, the slight overlap of images from the same package does not introduce any bias to the results.

4 Experimental Results

This section presents the results of the conducted experiments and the conclusions made from those. We analysed the two cases, at first the separation according to manufacturer (FGDM) and second the separation of packages all from the same manufacturer (SMDP).

Table 3: Mean accuracies (mAcc) and mean average precisions (mAP)

Data set	FGDM		SMDP	
Method	mAcc	mAP	mAcc	mAP
BSIF	0.428	0.403	0.138	0.171
DMD	0.97	1	0.328	0.423
DenseSIFT	0.91	1	0.37	0.476
GLCM	0.953	0.964	0.14	0.18
Histogram	0.603	0.662	0.145	0.176
LBP	0.758	0.863	0.265	0.272
LSB	0.71	0.818	0.113	0.182
RI-LPQ	0.842	0.888	0.158	0.226
WP	0.861	0.896	0.158	0.197

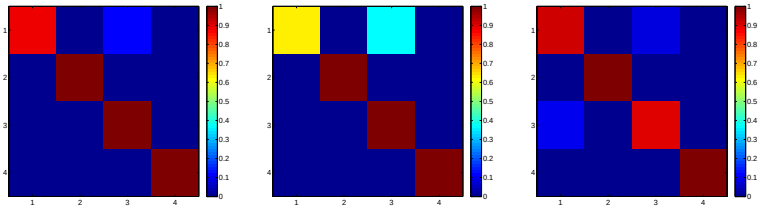

Fig. 3: Confusion matrix for DMD, DenseSIFT and GLCM in the FGDM case

Table 3 lists the mean accuracies (mAcc) and mean average precisions (mAP) for both cases. The mean accuracy corresponds to the mean of the values of the confusion matrix diagonal. It can be seen that for FGDM the results for DenseSIFT and DMD are close to 100% meaning that almost a perfect classification of the paper and thus the manufacturer is possible. Consequently, the true forgeries (corresponding to class 1) can be seperated from the other classes well.

Some example confusion matrices using a heat map for selected feature types (DMD, DenseSIFT and GLCM) can be seen in figure 3 and figure 5 for the FGDM and SMDP case, respectively. The numbers on the axes denote the classes according to table 2, which shows the correspondence of the class labels to the drug packages. Figures 4 and 6 show the corresponding average precision plots for FGDM and SMDP, respectively. These confirm that the recognition works well if the split is done according to different manufacturers and does not work if the split is done according to different drugs all from the same manufacturer.

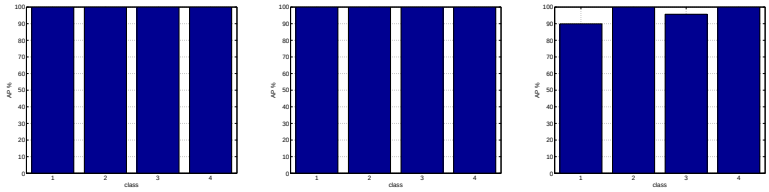

Fig. 4: Average precision for DMD, DenseSIFT and GLCM in the FGDM case

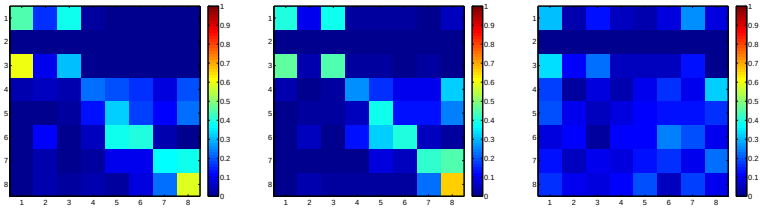

Fig. 5: Confusion matrix for DMD, DenseSIFT and GLCM in the SMDP case

We do not have any information about which kind of paper is used for the different drug packages. But the experimental results suggest (distinction between different types of drugs from the same manufacturer was not possible) that one manufacturer uses the same kind of paper and the same printing facility/printing process for his drug packages. As long as the forgers do not have access to the same kind of printing facility the genuine manufacturers utilizes, drug counterfeit detection is feasible using our proposed approach.

5 Conclusion

In this paper we investigated whether counterfeit drug package detection using texture classification based on the intrinsic paper texture is possible. The available data was split to investigate two different issues.

In the SMDP case (same manufacturer) a distinction between single packages of the same manufacturer was not possible. We concluded that this is not

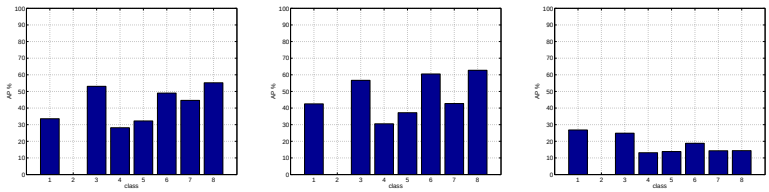

Fig. 6: Average precision for DMD, DenseSIFT and GLCM in the SMDP case

possible because all packages have very likely been produced using the same manufacturing process and therefore share a very similar paper structure.

In the FGDM case (different manufacturers) it was indeed possible to classify different genuine and forged packages with high accuracy. This indicates that it is possible to identify counterfeit packages not produced by the original manufacturer, since they are most likely being produced in a different manufacturing facility and hence do not share a similar paper structure. The class containing the forged packages and the classes containing genuine packages could all be clearly separated in this case.

This promising results however have to be taken with a grain of salt because of the small data set size and the availability of only a few real counterfeit packages. Hence the first step of our future work is the acquisition of more test data, i.e. a higher number of distinct types of drug packages and even more important more counterfeit and genuine packages of the same type of drug. In addition we want to acquire further information about the printing and manufacturing process of the packages.

Acknowledgments. This work is supported by the Munich based software venture eMundo which receives funding from the Central Innovation Program for SMEs by Germany's Federal Ministry of Economics and Technology (project "FakeFinder" no. ZIM-EP150145).

References

1. J. Buchanon, R. Cowburn, A.-V. Jausovec, S. Petit, D., G. P., Xiong, D. Atkinson, K. Fenton, D. Allwood, and T. Bryan. Forgery: Fingerprinting documents and packaging. *Nature*, 436:475, 2005.
2. M. Cimpoi, S. Maji, I. Kokkinos, S. Mohamed, and A. Vedaldi. Describing textures in the wild. In *Proceedings of the IEEE Conf. on Computer Vision and Pattern Recognition (CVPR)*, 2014.
3. W. Clarkson, T. Weyrich, A. Finkelstein, N. Heninger, J. Halderman, and E. Felten. Fingerprinting blank paper using commodity scanners. In *Proceedings of the 30th IEEE Symposium on Security and Privacy*, pages 301–314, 2009.
4. M. Diephuis, F. Beekhof, S. Voloshynovskiy, T. Holotyak, N. Standardo, and B. Keel. A framework for fast and secure packaging identification on mobile phones. In *Proceedings of SPIE Photonics West, Electronic Imaging, Media Forensics and Security V*, San Francisco, USA, January, 23 2014.
5. M. Diephuis, S. Voloshynovskiy, and F. Beekhof. Physical object identification based on famos microstructure fingerprinting: comparison of templates versus invariant features. In *8th International Symposium on Image and Signal Processing and Analysis*, Trieste, Italy, September, 4-6 2013.
6. M. Diephuis, S. Voloshynovskiy, and T. Holotyak. Sketchprint: Physical object micro-structure identification using mobile phones. In *European Signal Processing Conference (EUSIPCO)*, Nice, France, 31 August - 4 September 2015.
7. J. Kannala and E. Rahtu. BSIF: binarized statistical image features. In *Proceedings of the 21st International Conference on Pattern Recognition, ICPR 2012, Tsukuba, Japan, November 11-15, 2012*, pages 1363–1366, 2012.

8. D. G. Lowe. Distinctive image features from scale-invariant keypoints. *Int. J. Comput. Vision*, 60(2):91–110, Nov. 2004.
9. R. Mehta and K. Egiazarian. *Texture Classification Using Dense Micro-block Difference (DMD)*, pages 643–658. Lecture Notes in Computer Science. Springer-Verlag, Berlin, 2015.
10. E. Metois, P. Yarin, N. Salzman, and J. Smith. Fiberfingerprint identification. In *Proceedings of the 3rd Workshop on Automatic Identification*, New York City, USA, 2002.
11. A. K. Mikkilineni, P.-J. Chiang, G. N. Ali, G. T. C. Chiu, J. P. Allebach, and E. J. Delp III. Printer identification based on graylevel co-occurrence features for security and forensic applications. volume 5681, pages 430–440, 2005.
12. G. Muhammad. Multi-scale local texture descriptor for image forgery detection. In *Industrial Technology (ICIT), 2013 IEEE International Conference on*, pages 1146–1151, 2013.
13. OECD and EUIPO. Trade in counterfeit and pirated goods. *OECD Publishing*, page 138, 2016.
14. T. Ojala, M. Pietikainen, and D. Harwood. Performance evaluation of texture measures with classification based on kullback discrimination of distributions. In *Proceedings of the 12th IAPR International Conference on Pattern Recognition*, volume 1, pages 582 –585 vol.1, Oct. 1994.
15. V. Ojansivu, E. Rahtu, and J. Heikkila. Rotation invariant local phase quantization for blur insensitive texture analysis. In *Pattern Recognition, 2008. ICPR 2008. 19th International Conference on*, pages 1–4, Dec 2008.
16. W. H. Organization. International medical products taskforce - brochure. `http://apps.who.int/impact/FinalBrochureWHA2008a.pdf?ua=1`[last accessed: 29.04.16].
17. M. Varma and A. Zisserman. A statistical approach to material classification using image patch exemplars. *IEEE Transactions on Pattern Analysis and Machine Intelligence*, 31(11):2032–2047, Nov 2009.
18. S. Voloshynovskiy, M. Diephuis, F. Beekhof, O. Koval, and B. Keel. Towards reproducible results in authentication based on physical non-cloneable functions: The forensic authentication microstructure optical set (famos). In *Proceedings of IEEE International Workshop on Information Forensics and Security*, Tenerife, Spain, December 2–5 2012.
19. C. W. Wong and M. Wu. Counterfeit detection using paper puf and mobile cameras. In *Information Forensics and Security (WIFS), 2015 IEEE International Workshop on*, pages 1–6, Nov 2015.
20. C. W. Wong and M. Wu. A study on puf characteristics for counterfeit detection. In *Image Processing (ICIP), 2015 IEEE International Conference on*, pages 1643–1647, Sept 2015.
21. K. Zuiderveld. Graphics gems iv. chapter Contrast Limited Adaptive Histogram Equalization, pages 474–485. Academic Press Professional, Inc., San Diego, CA, USA, 1994.

On the feasibility of classification-based product package authentication

Rudolf Schraml, Luca Debiasi, Cristof Kauba, Andreas Uhl
University of Salzburg, Department of Computer Sciences, 5020 Salzburg
{rschraml, ldebiasi, ckauba, uhl}@cosy.sbg.ac.at

***Abstract*—Depending on the product category the authenticity of a consumer good concerns economic, social and/or environmental issues. Counterfeited drugs are a threat to patient safety and cause significant economic losses. Different from physical-marking based approaches this work investigates authentication of drugs based on intrinsic texture features of the packaging material. Therefore, it is assumed that the packaging material of a certain drug shows constant but discriminative textural features which enable authentication, i.e. to prove if the packaging material is genuine or not. This objective requires considering a binary classification problem with an open set of negative classes, i.e. unknown and unseen counterfeits. In order to investigate the feasibility a novel drug packaging texture databases was acquired. The experimental evaluation of two basic requirements in texture classification serves as an evidence on the basic feasibility.**

I. Introduction

Counterfeiting is an economic issue affecting all industries. The OECD [1] reports that in 2013 2.5% of the worldwide traded products were counterfeited ones. For the European Union (EU) a remarkably higher value of 5% for counterfeited and imported products is reported. In case of medicals, counterfeits cause an economic loss and are moreover a potential threat to the consumer and patient health. On the European level, the Falsified Medicines Directive (FMD) 2011/62/EU should be implemented until 2018. The overall aim is to improve patient safety stipulating an efficient anti-counterfeiting system. The actual solution is based on product serialization, i.e. each package is assigned a unique identifier (e.g. 2D barcode) which enables to track and identify each medical package along the supply chain. Hence a central database is required to enable authentication of each package. Such a system will not be available in developing countries. Furthermore, it suffers costs and is exposed to getting compromised by forgers. For example, packages will have to be equipped with safety features in order to avoid tampering. Summarizing, serialization-based product authentication requires to adapt the production, shows significant risks & costs and cannot be implemented in a set of countries.

For this reason, we move from serialization to classification. This means that a product is authenticated based on constant but discriminative intrinsic features of the product or packaging material. Therefore, we target at pill drugs which are packaged in blisters and housed in a cardboard packaging. In [2] we showed that 9 different drugs from 3 manufacturers and some forged ones can be classified based on their cardboard packaging material, in a closed-set multi-class scenario. Results were promising and showed a classification accuracy of 100% for all 8 drugs. However, the testset is fairly small and drug package material authentication is a simplistic two-class (binary classification) problem, i.e. a drug is classified as being genuine or not. Contrasting to the setup in [2], package authentication has to be considered as an open set binary classification problem. In the training stage, the authentication system can capture only a limited subspace of other (known) drugs and forged packagings. It is a basic requirement that the authentication system is able to reject unseen counterfeited packages not known or available at the time of training. For a drug packaging authentication system this requires that a specific drug is distinguished from other known and unknown forgeries and drugs which is referred to as open set recognition. The general open set recognition problem has recently been addressed in the works of [3], [4], [5] which are outlined in Section II. Furthermore, in [6], [7], [8] the authors investigate the performances of the invented open set classification approaches in different applications.

In this work, we investigate the feasibility of a classification-based drug authentication system based on images of the cardboard packaging and top & bottom blister surface textures. Within this work the cardboard packaging texture and the blister top & bottom textures are referred to as modalities. A substantial drug packaging texture database, consisting of images from 45 drugs (multiple instances, i.e. multiple packages in the range of 1 and 15 per drug are acquired). Due to security concerns, strategic purposes and legal issues (toll, pharma industry) no forged packages were available.

So far, packaging or paper authentication refers to identification or serialization of each instance. These are based on the concept of physically unclonable functions (PUFs) which rely on the mapping between a challenge and response function depending on the physical nature of the object. PUFs are unclonable and unpredictable and thus ideally suited to implement identification-based anti-counterfeiting approaches. These either rely on extrinsic or intrinsic PUFs, i.e. which are attached to the product or can be derived from a part of the product itself. The encrypted PUF signature can be attached to the product enabling off-line authentication. [9], [10], [11] showed that the microstructure in a certain region of a paper or package material is discriminative enough to identify it (Paper PUFs). Detailed investigations on paper identification, using a publicly available microstructure dataset [12], are presented

WIFS'2017, December, 4-7, 2017, Rennes, France. 978-1-5090-6769-5/17/$31.00

in [13], [14]. In [13] publicly availablethe authors explore the applicability of two approaches to overcome geometric distortions. The same approaches and a hybrid one are used to investigate package identification using mobile phones in [14]. Furthermore, in [15] a new feature descriptor for microstructure identification using mobile phones is introduced. By comparing the performances for different PUFs the results in [16] indicate that the approach by [11] outperforms the approaches by [12], [13], [14] but it requires a commodity scanner. Thus, in [17] the authors showed that mobile devices and the camera built-in flashlights can also be used to capture images as required for [11].

As identified in previous literature the fibre structure of paper or packaging material is positional highly unique and enables to identify single instances. The move from identification to classification, as done in this work, raises two fundamental research questions:

Positional invariance: Paper PUFs rely on the local uniqueness of the paper fibre texture. Thus, for the paper or cardboard packaging fibre structure it is not clear if (i) the fibre structure shows constant features across different regions and (ii) if those features are discriminative enough to distinguish between different types of paper or cardboard packaging.

Instance generalisation: The second question is a specialisation of the first for which the positional invariance is considered across different instances (i.e. packages) of a modality. Instance generalisation is a pre-requirement for a real-world application. For paper and packaging material it is not clear how the texture and the computed features vary between different instances, i.e. if a classifier which is trained with features from one instance is able to authenticate unseen features from another package instance and to distinguish them from other types of paper or cardboard packaging.

In this work, positional invariance and instance generalisation of the corresponding textural features are investigated for all three modalities. By considering these pre-requirements for classification-based drug packaging authentication, this work enables to draw fundamental conclusions. Based on the new insights the feasibility of a novel serialization-less anti-counterfeiting approach can be considered.

Section II introduces into open set drug package authentication: (i) Section II-A describes a possible scheme for an package authentication system and (ii) in Section II-B the open set recognition problem is considered in more detail. Section III introduces the acquired database. The classification pipeline is outlined in Section IV. Experiments and results are presented in Section V and Section VI concludes this paper.

II. Open-set drug package authentication

A. Drug package authentication system

For a given drug sample a mobile application guides the user to open/disassemble the drug packaging and to capture images of three different packaging modalities: The cardboard packaging texture I_{CB} as well as the textures visible on the top and bottom blister sides (I_{BT}, I_{BB}). Furthermore, the user is guided to capture the product code I_{PC} (e.g. EAN which is the European article number). All four images compose the authentication vector $\hat{AV} = (I_{CB}, I_{BT}, I_{BB}, I_{PC})$. I_{PC} is processed in order to determine the product code specifying the target product. I_{CB}, I_{BT}, I_{BB} are preprocessed (segmentation, image enhancement). For the resulting texture images T_{CB}, T_{BT}, T_{BB} a set of feature vectors $FV_{CB} = \{\hat{cb}_1, ..., \hat{cb}_i\}$, $FV_{BT} = \{\hat{bt}_1, ..., \hat{bt}_j\}$ and $FV_{BB} = \{\hat{bb}_1, ..., \hat{bb}_k\}$ are computed, where the number of feature vectors per modality i, j, k depends on the size of the preprocessed images and on the utilized feature extraction strategy. Based on the product code, the authentication system selects the corresponding precomputed classification models M_{CB}, M_{BT}, M_{BB} from a model repository. If the required models are not available on the device they could be requested from a remote repository. For each model M and a given feature vector $\hat{v}$ the prediction function $pF(M, v) = 1$ in case the vector is labelled as being genuine and -1 if not. For each model M_{CB}, M_{BT}, M_{BB} and the corresponding feature vector sets $FV_{CB}, FV_{BT}, FV_{BB}$ the prediction function is applied to all feature vectors which leads to the predictions for each modality of the packaging instance $P_{CB} = \{p_1, ..., p_i\}$, $P_{BT} = \{p_1, ..., p_j\}$ and $P_{BB} = \{p_1, ..., p_k\}$. Finally, a decision function $f(P_{CB}, P_{BT}, P_{BB}) = (v, p)$ needs to be defined, where $v \in \{1, -1\}$ gives the final authenticity vote of the authentication system and $p \in [0, 1]$ specifies a probability score for the final vote which are then presented to the user.

Such an authentication system relies on the assumption that different modalities of the packaging material of all instances from the same product show constant but discriminative features which enable to detect and distinguish the product from a known and unknown set (=open set) of other as well as from counterfeited products. For training of a classifier, only a limited subset of other drugs and available counterfeits is utilized. As a precondition for authentication, the classifier must be able to reject unseen data. This is a typical binary classification problem, either a given sample is labelled as genuine or not. The undefined set of unknown other classes leads to an open set recognition problem. This differs from closed-set classification where only known classes are separated from each other. Substantial efforts in the field of open set recognition were made in [3], [4], [5]. In [3] the authors introduce and formalize the open set recognition problem. Furthermore, in [3], [4], [5] the authors propose different SVM extensions which specifically address the open set recognition problem. In order to investigate the two research questions and as a consequence to prove the principal feasibility of an authentication system we base our experiments on the formalization of the open set recognition problem provided in [3], [4].

B. Formalization of the open set recognition problem

In [3] the authors define the *Open Space Risk* as $R_O(f) = \frac{\int_O f(x)dx}{\int_{S_O} f(x)dx}$. S_O needs to be considered as a large ball which is a subspace of the open space including all training samples. O is the open space. $f(x)$ is a recognition function where $f(x) = 1$ if x is recognized as the class of interest y and $f(x) = 0$ if

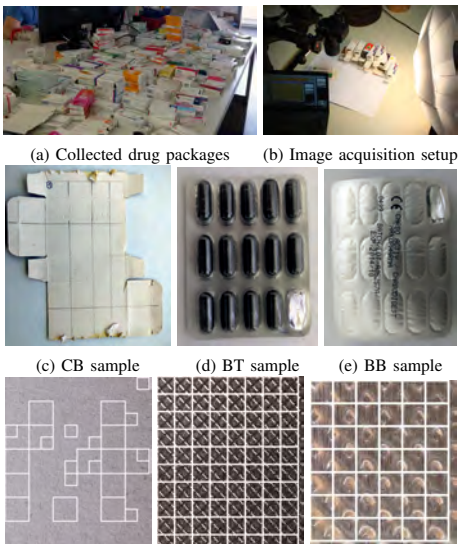

(a) Collected drug packages (b) Image acquisition setup

(c) CB sample (d) BT sample (e) BB sample

(f) CB image (g) BT image (h) BB image

Fig. 1: Image Acquisition Overview: 3rd Row: exemplary images showing the selected 128×128 and 256×256 image patches.

not. Consequently, the open set risk R_O is the fraction of the positively labelled open space in S_O compared to the positive labelled samples in O. The goal in open set recognition is to minimize the open space risk R_O whilst balancing it against the empirical (known) risk R_E computed over the available training data. Therefore, $\hat{P} = \{p_1, ..., p_n\}$ are samples from the positive training class P and $\hat{N} = \{n_1, ..., n_m\}$ are samples from a set of other known classes N. $\hat{N}$ is defined as the negative training data. U is the larger universe of negative unknown classes only utilized for evaluation and $E = \{e_1, ..., e_z\}, e_i \in P \cup N \cup U$ specifies all evaluation data. For a given training data $\hat{P} \cup \hat{N}$ and the open space and empirical risk functions R_O, R_E the open set recognition problem is to find a function f, where $f(x) > 0$ for positive recognitions, which minimizes the open set risk:

$$\underset{f}{arg\,min}\{R_O(f) + \lambda_r R_E(f(\hat{P} \cup \hat{N}))\} \quad (1)$$

where λ_r is a regularization constant.

Hence, open set recognition is a minimization problem which combines the open set and the empirical risk over the space of allowable recognition functions. Further, the empirical risk (i.e. the training error) can be optimized using predefined constraints. The stated minimization problem requires a set of known classes which are utilized for training and a set of known unknown classes in U which are only used for evaluation.

III. Drug Packagings Texture Database (DPT-DB)

For image acquisition, a large variety of drug packages were collected from different pharmacies (1st row in Fig. 1). From each drug package (=instance) the CB fibre texture on the inner raw side of the packaging, the BT texture (blister top side) and the BB texture (blister bottom side) were captured. For image acquisition a Canon 70D (100mm lens and flashlight), mounted on a tripod, was utilized (see Fig. 1b). From each CB,BT&BB instance images from different and non-overlapping sections were captured (e.g. Fig. 1c)). In total images for 45 drugs from 28 different producers were taken. For each drug between 1 and 15 package instances are available. All captured images were manually cropped ensuring that just texture remains.

IV. Classification Pipeline

Two different classification scenarios are considered: (i) CLASS to investigate the positional invariance of the CB,BT&BB texture. (ii) PACKAGE to prove instance invariance which is a step towards a real-world setup. In order to train and evaluate SVM-based classifiers data needs to be sampled and then partitioned into training (T) and evaluation (E) data. The amount of data (k) to be sampled is predefined for both scenarios. In this work, data relates to image texture patches of CB,BT&BB. For patch sampling, each CB,BT&BB image is subdivided into a grid which is specified by the size of the feature descriptor (e.g. 128×128 or 256×256 pixels). The 3rd row in Fig. 1 depicts sample images for CB,BT&BB for which the image patch grids are shown.

In case of CLASS k patches are sampled from all instances of each drug and modality. Contrary, for PACKAGE k patches are selected from each instance of each drug and modality. This is important in that for cross-validation the partitioning into T and E differs in principle as illustrated in Fig. 2. For CLASS the k patches of a drug and modality are partitioned so that different patches of each instance are included in T & E. On the other hand for PACKAGE the patches are partitioned instance-wise into T and E.

A. Feature vector computation

For each selected patch in CLASS or PACKAGE a set of discriminative features is computed. Prior to feature extraction Contrast Limited Adaptive Histogram Equalization (CLAHE) [18] is applied to each patch (parameters: block radius=50, bins=256, slope=40). Exemplary CLAHE enhanced patches are shown in the 1st and 2nd row of Fig. 3.

a) Feature Extraction: For the experiments feature extraction approaches producing low dimensional feature-vectors are utilized, mainly due to the fact that high dimensional features and feature encoding cause computational and memory issues when computing all classification configurations (CCs) for different SVMs, i.e. RAM & I/O limitations. We already did small-scale experiments on a subset of the CCs with SIFT,

Fig. 2: Training (T) and evaluation (E) data sampling and partitioning strategies applied for CLASS and PACKAGE

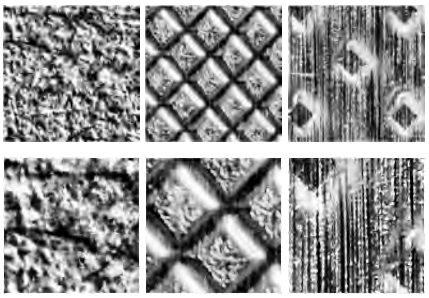

Fig. 3: Preprocessed patches of the CB,BT&BB images in Fig.1 - 1st Row: 256×256 pixels, 2nd Row: 128×128 pixels

SURF & feature encoding and the results indicate that the classification performance even increases.

The following features are utilized: Local Binary Pattern (LBP) [19], Local Ternary Pattern (LTP) [20], LiLBP (LiLBP) [21], Histogram of Gradients (HOG) [22], Dual Tree Complex Wavelet Transform (DTCWT) [23], Multifractal Spectrum (MFS) [24], Edge Co-Occurence Matrix (ECM) [25].

For each selected patch of CLASS & PACKAGE a feature vector for each listed feature extraction approach is computed.

B. Classification Approaches

For classification LIBSVM [26] and the open set extensions provided by [27] are utilized. From LIBSVM we use the ONE-CLASS and the C-SVC SVM (BINARY C-SVC)for one-class and binary classification, respectively. Additionally, as an approach specifically addressing open set recognition, the WSVM [4] is applied for binary classification. As the ONE-CLASS SVM uses a radial basis function (RBF) kernel, the same is chosen for BINARY C-SVC and WSVM.

In the experiments, the classification approaches are utilized to investigate a large set of different CCs. $D = \{d_1, ...d_{45}\}$ is the set of drugs and $DM = \{dm_1, ..., dm_{28}\}$ is the set of drug manufacturers in the testset where $fdm(d_i) : D \rightarrow DM$ specifies the drug manufacturer for each drug. $M = \{CB, BT, BB\}$ specifies the packaging modalities. $FE = \{fe_1, ..., fe_n\}$ is the set of feature extraction methods and $CS = \{CLASS, PACKAGE\}$ gives the classification scenarios. The feature vector sets for a certain drug $d \in D$ & modality $m \in M$, for the k-patches defined for the cla ssification scenario $cs \in CS$ computed with feature extraction method $fe \in F$, are given by $FV_{(d,m,f,cs)} = \{fv_1, ..., fv_k\}$. Following, a specific CC is defined by the tuple

$$CC = (d \in D, m \in M, fe \in FE, cs \in CS) \quad (2)$$

where d specifies the target drug which should be authenticated. The respective set of feature vector sets for CC is given by $FV_{CC} = \{FV_{(d_1,m,f,cs)}, ..., FV_{(d_{45},m,f,cs)}\}$ which is composed by the CC specific feature vector sets from each drug. The positive training data $P_{CC} = FV_{(d,m,f,cs)}$ is specified by the target drug d in CC. The negative training data $N_{CC} = \{FV_{CC}\} \setminus \{FV_{(d,m,f,cs)}\}$ is composed by all feature vector sets of all other drugs. The positive and negative training data P_{CC}, N_{CC} are then used for nested cross-validation using a specific classification approach.

C. Cross-fold validation

Optimization is crucial as the standard LIBSVM parameters did not succeed in our experiments. Therefore, cross-validation (CV) strategies have been carefully designed and employed in order to optimize the SVM parameters and to strictly avoid that training data is used for evaluation.

Therefore, the negative training data is split into known negatives KN_{CC} and unknown negatives $UN_{CC} = N_{CC}/KN_{CC}$. Therefore, for KN_{CC} the feature vector sets from a fixed number of drugs (e.g. 6) are selected, where the manufacturers are different to the target drug manufacturer of d in CC. Now, a set of positive training data P_{CC}, a set of known negatives KN_{CC} and unknown negatives UN_{CC} is available. Based on P_{CC}, KN_{CC}, UN_{CC} nested CV procedures for CLASS and PACKAGE are defined as illustrated in Fig.4.

For CLASS, we apply a k-fold data split strategy, i.e. P_{CC}, KN_{CC} are class-wise split into k-folds $\{P_1, ..., P_k\}$ and $\{KN_1, ..., KN_k\}$, i.e. all drug classes are distributed equally in the k folds. In the outer loop, we iterate over the k positive and k negative known data folds. Thereby, the ith positive and jth negative was selected for evaluation. The evaluation set is given by $E_{i,j} = P_i \cup KN_j \cup UN_{CC}$ and the training set by $Ti, j = \{P_1, ..., P_k\} \setminus \{P_i\} \cup \{KN_1, ..., KN_k\} \setminus \{KN_j\}$. Thus a large set of known unknown drugs UN_{CC} are used only for evaluation. Note that $|\{KN_1, ..., KN_k\} \setminus \{KN_j\}|$ is reduced to the same size of the positive training data $|P_i|$ in a classwise manner. For each $T_{i,j}$ in the inner CV loop the best hyperparameters are determined in a grid search. Same as in the outer loop, k-fold validation is performed repeatedly in order to test a set of SVM parameters. For the ONE-CLASS SVM just the positive samples in $T_{i,j}$ are split into k-folds and the known negative training samples are only used for validation. As a measure for the performance the F-Measure is utilized which is well suited to balance between specialisation and generalisation in binary classification tasks. For the binary SVM approaches, each prediction is assigned a probability. In the inner loop, the probabilities are used to determine a threshold which maximizes the F-Measure. The SVM parameters delivering the highest F-Measure (and the probability threshold in case of binary SVMs) are selected for

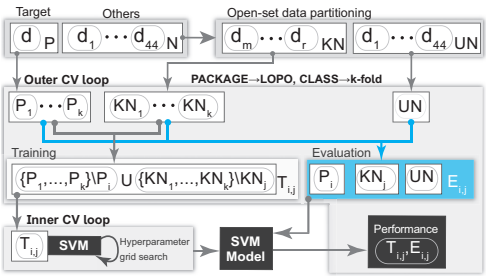

Fig. 4: Cross-validation scheme for CLASS and PACKAGE

	CLASS						PACKAGE					
	128×128			256×256			128×128			256×256		
CC	CB	BT	BB	CB	BT	BB	CB	BT	BB	CB	BT	BB
ONE-CLASS	LTP 0.83 ±7.9	LTP 0.9 ±6.2	LTP 0.92 ±5.8	LTP 0.91 ±4.4	LTP 0.85 ±13.6	LBP 0.87 ±13.5	LBP 0.81 ±8.7	LBP 0.86 ±6.3	LTP 0.84 ±11.3	LTP 0.85 ±9.1	LBP 0.88 ±5.0	LBP 0.85 ±7.1
BINARY	LTP 0.88 ±6.9	$LiLBP$ 0.94 ±3.2	LTP 0.93 ±4.1	LTP 0.91 ±5.2	$LiLBP$ 0.92 ±9.0	LTP 0.93 ±5.0	LTP 0.82 ±9.5	LTP 0.92 ±3.7	LTP 0.87 ±8.9	LTP 0.85 ±5.5	LTP 0.94 ±5.7	$LiLBP$ 0.87 ±10.0
WSVM	LTP 0.86 ±7.6	LTP 0.93 ±4.1	LTP 0.93 ±4.3	$LiLBP$ 0.88 ±6.0	LTP 0.88 ±7.6	MFS 0.88 ±9.1	LTP 0.85 ±8.2	LTP 0.91 ±4.2	$LiLBP$ 0.85 ±9.2	$LiLBP$ 0.83 ±8.5	LTP 0.89 ±8.7	$LiLBP$ 0.84 ±10.1

TABLE I: Classification performances: For each configuration the mean F-Measure (CLASS=45 & PACKAGE=8 target drugs) and the StDev for the best feature are presented. BEST CLASS/ PACKAGE configurations for each modality are layered green.

the outer loop. Finally, the SVM approach is trained with $T_{i,j}$ (for ONE-CLASS only the positive data P_i is utilized) and the selected hyper parameters from the inner CV loop. The trained model is evaluated using the evaluation data $E_{i,j}$ and probability threshold in case of binary SVMs.

For PACKAGE, a nested leave-one-package-out (LOPO) CV procedure is applied. Thereby, P_{CC} is split into k-folds in a package-wise manner, where k is given by the number of packages in P_{CC}, i.e. the number of available packages from the target drug. KN_{CC} is reduced to contain a fixed number of feature vectors from each class which are sampled package-wise. Furthermore, for KN_{CC} the features of each drug are split into two folds KN_1, KN_2 package-wise. Same as for CLASS, in the outer CV loop we iterate over the i positive and the $j = 2$ known negative training folds Ti, j and evaluate it with $E_{i,j}$, as done in the CLASS scenario. For ONE-CLASS in the inner CV loop the same procedure as for the outer loop is applied. However, for binary SVMs the inner CV loop has been adopted to better match the open set recognition problem. Therefore, the known negative training data in Ti, j is split classwise into two folds TKN_1 and TKN_2. One fold simulates known negatives and the other one unknown negatives in the inner loop. While the known negatives are further used for training and validation, the unknown negatives are just used for validation. This strategy adapts the inner CV loop and the parameter grid search to the open set recognition problem and is supposed to minimize the difference between the inner CV validation- and the outer CV evaluation-error.

V. Experiments

A. Experimental setup

All classification approaches (Section IV-B) were utilized to cross-validate all CC combinations (Eq.2) using the CS-specific CV strategies (Section IV-C). For both, PACKAGE and CLASS a patch number k of 500 is set. For CLASS the outer and inner CV loops are iterated twice and the data is split into 2-folds. In case of PACKAGE LOPO is performed for all package instances of drugs with at least 5 instances. For each LOPO CV the positive data is split into 2-folds, in the inner and outer CV loop. For both CSs, 5 drugs are selected for the known negative training data KN_{CC}. In order to enable a fair evaluation, all data splits for CLASS & PACKAGE are stored and reused for different features and classification approaches.

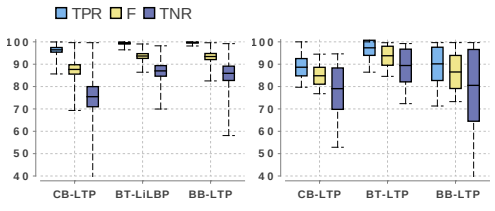

(a) CLASS - 128×128 (b) PACKAGE - 256×256

Fig. 5: CLASS vs. PACKAGE (Binary C-SVC): TPR = $\frac{TP}{TP+FN}$, TNR = $\frac{TN}{TN+FP}$ [Y-Axis: Mean accuracies, min, max and variance in %]

B. Results and discussion

Table I provides an overview of the results for each classification scenario, different patch sizes, modalities and SVMs. For CLASS the averaged results over all 45 drugs are shown. In case of PACKAGE, mean values for drugs with at least 5 instances are shown.

Considering positional invariance, the results for the best (green layered) CLASS configurations show high mean F-Measures over 0.9. This indicates that the textures from all three modalities show constant but highly discriminative features which enable to recognize the same drug class and to distinguish it from other classes. Regarding the question of instance invariance, the F-Measures for the best PACKAGE configurations provide an evidence on the feasibility of a drug package authentication system. The PACKAGE results show that the textural features are constant across different instances for all three modalities. This is a basic requirement for a classification-based authentication system. Although only low-level features have been utilized, the achieved F-Measures are very promising. Most of the best results for both scenarios and the different modalities were achieved with the BINARY C-SVC Y SVM. Fig. 5 provides a more detailed view on the BINARY C-SVC CLASS and PACKAGE results for the best features from each modality. Thereby, it is clearly visible that the performance decreases in case of the more difficult PACKAGE scenario. Furthermore, the comparison between the class accuracy (=true positive rate - TPR) and the others accuracy (=true negative rate - TNR) shows that for all results a higher class accuracy is achieved.

Finally, Fig. 6 shows accuracies and errors for PACKAGE,CB and all SVMs for the best features. For each tested drug (=8) and all SVMs, results show that the error for known data (KN=seen in training) is lower than the error for unknown data (UN=open set). Considering the different

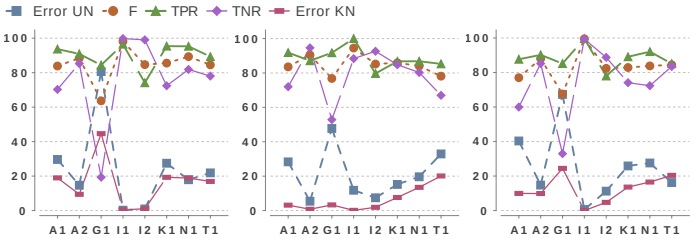

(a) ONE-CLASS (b) BINARY C-SVC (c) WSVM

Fig. 6: PACKAGE (256×256) – SVM performance comparison for CB and all target drugs with more than 5 instances (=8 drugs): Accuracies (TPR,TNR) and recognition errors for the unseen data (Error UN) and seen training data (KN) are shown [X-Axis: Target drug (d) ids: e.g. A1 = manufacturer A+drug number].

SVMs, the accuracies and errors for ONE-CLASS and WSVM vary more compared to the per-drug results of the BINARY C-SVC. Furthermore, the WSVM does not outperform the classical BINARY C-SVC in terms of achieving a lower error for recognizing unknown data (UN).

VI. Conclusion

Results showed that textural features of drug packaging material are constant and highly discriminative. Very important, the experiments indicate that a classifier can be trained with a set of known instances and is able to authenticate unseen instances.

In future work, we will use high-level features, feature encoding and fusion techniques and it is planned to employ deep learning techniques. Furthermore, causes for classification errors need to be investigated in detail, e.g. in case of a high false positive rate it can be that other drugs from the same manufacturer have the same packaging material.

References

[1] OECD and EUIPO, "Trade in counterfeit and pirated goods," *OECD Publishing*, p. 138, 2016.

[2] C. Kauba, L. Debiasi, R. Schraml, and A. Uhl, "Towards drug counterfeit detection using package paperboard classification," in *Procs. of the 17th Pacific-Rim Conf. on Multimedia (PCM'16)*, vol. 9917. Springer LNCS, 2016, pp. 136–146.

[3] W. J. Scheirer, A. Rocha, A. Sapkota, and T. E. Boult, "Towards open set recognition," *IEEE Trans. on Pattern Analysis and Machine Intelligence (T-PAMI)*, vol. 35, 2013.

[4] W. J. Scheirer, L. P. Jain, and T. E. Boult, "Probability models for open set recognition," *IEEE Trans. on Pattern Analysis and Machine Intelligence (T-PAMI)*, vol. 36, November 2014.

[5] L. P. Jain, W. J. Scheirer, and T. E. Boult, "Multi-class open set recognition using probability of inclusion," in *The European Conf. on Computer Vision (ECCV'14)*, 2014.

[6] B. Heflin, W. J. Scheirer, and T. E. Boult, "Detecting and classifying scars, marks, and tattoos found in the wild," in *The IEEE Int. Conf. on Biometrics: Theory, Applications and Systems (BTAS)*, 2012.

[7] F. O. Costa, E. Silva, M. Eckmann, W. J. Scheirer, and A. Rocha, "Open set source camera attribution and device linking," *Pattern Recognition Letters*, vol. 36, April 2014.

[8] A. Rattani, W. J. Scheirer, and A. Ross, "Open set fingerprint spoof detection across novel fabrication materials," *IEEE Trans. on Information Forensics and Security (T-IFS)*, vol. 10, 2015.

[9] E. Metois, P. Yarin, N. Salzman, and J. Smith, "Fiberfingerprint identification," in *Procs. of the 3rd Workshop on Automatic Identification*, 2002.

[10] J. Buchanon, R. Cowburn, A.-V. Jausovec, S. Petit, D., G. P., Xiong, D. Atkinson, K. Fenton, D. Allwood, and T. Bryan, "Forgery: Fingerprinting documents and packaging," *Nature*, vol. 436, p. 475, 2005.

[11] W. Clarkson, T. Weyrich, A. Finkelstein, N. Heninger, J. A. Halderman, and E. W. Felten, "Fingerprinting blank paper using commodity scanners," in *30th IEEE Symp. on Security and Privacy*, 2009, pp. 301–314.

[12] S. Voloshynovskiy, M. Diephuis, F. Beekhof, O. Koval, and B. Keel, "Towards reproducible results in authentication based on physical non-cloneable functions: The forensic authentication microstructure optical set (famos)," in *Procs. of IEEE Int. Workshop on Information Forensics and Security (WIFS'12)*, 2012.

[13] M. Diephuis, S. Voloshynovskiy, and F. Beekhof, "Physical object identification based on FAMOS microstructure fingerprinting: comparison of templates versus invariant features," in *8th Int. Symposium on Image and Signal Processing and Analysis*, Trieste, Italy, September, 4-6 2013.

[14] M. Diephuis, F. Beekhof, S. Voloshynovskiy, T. Holotyak, N. Standardo, and B. Keel, "A framework for fast and secure packaging identification on mobile phones," in *Procs. of SPIE Photonics West, Electronic Imaging, Media Forensics and Security V*, 2014.

[15] M. Diephuis, S. Voloshynovskiy, and T. Holotyak, "Sketchprint: Physical object micro-structure identification using mobile phones," in *European Signal Processing Conf. (EUSIPCO'15)*, 2015.

[16] C. W. Wong and M. Wu, "A study on PUF characteristics for counterfeit detection," in *IEEE Int. Conf. on Image Processing (ICIP'15)*, 2015, pp. 1643–1647.

[17] C. Wong and M. Wu, "Counterfeit detection using paper PUF and mobile cameras," in *IEEE Int. Workshop on Information Forensics and Security (WIFS'15)*, 2015, pp. 1–6.

[18] K. Zuiderveld, "Contrast limited adaptive histogram equalization," in *Graphics Gems IV*. Morgan Kaufmann, 1994, pp. 474–485.

[19] T. Ojala, M. Pietikäinen, and T. Mäenpää, "Multiresolution Gray-Scale and rotation invariant texture classification with local binary patterns," *IEEE Trans. on Pattern Analysis and Machine Intelligence*, vol. 24, no. 7, pp. 971–987, 2002.

[20] X. Tan and B. Triggs, "Enhanced local texture feature sets for face recognition under difficult lighting conditions," in *Analysis and Modelling of Faces and Gestures*, ser. LNCS, vol. 4778, 2007, pp. 168–182.

[21] Z. Li, G. Liu, Y. Yang, and J. You, "Scale- and rotation-invariant local binary pattern using scale-adaptive texton and subuniform-based circular shift," *IEEE Trans. on Image Processing*, vol. 21, no. 4, pp. 2130–2140, 2012.

[22] N. Dalal and B. Triggs, "Histograms of oriented gradients for human detection," in *Procs. of the IEEE Conf. on Computer Vision and Pattern Recognition, (CVPR'05)*, vol. 1, 2005, pp. 886–893.

[23] S. Hatipoglu, S. Mitra, and N. G. Kingsbury, "Texture classification using dual-tree complex wavelet transform," in *7th Int. Conf. on Image Processing and Its Applications*, vol. 1, Jul. 1999, pp. 344–347.

[24] Y. Xu, H. Ji, and C. Fermüller, "Viewpoint invariant texture description using fractal analysis," *Int. Journal of Computer Vision*, vol. 83, no. 1, pp. 85–100, 2009.

[25] R. Rautkorpi and J. Iivarinen, "A novel shape feature for image classification and retrieval," in *Procs. of the Int. Conf. on Image Analysis and Recognition (ICIAR'04)*, ser. LNCS, vol. 3211, 2004, pp. 753–760.

[26] C.-C. Chang and C.-J. Lin, "LIBSVM: A library for support vector machines," *ACM Transactions on Intelligent Systems and Technology*, vol. 2, pp. 27:1–27:27, 2011, software available at http://www.csie.ntu.edu.tw/ cjlin/libsvm.

[27] Lalit Jain, "Openset libsvm extensions," https://github.com/ljain2/libsvm-openset, 2014, [last accessed: 13.06.2017].

Real or Fake: Mobile Device Drug Packaging Authentication

Rudolf Schraml, Luca Debiasi, Andreas Uhl
University of Salzburg
Department of Computer Sciences
rschraml@cs.sbg.ac.at,ldebiasi@cs.sbg.ac.at,uhl@cs.sbg.ac.at

ABSTRACT

Shortly, within the member states of the European Union a serialization-based anti-counterfeiting system for pharmaceutical products will be introduced. This system requires a third party enabling to track serialized and enrolled instances of each product from the manufacturer to the consumer.

An alternative to serialization is authentication of a product by classifying it as being real or fake using intrinsic or extrinsic features of the product. Thereby, one approach is packaging material classification using images of the packaging textures. While the basic feasibility has been proven recently, it is not clear if such an authentication system works with images captured with mobile devices. Thus, in this work mobile device drug packaging authentication is investigated. The experimental evaluation provides results on single- and cross-sensor scenarios. Results indicate the principal feasibility and acknowledge open issues for a mobile device drug packaging authentication system.

ACM Reference Format:
Rudolf Schraml, Luca Debiasi, Andreas Uhl. 2018. Real or Fake: Mobile Device Drug Packaging Authentication. In *IH&MMSec '18: 6th ACM Workshop on Information Hiding and Multimedia Security, June 20–22, 2018, Innsbruck, Austria.* ACM, New York, NY, USA, 6 pages. https://doi.org/10.1145/3206004.3206016

1 INTRODUCTION

As the global markets get flooded with counterfeited products regulations and technical solutions for product authentication get implemented in various sectors of the economy. According to a report by the European Intellectual Property Office 4.4% of the sales and € 10 billion in the pharmaceutical sector correspond to counterfeited medicines [2]. Moreover, counterfeit drugs pose a significant risk to consumer or patient welfare. As a countermeasure against this problem the Falsified Medicines Directive (FMD) 2011/62/EU should be operational until 2019 within all member states of the European Union. The main purpose is to protect patients by reducing the risk of counterfeits entering the supply chain. Therefore, an anti-counterfeiting system based on product serialization will be implemented. Each drug package will be assigned a unique identifier (2D barcode) and secured by a tamper-proof seal. This enables to track and verify each drug package along the supply chain from the manufacturer to the consumer. As a drawback, a central database managed by the European Medicines Verification Organisation (EMVO) is required. Manufacturers need to register new packages at the EMVO and pharmacies have to check-out each sold package. Actually, it is planned that additional costs are covered by the manufacturers but it is likely that those are passed to the consumers. Finally, a centralized system is exposed to getting compromised by forgers, e.g. by entering 2D barcodes from forged packages.

An alternative to serialization is packaging authentication based on classification which is inspired by physical object identification approaches relying on the concept of physically unclonable functions (PUFs). A PUF is a mapping between a challenge and response function which depends on the physical nature of a object. By definition a PUF is unique and cannot be reproduced. Related to packaging authentication various works dealed with Paper PUFs. Paper PUFs either rely on extrinsic or intrinsic PUFs, i.e. which are attached to the product or can be derived from a part of the product itself. However, PUFs are intended to identify an object. In case of classification-based authentication, it is assumed that the packaging of a product shows constant but discriminative intrinsic features. Instead of identifying each single package instance, it can be classified if the product is packaged with a specific packaging material or not. The focus in our research is on drug pills which are packaged in a blister and housed in a cardboard. Recently, in [3, 8] we investigated the basic feasibility of drug packaging authentication. In [3] we showed that cardboard textures of 9 different drugs from 3 manufacturers can be classified with 100% accuracy in a closed multi-class scenario. The utilized dataset was fairly small and packaging material authentication is in fact a simplistic binary classification problem, i.e. a single class has to be distinguished from all other classes. For the training stage only a limited subspace of known other classes is available which is referred to as open-set recognition. Thus, in [8] we focused on the open-set recognition problem and we investigated two basic pre-requirements for classification-based drug packaging authentication: positional invariance and instance generalisation of the packaging material texture. Based on a substantial database, with images of 45 different drugs from multiple instances (packages), both pre-requirements were proved successfully. However, all images were taken with a DSLR camera in an optimal setting and such imagery will not be available in case of a mobile device based authentication system. Thus, for this work in addition to a DSLR camera two smartphones were used to acquire a substantial dataset.

Based on this dataset in this work mobile-sensor as well as cross-sensor drug packaging authentication is investigated. Furthermore, in [8] only the particular classification accuracies for different parts of the packaging material were presented. For an authentication system it is assumed that the fusion of the particular classification

IH&MMSec '18, June 20–22, 2018, Innsbruck, Austria

ACM ISBN 978-1-4503-5625-1/18/06…$15.00
https://doi.org/10.1145/3206004.3206016

results will increase the overall accuracy. Based on a simple majority voting approach, in this work the impact of fusion as well as feature selection will be elaborated. Finally, a closer look on possible authentication error sources will be presented. For example, it is assumed that parts of the packaging material from different drugs which are from the same manufacturer can be the same.

First, in Section 2 a possible scheme for a mobile device based drug packaging authentication system is introduced. Section 3 introduces the acquired database. The classification pipeline is outlined in Section 4. Experiments and results are presented in Section 5 and Section 6 concludes this paper.

2 MOBILE DEVICE DRUG PACKAGING AUTHENTICATION SYSTEM

A schematic illustration for a mobile-device based drug package authentication system is illustrated in Fig. 1. In order to proof the authenticity of a given drug the consumer will be guided by a mobile application. First, the user needs to disassemble the drug and to capture the textures of the cardboard (CB) and the blister top (BT) and blister bottom (BB) side. These three textures of the packaging material are denoted as modalities. The captured images are denoted as I_{CB}, I_{BT} and I_{BB}. Additionally, the user is advised to take a picture of the product code (I_{PC}), e.g. the European article number or the barcode printed on the cardboard. However, the product number can be entered manually or the respective drug can be selected from a list too. These four images compose the authentication vector $\hat{AV} = (I_{CB}, I_{BT}, I_{BB}, I_{PC})$ which is processed by the authentication system. First, the textural images I_{CB}, I_{BT} and I_{BB} are preprocessed. Preprocessing includes segmentation of the textural area and enhancement of the textural pattern. Subsequently, from each preprocessed image one patch is extracted for which a feature descriptor is computed. The product code image I_{PC} is used to determine the product code. Based on the product code, the system selects the corresponding precomputed classification models M_{CB}, M_{BT}, M_{BB} from a model repository. If the required models are not available on the mobile device they could be requested from a remote repository. Based on the corresponding models M_{CB}, M_{BT}, M_{BB} for each feature vector $FV_{CB}, FV_{BT}, FV_{BB}$ a probability score P_{CB}, P_{BT}, P_{BB} between $[0, 1]$ is computed. The closer to 1 the more likely the given feature vector is from a real sample, the closer to 0 the higher is the probability that the feature vector was computed from fake material. Finally, a decision function $f(P_{CB}, P_{BT}, P_{BB}) = (v, p)$ needs to be defined, where $v \in \{1, -1\}$ gives the final authenticity vote of the authentication system and $p \in [0, 1]$ specifies a probability score for the final vote which is then presented to the user.

3 DRUG PACKAGINGS TEXTURE DATABASE

For this study the same database as used in [8] and additional data captured with two different smartphones was utilized. Therefore, a Samsung S5 Mini & an IPhone 5 were utilized to capture images for a set of selected drugs. Therefore, mainly drugs with more than four instances from various manufacturers were selected. The acquisition setup is illustrated in Fig. 2f. Same as for the DSLR camera, the smartphones were mounted on a tripod and in addition a macro lens was utilized. For illumination a light source was placed laterally. An exemplary disassembled drug package is shown in

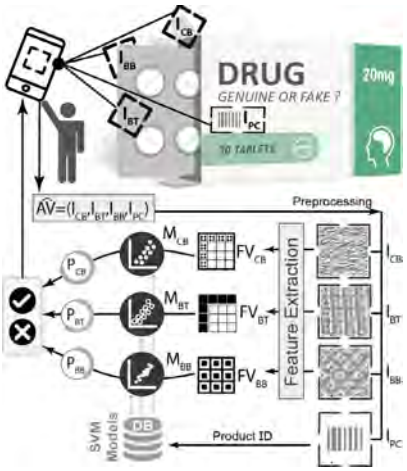

Figure 1: Mobile device drug packaging authentication

Fig. 2a. The initial dataset consists of images from 45 drugs from 28 different manufacturers which were captured with a Canon 70D. For each drug between 1 and 15 package instances are available. The Canon 70D was mounted on a tripod and a 100mm lens and a flashlight were utilized (see Fig. 2e). From each drug instance images from the corresponding CB,BT&BB modalities were captured. For CB the inner side, showing the fibre structure was captured. For BT,BB the corresponding blister textures were captured. Thereby, it was ensured that the images were taken from different and non-overlapping regions. Examples depicting the variety of the different samples for each modality are shown in Fig. 2b-2d. All captured images were manually cropped ensuring that just texture remains. The images in the 1st row in Fig.3 illustrate exemplary images from each modality captured with the different sensors.

4 CLASSIFICATION PIPELINE

Data selection is essential for the subsequent cross-validation procedure. Due to the varying number of instances and the corresponding CB,BT&BB images per drug, a keypoint selection strategy has been employed. Therefore, a fixed number of data (k) to be sampled is predefined. Data relates to image texture patches of CB,BT&BB. For patch sampling, each CB,BT&BB image is subdivided into a grid which is specified by the size of the feature descriptor. According to the results presented in [8] 256×256 pixel patches are utilized. The 2nd row in Fig. 3 depicts sample images for CB,BT&BB for which the image patch grids are shown. Basically, k patches are selected from each instance of each drug and modality. However, k is only an upper bound of patches which are selected. For example, in this work k=1000 and especially for BT and BB there are drugs where less patches are available.

Image Enhancement. Prior to feature extraction the images are converted to grey-scale and Contrast Limited Adaptive Histogram Equalization (CLAHE) [10] is applied to each patch (parameters: block radius=50, bins=256, slope=40). Exemplary CLAHE enhanced

(a) Drug sample (b) Cardboards (CB) (c) Blister top (BT) (d) Blister bottom (BB) (e) Digital camera (f) Mobile camera

Figure 2: Image Acquisition Overview

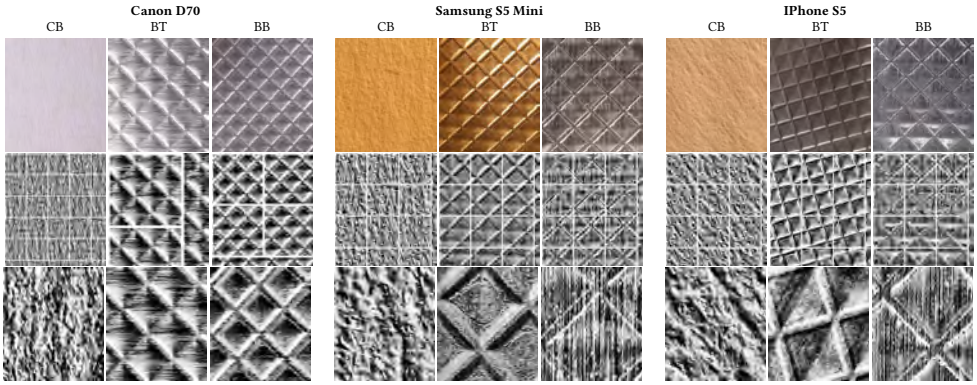

Figure 3: Preprocessing and data selection examples for Thrombo ASS produced by Lannacher Heilmittel (F1): 1st Row: Original images, 2nd Row: Preprocessed images showing the keypoint grid, 3rd Row: Exemplary 256×256 pixel patches from the top left keypoint in each image of the 2nd row.

images and selected patches for each modality and camera are shown in the 2nd and 3rd row of Fig. 3, respectively.

4.1 Feature Extraction and Feature Encoding

For each selected patch a feature vector using each of the following feature extraction approaches is computed: Local Binary Pattern (LBP) [5], Local Ternary Pattern (LTP) [9], Li Local Binary Pattern (LiLBP) [4], Speeded Up Robust Features (SURF) [1]. As noted in [8] IO and memory constraints are crucial when it comes to high dimensional features like SIFT and SURF. Furthermore, high dimensional feature vectors are computationally problematic in case of kernel-based SVM classifiers. As a first consequence the x,y step size for dense SURF method was increased to 16 pixel and we decided to compute both in a pyramid at three scales (1, 2, 4). Consequently, for each patch #768 × SURF feature descriptors are computed. In case of SURF this results in a feature vector dimension of 98304. In preliminary tests it turned out that this feature vector size is suited for the classification experiments if a linear SVM classifier is utilized but not applicable in case of kernel SVMs.

Furthermore, image classification research showed that feature vector encoding schemes are beneficial for the classification accuracy. In case of SURF it was shown that the fisher vector (FV) encoding scheme [6] combined with linear classifiers improves the classification performance. The FV scheme encodes a set of vectors into a single vector which is composed by the first and second order residuals of the vectors from a Gaussian mixture model (GMM). Basically, the dimensionality of the fisher vector output is $2 \times K \times D$. K is the number of GMM components and D gives the feature vector dimensionality. Commonly, the FV encoding scheme is combined with a dimensionality reduction approach like Principial Component Analysis (PCA). Thereby, PCA is used to reduce the size of a feature vector to a predefined number of principal components. For this work, the input feature vector is reduced to 80 components. For a reduced input feature vector dimensionality of $D = 80$ and $K = 256$ Gaussian components a single FV with the size of $2 \times 80 \times 256 = 40960$ is produced. In case of SURF the FV encoding reduces the dimension of the SVM input vector by more than the half.

4.2 Data partitioning

In order to provide reliable results cross-validation (CV) based classification is performed. For each drug a number of instances (=packages) from each modality is available. Thus, a nested leave-one-package-out (LOPO) CV procedure is well suited to avoid overfitting and to force the computation of unbiased evaluation results.

The acquired database is composed by a set of drugs $D = \{d_1, ..., d_{45}\}$ produced by different $DM = \{dm_1, ..., dm_{28}\}$ drug manufacturers. $fdm(d_i) : D \rightarrow DM$ specifies the drug manufacturer for each drug. $M = \{CB, BT, BB\}$ specifies the packaging modalities. Furthermore the drugs and modalities were captured with different sensors $S = \{CANON = S1, SAMSUNG = S2, IPHONE = S3\}$ and different feature extraction methods $FE = \{fe_1, ..., fe_n\}$ are utilized in the experiments. The feature vector sets for a certain drug $d \in D$ and modality $m \in M$, for the k-patches from sensor $s \in S$ computed with feature extraction method $fe \in F$, are given by $FV_{(d,m,s,fe)} = \{fv_1, ..., fv_k\}$.

For binary classification it is required to specify a target class, i.e. the drug and the corresponding modality which we want to

authenticate. In the scope of this work various classification configurations (CCs) are computed for each target drug d which are given by the following tuple: $CC = (d \in D, m \in M, s \in S, fe \in FE)$. The respective set of feature vector sets for a CC is given by $FV_{CC} = \{FV_{(d_1,m,s,fe)}, ..., FV_{(d_{45},m,s,fe)}\}$ which is composed by the CC specific feature vector sets from each drug. The positive training data $P_{CC} = FV_{(d,m,s,fe)}$ is specified by the target drug d in CC. The negative training data $N_{CC} = \{FV_{CC}\} \setminus \{FV_{(d,m,s,fe)}\}$ is composed by all feature vector sets of all other drugs. The positive and negative training data P_{CC}, N_{CC} are then used for nested cross-validation using a SVM classifier.

4.3 Cross-validation strategy

The overall goal of the CV strategy is to avoid two different types of over-fitting. The first ensures that no training data is used for evaluation as this leads to overestimation of the classification accuracy. CV excludes this type of over-fitting. The second type of over-fitting is crucial and concerns the training of the model. Thereby, hyperparameter selection plays a significant role in case of SVMs. The overall goal is to find parameters for a model which generalizes to the evaluation data, i.e. the ability of the model to classify unseen data. However, in binary open-set classification and especially in case of the considered drug authentication problem optimization is a trade-off between over- and under-fitting. Unseen data is composed by known data from the target drug and all other known drugs as well as a large set of data from unknown drugs. If the model is over-fitted to the training data it is likely that unseen evaluation data from other packages of the target drug are not recognized. On the other-hand under-fitting increases the risk that unseen as well as unknown packages from other drugs are misclassified as being the target drug.

Basically, for CV the positive and negative training data P_{CC} and N_{CC} for a certain CC are provided as input. For the LOPO CV strategy P_{CC} is split into n-folds $\{P_1, ..., P_n\}$ where each fold contains the feature vectors from a certain instance (=drug package sample). Thus, the number of folds n is given by the number of instances for the target drug d in CC which are available in the database. Same as in [8] the negative training N_{CC} data is split into known negatives KN_{CC} and unknown negatives $UN_{CC} = N_{CC}/KN_{CC}$. Therefore, for KN_{CC} the feature vector sets from a fixed number of drugs are selected, where the manufacturers are different to the target drug manufacturer of d in CC. The aim of this procedure is to simulate the real world, where only a limited set of other known drugs (faked and original ones) are available to train a classifier.

For the nested CV strategy in the outer loop we iterate over the n positive training folds. The current loop index is given by the variable i. In each iteration for KN_{CC} the features are split into two folds KN_1, KN_2 packagewise for each of the contained classes. Hence, half of the packages and the corresponding feature vectors of each class are contained in each fold. Subsequently, the ith positive and 2nd negative fold is selected for evaluation. The evaluation set is given by $E_{i,2} = P_i \cup KN_2 \cup UN_{CC}$. The unknown drugs UN_{CC} are only used for evaluation. The training set is composed by $T_{i,1} = \{P_1, ..., P_k\} \setminus \{P_i\} \cup \{KN_1\}$. Preliminary, $\{KN_1\}$ is reduced to a fixed number of feature vectors which are sampled equally distributed from all contained drug classes (=6) and the respective instances. In the inner CV loop for each $T_{i,1}$ the best hyperparameters are determined using a grid search approach. Same as in the outer loop, k-fold validation is performed repeatedly in order to test a set of SVM parameters. For this purpose, the known negative training data in $T_{i,1}$ is split classwise into two folds TKN_1 and TKN_2 (training known negatives). One fold simulates known negatives (=3 classes) and the other one unknown negatives (=3 classes) in the inner loop. While the known negatives are further used for training as well as for validation, the unknown negatives are just used for validation. It is assumed that this strategy is beneficial for the generalisation of the classifier. Hence, in the grid search procedure hyperparameters delivering a good classification accuracy in terms of the target class as well as known and unknwon classes accuracy are prioritized. As a measure for the performance the F-Measure is utilized which is well suited to balance between specialisation and generalisation in binary classification tasks. The utilized SVM classifiers assign each prediction a probability. In the inner loop, the probabilities are used to determine a threshold which maximizes the F-Measure. The SVM parameters and threshold delivering the highest F-Measure are selected for the outer loop. Those are then used to train and evaluate a classifier with the training and evaluation data from the outer loop, respectively.

5 EXPERIMENTS

For data selection at maximum k=1000, 256× 256 pixel patches were selected from each modality and sensor. For each patch feature vectors are computed with all features listed in Section 4.1. In the experiments the LIBSVM linear SVM and kernel SVM with a radial basis function are utilized as classification approaches. Both are applied in combination with FISHER feature vector encoding (FVE=FISHER) and without (FVE=NULL) to cross-validate all CC combinations. Basically, the employed CV strategy requires that only drugs with at least 5 instances can be selected as target drugs, ie. the drug which should be authenticated by the classifier. An overview on suited drugs is presented in Table 2. The table shows that for each selected target drug various numbers of instances are available and each was captured with a set of sensors (S1,S2,S3). For each target drug and sensor all CCs are computed using the outlined LOPO CV strategy. For each LOPO CV the positive data is split into 2-folds, in the inner and outer CV loop. 6 drugs are selected for the known negative training data KN_{CC}. In order to assess the cross-sensor scenario, for evaluation in the outer CV loop data from all different sensors are utilized. For training data from only one sensor are utilized. For example, in case of Mexalen (A3) in the outer loop in each LOPO iteration the evaluation is performed with #1.75k-2k features of the target drug and >#100m features from all other drugs and cameras. For a fair evaluation of the different classification approaches and features the data splits are stored and reused.

5.1 Single-sensor evaluation

An overview on the particular results for the different sensors, all modalities and classification approaches is presented in Table 1. For each CC and modality the averaged results over all target drugs (Table 2) are shown. Considering the results for different CCs, it can be concluded that the F-Measure differences between the elaborated classifiers are not significant. For L-SVM and FISHER encoding it

CC		Canon - S1			Samsung - S2			IPhone - S3		
FVE	CA	CB	BT	BB	CB	BT	BB	CB	BT	BB
NULL	RBF-SVM	*LTP* 0.87 ±6.9	*LTP* 0.94 ±3.5	*LiLBP* 0.84 ±17.6	*LTP* 0.92 ±6.8	*LTP* 0.96 ±4.0	*LiLBP* 0.91 ±5.8	*LBP* 0.83 ±6.1	*LTP* 0.95 ±6.5	*LTP* 0.88 ±8.1
	L-SVM	*LTP* 0.87 ±7.4	*LBP* 0.92 ±4.7	*LiLBP* 0.83 ±13.5	*LTP* 0.92 ±6.3	*LTP* 0.94 ±4.1	*LiLBP* 0.9 ±5.6	*LBP* 0.83 ±6.9	*LTP* 0.95 ±6.2	*LTP* 0.8 ±12.6
FISHER	L-SVM	*LiLBP* 0.84 ±7.4	*SURF* 0.93 ±3.8	*SURF* 0.89 ±10.6	*LBP* 0.88 ±9.3	*SURF* 0.97 ±4.8	*SURF* 0.91 ±4.9	*SURF* 0.82 ±6.3	*SURF* 0.95 ±7.9	*SURF* 0.84 ±12.0

Table 1: Single-sensor performances: For each sensor and all CCs the mean F-Measure and the StDev[%] for the best features of each modality are presented.

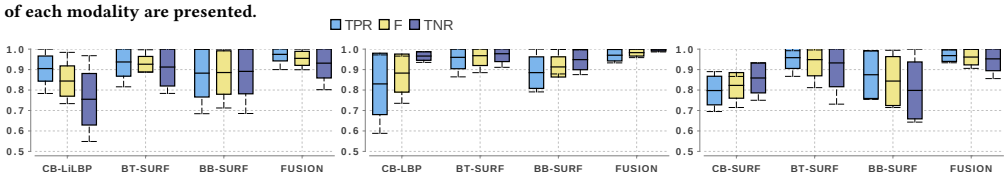

(a) S1 - Canon **(b) S2 - Samsung** **(c) S3 - IPhone**

Figure 4: Single-sensor results for FISHER L-SVM: For each sensor and modality the performances for the best features as well as for modality fusion are depicted. TPR = $\frac{TP}{TP+FN}$, TNR = $\frac{TN}{TN+FP}$ [Y-Axis: Mean, min, max, standard deviation].

seems that SURF as high level feature does not improve the performance as expected. Furthermore, the F-Measures are comparable to the results presented in [8]. However, in [8] less data was selected for training which shows that doubling the parameter k to 1000 does not improve the classification performance.

When comparing the F-Measures between the different sensors the values are in the same range, surprisingly. Basically, for the mobile sensors fewer drugs were available for evaluation, i.e. no unknown drugs remain for evaluation. Thus, it would be assumed that less variety (=closed-set) in the evaluation data improves the classification performance. This new finding is interesting because this increases the chance that the classification performances are robust in a real world application.

Modality fusion. In the experiments in [8] only the modality performances were considered. As shown in the exemplary drug packaging authentication scheme in Fig. 1 the three probability scores from each modality (P_{CB}, P_{BT}, P_{BB}) should be combined to a final decision. For this purpose, a simple majority voting approach

Manufacturer/Drug	#Samples		Camera		
	CB	BT&BB	Canon (S1)	IPhone (S2)	Samsung (S3)
(A) ratiopharm					
(A1) Danselle	10	10	✓	-	-
(A2) Danseo	9	9	✓	-	-
(A3) Mexalen	8	8	-	✓	✓
(F) Lannacher					
(F1) Thrombo ASS	5	5	✓	✓	✓
(I) Kwizda Pharma					
(I1) Liberel mite	15	15	✓	-	-
(I2) Delia	11	11	✓	✓	✓
(J) Rotexmedia					
(J1) Dexamethason	5	0	✓	-	-
(N) Gynial					
(N1) Bilinda	6	6	✓	✓	✓
(X) Pelpharma					
(X1) Peliette	17	17	✓	✓	✓

Table 2: List of drugs with at least 5 instances which were selected as target drugs. Only drugs which were captured with the corresponding sensors show a check-mark.

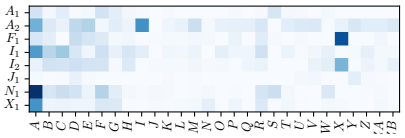

(a) CB - LiLBP

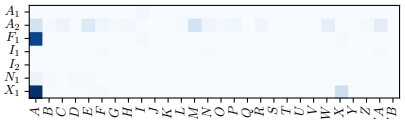

(b) BT - SURF

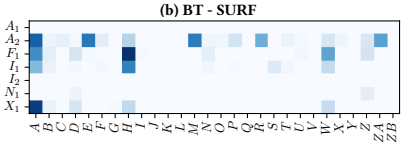

(c) BB - SURF

Figure 5: Single-sensor results for Canon (S1) FISHER L-SVM: (FN+FP) Error matrix for each modality. [X-Axis: Producers from the evaluation data, Y-Axis: Target Drugs]. The darker the cell, the higher is the classification error.

is applied which still offers possibilities for optimization. Initially, the modality specific classifier thresholds are used to determine a decision vector $\hat{D} = (D_{CB}, D_{BT}, D_{BB})$ from the probability scores. The decision values are either 1 or -1. In case that at least two decision values are 1 the final decision is that the package material is from a real package, i.e. it is not a fake sample. For the selection of the features which achieve the highest F-Measure SFFS (Sequential Floating Forward Selection) [7] is applied. For this purpose, the particular modality decisions are randomly shuffled to to get a set of decision vectors. The shuffling is repeated several times in order to compute the averaged classification performances of the modality fusion. For each sensor the particular modality performances as well

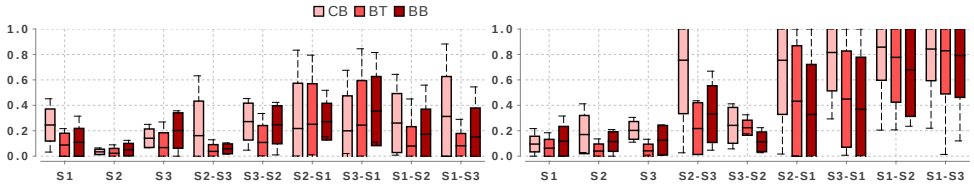

(a) False positve rates: FPR= $\frac{FP}{TP+FP}$ (b) False negative rates: FNR= $\frac{FN}{TN+FN}$

Figure 6: Cross-sensor performances for FISHER L-SVM: For all training and evaluation sensor combinations the FPR and FNR for each modality are shown. For each combination and modality the results for the best feature were selected. [Y-Axis: FPR/FNR mean, min, max and standard deviation].

as the fusion performance is illustrated in Fig. 4. It can be concluded that modality fusion significantly improves the classification and authentication accuracy.

Error sources. Basically, it is assumed that other drugs from the same or different manufacturer might have the same packaging material, e.g. if two different manufacturers have the same cardboard or blister supplier. The error matrix plots in Fig. 5 visualize the number of false positive (FP) + false negative (FN) votes for each target drug and the evaluated drugs which are grouped into manufactures. The darker the higher the amount of misclassification's. FP votes are from samples which are incorrectly authenticated and FN votes are from samples which were incorrectly not authenticated. When considering the columns it can be observed how likely the drugs of a certain manufacturer cause FP or FN votes. FN votes are only possible when the target drug (e.g. A1) and the manufacturer (A) in the columns are the same. For example, for all three modalities the drugs of ratiopharm (A) cause FP votes for drugs from other manufacturers as well as FN votes for A1 and A2. Furthermore, each target drug and the corresponding row can be considered. The darker the more FP and FN votes were observed in the CV strategy. In case of CB, the drug A2 shows a high amount of errors. Furthermore, in each error matrix there are some dark spots which show up high error rates. For example, for BB a high amount of samples from manufacturer H are incorrectly classified as drug F1 = FP votes. Comparing the error matrices for all three modalities it is obvious that the most errors are visible in case of CB and BB and there are less errors for the BT textures.

5.2 Cross-sensor evaluation

In order to assess the cross-sensor performances, all CCs were evaluated with data from other sensors. Thereby, the classifier was always trained with data from only one sensor. The two charts in Fig.6 show the FP and FN rates which were achieved for different training and evaluation sensor combinations. Actually, S1,S2&S3 show the single sensor FPR and FNR for each modality. All other combinations show results where the classifier has been trained with data from one sensor and has been evaluated with data from another sensor, i.e. cross-sensor results. The single-sensor error rates are in general lower than the cross-sensor results for almost all modalities. Especially, the cross-sensor combinations where either the DSLR or a mobile camera are used for training and the other camera type is used for evaluation show inferior FNR values and also worse FPR values. This could be attributed to the different texture scales in case of images acquired with the DSLR camera and images acquired with the mobile devices (see Fig. 3). Backing for this argument is that the error rates for the mobile-device cross-sensor combinations are better. Furthermore, the cross-sensor FNR values are inferior to the FPR values compared to the single sensor results. Thus, in the considered cross-sensor scenario it is easier for the classifier to reject samples from other drugs than to detect samples from the same drug captured with a different sensor.

6 CONCLUSION

In this work different aspects for a mobile device based drug packaging authentication system were considered. Results showed that data captured with mobile devices and low level features are principally suited for drug packaging authentication. Furthermore, modality fusion improves the performance significantly. However, if different sensors are used and the imaging conditions get more realistic the authentication performance degrades significantly.

Future work on a mobile device based application needs to deal with all issues caused by unconstrained imaging conditions (scale, rotation, tilt & illumination variations). Furthermore, more sophisticated approaches for modality fusion, state-of-the art features and a CNN-based solution should be employed.

REFERENCES

[1] Herbert Bay, Andreas Ess, Tinne Tuytelaars, and Luc Van Gool. 2008. Speeded-Up Robust Features (SURF). *Comput. Vis. Image Underst.* 110 (June 2008), 346–359. Issue 3. https://doi.org/10.1016/j.cviu.2007.09.014
[2] EUIPO. 2016. The economic cost of IPR infringement in the pharmaceutical industry. http://authenti-city.eu/wp-content/uploads/2016/10/The-Economic-Cost-of-IPR-Infringement-in-the-Pharmaceutical-Industry-EN.pdf. (2016).
[3] Christof Kauba, Luca Debiasi, Rudolf Schraml, and Andreas Uhl. 2016. Towards Drug Counterfeit Detection Using Package Paperboard Classification. In *Advances in Multimedia Information Processing – Proceedings of the 17th Pacific-Rim Conference on Multimedia (PCM'16)* (September 15 - September 16) *(Springer LNCS)*, Vol. 9917. Xi'an, CHINA, 136–146. https://doi.org/10.1007/978-3-319-48896-7_14
[4] Z. Li, G. Liu, Y. Yang, and J. You. 2012. Scale- and Rotation-Invariant Local Binary Pattern Using Scale-Adaptive Texton and Subuniform-Based Circular Shift. *IEEE Transactions on Image Processing* 21, 4 (April 2012), 2130–2140.
[5] T. Ojala, M. Pietikäinen, and T. Mäenpää. 2002. Multiresolution Gray-Scale and Rotation Invariant Texture Classification with Local Binary Patterns. *IEEE Transactions on Pattern Analysis and Machine Intelligence* 24, 7 (July 2002), 971–987.
[6] F. Perronnin and C. Dance. 2007. Fisher Kernels on Visual Vocabularies for Image Categorization. In *Proceedings of the IEEE Conference on Computer Vision and Pattern Recognition (CVPR'07)*. 1–8.
[7] P. Pudil, J. Novovicova, and J. Kittler. 1994. Floating Search Methods In Feature-Selection. *Pattern Recognition Letters* 15, 11 (November 1994), 1119–1125.
[8] Rudolf Schraml, Luca Debiasi, Christof Kauba, and Andreas Uhl. 2017. On the feasibility of classification-based product package authentication. In *IEEE Workshop on Information Forensics and Security (WIFS'17)*. Rennes, FR.
[9] Xiaoyang Tan and Bill Triggs. 2007. Enhanced Local Texture Feature Sets for Face Recognition under Difficult Lighting Conditions. In *Analysis and Modelling of Faces and Gestures (LNCS)*, Vol. 4778. 168–182.
[10] K. Zuiderveld. 1994. Contrast Limited Adaptive Histogram Equalization. In *Graphics Gems IV*, Paul S. Heckbert (Ed.). Morgan Kaufmann, 474–485.

mathematics

MDPI

Article

Matching Score Models for Hyperspectral Range Analysis to Improve Wood Log Traceability by Fingerprint Methods

Rudolf Schraml [1], Karl Entacher [2,3], Alexander Petutschnigg [3,*], Timothy Young [4] and Andreas Uhl [1]

[1] Department of Computer Sciences, University of Salzburg, 5020 Salzburg, Austria; rudi.schraml@gmail.com (R.S.); uhl@cosy.sbg.ac.at (A.U.)
[2] Holztechnikum Kuchl, 5431 Kuchl, Austria; karl.entacher@holztechnikum.at
[3] Department of Forest Products Technology and Timber Construction, University of Applied Sciences Salzburg, 5412 Puch bei Hallein, Austria
[4] Center for Renewable Carbon, University of Tennessee, Knoxville, TN 37996, USA; tmyoung1@utk.edu
* Correspondence: alexander.petutschnigg@fh-salzburg.ac.at

Received: 8 May 2020; Accepted: 14 June 2020; Published: 2 July 2020

check for updates

Abstract: Traceability of natural resources, from the cradle to the final product is a crucial issue to secure sustainable material usage as well as to optimize and control processes over the whole supply chain. In the forest products industries the material can be tracked by different technologies, but for the first step of material flow, from the forest to the industry, no systematic and complete technology has been developed. On the way to close this data gap the fingerprint technology for wooden logs looks promising. It uses inherent properties of a wood stem for identification. In this paper hyperspectral cameras are applied to gain images of Norway spruce (Picea abies [L.] Karst.) log end faces in different spectral ranges. The images are converted to a biometric template of feature vectors and a matching algorithm is used to evaluate if the biometric templates are similar or not. Based on this, matching scores specific spectral ranges which contain information to distinguish between different log end faces are identified. The method developed in this paper is a necessary and successful step to define scanning system parameters for fingerprint recognition systems for wood log traceability from the forest.

Keywords: wood traceability; biometric identification; fingerprint detection, hyperspectral imaging

1. Introduction

Traceability of wooden logs is a recent topic of research, as customers are getting more interested in the origin of their products. This led to certificates like the one of the Forest Stewardship Council [1] or the Program for the Endorsement of Forest Certification [2] that are documenting the sustainable production of wood. Even more legal actions and agreements like the European timber regulation EUTR No. 995 2010 [3] were developed. This was done to claim disclosure of the provenance of timber and timber products that are placed on the European market in order to impede deforestation and illegal trading of timber. The availability of unambiguous tracking methods for logs from forest to forest products industries will guarantee the database for process analysis and process optimization and can therefore be seen as a necessity for further development. This topic is in the view of recent research all over the world and even scientific hackathons are organized (e.g., the Evergreen innovation camp 2019 in Vienna [4]) to solve the question of traceability of wood from the forest to the related industry. Different methods of log tracking systems were investigated in the past and they reach from the application of barcodes up to the usage of radio frequency identification (RFID) transponders (e.g., [5]

or [6]), but tracking systems are only used for relatively high priced lumber up to now, due to technical and economical shortcomings when these systems are applied for rather inexpensive mass round wood. In this paper the main approach is based on inherent properties of a log based on biometric log end face characteristics as shown in [7–10]. The usage of log characteristics for tracking logs is not a new idea, e.g., in [11] and [12] surface properties of wood logs were used for identification and in [13] and [14] additional measurements with tracheid effect and X-ray were used. These applications can be used successfully in the sawmill environment, but they are not applicable on the forest site. In other research it was found that the log end faces contain a lot of information that can be used for biometric purposes [15–17]. To be successful on the forest site the measurement equipment has to be simple and insensitive to surrounding mechanical and other physical disturbances. For these reasons in [18] the application of commercial action cameras, which can be used in harsh environments, to collect log end images in the forest were tested. It was shown that the collection of images was satisfying in the forest, but the log end faces changed significantly during transport. Dirt accumulation, mechanical damages and color changes on the log end surface occurred during transport conditions. Based on these findings the following assumption is derived.

It is assumed that a hyperspectral image which contains not only the visible spectra, but depending on the technology also parts of the ultraviolet (UV)-spectra and near infrared (NIR) spectra, will be able to improve the detection of significant parts of log end faces.

The usage of hyperspectral imaging technologies ranges from large scale imaging down to lab scale sensors used in food safety, pharmaceutial applications forensic, etc. (examples are shown in [19] or [20]) and therefore is very common in use. One main tasks for the successful application of these technologies is the development and usage of sophisticated analysis technologies for the given data quantities. e.g., [21] give an overview of main tasks and methods for hyperspectral remote sensing data analysis and in [22] the concept of active learning methods to improve data analysis models are shown. These papers show the direction of actual developments in the field of hyperspectral image analysis.

For wooden log tracking these hyperspectral methods are not investigated up to now, but results of other research groups (e.g., [23,24] or [25]) let assume that hyperspectral images might overcome the problems of the conventional methods as well as the shortcoming of the research approaches shown above.

Following this assumption, it is from special interest which spectra contains different information compared to other spectra, or the other way around, which spectra contain the same information than others. This knowledge is crucial to reduce the technical efforts and expenses while collecting the data in the forest. Within this paper a method is shown, which is able to calculate distance measures between different spectral images of complex shaped wooden log end faces. This enables the investigation of spectral ranges which contain different information and are thus valuable to improve image acquisition for fingerprint methods in the future.

2. Materials and Methods

2.1. Wood Samples

Initially, 100 different Norway (*Picea Abies*) spruce logs logs (4̃.5 m length) were collected on 24 and 25 September2018 in a grove near Corcieux, France (48.1968 N; 6.8869 E). Since the logs were selected from piles, it is not possible to know which logs belong to the same tree. Norway spruce was chosen for this study as it is the main tree species in Austria. These logs were transported to Freiburg in Germany where they were used for further data acquisitions. For the experiments in this paper a wood disc was cut from the lower end of each log. The outside of each disc was sanded with a mesh width of 120 to reduce the influence of manual chainsaw cuts at scanning. This mesh width was chosen as it gave good results for the wet samples. To avoid surface cracks due to wood shrinkage

and discoloration due to oxidation processes the slices were packed individually in plastic bags during transport and intermediate storage.

2.2. Scanning System

The samples were scanned at Stemmer Imaging in Munich by two pupils of the Holztechnikum Kuchl, which used two different multispectral line scanners. The first scanner was a so called Specim FX10, which scans the spectra between a wavelength from 445 nm to 983 nm with a bandwidth of approx. 3 nm. The second scanner was a Specim FX17 which provides scans between 990 nm to 1665nm also with a bandwidth of approx. 3 nm. Therefor the Specim FX10 uses mainly the visible light (VIS) spectra and the Specim FX17 uses mainly parts of the NIR spectra. For the scanning setup a resolution of 640 × 640 pixel was chosen. The scanning system is shown in Figure 1a—Halogen light was used for lighting. Each wood disc was scanned with both cameras. For this purpose, each disc was pushed through the system by hand and the speed was synchronized with a trigger. The hyperspectral data, i.e., the translation from line scanning data to a hyperspectral cube, was performed by the acquisition software Perception Studio.

(**a**) Scanning system (**b**) Wood disc storage (**c**) Hyperspectral cube cropping

Figure 1. The sensor system shows the line scanner Specim FX10 which was mounted on a metal frame and the slice is moved perpendicular to the scanned line manually. The stored samples were closed airtight to avoid surface changes. Each hyperspectral cube was cropped to reduce the massive amount of data.

3. Image Analysis

The hyperspectral data (captured with the FX10 or FX17 camera) from each disc were stored in a special format (HSD—hyperspectral data) utilized by Perception Studio. A HSD file contains all spectral bands of a disc in kind of of a hyperspectral cube. It was necessary to convert the data to the ENVI format for which open source image processing libraries are available. Subsequently, for each hyperspectral cube the grayscale images (PNG) for each band were extracted and are denoted as cross-section (CS) images. In case of the FX10 this results in 202 CS-Images and for the FX17 in 196 CS-Images per wood disc. This conversion enables to apply standard image processing algorithms.

For each camera, CS-Images for selected bands of wood disc #E001B are illustrated in Figure 2. It can be recognized that the width of the wood disc for the FX10 and FX17 images differs. We assume that this is caused by the acquisition software and an inaccurate trigger synchronization. In order to assess the similarity between different CS-Images, i.e., to compute distance measures between CS-Images, biometric features for each CS-Image are computed. Biometric features of a CS-Image are denoted as templates. Template computation is performed in two consecutive steps: CS-Registration and Feature Extraction which are described, subsequently.

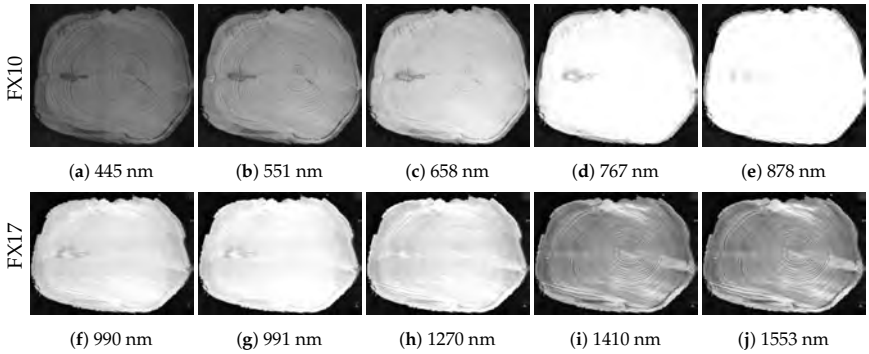

(**a**) 445 nm (**b**) 551 nm (**c**) 658 nm (**d**) 767 nm (**e**) 878 nm

(**f**) 990 nm (**g**) 991 nm (**h**) 1270 nm (**i**) 1410 nm (**j**) 1553 nm

Figure 2. Exemplary cross-section (CS)-Images from different hyperspectral bands of the wood disc #E001B.

3.1. CS-Registration

Initially, the CS area in each CS-Image needs to be localized, i.e., segmented from the background. For this purpose, the feature-based segmentation approach by [26], which is based on a combination of superpixels and GraphCut regularization, was utilized. For our experiments we utilized the Python code (https://borda.github.io/pyImSegm/) provided by the authors. Color features were utilized and each CS-Image was segmented into two labels in order to segment fore- and background. Figure 3a,b show exemplary segmentation results for wood disc #E001B for the first band captured with the FX10 and FX17, respectively. The superpixel clustering is based on Simple Linear Iterative Clustering (SLIC) for which we utilized a superpixel size of 40 pixel and for the regularization parameter a value of 0.25. The segmentations are computed using the variant where the Gaussian Mixture Model (GMM) is created from a set of images, in our case from all CS-Images of a band and camera. Each segmentation result was further processed in order to remove holes and to select the largest area for which the concave hull was determined. The concave hull coordinates were stored for each CS-Image.

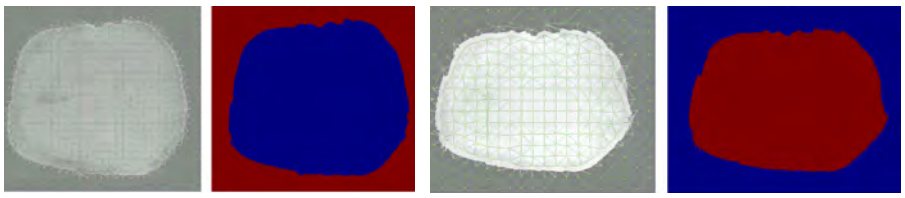

(**a**) FX10—#E001B at 445 nm (**b**) FX17—#E001B at 990 nm

Figure 3. Unsupervised segmentation using superpixel, model estimation and GraphCut.

All computations which are described subsequently, were performed using Java code which was was developed in the context of the respective publications and extended for this work. For specific details, we refer to the referenced publications. Same as in previous works (e.g., [10]), biometric templates of CS-Images are computed in order to assess the similarity of CS-Images of a wood disc captured at different wavelengths. Therefore, the CS is registered to a unique position in terms of rotation and scale. The pith position serves as unique reference point and is determined using the approach proposed in [17]. Local orientation estimates and their intersections are utilized to determine a candidate for the pith position. Local orientation estimates are computed in the segmented CS area. In Figure 4, the pith estimation results for wood disc #E001B captured with the spectral camera FX10 and F17 are shown in the first and second row, respectively. Furthermore, the center of mass (CM) is computed and the pith position to CM vector is used to rotationally align the CS to the horizontal axis

as shown in images of the first and second column of Figure 4. Rotated images are scaled to a width of 400 pixels which results in a registered CS-Image. Consequently, for all registered CS-Images the pith to CM boundary vector has a fixed length of 200 pixels. This differs to the width utilized in our previous works due to the lower image resolution provided by the spectral cameras. Furthermore, our feature extraction approach is based on a circular grid as described in the next section.

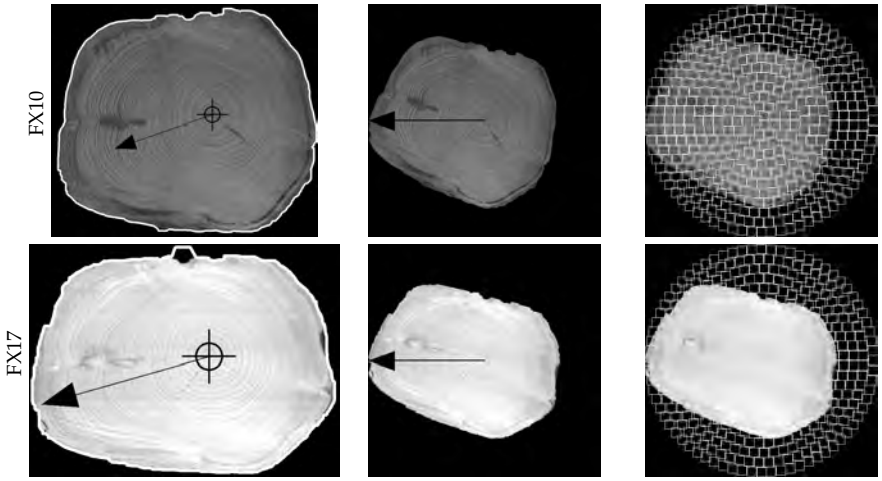

(**a**) Pith Estimation/Segmentation (**b**) Registrated CS (**c**) Circular grid

Figure 4. Illustration of the feature extraction pipeline for wood disc #E001B for the first band of both cameras.

3.2. Feature Extraction

As in [10], the texture-feature based approach by [27] is adopted and extended to compute and compare CS-Codes from CS-Images. Thus, the Gabor filterbank is extended to six different filters based on the following parameters: $G(\lambda,\theta,\sigma,\gamma) = G(\lambda,\sigma) = ((2,1),(3.5,2),(4.5,3),(5.5,3),(6.5,3),(7.5,3)),\theta = \{0,22.5,...,135,157.5\},\gamma = 0.7$. λ is the filter wavelength, θ represents the orientation, σ is the standard deviation and γ specifies the filter aspect ratio. This filterbank enables to capture the annual ring pattern frequency and orientation in local regions.

For feature extraction, the Gabor filterbank is applied to the local image regions of the registrated CS-Image, predefined by the circular grid as shown in the images in the right column of Figure 4.

Only local image regions within the CS area are processed. For each local region the Gabor filterbank is applied which results in a filter response for each filter. For each filter response the standard deviation is computed which leads to a feature vector with 48 standard deviation values per local region. Finally, the biometric template of a CS-Image is composed by all feature vectors computed for the local regions in the circular grid. Feature vectors of local regions outside the CS are set to NULL. Note, that in previous works a rectangular grid was utilized. This should have less impact on the biometric templates but is suited to reduce the size of the biometric templates because a large amount of background region is ignored while the shape information still is part of the biometric template.

3.3. Template Matching

In [8], three different matching procedures have been introduced. Note, that for this work no rotation compensation in the matching procedure is required. There are no rotational variations to compensate for. The first matching procedure of [8] which is focused on annual ring pattern

information is utilized. This procedure is denoted as an annual ring pattern matching score (MS_{AP}). The aim of the other two procedures is to include shape information and the results in [8] confirmed the positive impact in terms of discriminative power resulting in a higher recognition accuracy. We are mainly interested in changes of the textural information shown at different wavelengths and thus shape information is not valuable. MS_{AP} for two CS templates is computed by

$$MS(CS_1, CS_2) = \frac{1}{M} \sum_{i=0}^{n} D(CS_1(i), CS_2(i)) \quad (1)$$

where CS_1, CS_2 are two feature vectors of the CS-Codes which are compared, i specifies the index of the local region. As distance function (D) the L1 norm is utilized which outperformed the L2 norm in a previous work [28]. The distance function (D_{AP}) ignores feature vector pairs which are not in the intersection of both CSs. In the current implementation this is the case if one of both feature vectors is set to NULL. For normalization, M is defined by the amount of considered feature value pairs.

4. Experiments and Results

For the experimental evaluation for all spectral CS-Images of each wood disc, captured with FX10 or FX17, biometric templates were computed. For each wood disc and the captured spectral CS-Images with a camera, the segmentation result computed for the first band (FX10 = 444 nm, FX17 = 990 nm) and the group segmentation model is utilized for all other spectral CS-Images. In the exactly identical way the pith is estimated for the segmented CS-Image from the first band and utilized for the remaining.

This ensures that all CS-Images of a wood disc captured with a camera are registrated in the exact same way. This is crucial in order to avoid side affects caused by varying segmentation and pith estimation results. Furthermore, for some bands CS segmentation is very difficult and pith estimation is impossible due to the absence of a clear annual ring pattern (see Figure 2). For feature extraction, a local region size of 16 pixel was utilized and biometric templates were computed for all CS-Images.

Matching scores were computed for all pairs of biometric templates from each wood disc captured with a camera. In human biometrics scores computed between templates of one individual are are referred to as intraclass scores. Interclass scores are computed between templates from different individuals. For this work, we denote intraclass scores which are computed between templates from on individual but different bands as spectral scores. Interclass scores are computed between biometric templates from different wood discs for the same band.

Based on the spectral scores, the similarity and non-similarity of different spectral bands is analyzed. The interclass scores for each band enable to draw conclusions on the suitability of the different bands to discriminate between different wood discs. The overall mean spectral distances of all pairs of spectra for 100 wood discs of each camera are shown in the distance matrices of Figure 5. This distance matrix is calculated for all CS's hence it can be seen if the spectral score between different spectra bands can be observed for all CS's or not.

The matrices in Figure 5 are symmetric and bright areas indicate that the feature vectors between two spectra bands are similar while dark areas indicate that feature vectors between two spectra bands are different. In Figure 5a,b the results for one specific CS-image (#E001B) are shown and compared to the mean values over all CS-images in Figure 5c,d. Based on this matrix for the spectral camera FX10 (see Figure 5c) two different spectral ranges are estimated by visual inspection. These are the spectral ranges from 450 nm to approx. 740 nm and from 740 to 950 nm. These two ranges seem to show different features, as the feature vectors are different. For the spectral camera FX17 (see Figure 5d) it is estimated that there are three different spectral ranges (from 900 nm to 1150 nm, from 1050 nm to 1360 nm and from 1360 nm to 1800 nm) where the feature vectors show different values based on the matching score.

To get an impression about the usability of different spectral bands for log traceability the mean interclass scores per band for all CSs are shown in Figure 6. Note that no normalization has been applied. A high mean-interscore expresses that the matching scores between CS-Images from different

wood discs are high and the wood discs are not similar to each other. A low mean-interscore shows that different wood discs are very similar to each other which is a problem for a biometric system.

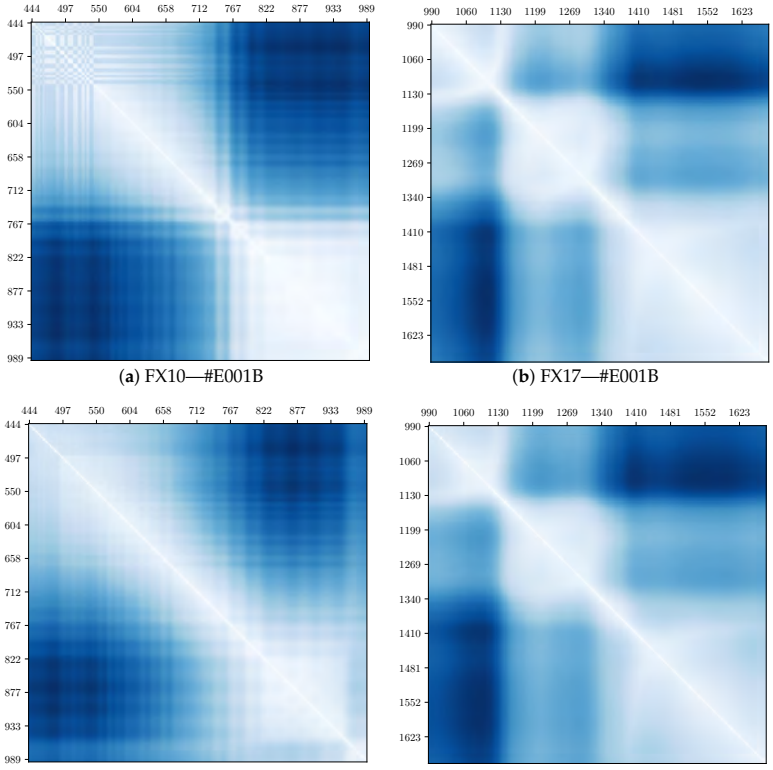

(**a**) FX10—#E001B (**b**) FX17—#E001B

(**c**) FX10—Mean spectral distances (**d**) FX17—Mean spectral distances

Figure 5. The distance matrices illustrate the spectral distances computed for all bands captured with the FX10 and FX17 hyperspectral camera. In the first row, the distance matrices for disc #E001B are shown and in the second row the mean distance matrices for all 100 discs are illustrated.

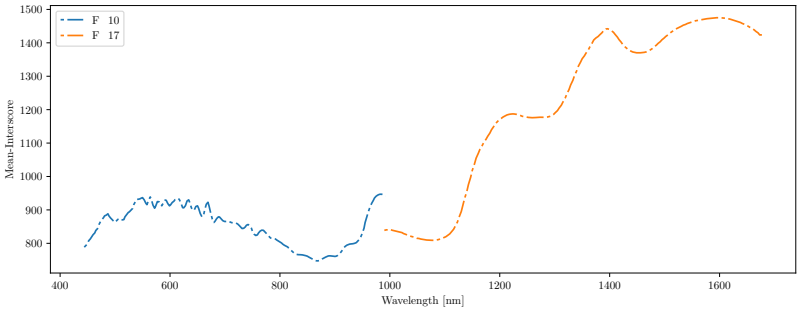

Figure 6. Mean interscores for all captured spectral bands.

The higher the mean-interscore, the more discriminative are the CS-Images of the 100 discs in the chosen spectral band, i.e., if this value is high, this spectral band is good to identify different log end faces. Based on the interclass-scores in Figure 6, it seems that the NIR spectra (>760nm) are much better for detecting different log end faces as the interclass scores are much higher for the spectral bands of spectral camera FX17 compared to the spectral camera FX10. Furthermore, approx. five local maxima can be expected out of the mean-interscore plot, two for the spectral camera FX10 and four for camera FX17 while one peak appears in the crossing spectra measured by camera FX10 and camera FX17 and is only counted as one. The wavelength at the peaks in the NIR spectra correspond to specific overtones of OH-bond and CH-bond vibration modes what allows a chemical interpretation of these observations.

5. Conclusions

The results of the spectral analysis showed that log end face images improved with hyperspectral camera systems in the spectral range between 400 nm and 1800 nm lead to different images. This supports the assumption that it is possible to gain additional information about one log end face if images in different spectral ranges are taken.

The fingerprint related method of feature extraction was applied successfully which led to specific feature vectors per image. These vectors are the basis to calculate pattern matching scores. The matching scores are used to investigate the similarity of spectral bands per log end face and the differences between the different log end faces per spectral band. The following observations were made for the investigated samples: In the spectral range between 450 nm and 1000 nm two intervals to gain different spectral images were observed and in the spectral range between 1000 nm and 1700 nm three intervals to gain different spectral images were observed. Based on this observation, it is assumed that up to 5 spectral bands (one of each spectral range) contain most of the information within the feature vectors. This assumption is supported by the results of the interscores between the log end faces per spectra. Here it can also be seen that the differentiation between logs takes local maxima in five different spectral band regions. There is evidence that the NIR spectra create a better distinction between different log end faces than the visible spectra. The objective of this study was the development of a methodological basis to use hyperspectral images for log tracking. The results are promising for the development of a system based on the methods described, but it is not possible to derive an overall valid model for Norway spruce wood (picea abies [L.] Karst.) or other wood species from this specific sample.

Nevertheless, the method shown is applicable to use hyperspectral imaging for different wood samples and species and we invite different research groups in log tracking all over the world to work on this approach to develop the basis for a globally accepted log tracking system, as wood trade is a global issue.

Further investigations should and will focus on following questions:

- More detailed analysis on the 'best' spectral bands for the camera system. It is assumed that cameras which works in two up to four different spectral bands will be applied in the future.
- Usage of wood log end faces from different locations and different wood species to be able to work in practical surroundings.
- Development and implementation of statistical process control methods to optimize the production processes between forest and forest product industries.

Summarizing the usage of hyperspectral images are promising to reach a tracking method for wood logs and the next steps will be from lab scale to field application. Therefore the technical equipment necessary has to be reduced and the analysis algorithms have to be improved. For both tasks the findings in this work are useful and existing results of other fields of research (e.g., algorithms from remote sensing) will be utilized in future research.

Author Contributions: Conceptualization: A.P. and R.S.; methodology: A.P. and R.S.; software: R.S.; validation: A.P. and R.S.; formal analysis: A.P. and K.E.; data curation: R.S.; writing—original draft preparation: A.P., K.E. and R.S.; writing—review and editing: T.Y., A.U. and K.E.; visualization: R.S. All authors have read and agreed to the published version of the manuscript.

Funding: This research was funded by the Austrian Science Fund (FWF) under the grant number I 3653.

Acknowledgments: The authors thank the support of open access funding by the Austrian Science Fund (FWF).

Conflicts of Interest: The authors declare no conflict of interest.

Abbreviations

The following abbreviations are used in this manuscript:

CS	Cross-section
UV	Ultra-violet
VIS	Visible-light
NIR	Near-infrared
MS	Matching score
CM	Center of Mass

References

1. FSC. Homepage of the Forest Stewardship Council. Available online: www.fsc.org (accessed on 21 April 2020).
2. PEFC. Homepage of the Programme for the Endorsement of Forest Certification. Available online: www.pefc.at (accessed on 21 April 2020).
3. EuropeanParliament. *Regulation (EU) No 995/2010 of the European Parliament and of the Council of 20th October 2010 Laying Down the Obligations of Operators Who Place Timber and Timber Products on the Market*; EuropeanParliament: Brussels, Belgium, 2010.
4. Evergreen. Homepage of the Evergreen Innovation Camp 2019 in Vienna. Available online: www.evergreen-innovationcamp.io (accessed on 21 April 2020).
5. Tzoulis, I.; Andreopoulou, Z. Emerging Traceability Technologies as a Tool for Quality Wood Trade. *Procedia Technol.* **2013**, *8*, 606–611. [CrossRef]
6. Björk, A.; Erlandsson, M.; Häkli, J.; Jaakkola, K.; Nilsson, Å.; Nummila, K.; Puntanen, V.; Sirkka, A. Monitoring environmental performance of the forestry supply chain using RFID. *Comput. Ind.* **2011**, *62*, 830–841. [CrossRef]
7. Schraml, R.; Petutschnigg, A.; Uhl, A. Validation and Reliability of the Discriminative Power of Geometric Wood Log End Features. In Proceedings of the IEEE International Conference on Image Processing (ICIP'15), Quebec City, QC, Canada, 27–30 September 2015. [CrossRef]
8. Schraml, R.; Hofbauer, H.; Petutschnigg, A.; Uhl, A. Tree Log Identification Based on Digital Cross-Section Images of Log Ends Using Fingerprint and Iris Recognition Methods. In Proceedings of the 16th International Conference on Computer Analysis of Images and Patterns (CAIP'15), Valletta, Malta, 2–4 September 2015, Springer: Berlin, Germany, 2015; pp. 752–765. [CrossRef]
9. Schraml, R.; Charwat-Pessler, J.; Petutschnigg, A.; Uhl, A. Towards the applicability of biometric wood log traceability using digital log end images. *Comput. Electron. Agric.* **2015**, *119*, 112–122. [CrossRef]
10. Schraml, R.; Hofbauer, H.; Petutschnigg, A.; Uhl, A. On rotational pre-alignment for tree log end identification using methods inspired by fingerprint and iris recognition. *Mach. Vis. Appl.* **2016**, *27*, 1289–1298. [CrossRef]
11. Chiorescu, S.; Grönlund, A. The Fingerprint approach: using data generated by a 2-axis log scanner to accomplish traceability in the sawmill's log yard. *For. Prod. J.* **2003**, *53*, 78–86.
12. Chiorescu, S.; Grönlund, A. The Fingerprint Method: Using Over-bark and Under-bark Log Measurement Data Generated by Three-dimensional Log Scanners in Combination with Radiofrequency Identification Tags to Achieve Traceability in the Log Yard at the Sawmill. *Scand. J. For. Res.* **2004**, *19*, 374–383. [CrossRef]
13. Flodin, J.; Oja, J.; Grönlund, A. Fingerprint traceability of logs using the outer shape and the tracheid effect. *For. Prod. J.* **2008**, *58*, 21–27.

14. Flodin, J.; Oja, J.; Grönlund, J. Fingerprint traceability of sawn products using industrial measurement systems for x-ray log scanning and sawn timber surface scanning. *For. Prod. J.* **2008**, *58*, 11.
15. Longuetaud, F.; Mothe, F.; Kerautret, B.; Krähenbühl, A.; Hory, L.; Leban, J.M.; Debled-Rennesson, I. Automatic knot detection and measurements from X-ray CT images of wood: A review and validation of an improved algorithm on softwood samples. *Comput. Electron. Agric.* **2012**, *85*, 77–89. [CrossRef]
16. Breinig, L.; BrüChert, F.; Baumgartner, R.; Sauter, U.H. Measurement of knot width in CT images of Norway spruce (Picea abies [L.] Karst.)-Evaluating the accuracy of an image analysis method. *Comput. Electron. Agric.* **2012**, *85*, 149–156. [CrossRef]
17. Schraml, R.; Uhl, A. Pith Estimation on Rough Log End Images using Local Fourier Spectrum Analysis. Proceedings of the 14th Conference on Computer Graphics and Imaging (CGIM'13), Innsbruck, Austria, 12–14 February 2013. [CrossRef]
18. Charwat-Pessler, J.; Schraml, R.; Entacher, K.; Petutschnigg, A. Tracking logs with RGB images within the wood supply chain: a preliminary study on image acquisition. *For. Prod. J.* **2015**, *66*, 176–184.. [CrossRef]
19. Camps-Valls, G.; Tuia, D.; Gómez-Chova, L.; Jiménez, S.; Malo, J. *Remote Sensing Image Processing*; Morgan and Claypool: San Rafael, CA, USA, 2011.
20. Richards, J.A.; Jia, X. *Remote Sensing Digital Image Analysis: An Introduction*; Springer: New York, NY, USA; Berlin/Heidelberg, Germany, 2006.
21. Bioucas-Dias, J.; Plaza, A.; Camps-Valls, G.; Scheunders, P.; Nasrabadi, N.; Chanussot, J. Hyperspectral Remote Sensing Data Analysis and Future Challenges. *IEEE Geosci. Remote Sens. Mag.* **2013**, *1*, 6–36. [CrossRef]
22. Svendsen, D.H.; Martino, L.; Camps-Valls, G. Active emulation of computer codes with Gaussian processes—Application to remote sensing. *Pattern Recognit.* **2020**, *100*, 107103. [CrossRef]
23. Ruano, A.; Zitek, A.; Hinterstoisser, B.; Hermoso, E. NIR hyperspectral imaging (NIR-HI) and μXRD for determination of the transition between juvenile and mature wood of Pinus sylvestris L. *Holzforschung* **2019**, *73*, 621–627. [CrossRef]
24. Chen, J.; Li, G. Prediction of moisture content of wood using Modified Random Frog and Vis-NIR hyperspectral imaging. *Infrared Phys. Technol.* **2020**, *105*, 103225. [CrossRef]
25. Ma, T.; Inagaki, T.; Ban, M.; Tsuchikawa, S. Rapid identification of wood species by near-infrared spatially resolved spectroscopy (NIR-SRS) based on hyperspectral imaging (HSI). *Holzforschung* **2019**, *73*, 323–330. [CrossRef]
26. Borovec, J.; Švihlík, J.; Kybic, J.; M.D., D.H. Supervised and unsupervised segmentation using superpixels, model estimation, and graph cut. *J. Electron. Imaging* **2017**, *26*, 1–17. [CrossRef]
27. Jain, A.; Ross, A.; Prabhakar, S. Fingerprint matching using minutiae and texture features. In Proceedings of the International Conference on Image Processing (ICIP'01), Thessaloniki, Greece, 7–10 October 2001; Volume 3, pp. 282–285.
28. Schraml, R.; Charwat-Pessler, J.; Uhl, A. Temporal and longitudinal variances in wood log cross-section image analysis. In Proceedings of the IEEE International Conference on Image Processing (ICIP'14), Paris, France, 27–30 October 2014. [CrossRef]

This article has been accepted for publication in a future issue of this journal, but has not been fully edited. Content may change prior to final publication. Citation information: DOI 10.1109/TII.2020.3006933, IEEE Transactions on Industrial Informatics

Towards fish individuality-based aquaculture

Rudolf Schraml[1,*], Heinz Hofbauer[1], Ehsaneddin Jalilian[1], Dinara Bekkozhayeva[2], Mohammadmehdi Saberioon[2], Petr Cisar[2], and Andreas Uhl[1]

[1]Department of Computer Sciences, University of Salzburg, Austria
[2]Institute of Complex Systems, University of South Bohemia in České Budějovice, Czech Republic

***Abstract*—By bringing concepts of precision farming to intensive aquaculture fish production, it can be optimized to be more sustainable while focusing on fish welfare criteria. This requires a shift from mass to smart production and to consider each fish as an individual. Therefore, it is required to be able to identify each fish in a tank or sea cage. In this paper, we prove the feasibility of fish identification using the iris as a biometric characteristic. Based on a new dataset, captured in a controlled out of water environment (i) a fully automated iris recognition system is presented and utilized for the experiments and (ii) the distinctiveness and the stability of the iris pattern of Atlantic salmon (*Salmo salar*) is assessed. Results prove the distinctiveness, which indicates that the iris pattern of Atlantic salmon is suited for biometric identification. However, the iris pattern has a low stability, which means it changes over time. Due to frequent interaction of fish and system, usually multiple times a day during feeding, there is ample opportunity keep the biometric template up-to-date which makes the lack of long-term stability a non-issue. It can be concluded that a biometric fish identification system is feasible, with the precondition that biometric templates of each fish are periodically updated to combat the low stability.**

***Index Terms*— Precision Fish Farming, Fish Iris Identification**

I. Introduction

The production requirement of aquaculture in the last 30 years has risen steeply and continues to do so. The edible fish consumption per capita is rising and outpaces the naturally occurring fish population, making this consumption sustainable only through aquaculture production. This trend will not decline and aquaculture production plays a crucial role to ensure sustainable development in economic, social and environmental terms [1].

For intensive aquaculture, the fish is cultivated in tanks or sea cages. An increase in production can often only be achieved through a higher density of fish. This exacerbates problems in the management of disease and health of the fish. Optimization of fish production therefore also requires an improvement of fish welfare. Towards Precision Fish Farming (PFF) control-engineering principles are applied to fish production, thereby improving the farmer's ability to monitor, control and document biological processes [2]. The move from mass to smart production allows application of control-engineering principles to individual fish instead of the population as a whole. It is all about data which is collected, analyzed and exchanged almost in real time, allowing for medication or removal of individual fish as well as the optimization of yield per fish. Smart production requires that data is assigned or linked to a set of objects or single (living) objects in the production. Data and information enable to improve and/or completely rethink well-established processes.

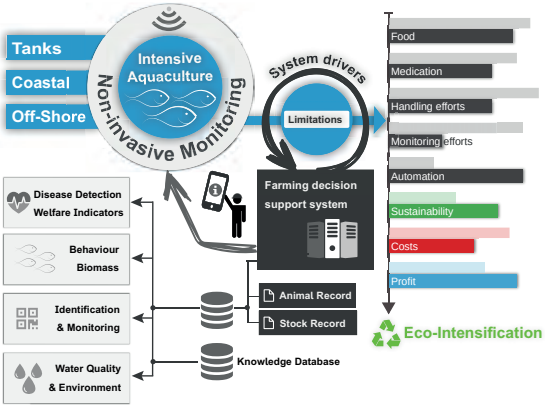

Fig. 1: Farming decision support system (FDSS)

Further, regarding intensive aquaculture considering each fish as an individual, requires non-invasive monitoring to set up a farming decision support system (FDSS). *This type of smart fish farming as envisioned by a FDSS relies on the identification of individual fish*. Fig. 1 illustrates our vision for such a system which follows the paradigm of ecological intensification. This system enables to assign information about fish traits such length, weight, sex and maturity and fish skin colour during different growth stages to the corresponding animal or stock record, to monitor growth status for better management [3]. Common ways for individual identification of fish are invasive methods relying on tagging and marking [4]. Invasive methods may cause technical as well as health and animal behavioral problems amplifying a problem we want to solve. Even currently available non-invasive approaches (e.g. external colorants) may cause behavioural alteration and pose health risks which require to take care of welfare issues [5]. Furthermore, invasive identification is time consuming and incurs a substantial cost. *To avoid these problems and additional cost it would be optimal to be able to have a non-invasive and contact free identification method.*

For this work, and the envisioned FDSS, the focus is on non-invasive fish identification using biometric characteristics of the fish body. Specifically, we will evaluate the suitability of the iris for this purpose since it is always visible (due to lack of eyelids), permanent (as opposed to skin patterns e.g. [6]) and has a good track record for humans and other animals (e.g. for cow identification [7]).

* Corresponding author. E-mail: rudi.schraml@gmail.com
This work is partially funded by the Austrian Science Fund (FWF) under Project No. I 3653 and by the AquaExcel2020 TNA Project AE050006.

This article has been accepted for publication in a future issue of this journal, but has not been fully edited. Content may change prior to final publication. Citation information: DOI 10.1109/TII.2020.3006933, IEEE Transactions on Industrial Informatics

First, in Sec. II, a review on related work is presented, followed by the main contributions of this work. Sec. III introduces the computation and matching of fish iris codes. The experimental setup and evaluation is presented in Sec. IV followed by the conclusions in Sec. V.

II. Related Work and Contributions

Literature on fish identification can be categorized based on (i) the direction from which the fish and the biometric characteristic is captured: Lateral, Dorsal or Ventral and (ii) based on the utilized feature extraction/ matching approach, e.g. skin pattern or shape features. Although there exists plenty of research, only a few approaches make use of machine vision methods.

In the works of [8], [9], [10] the identification of different fish species was examined on the basis of lateral images. The regions, utilized for biometric feature extraction, were selected manually. For Patagonia catfish identification in [8] skin pattern spots were marked manually (position, size) and three reference points set the region of interest (ROI). For 45 fish, which were captured 14 times for 254 days, a Rank-1 identification accuracy of 96% was reported. Similarly, for Atlantic salmon identification in [9] spots were marked manually and utilized for a specific matching algorithm, requiring at least 3 spots. At the age of 12 months most fish showed less than three spots and 17 out of the 20 remaining fish were identified correctly. For lionfish identification in [10] three different ROIs were selected in which SURF (Speeded up robust features) keypoints are detected, computed and used for matching. For the best body part (flank) and 48 individuals, captured at one point in time, the authors report a Rank-1 identification accuracy of 68%.

In [11], [12] dorsal head view images were assessed as biometric characteristic. For Chinook salmon identification in [11] the ROI was marked manually, the spot pattern was binarized and the spot centroid coordinates were used as biometric features. Results show 100% identification accuracy for fish which developed a pattern, which was only the case for 42% of all fish (=295 fish captured seven times over 251 days). The authors of [12] used a reverse image search engine to assess delta smelt identification based on three manually selected ROIs. Fish were captured at three points in time and for the fusion of the two best areas, an identification rate of 94% for adjacent sessions and 59.2% between the first and the last session was reported.

In [5] naked-eye and computer-assisted identification of armored catfish based on ventral images, captured in laboratory and field conditions, were evaluated. The computer-assisted approach is based on SIFT (Scale invariant feature transform) key points. ROIs were selected manually and results for 120 comparisons from the laboratory and 224 comparisons from the field data showed an identification accuracy (Rank-1) of 82.2% and 93.8%, respectively. These prior works have two major shortcomings:

- Manual annotation of the ROI and/or the utilized biometric information/pattern is required. Such an approach is well suited for small-scale experiments, but it is not applicable on a large scale, i.e. for intensive aquaculture and the envisioned FDSS. For example, the authors in [5] reported that for 225 comparisons, 17 minutes were required for computer assisted identification.
- Related literature has shown that the skin pattern is not universal; some fish do not form them and are not stable once formed. That is, the assessed skin patterns change over time and some fish showed no pattern at all or only formed them at some later stage of growth. This can even vary for minimal divergence from a base strain of fish; for example, [6] showed that some Zebrafish mutations show no more pattern at all.

Regarding these shortcomings, we will look at iris patterns in Atlantic salmon as member of the Salmonidae family. All members of this family have eyes and are lidless, making the iris a universal trait. The basic layout of the iris biometric toolchain known from human iris biometric identification will be used (and be described later). While this solution sounds reasonable, the following has been evaluated in order to see if the iris is a usable biometric characteristic.

Localization and Orientation of the Iris: To establish fully automated fish identification, it is required to detect the iris region automatically and to rotationally pre-align each iris preliminary to feature extraction and matching. Hence, for the Atlantic salmon iris, a segmentation approach is introduced, and a set of rotational pre-alignment strategies is tested.

Stability: The lifespan of an intensive aquaculture fish is short, but the fish grows rapidly within this timespan. Thus, another contribution of this work is to evaluate the stability of the Atlantic salmon iris pattern, i.e. if and how the pattern changes over time.

Automatic Iris Recognition System: In contrast to other works in this field, the evaluation is done using state-of-the-art biometric system evaluation protocols and metrics. Regarding fish iris image processing and biometric identification a fully automated system will be assessed.

R^3 Research principles: Replicability, Reproducibility and Reusability. In order to repeat, improve or develop new methods for fish iris biometry a database is required. Thus, we make public the acquired database of fish iris images (see Sec. IV-A) including source code and libraries at a GitHub repository[1].

To sum up: Our contribution is a state-of-the-art based fish iris identification system based on a universal trait. However, we note that the main objective of this work is to assesses the basic feasibility of such a system and that the experimental evaluation is based on fish iris images acquired in a controlled out of water environment.

III. Fish Iris Codes (FICs)

The first step in the biometric toolchain is to acquire an iris image for which an FIC is computed in four consecutive steps (see Fig. 2): iris segmentation, rotational pre-alignment, iris normalization and feature extraction.

A. Fish iris anatomy

The anatomy of fish eyes is similar to the human eye anatomy on a basic level. Considering the human eye we are

[1] https://github.com/rschraml/fishid

This article has been accepted for publication in a future issue of this journal, but has not been fully edited. Content may change prior to final publication. Citation information: DOI 10.1109/TII.2020.3006933, IEEE Transactions on Industrial Informatics

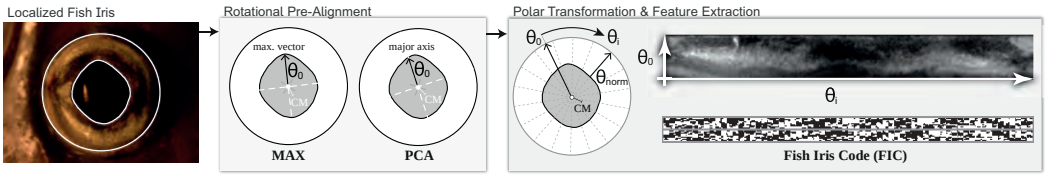

Fig. 2: Illustration of the pipeline to generate the fish iris code (FIC) from a segmented image.

looking at the stroma, a fibrovascular layer connecting the sphincter (for closing the iris) and dilation (for opening the iris) muscles or the eye. The layer consists of fibers (fibro-), some running in a circular pattern, but mostly radially mixed with nerves and blood vessels (-vascular). In addition to the fibres the dilation muscle also runs along the radial axis. The formation of the fibres in the stroma is different for individuals and stable over time which makes it a perfect candidate for biometric recognition of humans. If the stroma contains pigments it appears dark and the structures are not apparently visible. To counteract this, the human iris is captured with near-infrared cameras where the pigmentation does not interfere with image acquisition.

For fish there are differences pertaining the iris which are not uniform over classes of fish. Iris of different fish species can differ in terms of muscle, shape and function, which leads to a non-circular iris pattern, for example. As such the usability of the iris for fish identification has to be judged for different fish classes and species. For salmon the iris is non-functional in that it does not open or close to moderate light, i.e. it does not exhibit a photometric response. Instead, the salmon uses retinomotor movement of photoreceptors and retinal pigmentation to change the light exposure of rods and cones [13], [14]. The iris is well formed and prominent despite its vestigial function. It is an extension of the epithelial pigment layer of the retina (which is used to moderate illumination)[15]. The pupillary opening shows rounded diamonds shape (see Fig.2).

B. Fish iris segmentation

For iris recognition the pupillary boundary, i.e., between pupil and iris, and the limbic boundary, i.e. , between iris and sclera (the white of the eye in humans), need to be detected. This allows (i) to segment the ROI containing the biometric information and (ii) to polar transform this ROI to an uniform rectangular representation. Traditional human iris segmentation approaches are not well suited as they often rely on the circular shape of the human iris. For example, we mention the segmentation approaches CAHT (Contrast-adjusted Hough Transform) [16] and WAHT (Weighted Adaptive Hough and Ellipsopolar Transform) [17]. Preliminary experiments using a traditional morphological-based segmentation approach led to poor results which are not worth to be considered. However, recent research showed segmentation approaches based on Convolutional neural networks (CNN) which are well suited for human iris segmentation. For instance the authors in [18] show that a CNN-based semantic segmentation approach outperforms traditional approaches like CAHT in case of low quality databases. Based on this insight, the inapplicability of traditional iris segmentation methods and the insufficient results with the tested morphological approach a CNN-based

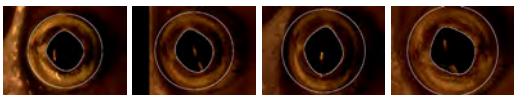

Fig. 3: CNN-based segmentation results for fish #0F571E captured in 4 time delayed sessions. As shown, the iris is growing significantly from Session 1 to 4, accompanied by changes in the iris pattern.

semantic segmentation approach, requiring groundtruth data, has been envisioned. Thus, for all images in the utilized database the pupil (=inner boundaries shown in Fig. 3) was detected in a semi-automated manner. The black pixels of the pupil where clustered, holes where filled and the boundaries were corrected manually to avoid under/over segmentation. The limbic boundary (=outer boundary) was approximated based on the pupillary boundary. Basically, by a circle the center of which is defined as the pupil center of mass (CM). The radius is $2\times$ larger as the mean distance between the CM to pupillary boundary vector lengths. Thw semi-automated estimated pupillary boundary and approximated limbic boundary are supposed to bound the groundtruth for the iris.

CNNs are a multi-layered class of artificial neural networks that gained great success in resolving many key computer vision challenges such as visual segmentation. The network architecture we used to segment the fish pupil is identical to the "SegNet-Basic" fully convolutional encoder-decoder network [19]. The network's encoder architecture is organized in four stocks, containing a set of blocks. Each block comprises a convolutional layer, a batch normalization layer, a ReLu layer, and a Pool layer with kernel size of 2×2 and stride 2. The corresponding decoder architecture, likewise, is organized in four stocks of blocks, whose layers are similar to those of the encoder blocks, except that here each block includes an up-sampling layer. The decoder network ends up to a softmax layer which generates the final segmentation map. The network implementation is realized in the Caffe deep learning framework. As ground-truth data the semi-automated segmented pupils were utilized. In order to perform the segmentation on all available images in the database and yet keep the training and testing separate, we used the Two-Fold training scheme. In particular, we divided the whole database into two equal parts, and used one part as our testing data and the other one as our training data. Then, we switched the training and testing folds, and so we obtained the pupillary boundary for each iris image in the database. The limbic boundary was approximated in the same way as for the semi-automated segmentation. Exemplary results are shown in Fig. 3.

C. Rotational pre-alignment & polar transformation

During matching of two FICs rotation compensation can be performed by comparing shifted versions of the FICs. However, the available fish iris data shows exceptionally strong

This article has been accepted for publication in a future issue of this journal, but has not been fully edited. Content may change prior to final publication. Citation information: DOI 10.1109/TII.2020.3006933, IEEE Transactions on Industrial Informatics

rotational differences between images of the same iris (see Fig. 3). Compensating for such large angular differences is too slow. The goal of rotational pre-alignment preliminary to feature extraction is to reduce the rotational differences to an extent where they can be compensated in the matching phase without undue loss of speed. For this work two different pre-alignment strategies (PCA, MAX) have been implemented which are assessed in the experimental evaluation (see Fig. 2). Both strategies rely on the observation that the fish pupil is not circular and thus it is assumed that a pre-alignment vector (Θ_0) can be determined. For the first strategy, principal component analysis (PCA) is applied to the points of the pupillary area which leads to two perpendicular eigenvectors giving the major axes of the pupillary. The dominant axis is then used as pre-alignment vector. For MAX the pupillary boundary is first smoothed with a Gaussian filter and the vector with the maximum CM to pupillary boundary distance is utilized as pre-alignment vector (Θ_0). In the experiments it was observed that for both approaches it happens that for iris images captured at different dates the pre-alignment can lead to 90° flipped versions.

D. Normalized polar transformation

Features are extracted from a normalized iris texture. Note that no image enhancement has been applied to the iris texture. The iris is polar transformed using Daugman's rubber-sheet model [20], this is in essence an unrolling of the iris texture, and stretching to a uniform size. This normalization corrects two factors which can lead to a different iris texture area: 1) The distance and angle between the camera and iris can vary which introduced a scale change and geometric distortion; and 2) as the fish grows, so does the skeletal and soft tissue, including the eye. The polar transformation on the other hand allows for a rotation of the eye to be expressed as a horizontal shift, which is much easier to compute. Such a rotation can happen due to a rotation of the fish in the water or of the eyeball in the eye-socket. For our normalized polar transform Θ_0 (calculated in prior steps) is used as initial vector to unroll the iris into the polar domain and is aligned at the left boundary of the transformed fish iris (see Fig. 2). For normalization each pixel in the polar image is stretched according to the length of Θ_{norm} which is specified as the largest pupillary to limbic boundary vector. For the transformation bicubic interpolation is applied.

E. Feature Extraction

For feature extraction and matching of FICs we use the open University of Salzburg Iris Toolkit (USIT) [21]. A note on transfer learning and domain specific improvement: To transfer knowledge from one domain (human iris) to another (fish iris), we simply used the USIT methods as is to see what does work and what doesn't. Specifically, the 1-D-Log-Gabor [16] based feature extraction worked very well and we kept that as is, the segmentation on the other hand did not work at all, mostly due to a difference in the shape of the iris and periocular tissue, so most of our attempts to improve the knowledge transfer fell into this part (=feature extraction) and the polar transformation of the iris biometric toolchain.

(a) Dino-Lite AM3113T with spacer

(b) Fish with ID #0F571E –Session 1

Fig. 4: SSIDB: Utilized sensor and exemplary lateral image of an Atlantic salmon fish from the LT dataset

1-D local Gabor features are extracted from a number of 1-D signals. To generate the 1-D signals from the texture we first split the texture into horizontal bands with a height of roughly 8% of the distance from pupillary to limbic boundary. Then the remaining verticality is removed by averaging the values for each horizontal position. This combination of information along the radial axis counteracts sampling artifacts due to resolution and different pupillary dilations. Since the outer boundary is only an approximation we will not use the outermost parts (about 20%) in the comparison since they might contain scleral or non-eye textures. The Gabor filter used has a real and an imaginary component which roughly equate to an edge (change in signal) and a line (constant signal) filter. This relates to radial edges and lines features in the unrolled image. Note: To reduce the size of the FIC we only use the signs of the line & edge filters which represent the absence of lines and edges respectively.

IV. Experiments & Results

A. Salmon Iris Image Database (SIIDB)

SIIDB was captured 2018 by the authors within the AquaExcel2020 TNA project AE050006, FISHID. SIIDB is hosted at https://github.com/rschraml/fishid. For image acquisition 330 adult Atlantic Salmon (~1kg, 42–46 cm length) were selected initially. The cultivation period is usually between 12 to 18 months in tanks and between 12 to 24 months in sea cages. For iris image acquisition the USB microscope Dino-Lite AM3113T (no additional light) was utilized. A spacer (Fig. 4a) was utilized to keep the distance, roughly constant. Each fish was anesthetized (Fig. 4b) and one iris (head showing to the left) was captured several times (8–16×) with minor rotations caused by movements of the fish. Unusable images due to blur of focus problems were removed. The database is subdivided into a short-term (ST) and a long term (LT) dataset. A schematic overview of the database structure is illustrated in Fig. 5. The ST dataset is composed of iris images from 330 different salmon fish which were captured within

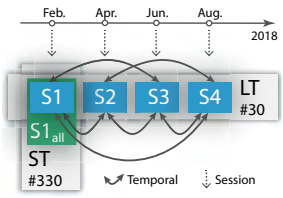

Fig. 5: Testset structure overview

This article has been accepted for publication in a future issue of this journal, but has not been fully edited. Content may change prior to final publication. Citation information: DOI 10.1109/TII.2020.3006933, IEEE Transactions on Industrial Informatics

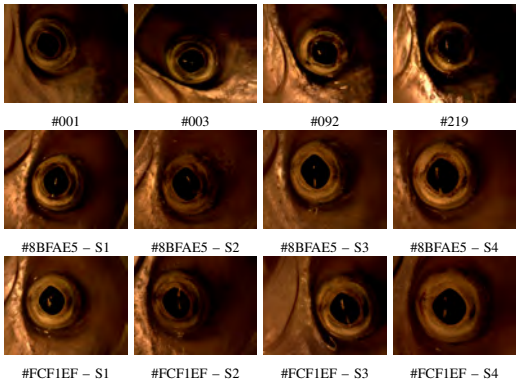

Fig. 6: Exemplary iris images of the ST (row 1) and LT dataset (row 2 & 3)

one week. For the LT dataset a subset consisting of 30 fish from Session 1 (S1) was captured again in three subsequent sessions (S2,S3,S4) with approximately two months time span in between. Exemplary iris images for four different fish of the ST dataset and two fish of the LT dataset are depicted in Fig. 6.

B. Experimental setup

For all fish iris images in the LT and ST dataset FICs were computed for different rotational pre-alignment strategies which results in a set of configurations (MAX, PCA, MAX_{OPT}, PCA_{OPT}) as described in Sec. III-C.

Furthermore, two additional configurations based on PCA and MAX were used, utilizing four FICs per iris image. One FIC is the same as for regular PCA and MAX and the other three have a 90°, 180°and 270°rotational offset from the first. These configurations are denoted as PCA_{ROT} and MAX_{ROT}. The goal is to avoid errors caused due to 90° rotated versions of the same fish iris. During matching the best match (=highest similarity) between the four FICs of each iris is determined and used as matching score (MS). One baseline configuration (NO) is computed without applying rotational pre-alignment. All configurations were computed for semi-automated (GT) and CNN segmented (CNN) fish irides in SIIDB.

For each configuration and all combinations of FICs MSs are computed. MSs which are computed between FICs from the same session are denoted as session MSs and MSs computed between FICs from different sessions as temporal MSs (see Fig. 5). Session MSs are computed for the ST dataset together with the data of S1 from the LT dataset. The corresponding score distribution (SD) is denoted as S1_{all}. Furthermore, session MSs are computed for the different sessions of the LT dataset which results in four different SDs denoted S1,S2,S3 and S4 respectively. Temporal MSs are computed between the different sessions of the LT dataset which leads to six different comparisons: S1↔S2, S2↔S3, S3↔S4, S1↔S3, S2↔S4 and S1↔S4. Note that each session and temporal SD is further subdivided into an intra- and interclass SD which correspond to the genuine and impostor SDs in biometrics [22]. Genuines are MSs computed between FICs from the same fish and impostor MSs are computed between FICs from different fish.

a) Fish iris distinctiveness and stability: The results for ST and LT evaluations present an insight into the distinctiveness (same session performance) and stability (change over time) of the Atlantic salmon fish iris. Both are quality criteria of a biometric characteristic. Distinctiveness is the main prerequesite and expresses that the biometric characteristic enables the distinction between different individuals. Stability is crucial for the robustness of a biometric system and expresses that the biometric characteristic does not change or vary over time. Intrinsic changes mainly result from ageing. Extrinsic changes are caused by different acquisition conditions, e.g., light or position (rotation, tilt, camera distance) of the fish.

In the following we experimentally assess fish iris distinctiveness and stability. The session SDs enable to draw conclusions on the distinctiveness of the fish iris and the temporal SDs enable to assess fish iris stability. Furthermore, results for semi-automated and CNN-based segmentation enable to draw conclusions on the theoretical performance as well as for a fully automated biometric system.

C. Results and Discussion

The experimental evaluation is done in four steps: (i) It is assessed how much rotation is in the data. Since rotation negatively influences the MSs we need to ascertain if rotational pre-alignment is required or if rotation compensation in the matching stage is sufficient (Sec. IV-C1). Thus, rotational differences in the session and temporal SDs are assessed by comparing the results of the baseline configurations where no rotational pre-alignment (NO) is applied. (ii) We assess the basic suitability of the different rotational pre-alignment strategies by analyzing the verification performances for the temporal and session SDs. (Sec. IV-C2). (iii) Identification performance results are presented. Results for the temporal and session SDs reflect real world scenarios in terms of repeated identification with no time delay and varying time delays for tracking and monitoring of a fish (Sec. IV-C3). (iv) Finally, the presented results are contrasted with the results presented in related literature.

1) Rotation compensation performance: In order to get an impression of the rotation which is contained in the LT & ST dataset an analysis of the verification performances of NO for the session and temporal SDs is performed. For verification performance evaluation the equal error rate (EER) is a general benchmark. Basically, the question is if shifting during matching is sufficient to overcome rotational variations, i.e. to show the need for rotational pre-alignment. To avoid side affects caused by segmentation errors the semi-automated segmented fish irides (GT) were utilized.

It is expected that with an increasing shifting value the EER decreases until a lower boundary is reached. Therefore, the shifting value in the matching stage is varied from 0 to 16 for the session SDs and from 0 to 64 (stepsize 2) for the temporal SDs and it is assessed how the EERs change. A shifting value of 1 corresponds to a rotation of 360°/512=0.7°where 512 is the width of the polar transformed and normalized iris. This

This article has been accepted for publication in a future issue of this journal, but has not been fully edited. Content may change prior to final publication. Citation information: DOI 10.1109/TII.2020.3006933, IEEE Transactions on Industrial Informatics

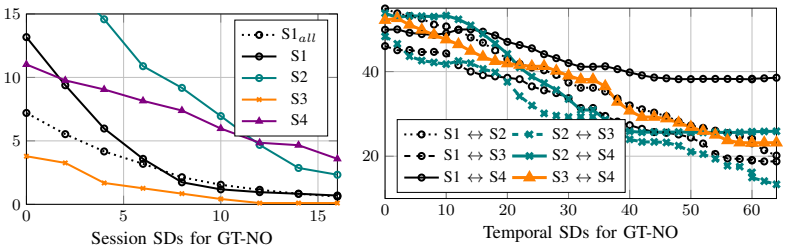

Fig. 7: EERs for different rotation compensation shifting values [X-Axis: Rotation Compensation in ±Bit, Y-Axis: EER in %]

means that the maximum amount of rotation, in case of the temporal SDs, which has been compensated for is +/- 44.8°.

The charts in Fig. 7 show the EERs achieved for different shifting values and the different session- and temporal SDs, respectively. For the session SDs rotation compensation in the matching stage is sufficient to achieve good performances (EERs<4%) with a shifting value set to 16. Even with a lower shifting value of 8 EERs below 9% are achieved. However, rotation compensation is required to attain acceptable EERs for the temporal SDs. The difference between the session and temporal SDs can be attributed to the data acquisition. Within a session the rotational variation for the iris images of a fish were nominal and mainly caused by body movements of the fish. For each new acquisition session each fish was once again positioned on a table which leads to stronger rotational differences in the temporal SDs. For the temporal SDs in the right chart of Fig.7 it is obvious that this shift-based rotation compensation is not sufficient to overcome the rotational variations. Even with very high shifting values no acceptable EERs are achieved. Whereas for the session SDs a shifting value of 16 is suited to achieve EERs below 4%, for the temporal SDs all EERs stay over 39%. While it would be possible to use a higher shift-based rotation compensation this affects the outcome in terms of timeliness, i.e., matching would take longer, as well as in performance since interclass FIC matches are also improved, see [23] for research on this topic as pertaining to the human iris. Based on these results it can be concluded that for fish iris images captured at different dates (as present in the LT dataset) rotational pre-alignment is required, in addition to rotation compensation in the matching stage. This finding also applies to data recorded in a realistic application, since this will result in different rotations of the iris from the same fish.

The low EERs (<4%) for the session SDs already give a first evidence that the fish iris shows a high distinctiveness, i.e. it enables to discriminate between fish in the individual sessions (S1$_{all}$ = 330 fish). On the other hand, the temporal SD EERs are affected by external variations (i.e. rotational variations) and it is not possible to draw conclusions on the stability of the fish iris.

2) Rotational pre-alignment and verification performance analysis: The verification performances, expressed as EERs, for the different rotational pre-alignment strategies as well as the session- and temporal SDs enable to draw first conclusions on the stability. The results allow to determine to which degree the verification performance is affected by intrinsic changes of the fish iris and if pre-alignment is suited to overcome extrinsic changes, i.e. , rotational variations. Also, it is not clear how the results for the session SDs, which show less rotational variations, are affected by rotational pre-alignment. Again, all results were computed for the semi-automated segmented fish irides to avoid side effects. Results for CNN-based segmentation enable to investigate the feasibility of a fully automated fish identification system and how it impacts the verification performances.

Results are summarized in Table I. Based on the insights of the rotation compensation analysis all EERs are computed with shifting values 16 and 32. It is not clear if a shifting value of

Segment.	Config.	Session SDs (ST)					Temporal SDs (LT)					
		S1$_{all}$	S1	S2	S3	S4	S1↔S2	S2↔S3	S3↔S4	S1↔S3	S2↔S4	S1↔S4
SHIFT 16												
GT	NO	0.65	0.71	2.52	0.15	3.91	/	/	/	/	+	-
	PCA	0.92	1.03	0.29	0.19	*	/	11.69	/	/	+	-
	MAX	3.94	0.45	0.21	0.06	*	15.52	10.32	/	15.42	29.28	-
	PCA$_{ROT}$	*	*	*	*	*	/	12.81	/	/	+	-
	MAX$_{ROT}$	*	*	*	*	*	14.96	9.87	19.6	15.96	24.44	32.56
CNN	NO	0.62	0.96	2.9	1.43	*	/	/	/	/	+	-
	PCA	0.52	0.77	1.13	1.39	4.92	/	12.73	/	/	+	-
	MAX	1.14	0.4	1.3	1.2	*	15.52	10.89	/	16.73	26.31	-
	PCA$_{ROT}$	*	*	*	*	*	/	12.92	/	/	+	-
	MAX$_{ROT}$	*	*	*	*	*	15.52	11.46	19.7	16.85	24.85	33.01
SHIFT 32												
GT	NO	0.21	0.41	0.0	0.06	1.04	/	/	/	/	+	-
	PCA	0.27	0.47	0.02	0.02	2.94	17.58	9.71	18.21	19.23	+	-
	MAX	4.11	0.48	0.01	0.05	*	15.67	9.72	/	15.83	28.84	-
	PCA$_{ROT}$	*	*	*	*	*	18.4	10.21	19.41	18.69	29.83	-
	MAX$_{ROT}$	*	*	*	*	*	14.6	10.17	17.24	15.15	23.54	34.02
CNN	NO	0.17	0.45	1.09	1.44	2.04	/	/	/	/	+	-
	PCA	0.18	0.37	1.09	1.41	1.95	17.87	11.15	19.55	/	+	-
	MAX	1.11	0.35	1.17	1.25	*	15.46	11.59	/	16.4	26.43	-
	PCA$_{ROT}$	*	*	*	*	*	17.65	11.79	19.65	/	+	-
	MAX$_{ROT}$	*	*	*	*	*	14.58	10.86	18.87	15.98	24.58	33.77

TABLE I: Verification performances (EERs [%]) for the session and temporal SDs, different rotational pre-alignment configurations, rotation compensation shifting values 16/32 and for semi-automated (GT) and CNN segmented (CNN) fish irides. Irrelevant EERs are replaced as follows: Session SDs EERs worse than 5% are replaced by a star (∗). Green coloured results signalize all EERs $< 1\%$ in the session SD results. For the first four columns in the temporal SDs EERs worse than 20% are replaced by a slash (/). For the S2↔S4 EERs results worse than 30% and for S2↔S4 EERs worse than 35% are replaced by a plus (+) and minus (-), respectively. For all temporal SDs yellow coloured results highlight EERs $< 10\%$.

This article has been accepted for publication in a future issue of this journal, but has not been fully edited. Content may change prior to final publication. Citation information: DOI 10.1109/TII.2020.3006933, IEEE Transactions on Industrial Informatics

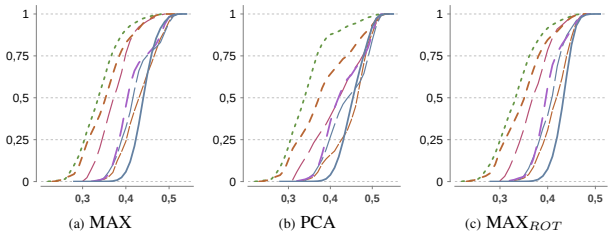

(a) MAX (b) PCA (c) MAX_{ROT}

Fig. 8: Intra-/Interclass CDFs of the temporal SDs and selected rotational pre-alignment strategies (GT, SHIFT 16) [X-Axis: Matching Score, Y-Axis: Cumulative Probability]

32 always improves the EER. Basically, a higher shifting value increases the chance to find the correct rotational alignment of two FICs from the same fish, but it also increases the risk of finding a rotational alignment of two FICs from different fish at which they are more similar to each other.

Results for GT and NO show that for the session SDs a shifting value of 16 is sufficient to achieve acceptable EERs $< 4\%$ which improves to EERs $< 1.04\%$ when shifting with a value of 32. As already stated, this indicates the distinctiveness of the salmon fish iris pattern. Fortunately, the EERs for the CNN results of NO (SHIFT 16 and 32) are close to the GT EERs which indicates that the employed CNN segmentation performs well and enables to set up a fully automated system.

When considering the temporal EERs for NO (GT&CNN) two assumptions can be made: (i) as already concluded in Sec. IV-C1 there is more rotational variation in the temporal SDs compared to the session SDs and (ii) the salmon fish iris definitely changes over time. The first assertion is shown by comparing the NO temporal SD results (GT&CNN) to all others where rotational pre-alignment, as well as a shift of 16, is applied. In contrast to the session SDs the EERs of the temporal SDs improve when applying rotational pre-alignment. This means that in case of the session SDs, which contain only little rotational variations, some of the rotational pre-alignment strategies add rotation to the data (EERs increase) and for the temporal SDs the majority of strategies reduce rotational variations significantly, i.e., the EERs decrease.

Results also show that for all pre-alignment strategies the higher shifting value 32 improves the EERs for the majority of results. Another interpretation of the results is that the current pre-alignment is future work and should be improved. Due to the good performance of the CNN-based segmentation most of the results are similar to the GT results. Thus, all subsequent conclusions hold for GT as well as for CNN. For the session SDs, S1 and S4 the results for SHIFT 16 and SHIFT 32 show that PCA performs better than MAX. For S2 and S3 there is no significant difference.

Contrary to the session SDs, for the temporal SDs MAX significantly outperforms PCA, especially when considering the SHIFT 16 EERs. Fig. 8a, Fig. 8b illustrate the cumulative MS distribution functions (CDF) for the different intraclass temporal SDs of MAX and PCA (GT), respectively. Furthermore, the interclass CDF computed over all temporal SDs (GT) is shown. The CDF of a SD gives the probability that a certain MS exists which is less or equal to that MS. The CDFs of certain intraclass SDs and the interclass SD are used to observe their overlap and to draw conclusions about their separability. It is easy to see that compared to PCA for MAX the intraclass CDFs shift away from the interclass CDF. However, there still remains an intersection with the interclass

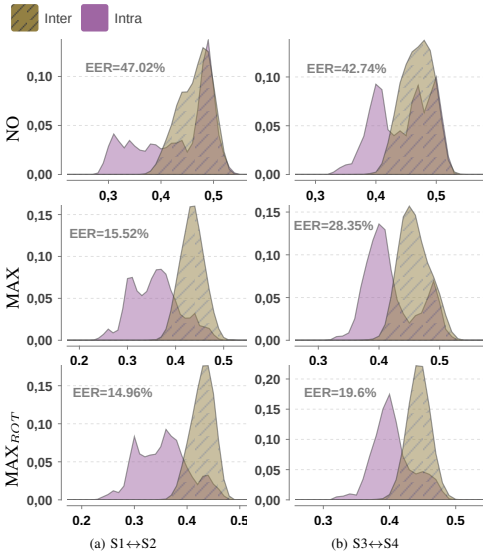

(a) S1↔S2 (b) S3↔S4

Fig. 9: Intra-/Interclass distribution charts for selected temporal SDs and selected rotational pre-alignment strategies (GT, SHIFT 16). [X-Axis: Matching Score, Y-Axis: Probability]

CDF for all temporal CDFs where S4 is involved. This is also reflected by the high EERs achieved for all temporal SDs which indicates that the salmon iris pattern changed from S3 to S4. This is further substantiated by the fact that for the session SDs and S4 with SHIFT 32 and NO (GT) an EER of 1.04% is achieved. Thus, it is very likely that the high EERs for all temporal SDs with S4 are caused by internal variations of the iris, i.e. growth of the fish eye and changing iris pattern.

Considering MAX_{ROT} and PCA_{ROT} the session SDs show that the EERs (Table I) increase significantly compared to NO. Note that EERs worse than 5% are replaced by a star (*) in the table. An explanation for this effect is that four FICs per iris and additional shifting significantly increases the risk of finding rotational alignments where the iris of different fish are similar to each other. However, the MAX_{ROT} EERs for the temporal SDs are superior to all other results. This is independent of the shifting value, confirming the assumption that if the rotational pre-alignment works further shift based compensation beyond what is required for a single session is not needed. Interestingly, PCA_{ROT} is not suited to improve the verification performances of the temporal SDs. The corresponding intraclass CDFs for the temporal SDs of MAX_{ROT} (GT, SHIFT 16) are shown in Fig. 8c. Compared to the MAX CDFs in Fig. 8a it is obvious that the intersection of

This article has been accepted for publication in a future issue of this journal, but has not been fully edited. Content may change prior to final publication. Citation information: DOI 10.1109/TII.2020.3006933, IEEE Transactions on Industrial Informatics

the intraclass CDFs with S4 and the interclass CDF decreases. Finally, Fig.9 enables to compare the intra- and interclass SDs for the temporal SDs S1↔S2 and S3↔S4 (GT, SHIFT 16) computed with NO, MAX and MAX_{ROT}. For NO the charts illustrate that rotational misalignment causes an overlap of intraclass SDs with the interclass SDs. Considering MAX this overlap is significantly reduced by rotational pre-alignment and rotation compensation. For MAX there still is a high overlap of the inter- and interclass SD which is reduced when applying MAX_{ROT} for rotational pre-alignment.

3) Identification and real world scenario performances: By considering the identification performances for the session and temporal SDs first conclusions on the feasibility of salmon fish iris identification in a real world scenario can be drawn. Hence, the CNN-based segmented fish irides were utilized for the identification performance experiments.

Basically, session SDs indicate the feasibility of short term identification and temporal SDs show the performance for long term identification. Identification performances are assessed based on the Rank-1 recognition rate (RR). In Fig. 10 and Fig. 11 the Rank-1 RR for the rotational pre-alignment strategies and the session and temporal SDs are summarized, respectively. The temporal SDs results are comparable to the verification results for SHIFT 16 and the general statements are the same. Summarized, PCA performs better than MAX and MAX_{ROT} and PCA_{ROT} improves the performance for S4 slightly. With PCA, except for S4, all Rank-1 RRs are higher than ∼98.5%. The best performance for S4 is achieved with PCA_{ROT} showing a Rank-1 RR close to ∼96%.

Results confirm that the salmon fish iris is highly distinctive and enables short term fish identification. However, same as for the verification results the identification performances for the temporal SDs again show that intrinsic variations, i.e. aging, cause decreasing Rank-1 RRs. Again, the best performances are achieved with MAX and MAX_{ROT}. The best performance is shown for the temporal SD S2↔S3 with ∼80% followed by S1↔S2 and S1↔S3. Again, this indicates that the iris changed significantly from the S3 to S4. Even S1↔S3 with ∼65% is better than ∼50% achieved for S3↔S4 with a shorter time-span between the acquisition sessions. Together with the verification performance results it can be concluded that the robustness of fish iris biometrics suffers from a missing long term stability of the fish iris. However, the S1↔S2, S2↔S3 and S1↔S3 results indicate that identification in a real world scenario is feasible but the system needs to consider this issue by updating the biometric templates of each fish (FIC) in short periods. Especially, at an age over 6 months this becomes crucial as the pattern changes significantly at this age.

This is also an interesting result with regard to the biometry of the human iris, since the human iris shows ageing effects, although the severity of the impact is controversial (see [24]). The fish under study have now also shown an ageing effect, which can much more readily observed and researched owing to the faster life cycle of the Atlantic salmon.

4) Comparison to related literature: Finally, the Atlantic fish iris identification results are compared and discussed with the literature presented in Section II. Different to the low stability of the Atlantic salmon iris, the results for Patagonian catfish in [8] showed that the lateral skin spot pattern has a high distinctiveness as well as long term stability. A direct comparison of the results is not feasible, as the approach in [8] relies on I^3S [25] which is a computer-aided photo identification application for underwater animals. With the help of this software, three reference points and all spots in each lateral image were annotated manually and the software performed the matching. If the authors achieve similar results in the future with an automated method, the approach would have great potential in terms of distinctiveness and stability.

If the skin pattern is used as a characteristic it is often not clear if it is present for all fish of the same species and if this pattern is present at all ages. The results for Atlantic salmon identification in [9] which are based on the lateral opercolum pattern indicate the non-suitability as a biometric characteristic because some fish showed no pattern or it disappeared. Similarly, in [11] the absence of the dorsal head view pattern of Chinook salmon for a large amount of individuals has been reported.

The results presented by [12] for delta smelt identification based on dorsal head view images are comparable to ours in terms of stability. Even if the pattern was localized manually, results for automated matching indicated that the pattern changes over time and matured fish show more distinctive

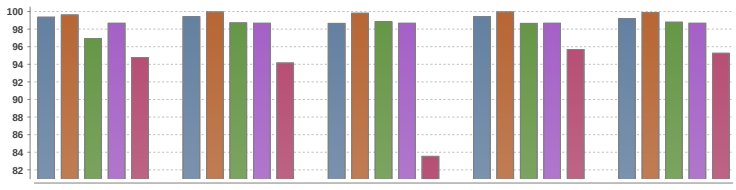

Fig. 10: Session SDs (CNN, SHIFT 16) – Identification performance evaluation [Y-Axis: Rank-1 recognition rate %]

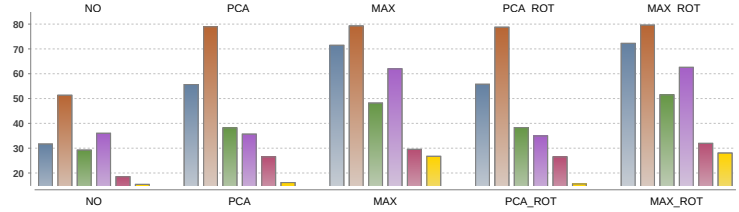

Fig. 11: Temporal SDs (CNN, SHIFT 16) – Identification performance evaluation [Y-Axis: Rank-1 recognition rate %]

This article has been accepted for publication in a future issue of this journal, but has not been fully edited. Content may change prior to final publication. Citation information: DOI 10.1109/TII.2020.3006933, IEEE Transactions on Industrial Informatics

patterns. On the contrary, our results show that the distinctiveness of Atlantic salmon based on the iris pattern could get a little worse with older age. A comparison regarding the distinctiveness is not possible because the fish sample size was smaller and no results for one point in time (= session SDs in our work) were presented.

Compared to our session SD results the experiments for armored catfish identification using ventral images [5] and lionfish identification using lateral images [10] showed poorer recognition accuracies, although manual localization was performed.

It can be concluded, that the suitability of the skin pattern as a biometric characteristic must be examined closely, same as for the iris pattern. In the future approaches with automated skin pattern localization should be sought by the community.

The basic advantage of the iris is that most fish species show a visible iris pattern which is likely suited as a biometric characteristic to set up a FDSS. Additionally, as shown in our work the iris pattern can be localized automatically which enables automated identification.

V. Conclusion

Fish identification is a basic tool required to move from mass to smart production in intensive aquaculture. Non-invasive methods are fast, cheap and beneficial for fish welfare. Biometric approaches based on the individuality of the skin pattern lack of visible patterns in general and missing patterns in various life phases of a single fish. Therefore, this work demonstrated the principal feasibility of Atlantic salmon fish identification using iris images as biometric characteristic. Distinctiveness and stability of the salmon fish iris were assessed based on a short and long term dataset.

Results for 330 different fish in the short term dataset showed that the fish iris is highly distinctive. For all subsets in the short term dataset identification rates of over 95% could be achieved. The stability of the fish iris was assessed based on the long term dataset. Due to different rotational alignments between iris images of the same fish captured at different points in time a set of rotational pre-alignment strategies were applied and evaluated. Experiments showed that rotation compensation in the matching stage, even with a high shifting value, is not sufficient to achieve acceptable EERs. The best results for the long term dataset were achieved with the rotational pre-alignment strategy MAX which uses the maximum length pupillary center of mass to boundary vector for alignment. An additional improvement could be achieved by enrolling four 90°rotated templates of each iris (MAX_{ROT}), reducing errors caused by rotational pre-alignment resulting in at most 45°rotational error in iris images.

Results showed that the verification performances decrease with an increasing time span between the different acquisition sessions. Interestingly, results for the first two (S1↔S2 = 14.96%) and the last two successive session (S3↔S4 = 19.6%) sessions are worse than for the middle sessions (S2↔S3 = 9.87%). This leads to two main conclusions: (i) The salmon fish iris shows a weak stability, i.e. due to ageing (=size and pattern changes). (ii) The variations caused from ageing from month 2 to 4 and 6 to 8 are much stronger than in-between from month 4 to 6.

Results achieved with semi-automated segmented fish irides were compared to those computed with a fully automated CNN-based approach. The results show that automated segmentation is possible and comparable to that achieved with the semi-automated segmented irides. This is crucial in order to establish a fully automated fish identification system. Additionally, for a real world scenario the identification performance of the long term dataset is of relevance and the identification rates for MAX_{ROT} on the different subsets vary between 28% and 80%. Based on the missing stability of the salmon fish iris and the accuracies for the successive subsets S1↔S2 = 72.00%, S2↔S3 = 80.00% and S3↔S4 = 51.00% the following conclusion can be made: Salmon fish iris identification is feasible in a real world scenario with the precondition that the biometric template of each fish in the database of the biometric system is updated periodically, especially when the fish gets older than 6 months. In human biometrics this is referred to as adaptive biometric systems.

A. Future Work

It was not feasible to consider the impact and change of pigmentation with age in this work. The change in pigmentation can be disregarded for short time spans. However, given the decrease in identification performance between image acquisition sessions that are further apart in time, this may be the reason for the decrease.

Future work needs to consider a realistic environment, i.e. underwater iris images of swimming fish. For example, fish could be forced to pass through a narrative tube with their lateral side to the camera at a relatively constant distance similar to what explained in [26], [27]. In order to compensate for differences between iris images from different sessions future experiments should consider iris image preprocessing.

Furthermore, the use of near-infrared imaging could improve the identification performance since the iris is likely pigmented given that it is an extension of the epithelial layer. It is known that the speed of adaptation and the pigmentation of the epithelial layer changes, stronger pigmentation with increasing age [15]. The impact on the pigmentation of the iris is unknown but is likely to happen. Independent of visible light or near infrared imaging, an appropriate illumination as common in human iris imaging needs to be considered. However, special care must be taken to ensure that the lighting does not pose any health risks or impacts fish welfare.

Finally, the use of other or additional biometric performance metrics should be considered in future work. The use of other metrics will depend in particular on the respective application or the focus of the investigation.

References

[1] FAO, *The State of World Fisheries and Aquaculture 2018 (SOFIA): Meeting the Sustainable Development Goals*. Food & Agriculture Organization, 2018.

[2] F. Antonucci and C. Costa, "Precision aquaculture: a short review on engineering innovations," *Aquaculture International*, pp. 1–17, 2019.

[3] M. Saberioon, A. Gholizadeh, P. Cisar, A. Pautsina, and J. Urban, "Application of machine vision systems in aquaculture with emphasis on fish: state-of-the-art and key issues," *Reviews in Aquaculture*, vol. 9, no. 4, pp. 369–387, 2017.

This article has been accepted for publication in a future issue of this journal, but has not been fully edited. Content may change prior to final publication. Citation information: DOI 10.1109/TII.2020.3006933, IEEE Transactions on Industrial Informatics

[4] M. Sandford, G. Castillo, and T.-C. Hung, "A review of fish identification methods applied on small fish," *Reviews in Aquaculture*, mar 2019.
[5] R. Dala-Corte, J. A. Moschetta, and F. Becker, "Photo-identification as a technique for recognition of individual fish: a test with the freshwater armored catfish," *Neotropical Ichthyology*, vol. 14, 2016.
[6] J. Delcourt, M. Ovidio, M. Denoël, M. Muller, H. Pendeville, J.-L. Deneubourg, and P. Poncin, "Individual identification and marking techniques for zebrafish," *Reviews in Fish Biology and Fisheries*, vol. 28, no. 4, pp. 839–864, sep 2018.
[7] Y. Lu, X. He, Y. Wen, and P. Wang, "A new cow identification system based on iris analysis and recognition," *Int. Journal of Biometrics*, vol. 6, pp. 18–32, 2014.
[8] J. P. Barriga, J. M. Chiarello-Sosa, R. Juncos, and M. Á. Battini, "Photo-identification and the effects of tagging on the patagonian catfish hatcheria macraei," *Environmental Biology of Fishes*, vol. 98, no. 4, pp. 1163–1171, sep 2014.
[9] L. H. Stien, J. Nilsson, S. Bui, J. E. Fosseidengen, T. S. Kristiansen, Ø. Øverli, and O. Folkedal, "Consistent melanophore spot patterns allow long-term individual recognition of atlantic salmon salmo salar," *Journal of Fish Biology*, vol. 91, no. 6, pp. 1699–1712, nov 2017.
[10] L. C. T. Chaves, J. Hall, J. L. L. Feitosa, and I. M. Côté, "Photo-identification as a simple tool for studying invasive lionfish populations," *Journal of Fish Biology*, vol. 88, no. 2, pp. 800–804, 2015.
[11] J. Merz, P. Skvorc, S. Sogard, C. Watry, S. Blankenship, and E. V. Nieuwenhuyse, "Onset of melanophore patterns in the head region of chinook salmon: A natural marker for the reidentification of individual fish," *North American Journal of Fisheries Management*, vol. 32, no. 4, pp. 806–816, aug 2012.
[12] G. Castillo, M. Sandford, T.-C. Hung, G. Tigan, J. Lindberg, W.-R. Yang, and E. V. Nieuwenhuyse, "Using natural marks to identify individual cultured adult delta smelt," *North American Journal of Fisheries Management*, vol. 38, no. 3, pp. 698–705, may 2018.
[13] B. Burnside and B. Nagle, "Retinomotor movements of photoreceptors and retinal pigment epithelium: Mechanisms and regulation," *Progress in Retinal Research*, vol. 2, pp. 67 – 109, 1983.
[14] F. Munz, "Vision: Visual pigments," in *Sensory Systems and Electric Organs*. Academic Press, 1971, vol. 5, pp. 1 – 32.
[15] M. A. Ali, "The ocular structure, retinomotor and photo-behavioral responses of juvenile pacific salmon," *Canadian Journal of Zoology*, vol. 37, no. 6, pp. 965–996, 1958.
[16] L. Masek, "Recognition of human iris patterns for biometric identification," Master's thesis, University of Western Australia, 2003.
[17] P. W. Andreas Uhl, "Weighted adaptive hough and ellipsopolar transforms for real-time iris segmentation," in *Procs. of the IAPR/IEEE Int. Conf. on Biometrics (ICB'12)*, New Delhi, India, 2012, pp. 1–8.
[18] H. Hofbauer, E. Jalilian, and A. Uhl, "Exploiting superior cnn-based iris segmentation for better recognition accuracy," *Pattern Recognition Letters*, vol. 120, pp. 17–23, 2019.
[19] V. Badrinarayanan, A. Kendall, and R. Cipolla, "Segnet: A deep convolutional encoder-decoder architecture for image segmentation," *IEEE Trans. on pattern analysis and machine intelligence*, vol. 39, no. 12, pp. 2481–2495, 2017.
[20] J. Daugman, "The importance of being random: Statistical principles of iris recognition," *Pattern Recognition*, vol. 36, no. 2, pp. 279–291, 2003.
[21] University of Salzburg, "USIT – University of Salzburg iris toolkit," http://www.wavelab.at/sources/USIT, University of Salzburg, 2017.
[22] D. Maltoni, D. Maio, A. K. Jain, and S. Prabhakar, *Handbook of fingerprint recognition*. Springer New York, 2009.
[23] A. U. Christian Rathgeb, Heinz Hofbauer and C. Busch, "Triplea: Accelerated accuracy-preserving alignment for iris-codes," in *Procs. of the 9th IAPR/IEEE Int. Conf. on Biometrics (ICB'16)*, 2016, pp. 1–8.
[24] H. Hofbauer, I. Tomeo-Reyes, and A. Uhl, "Isolating iris template ageing in a semi-controlled environment," in *Procs. of the Int. Conf. of the Biometrics Special Interest Group (BIOSIG'16)*, Darmstadt, Germany, 2016, p. 8.
[25] J. den Hartog and R. Reijns, "I3s: Interactive individual identification system," http://www.reijns.com/i3s/index.html, 2019, last accessed: 25.04.2019.
[26] J. M. Miranda and M. Romero, "A prototype to measure rainbow trout's length using image processing," *Aquacultural Engineering*, vol. 76, pp. 41 – 49, 2017.
[27] B. Zion, V. Alchanatis, V. Ostrovsky, A. Barki, and I. Karplus, "Real-time underwater sorting of edible fish species," *Computers and Electronics in Agriculture*, vol. 56, no. 1, pp. 34 – 45, 2007.

Rudolf Schraml is a PhD student at the University of Salzburg. His research interests are in physical object identification and authentication in different fields of applications.

Heinz Hofbauer holds a doctoral degree in computer science. He works as a researcher at the University of Salzburg and has published extensively in the fields of content and media security and biometrics.

Ehsaneddin Jalilian is a PhD student at the University of Salzburg. His research interests include: Visual recognition, Deep learning, and Biometrics.

Dinara Bekkozhayeva is a PhD student at the University of South Bohemia in České Budějovice, Czech Republic. Her research interests are fish morphology, fish taxonomy, fish identification and fish welfare.

Mohammadmehdi Saberioon holds a doctoral degree in precision farming engineering. His current research interests include applied remote sensing, field and imaging spectroscopy, and advanced artificial intelligence in different disciplines of agriculture and environmental studies.

Petr Cisar holds a doctoral degree in cybernetics (visual speech recognition). His research interest is application of computer vision and signal processing in the aquaculture. He develops the systems and methods for fish/crayfish behaviour/appearance monitoring and analysis.

Andreas Uhl is a full professor at the Computer Sciences Department at the University of Salzburg, Austria, where he leads the Multimedia Signal Processing and Security Lab. His research interests are in image and video processing, biometrics, visual data encryption, medical image analysis and high-performance computing.

4. Conclusion

The main paradigm in the scope of Industry 4.0, is that the real world conflates with the virtual in the IoT. The most common approach to integrate non-electric and non-communicating objects is physical labeling using RFID transponders. As shown in this thesis, physical object identification is a promising alternative to recognize non-electric and non-communication objects in the industry. The greatest advantages are that the objects are not physically marked and that the use of the object's own features can increase security against counterfeiting.

For this thesis, roundwood and fish identification were investigated. The benefits for roundwood identification are manifold. Within the forest-based industries it is a key technology to increase the digitization and on a global scale it could be a method, to fight against illegal logging. Fish identification (on the other hand) is a pre-requisite in intensive aquaculture to move from mass to precision fish farming. By considering each fish as an individual, health and cultivation related information for each fish as well as for the total stock can be gathered and utilized to improve the production by focusing on fish welfare criteria.

We investigated the basic feasibility of roundwood tracking using log end images and Atlantic salmon identification using iris images. For both applications, datasets were acquired and verification and identification performance experiments were performed. Moreover, distinctiveness and stability of the utilized biometric characteristic were assessed.

In case of roundwood tracking, the applicability of fingerprint and iris recognition methods for roundwood identification using log end images has been demonstrated. Results indicate that the annual ring pattern is highly distinctive. Regarding the stability of the annual ring pattern, longitudinal, temporal and surface variations were investigated. Results show a high stability in case of log end cutting, i. e. the annual ring pattern does not change significantly if a thin slice is cut off from the log end. Furthermore, results indicate a high robustness to temporal variations caused by light and humidity, which result in deformations and discolourations. Finally, surface variations were assessed, which result from using different cutting tools for the first cut in the forest and the clearance cut in the sawmill. Results show, that surface variations have no impact on the performance and stability of log end biometrics.

For the Atlantic salmon iris, we were also able to prove its distinctiveness, i. e. the results demonstrate, that the iris as biometric characteristic is suited to discriminate between #330 fish. However, regarding stability our experimental evaluation on the long term dataset showed a weak stability of the iris, i. e. the Atlantic salmon iris changes rapidly over time which relates to ageing effects in human biometrics. This led to the conclusion, that for Atlantic salmon iris identification the biometric template of each fish needs to updated periodically, which is referred to as an adaptive biometric system.

Finally, we demonstrated the feasibility of classification-based drug packaging authentication which is an alternative to serialization-based authentication. In our experiments we investigated two basic requirements: positional and instance generalization of the packaging material texture. Our experiments for 45 different drugs proved both requirements successfully. Furthermore, single sensor and cross-sensor experiments towards a mobile-device based system were performed. Results indicate the principal feasibility of mobile-device based drug packaging authentication, however, in case of the cross-sensor scenario the authentication performance degraded significantly.

In summary, we were able to show the principal feasibility of physical object identification

and authentication for all three applications. Confirming the basic feasibility is however only the first step toward a real world application. As outlined in the open challenges section for each application future work needs to consider realistic data acquisition in order to enable the move from technology to scenario and operational evaluation.

Bibliography

[1] A. I. Awad. From classical methods to animal biometrics: A review on cattle identification and tracking. *Computers and Electronics in Agriculture*, 123:423–435, apr 2016.

[2] W. Barrett. Biometrics of cut tree faces. In T. Sobh, editor, *Advances in Computer and Information Sciences and Engineering*, pages 562–565. Springer Netherlands, 2008.

[3] U. G. Barron, G. Corkery, B. Barry, F. Butler, K. McDonnell, and S. Ward. Assessment of retinal recognition technology as a biometric method for sheep identification. *Computers and Electronics in Agriculture*, 60(2):156–166, mar 2008.

[4] M. Carpentier, P. Giguère, and J. Gaudreault. Tree species identification from bark images using convolutional neural networks. *CoRR*, abs/1803.00949, 2018.

[5] S. Chiorescu and A. Grönlund. The fingerprint approach: using data generated by a 2-axis log scanner to accomplish traceability in the sawmill's log yard. *Forest Products Journal*, 53:78–86, 2003.

[6] S. Chiorescu and A. Grönlund. The fingerprint method: Using over-bark and under-bark log measurement data generated by three-dimensional log scanners in combination with radiofrequency identification tags to achieve traceability in the log yard at the sawmill. *Scandinavian Journal of Forest Research*, 19(4):374–383, 2004.

[7] N. R. Council. *Biometric Recognition: Challenges and Opportunities*. The National Academies Press, Washington, DC, 2010.

[8] D. Deb, S. Wiper, S. Gong, Y. Shi, C. Tymoszek, A. Fletcher, and A. K. Jain. Face recognition: Primates in the wild. In *2018 IEEE 9th International Conference on Biometrics Theory, Applications and Systems (BTAS)*. IEEE, oct 2018.

[9] J. Flodin, J. Oja, and A. Grönlund. Fingerprint traceability of sawn products using x-ray log scanning and sawn timber surface scanning. In *Proccedings of Quality control for wood and wood products: COST Action E 53 the first conference*, 2007.

[10] J. Flodin, J. Oja, and A. Grönlund. Fingerprint traceability of logs using the outer shape and the tracheid effect. *Forest Products Journal*, 58(4):21–27, 2008.

[11] J. Flodin, J. Oja, and J. Grönlund. Fingerprint traceability of sawn products using industrial measurement systems for x-ray log scanning and sawn timber surface scanning. *Forest Products Journal*, 58:11, 2008.

[12] ISO/IEC 2382-37:2017(E). Information technology - Vocabulary - Part 37: Biometrics. Technical report, ISO/IEC, 2017.

[13] ISO/IEC DIS 19795-2:2007 (E). Information technology - Biometric performance testing and reporting - Part 2: Testing methodologies for technology and scenario evaluation. Technical report, ISO/IEC, 2007.

[14] A. Jain, A. Ross, and S. Prabhakar. Fingerprint matching using minutiae and texture features. In *Procs. of the International Conference on Image Processing (ICIP'01)*, volume 3, pages 282–285, Thessaloniki, GR, 2001.

[15] E. Johansson, D. Johansson, J. Skog, and M. Fredriksson. Automated knot detection for high speed computed tomography on pinus sylvestris l. and picea abies (l.) karst. using ellipse fitting in concentric surfaces. *Computers and Electronics in Agriculture*, 96:238 – 245, 2013.

[16] C. Kauba, L. Debiasi, R. Schraml, and A. Uhl. Towards drug counterfeit detection using package paperboard classification. In *Advances in Multimedia Information Processing – Proceedings of the 17th Pacific-Rim Conference on Multimedia (PCM'16)*, volume 9917 of *Springer LNCS*, pages 136–146, Xi'an, CN, 2016.

[17] S. Kwok, O. P. Ng, A. H. Tsang, and H. Liem. Physimetric identification (physi-id) - applying biometric concept in physical object identification. *Computers in Industry*, 62(1):32–41, 2011.

[18] S. Z. Li and A. Jain, editors. *Biometric System Components*, pages 135–135. Springer US, Boston, MA, 2009.

[19] R. Maes and I. Verbauwhede. Physically Unclonable Functions: A Study on the State of the Art and Future Research Directions. In A.-R. Sadeghi and D. Naccache, editors, *Towards Hardware-Intrinsic Security*, Information Security and Cryptography, pages 3–37. Springer Berlin / Heidelberg, 2010.

[20] T. Pahlberg, O. Hagman, and M. Thurley. Recognition of boards using wood fingerprints based on a fusion of feature detection methods. *Computers and Electronics in Agriculture*, 111:164–173, 2015.

[21] T. Pahlberg, E. Johansson, O. Hagman, and M. Thurley. Wood fingerprint recognition using knot neighborhood k-plet descriptors. *Wood Science and Technology*, 49(1):7–20, 2015.

[22] M. Sandford, G. Castillo, and T.-C. Hung. A review of fish identification methods applied on small fish. *Reviews in Aquaculture*, mar 2019.

[23] W. J. Scheirer, A. Rocha, A. Sapkota, and T. E. Boult. Towards open set recognition. *IEEE Transactions on Pattern Analysis and Machine Intelligence (T-PAMI)*, 35, July 2013.

[24] R. Schraml, J. Charwat-Pessler, K. Entacher, A. Petutschnigg, and A. Uhl. Roundwood tracking using log end biometrics. In *Proceedings of the Annual GIL Meeting (GIL'2016)*, LNI, pages 189–192. Gesellschaft für Informatik, 2016.

[25] R. Schraml, J. Charwat-Pessler, A. Petutschnigg, and A. Uhl. Towards the applicability of biometric wood log traceability using digital log end images. *Computers and Electronics in Agriculture*, 119:112–122, 2015.

[26] R. Schraml, J. Charwat-Pessler, and A. Uhl. Temporal and longitudinal variances in wood log cross-section image analysis. In *IEEE International Conference on Image Processing (ICIP'14)*, pages 5706–5710, Paris, FR, Oct. 2014.

[27] R. Schraml, L. Debiasi, C. Kauba, and A. Uhl. On the feasibility of classification-based product package authentication. In *IEEE Workshop on Information Forensics and Security (WIFS'17)*, page 6, Rennes, FR, December 2017.

[28] R. Schraml, L. Debiasi, and A. Uhl. Real or fake: Mobile device drug packaging authentication. In *Proceedings of the 6th ACM Workshop on Information Hiding and Multimedia Security (IH&MMSec 2018)*, pages 121–126, Innsbruck, AUT, 2018.

[29] R. Schraml, K. Entacher, A. Petutschnigg, T. Young, and A. Uhl. Matching score models for hyperspectral range analysis to improve wood log traceability by fingerprint methods. *Mathematics*, 8(7):10, 2020.

[30] R. Schraml, H. Hofbauer, E. Jalilian, D. Bekkozhayeva, M. Saberioon, P. Cisar, and A. Uhl. Towards fish individuality-based aquaculture. *IEEE Transactions on Industrial Informatics*, page 10, 2020. in press.

[31] R. Schraml, H. Hofbauer, A. Petutschnigg, and A. Uhl. Tree log identification based on digital cross-section images of log ends using fingerprint and iris recognition methods. In *Proceedings of the 16th International Conference on Computer Analysis of Images and Patterns (CAIP'15)*, LNCS, pages 752–765, Valetta, MLT, 2015. Springer Verlag.

[32] R. Schraml, H. Hofbauer, A. Petutschnigg, and A. Uhl. On rotational pre-alignment for tree log end identification using methods inspired by fingerprint and iris recognition. *Machine Vision and Applications*, 27(8):1289–1298, 2016.

[33] R. Schraml, A. Petutschnigg, and A. Uhl. Validation and reliability of the discriminative power of geometric wood log end features. In *Proceedings of the IEEE International Conference on Image Processing (ICIP'15)*, pages 3665–3669, Quebec, CAN, 2015.

[34] R. Schraml and A. Uhl. Similarity based cross-section segmentation in rough log end images. In L. Iliadis et al., editors, *Proceedings of the 10th Artificial Intelligence Applications and Innovations Conference (AIAI'14)*, volume 436 of *Springer IFIP AICT*, pages 614–621, Rhodes, GR, Sept. 2014.

[35] S. Villon, D. Mouillot, M. Chaumont, E. S. Darling, G. Subsol, T. Claverie, and S. VillÃ©ger. A deep learning method for accurate and fast identification of coral reef fishes in underwater images. *Ecological Informatics*, 48:238 – 244, 2018.

A. Appendix

A.1. Breakdown of Authors' Contribution

This section lists a breakdown of authors' contribution with respect to the papers included in this thesis. Andreas Uhl is the thesis advisor of Rudolf Schraml, likewise Alexander Petutschnigg and Karl Entacher were the thesis advisors of Johann-Charwat Pessler. Furthermore, Alexander Petutschnigg was project manager of the FWF TreeBio project and he is project coordinator of the TreeTrace FWF project. Petr Cisar is the thesis advisor of Dinara Bekkozhayeva. Since the explicit contribution of an advisor or project manager cannot be stated for a single paper, it is omitted in the following breakdown. However, for [29] Alexander Petutschnigg and Karl Entacher contributed as authors.

	Contribution (in %)												
Publication	Rudolf Schraml	Heinz Hofbauer	Luca Debiasi	Cristof Kauba	Johann Charwat-Pessler	Ehsaneddin Jalilian	Karl Entacher	Petr Cisar	Dinara Bekkozhayeva	Mohammadmehdi Saberioon	Alexander Petutschnigg	Timothy Young	Andreas Uhl
R. Schraml, J. Charwat-Pessler, and A. Uhl. Temporal and longitudinal variances in wood log cross-section image analysis. In *IEEE International Conference on Image Processing (ICIP'14)*, pages 5706–5710, Paris, FR, Oct. 2014	95				5								
R. Schraml, A. Petutschnigg, and A. Uhl. Validation and reliability of the discriminative power of geometric wood log end features. In *Proceedings of the IEEE International Conference on Image Processing (ICIP'15)*, pages 3665–3669, Quebec, CAN, 2015	100												
R. Schraml, H. Hofbauer, A. Petutschnigg, and A. Uhl. Tree log identification based on digital cross-section images of log ends using fingerprint and iris recognition methods. In *Proceedings of the 16th International Conference on Computer Analysis of Images and Patterns (CAIP'15)*, LNCS, pages 752–765, Valetta, MLT, 2015. Springer Verlag	65	35											
R. Schraml, J. Charwat-Pessler, A. Petutschnigg, and A. Uhl. Towards the applicability of biometric wood log traceability using digital log end images. *Computers and Electronics in Agriculture*, 119:112–122, 2015	95				5								
C. Kauba, L. Debiasi, R. Schraml, and A. Uhl. Towards drug counterfeit detection using package paperboard classification. In *Advances in Multimedia Information Processing – Proceedings of the 17th Pacific-Rim Conference on Multimedia (PCM'16)*, volume 9917 of *Springer LNCS*, pages 136–146, Xi'an, CN, 2016	20		40	40									

Appendix A. Appendix

Publication	Contribution (in %)												
	Rudolf Schraml	Heinz Hofbauer	Luca Debiasi	Cristof Kauba	Johann Charwat-Pessler	Ehsaneddin Jalilian	Karl Entacher	Petr Cisar	Dinara Bekkozhayeva	Mohammadmehdi Saberioon	Alexander Petutschnigg	Timothy Young	Andreas Uhl
R. Schraml, J. Charwat-Pessler, K. Entacher, A. Petutschnigg, and A. Uhl. Roundwood tracking using log end biometrics. In *Proceedings of the Annual GIL Meeting (GIL'2016)*, LNI, pages 189–192. Gesellschaft für Informatik, 2016	100												
R. Schraml, H. Hofbauer, A. Petutschnigg, and A. Uhl. On rotational pre-alignment for tree log end identification using methods inspired by fingerprint and iris recognition. *Machine Vision and Applications*, 27(8):1289–1298, 2016	70	30											
R. Schraml, L. Debiasi, C. Kauba, and A. Uhl. On the feasibility of classification-based product package authentication. In *IEEE Workshop on Information Forensics and Security (WIFS'17)*, page 6, Rennes, FR, December 2017	80		10	10									
R. Schraml, L. Debiasi, and A. Uhl. Real or fake: Mobile device drug packaging authentication. In *Proceedings of the 6th ACM Workshop on Information Hiding and Multimedia Security (IH&MMSec 2018)*, pages 121–126, Innsbruck, AUT, 2018	95		5										
R. Schraml, K. Entacher, A. Petutschnigg, T. Young, and A. Uhl. Matching score models for hyperspectral range analysis to improve wood log traceability by fingerprint methods. *Mathematics*, 8(7):10, 2020	40						15				40	5	
R. Schraml, H. Hofbauer, E. Jalilian, D. Bekkozhayeva, M. Saberioon, P. Cisar, and A. Uhl. Towards fish individuality-based aquaculture. *IEEE Transactions on Industrial Informatics*, page 10, 2020. in press	55	30				5			5	5			